Loughborough University

This item was submitted to Loughborough University as a PhD thesis by the author and is made available in the Institutional Repository (https://dspace.lboro.ac.uk/) under the following Creative Commons Licence conditions.

creative commons

COMMONS DEED

Attribution-NonCommercial-NoDerivs 2.5

You are free:

- to copy, distribute, display, and perform the work

Under the following conditions:

Attribution. You must attribute the work in the manner specified by the author or licensor.

Noncommercial. You may not use this work for commercial purposes.

No Derivative Works. You may not alter, transform, or build upon this work.

- For any reuse or distribution, you must make clear to others the license terms of this work.
- Any of these conditions can be waived if you get permission from the copyright holder.

Your fair use and other rights are in no way affected by the above.

This is a human-readable summary of the Legal Code (the full license).

Disclaimer

For the full text of this licence, please go to:
http://creativecommons.org/licenses/by-nc-nd/2.5/

Microstructural Evolution in Coated Conventionally Cast Ni-Based Superalloys

Scott David Newman

Department of Materials
Loughborough University

A doctoral thesis submitted in partial fulfilment of the requirements for the award of Doctor of Philosophy

December 2011

Acknowledgements

I would like to thank my project supervisors Professor Rachel Thomson for support and encouragement throughout the duration of the research and Dr Geoff West for assistance with experimental techniques, in particular for assistance with collecting three dimensional datasets.

The project was funded with support from the Engineering and Physical Science Research Council (EPSRC) and with support from the following industrial and academic partners: Alstom Power Ltd., E.ON Engineering Ltd., Doosan Babcock Energy Ltd., National Physical Laboratory, Praxair Surface Technologies, QinetiQ, Rolls-Royce plc, RWE npower, Siemens Industrial Turbomachinery Ltd. and Tata Steel Ltd. The partner universities are Bristol University, Cranfield University and the University of Nottingham. I am particularly grateful for the support from Dr Jon Wells from RWE npower for providing the opportunity to study ex-service components and who enabled me to be involved with an engine trial of components.

I would like to acknowledge members of the department for technical assistance and also thank members of the metals research group for their support throughout the duration of the research.

Abstract

The aim of this research project was to investigate the microstructural changes of MCrAlY coated Ni-based superalloys that are routinely used in industrial gas turbine engines for power generation. One of the main aims of the characterisation was to understand ageing time and temperature effects on the microstructural evolution so that a methodology could be developed where the characterisation of a thermally exposed microstructure can be used to estimate unknown service exposure conditions.

Industrial gas turbine engines normally operate at elevated temperatures for prolonged periods, resulting in the need for materials that can not only withstand the high temperatures but also the aggressive operating environments. Ni-based superalloys are usually chosen for components as they have excellent high temperature resistance whilst retaining high strength at operating temperatures. In order to provide protection against oxidation and corrosion, and to minimise the risk of a service failure the alloys are often coated.

A coating system is typically used which is made up of multiple layers of different compositions. An inner layer is applied to provide a bond for an outer high temperature thermal barrier coating (TBC). The inner MCrAlY overlay coating also provides an increase in resistance to oxidation and corrosion. These coatings work by forming dense thermally grown oxides (TGO). The dense TGO layer provides protection by selective oxidation of aluminium to form a continuous external alumina scale at the surface of the bondcoat. The alumina layer then acts as a diffusion barrier to suppress the formation of other detrimental oxides during extended thermal exposure, therefore helping to protect the substrate from further oxidation and improving the durability of the coating system under service conditions.

The microstructural characterisation of MCrAlY coated IN738LC isothermally aged samples with and without a TBC layer was investigated using various types of electron microscopy. Isothermally aged material was used to benchmark a thermodynamic and kinetic model developed within the research group which is able to predict the microstructure after thermal exposure. The characterisation methodologies were then used to investigate possible tools for determining effective service temperatures of complex components. In this work a series of microstructural features were quantified, which showed a correlation with ageing time and temperature, and were used to develop a temperature estimation technique for ex-service material based on microstructural evolution. Temperature estimation tools are the first steps in

developing remaining useful lifetime models. The benchmarking of the model using the quantification of features within the microstructure of isothermally aged material did show that the model is accurately able to predict the microstructure after thermal exposure.

The microstructural characterisation of isothermally aged samples with and without an Air Plasma Sprayed Thermal Barrier Coating (TBC) showed that the rate of oxidation of the MCrAlY layer was dependent on the presence of an outer protective TBC layer. The TGO layer was characterised and it was observed that there was a correlation between increasing thickness and ageing time; however, it was found that the TGO thickness was more dependent on the exposure temperature. The chemistry of the oxide forming was found to be dependent on both the presence of a TBC layer and ageing temperature in this case.

Within this research, coated heat shield tiles were run in a commercial gas turbine engine, and exactly the same tiles were heat treated isothermally in the laboratory. This allowed for the characterisation of ex-service components and comparisons to be made with isothermally aged material that had an identical coating system composition. Isothermal aging conditions were selected to replicate service exposure. An ex-service gas turbine blade was also characterised, with the focus on the microstructural changes around the profile of the blade. The temperature estimation model was used to determine the exposure condition variation around the profile of the blade.

Conventional characterisation techniques are only able to provide information in 2D. This limits the information that can be obtained on phase interconnectivity and overall grain size and shape. In this work a 3D characterisation technique was developed using a focussed ion beam (FIB) field emission gun scanning electron microscope (FIG-SEM), which was possible due to advances in electron microscopy hardware and software. A series of 2D data sets were collected and processed offline to form quantitative 3D microstructure models. In particular, it was shown that the beta NiAl phase present in many coating systems was interconnected in 3D.

1 Introduction

1.1 Project Overview

This research is part of a project funded by the Engineering and Physical Sciences Research Council (EPSRC). The programme, "SUPERGEN 2" is entitled "Lifetime Extension of Conventional Power Plant". The focus of this project is on both conventional power plant lifetime extension and improving the operating and economic efficiency. This project is a consortium of four universities and ten industrial partners; the industrial partners are Alstom Power Ltd., E.ON Engineering Ltd., Doosan Babcock Energy Ltd., National Physical Laboratory, Praxair Surface Technologies, QinetiQ, Rolls-Royce plc, RWE npower, Siemens Industrial Turbomachinery Ltd. and Tata Steel Ltd. The partner universities are Bristol University, Cranfield University and the University of Nottingham.

The purpose of the research was to study the microstructural characterisation and performance of MCrAlY coated Ni-based superalloys that are used in critical components of land based gas turbine engines. The addition of a high temperature protective thermal barrier coating (TBC) was also investigated and the microstructural evolution of isothermally aged material compared with serviced exposed components. The characterisation methodologies were also used to investigate possible tools for determining effective service temperatures of complex components.

1.2 Project Background

The demand for increasingly fuel efficient engines has increased the demands on critical components of a gas turbine engine. The lifetime of the engine components can be limited by the performance of the materials used in the high temperature and aggressive environments. Nickel based superalloys are used in gas turbines for power generation because of their ability to operate at high temperatures in oxidative and often corrosive environments for prolonged periods of time. In order to provide protection against oxidation and corrosion and to minimise the risk of a service failure the alloys are often coated. The substrate in this work is a conventionally cast Ni-based superalloy, to which a coating system is applied. The system can be made of multiple layers of different compositions to maximise oxidation and/or corrosion resistance together with a ceramic thermal barrier coating (TBC) to reduce the temperature that the base alloy is exposed to. A typical two-layered coating system comprises

an MCrAlY overlay coating, that also acts as a bond layer for an outer high temperature resistant TBC. The inner MCrAlY overlay coating also provides an increase in resistance to oxidation and corrosion. The 'M' in the MCrAlY is generally either Ni or Co or a combination of the two; in this work coatings with a range of compositions have been studied. These coatings work by forming preferential protective dense thermally grown oxides (TGO). Under service conditions the microstructure of the superalloy system evolves, therefore it is highly desirable to understand how a particular substrate/coating system will perform in a given environment. During high temperature exposure, elements from within the coating and substrate layers can move across the substrate/coating interface by interdiffusion. In this research the focus is on the interdiffusion region and the MCrAlY coating layer. To understand when a coating has reached the end of its useable lifetime is crucial in ensuring that component failure, resulting in potentially catastrophic failure of the engine, does not occur. The first stage of developing a remaining lifetime tool is to be able to predict the localised temperature experienced during service, based on the post-service microstructure. A methodology for this has been developed during this research so that localised temperature estimation can be made from collecting micrographs from within the MCrAlY layer. It is important to understand how the service exposure affects the long term degradation of components. A series of ex-service components and laboratory aged samples were used in this research to understand the microstructural evolution. Two types of ex-service components were used; combustion chamber heat shield tiles and gas turbine blades. Isothermally aged material was also used so that a time/temperature matrix could be used to understand the effect of increasing temperature and/or exposure time on the microstructural evolution of the MCrAlY coating system.

Currently tools for characterising the microstructures of coated superalloys are generally limited to two dimensional (2D) techniques. To improve the understanding of coating performance and the evolution of phases during high temperature exposure, techniques are required that reveal the three dimensional (3D) properties. During this project the coatings characterised contained the beta phase, the presence of which is often referred to as the life limiting factor of resistance to oxidation provided by MCrAlY coatings. The interconnectivity of the phases within MCrAlY coatings, notably the beta phase, was investigated by developing a technique for revealing 3D information from a series of 2D images.

1.3 Organisation of the Thesis

Within this thesis the research is split into distinct chapters. Chapter 2 includes a review of MCrAlY and TBC coatings and their application for the protection of Ni-based superalloys for use in high temperature environments. This includes the various methods of MCrAlY and TBC coating application method and types of coating system used.

Chapter 3 discusses the experimental methods and characterisation techniques used, which covers various types of electron microscopy and also includes an introduction to the 3D characterisation and evaluation technique developed within this work, the preparation of samples for characterisation is also detailed. Various forms of macro analysis used to characterise a series of ex-service components are described and microstructure modelling techniques introduced, and the sub-components of the model explained.

In Chapter 4, the microstructural characterisation of MCrAlY coated IN738LC isothermally aged samples with and without a TBC layer is discussed. The samples were aged at a range of times and temperatures that reflect the likely exposure conditions experienced during service in an industrial gas turbine engine. The oxidation of the MCrAlY layer is investigated and the interdiffusion of elements across the substrate/coating interface characterised. Isothermal characterisation was also compared against predictions of microstructural evolution made by a thermodynamic/kinetic model.

Chapter 5 focuses on the study of ex-service combustion chamber heat shield tiles that have an MCrAlY and TBC layer applied. The ex-service components are also compared with material that was aged isothermally, at conditions identical to those discussed in Chapter 4. The isothermally aged material was taken from a section of a tile that did not enter into service. All coating processes were, therefore, identical for the isothermal and service exposed material which allowed for a direct comparison of the microstructural evolution. The components characterised in this chapter were found to have distorted during service, therefore, techniques were used to measure the deformation across each of the combustion chamber tiles. The characterisation results of the isothermally aged material were compared with the microstructural model. The model was then used to aid in the estimation of the temperature experienced during service for each tile based on the microstructural evolution.

Chapter 6 discusses the characterisation of an MCrAlY coated IN738LC ex-service blade. The blade was sectioned and various positions around the profile characterised. The microstructure within the coating region was focussed on and the microstructure model used to derive an estimation of variation in exposure temperature experienced around the profile of the blade.

In Chapter 7 a technique was developed in order to characterise microstructural evolution in 3D. The driver for this work was to investigate microstructural properties that cannot be obtained by conventional 2D techniques, including phase interconnectivity. The technique is based on using a focussed ion beam (FIB) field emission gun scanning electron microscope (FEG-SEM) to collect a series of 2D data sets including images and electron backscatter diffraction (EBSD) data sets in addition to chemical information. An offline process was developed to evaluate the data and combine the 2D datasets to form a quantitative 3D representation of the microstructure.

Chapter 8 presents the overall conclusions derived from the results chapters and also details suggested further work.

2 Literature Review

2.1 Introduction

The operation of an industrial gas turbine engine is dependent on the performance of the turbine components. Nickel based superalloys are used in gas turbines for power generation because of their ability to operate at high temperatures in oxidative and often corrosive environments for prolonged periods of time. In order to provide protection against oxidation and corrosion and to minimise the risk of a service failure the alloys are often coated.

This literature review covers the area of use for superalloys in industrial gas turbine engines. The methodology and the reasoning behind the coating of superalloy substrates to improve the high temperature and hot corrosion performance has also been detailed. The various coating application methods and the different coating types have also been discussed. The development of electron microscopy techniques allowing for 3D analysis of microstructures has also been reviewed and previous findings highlighted.

2.2 The Gas Turbine

A gas turbine extracts energy from a flow of hot gas produced by combustion of gas in a stream of compressed air. Air is drawn in and compressed; it then flows into a combustion chamber, and then on expansion drives a gas turbine. A gas turbine is an internal combustion engine employing continuous combustion (1). Energy is released when compressed air is mixed with fuel and ignited in the combustor. The resulting gases are directed over the turbine blades; the turbine is coupled to the compressor so the combusted gas powers the upstream compressor. This process can best be described by the Brayton cycle as illustrated in Figure 2.1.

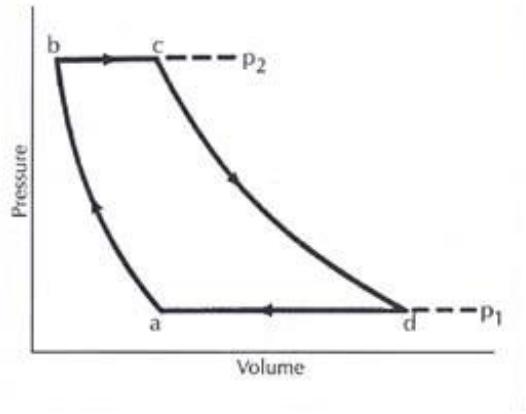

Figure 2.1 The Brayton Cycle is illustrated, the cycle describes the relations between the volume and pressure of the gas. Air is compressed from **(a-b)**, heated at constant pressure from **(b-c)**, heat is added by injecting fuel into the combustor and igniting it on a continuous basis, hot compressed air is allowed to expand, **(c-d)**, reducing pressure and temperature. In the engine **(d-a)** is when the hot air spins the turbine shaft, generating power. The Brayton cycle is completed by a process in which the volume of the air is decreased as temperature decreases as heat is absorbed into the atmosphere (2).

A gas turbine that is configured and operated to closely follow the Brayton cycle is known as a simple cycle gas turbine; some peak load power plant work in the simple cycle configuration due to the short timeframe required to go online. In most land applications to improve efficiency and increase output additional components are added. The simple cycle gas turbine engine is an open cycle gas turbine engine (OCGT). Once the gas has passed through the turbine it is not used again, and it is transferred to the atmosphere for cooling. However, in a combined cycle gas turbine engine (CCGT) the waste gas is utilised through a steam turbine to extract the maximum amount of power (3).

2.3 Superalloys

Advances in technology notably in the aerospace and power industry resulted in a requirement for materials suitable for operation at elevated temperatures in aggressive environments. The development of creep and corrosion resistant alloys dates back to before the first world war, where alloys were required for exhaust valves and superchargers for aircraft engines (4). Superalloys were then developed in order to fulfil the properties required.

A superalloy is essentially designed to achieve excellent strength properties at high temperatures, and they are based on group VIIIA elements (4). Superalloys all contain a FCC (face centred cubic) "austenitic" crystal structure of the matrix phase. There are three classes of superalloys; nickel-based, cobalt based and iron-based. Cobalt and nickel based sheet alloys use solid solution strengthening and carbides to obtain the level of strength required for application. Other wrought and cast nickel based alloys are additionally strengthened by precipitation of an intermetallic phase (5).

Superalloys have an important property by being able operate at a higher proportion of their actual melting point than any other metallurgical material, this along with the high temperature strength and corrosion resistance, make superalloys excellent candidate materials for use in industrial power plant gas turbines.

2.3.1 Strengthening mechanisms in superalloys

The strength of superalloys arises from a combination of hardening mechanisms, including contributions from solid-solution elements and precipitates.

Solid Solution Strengthening

Solution heat treating involves the formation of a single phase solid solution via high temperature heat treatment followed by quenching. Solid solution strengthening can be used to improve the strength of an alloy. The strength is dependent on how easily dislocations in the crystal lattice can be propagated. These dislocations create stress fields within the material; when solute atoms are introduced, local stress fields are formed that interact with those of the dislocations, impeding their motion and causing an increase in the yield stress of the material, therefore, an increase in strength. Commercial Co, Fe and Ni base superalloys always contain substantial alloying additions in solid solution to provide strength and creep resistance. Strengthening of these materials is achieved by the addition of solid solution strengthening elements to an austenitic gamma phase; the gamma phase constitutes the matrix of the alloys. The added elements dissolve in the gamma matrix replacing the matrix Ni

atoms. In Ni base alloys the elements that dissolve are Cr, Co, Fe, Mo, Ta, W, Re, and Ni, Cr, Mo, W, Nb, Ta in Co base alloys (4). Due to the size difference compared to the matrix, the added solute atoms impede dislocation motion by distorting the atomic lattice. Slowing dislocation movement is how the increased strength is derived (5, 6).

Precipitation Strengthening

A considerable increase in the creep strength of alloys for high temperature applications can be obtained by precipitation hardening; this process is also known as age hardening. It works by fine particles formed during a change in temperature, which impede the movement of dislocations, which therefore increases the hardness. The process requires the material to be held at an elevated temperature for a considerable length of time to allow precipitation to take place. As mentioned previously, the presence of second phase particles often causes lattice distortions. These lattice distortions result when the precipitate particles differ in size from the host atoms. Smaller precipitate particles in a host lattice leads to a tensile stress, whereas larger precipitate particles leads to a compressive stress. Above the dislocation there is a compressive stress and below there is a tensile stress. The size and spacing of the particles and therefore their volume fraction are important factors. Typical Ni based superalloys are variations of an austenitic Ni-Cr matrix. They can be further hardened by gamma prime Ni_3 (Ti,Al) particles (4). The addition of Al, Ti, Nb and Ta leads to the precipitation of a finely dispersed gamma prime phase in the gamma matrix. The precipitation of this phase leads to age hardening of the material with significant increases in strength (6). Pure gamma prime is unusual in that its strength is lower at low temperatures and increases with temperature, up to a max at 700-750^{o}C (5). These elements are only soluble to a limited extent, with the result that by heat treatment finely distributed precipitates can be generated in the matrix from a supersaturated solid solution. The resulting precipitates are generally the Ni_3(Ti,Al) gamma prime phase and Ni_3Nb gamma double-prime, depending on the bulk alloy composition. The precipitates inhibit the movement of dislocations, because the movement of a dislocation in the matrix can only take place by cutting through or by passing the precipitated particles (6). Precipitates of various carbides within the grains and at the grain boundaries can also provide additional strengthening. Carbon which is present in the matrix, forms carbides with some of the alloying elements during processing and heat treatment.

2.3.2 Microstructure of Ni-based Superalloys

The chemical composition of the alloy establishes the phases present, and in turn the phases establish the microstructure. Ni based superalloys are complex, yet the relationship of properties is the best known of all materials for use in the 650^{o}C-1100^{o}C range (4). Ni based superalloys provide excellent high temperature tensile strength, creep rupture strength and hot-corrosion resistance. Ni based superalloys often contain at least twelve important elements. Most Ni alloys contain Cr 10-20 wt%, Al/Ti up to 8 wt%, Co 5-10 wt% and small amounts of B and Zr. Other common additions are Mo, W, Nb, Ta and Hf. Elements from groups V, VI, VII make up the face centre cubic (FCC) austenitic gamma matrix and include Ni, Co, Fe, Cr, Mo and W (4).

2.3.2.1 Grain Boundaries

Grain boundaries are interfaces where crystals of different orientations meet, and they are generally only a few nanometres wide. A grain boundary is an interface with crystals on each side of the boundary that are the same but with a different orientation. They disrupt the motion of dislocations through a material. Dislocation propagation is impeded because of the stress field of the boundary defect region and the lack of slip planes and slip directions and overall alignment across the boundaries. Reducing grain size is therefore a common way to improve strength, without any sacrifice in toughness because the smaller grains create more obstacles in the slip plane. Grain boundary migration plays an important role in many of the mechanisms of creep. Grain boundary migration occurs when a shear stress acts on the boundary plane and causes the grains to slide. This means that fine-grained materials actually have a poor resistance to creep compared to coarser grains, especially at high temperatures. Grain boundaries also cause deformation as they are sources and sinks of point defects. Voids in a material tend to gather in a grain boundary and if this happens, the material could fracture.

2.3.2.2 Phases in Ni-based Superalloys

Gamma Matrix

The continuous matrix is an FCC Ni based austenitic phase called gamma, that usually contains a high percentage of solid solution elements mentioned such as Co, Cr, Mo, W, and Fe. The gamma matrix is favoured by most gas turbine designers for the most severe temperatures and long life use. Some of the alloys can be utilised at 0.9 of the melt temperature, and for up to 100,000 hrs at lower temperatures (4).

Reasons for such properties are that nickel has a high tolerance for alloying without phase instability which is attributable to its nearly filled third electron shell. Also there is a tendency at high temperatures for the formation of Al_2O_3 rich scales which have exceptional resistance to oxidation (4).

Gamma Prime

Gamma prime, $Ni_3(Al,Ti)$ is a unique intermetallic phase. It contributes to strengthening by dislocation interaction. The strength of gamma prime increases as temperature increases. Gamma prime is introduced within the austenitic nickel based matrix by precipitation hardening which was discussed in Section 2.3.1. In the gamma prime crystal structure the Ni sites may also contain Co, Cr, and Mo whereas the Al sites may contain Ti and Nb. The unique characteristic of the gamma prime structure is that it is coherent with the gamma matrix, meaning that there is perfect lattice match. Coherent interfaces have low energy, the precipitates therefore have little driving force to grow in size. This is how gamma prime strengthened superalloys retain their strength over a wide high-temperature range. The fine precipitates impede dislocation motion, resulting in the increase in strength. The size and volume fraction of the gamma prime are critical parameters affecting creep and fatigue strength. Small sized gamma prime precipitates have a spherical morphology whereas larger sizes tend to be cuboidal.

In some superalloys, where Fe is present, the predominant strengthening phase is gamma double-prime, which has a BCT structure with composition Ni_3Nb. The gamma double-prime phase is coherent with the gamma matrix and provides high strength in the moderate to low temperature region, however, above 650^{o}C gamma double prime decomposes to either gamma prime or sigma, resulting in a significant drop in strength (7).

Gamma Prime Coarsening

Coarsening is a mechanism by which the average particle size increases after precipitation has finished. As superalloys are age hardened by the fine dispersion of gamma prime particles, the mechanical properties of the alloys are dependent on the size and distribution of the gamma prime precipitates. The gamma prime precipitates grow and fuse together, coalesce, at high temperatures during ageing for long periods, which is a condition of in service use. It is therefore important to be able to predict the kinetics of coarsening of the precipitate, this can then be used as an examination tool during inspection and maintenance. During service operation in addition to an increase in their mean size, the particles also undergo a change in morphology. The cuboidal precipitates tend to group together in short chains or blocks,

distributed uniformly, which then fuse together (5). During service turbine blades are not loaded uniformly, they are subjected to gradients in both temperature and stress, which also vary in time. Coarsening of the gamma prime particles is therefore more pronounced in some zones than in others.

Rafting

Rafting is affected by many factors including the gamma/gamma prime lattice misfit, temperature, applied stress and initial microstructure. The precipitated gamma prime particles which are distributed in the gamma matrix, align in a particular direction, fuse together and form rafted structures (5). When a stress is applied during high temperature exposure, the rafting phenomenon becomes more pronounced and is fully anisotropic. It is present in all single crystal superalloys and is an essential factor in their high temperature creep strength. The raft orientation depends on the direction of the applied stress and lattice misfit between gamma and gamma prime.

Carbides

Carbon, added at levels of about 0.05-0.2 wt%, combines with reactive and refractory elements such as Ti, Ta and Hf to form MC carbides (4). The role of carbides in superalloys is complex; firstly carbides appear to prefer grain boundaries as location sites in Ni alloys, whereas in Co and Fe superalloys, intergranular sites are common. The common Ni-base alloy carbides are MC, $M_{23}C_6$ and M_6C. MC usually takes a coarse, random cubic morphology whereas $M_{23}C_6$ has a tendency to form at grain boundaries. M_6C can also precipitate in a block form in grain boundaries. Carbides within grains impede dislocation motion, therefore increasing strength. Grain boundary particles pin boundary movement discouraging grain growth, and this also impedes grain boundary sliding. The carbides, together with solid solution elements, also provide the primary mechanism for strengthening of Co base superalloys. For Ni base superalloys these mechanisms are secondary to gamma prime and gamma double-prime precipitation strengthening (7).

MC carbides

MC carbides usually form in superalloys during “freezing”; they occur as particles distributed throughout the alloy, both in intergranular and transgranular positions. MC carbides are a major source of C for the alloy to use during heat treatment and service (4).The primary MC carbides are FCC; they are dense, closely packed structures and are very strong. They occur from simple combination of carbon with reactive and refractory metals, classically possessing a formula such as TiC, TaC, NbC, MoC or WC.

$M_{23}C_6$ carbides

$M_{23}C_6$ carbides are abundant in alloys with moderate to high Cr levels. They form during lower temperature heat treatment and service; typically in the range 760-980^{o}C. It has however also been shown that considerable amounts of Ni can substitute in the carbide, and it is also suspected that small portions of Co or Fe could substitute for Cr (4). $M_{23}C_6$ carbides have a significant effect on the Ni alloy properties. Their critical location at grain boundaries promotes a significant effect on rupture strength through inhibition of grain boundary sliding. Eventually rupture failure can initiate by fracture of the grain boundary $M_{23}C_6$ particles.

Topologically Close Packed (TCP's)

In certain alloys, where composition has not been carefully controlled, undesirable phases can form either during heat treatment or during service. The properties of superalloys can deteriorate if TCP phases precipitate. They may appear as thin linear plates, often nucleating on grain boundary carbides. Those commonly found in nickel alloys are σ, μ, P and R. Usually TCPs are composed principally of the elements Ni, Cr, Mo, W and Re, therefore any precipitation of TCPs during service will deplete the matrix of these elements and reduce their strengthening effect. The precipitation of TCP's at high temperatures is frequently associated with the formation of voids which may act as initiation sites for fracture (8). TCP phases form when the ratio of refractory metals and Cr to Co and Ni exceeds certain levels (9).

The addition of Re promotes TCP formation, so alloys containing it must have their Cr, Co, W or Mo concentrations reduced to compensate. The low concentration of Cr content is not as issue because although it protects against oxidation the component can be coated, as discussed later.

Sigma has a specific and detrimental effect on alloy properties. Its hardness and morphology are a source for crack initiation leading to low temperature brittle failure. Sigma contains a high refractory metal content taken from the gamma matrix, which can result in a loss of solution strengthening. High temperature rupture fracture can occur along σ plates rather than normal intergranular fracture, resulting in severe loss in rupture life (4).

In Ni superalloys the μ phase has been shown to have a detrimental effect on mechanical properties, due to its tendency to cause embrittlement by intergranular precipitates. The presence of μ is normally in the form $(Co,Fe,Ni)_7(Mo,W,Cr)_6$ (5).

2.3.3 Superalloy Manufacture

In order to increase the operating temperatures of superalloy components by using higher gamma prime volume fractions, the most common solution is to cast the component. Due to the increase in volume fraction of gamma prime, the volume fraction of the matrix decreases. This limits the amount of alloying elements present in the matrix, notably Cr, Mo and W (5). The lower levels of Cr result in a loss in oxidation resistance previously discussed and this results in coatings becoming necessary in applications when cast materials are exposed to hot corrosion. IN738 with higher Cr content and lower gamma prime was designed for use in such applications.

Equiaxed grain castings were first in use in the 1940s, then directionally solidified (DS) materials were developed during the 1960s before the use of single crystal materials in the 1970s. These developments have resulted in an increase of operation temperature. The reason behind the advancement is that creep strength and ductility of the alloy can be improved by the use of directional solidification to produce components with a columnar grain structure. The directional solidification process has allowed for advancement to single crystal materials, in which the manufacturing process is similar but only one grain is selected to grow into a complete component. With the removing of grain boundaries, boundary strengthening elements such as C, B and Zr are not required, resulting in a rise in the melting point of the alloy.

More recent single crystal alloys, like CMSX4 contain additions of Re to further increase high temperature creep strength. The high temperature capability of these types of alloys are achieved by using a large amount of refractory elements including W, Ta and Re. These additions do however increase the density of the alloy. Cast Ni base superalloys have a higher volume fraction of gamma prime than wrought superalloys, resulting in a relatively low volume fraction of matrix. Inconel 738 Low Carbon (IN738LC) is a Ni based superalloy that is utilised at high temperatures in aggressive environments. The durability of IN738 is dependent on the strengthening of gamma prime precipitates as previously discussed. IN738 with higher Cr content and lower gamma prime was designed for use in applications in which cast materials are exposed to hot corrosion.

2.3.4 Gas Turbine Engine Environment

Temperature limitations are crucial limiting factors to gas turbine efficiency. The problem is that materials and alloys that can operate at high temperatures are very expensive both to buy and to manufacture components from. Gas turbine components must operate under a variety of stresses, temperature and corrosion conditions. The combustor operates under high temperature, low stress conditions. Turbine blades operate under extreme conditions of stress, temperature and corrosion. These conditions are more extreme in gas turbines than for steam turbines (10,11).

The required material characteristics in a turbine blade for high performance and long life include; limited creep, high rupture strength, resistance to corrosion, good fatigue strength, and low coefficient of thermal expansion. The failure mechanism of a turbine blade is related primarily to creep and corrosion and secondarily to thermal fatigue. Since 1950 turbine material capability has advanced approximately 470^{o}C, just short of 10^{o}C per year. The importance of the increase can be appreciated by noting that an increase of 56^{o}C in turbine firing temperature can provide a corresponding increase of 8-13% in output and a 2-4% improvement in simple-cycle efficiency (10).

2.3.5 Creep

Creep is one of the main reasons for the failure of Ni based superalloys used in gas turbines. Creep is progressive deformation of a material which occurs when a material is under constant stress at a high temperature, the important factor is that the stress is less than the yield strength of the material. The creep curve normally consists of three identifiable regions, primary, secondary and tertiary. The initial stage of creep is known as primary creep, where the strain rate is high, but slows as strain increases. The strain rate eventually reaches a constant level; this is known as secondary steady-state creep. The secondary creep is important because the material is in secondary, steady creep during the majority of its lifetime involving continuous loading. In tertiary creep, the strain rate exponentially increases with strain. The melting point of different superalloys varies considerably and their corresponding strengths at various temperatures are different. At low temperatures all materials deform elastically, then plastically, and are time dependent. However at higher temperatures deformation occurs under constant load conditions. The nature of creep depends on the material, stress, temperature and environment. Cast superalloys fail with only a minimum elongation.

2.3.6 Corrosion

Corrosion exists in gas turbine use as hot corrosion. The hot corrosion of the component is accelerated by the presence of salt. In a gas turbine compounds such as Na_2SO_4, $CaSO_4$ and V_2O_5 which are produced by reactions between impurities contained in the fuel such as S, can adhere to the surface of the material and accelerate the hot corrosion (12).

Hot corrosion is a rapid form of attack that is generally associated with alkali metal contaminants, such as Na and K, reacting with S in the fuel to form molten sulphates. The presence of only a few parts per million of such contaminants in the fuel or air is sufficient to cause this corrosion. There are two distinct forms of hot corrosion; high temperature, Type 1 and low temperature, Type 2 hot corrosion. High temperature hot corrosion is an extremely rapid form of oxidation that takes place at temperatures between 825^{o}C and 925^{o}C in the presence of Na_2SO_4. Low temperature hot corrosion was recognised as a separate mechanism of corrosion attack in the mid 1970s. It takes place in the 650-775^{o}C range. It is caused by low melting compounds resulting from the combination of Na_2SO_4 and some of the alloy constituents such as Ni and Co (10).

The two types of hot corrosion cause different types of attack. High-temperature corrosion causes intergranular attack. The higher the temperature the more rapidly the process takes place, creating the potential for failure of the component if too much of the substrate is consumed in the formation of an oxide. Low temperature corrosion characteristically shows no intergranular attack and a layered type of corrosion. There is evidence from the Pratt & Whitney TBC development programme of simultaneous presence of Type 1 and Type 2 hot corrosion on a component (13). The two forms of sulphidation corrosion were distinguished by the metallographic appearance. Type 1 high temperature corrosion is characterised by a broad-front attack, with internal chromium-rich sulphides in the zone depleted of reactive elements occurring at temperatures of 800^{o}C and above. Type 2 corrosion, shows a pitting attack, with little or no presence of internal sulphides or depleted zone, and is primarily observed in the temperature range 650-775^{o}C (10),(13).

Protection against both forms of corrosion are similar; the contaminates can be reduced or high corrosion resistant materials used. A third option investigated later, is to use a coating. As low grade fuels with S, Na and V content are used mainly for firing in power generation, corrosion is an issue. S is one of the most corrosive contaminants in high–temperature environments. Sulfidation in oxidising environments is due to S in the fuel reacting with O_2

to form SO_3 and SO_2, and is accelerated frequently by fuel impurities, such as Na, Cl, and K, which may react themselves with S to form salt vapour, Na_2SO_4 and NaCl during combustion (10).

The salt vapour may deposit onto cooler component surfaces, resulting in accelerated corrosion. Hot corrosion is commonly accompanied by the formation of a porous and non-protective oxide scale which has been attributed mostly to the condensation of Na_2SO_4 that attacks the protective oxide scale. The presence of NaCl ingested in the intake air together with Na_2SO_4 leads to more severe corrosion of components (14).

The presence of NaCl in deposits inhibits the formation of a protective-oxide scale in the initial stage and causes the propagation of hot corrosion of the alloy, resulting in an increasing extent of corrosion with NaCl content (14).

2.4 Power Plant Operating Environments

When turbine engines work in marine environments, for example in coastal locations, salt and water vapour from the atmosphere are drawn into the turbine engine and high temperature corrosion involving salt and water vapour may occur during operation. General Electric for example have made provisions for such factors, General Electric industrial gas turbines are able to operate successfully in a wide variety of climates and environments due to inlet air filtration systems that are specifically designed to suit the plant location (15).

A study has shown that the cyclic oxidation of a NiCrAlY bondcoat + YSZ TBC in the presence of NaCl vapour was shortened compared with air. It was found that the higher the temperature, the shorter the oxidation life of the coating will be. The presence of water vapour also accelerated the failure of the TBC in NaCl vapour and significantly enhanced the corrosion of the coating. Further work on coating failure will be detailed in Section 2.5.5(16).

As mentioned, some original equipment manufacturers (OEMs) account for contamination by fitting filtration systems. General Electric use an inlet system which has the capability to process the air by removing contaminants to levels below those that are harmful to the compressor and turbine. These contaminants may be present in the solid, liquid or vapour phase. Chlorides, nitrates and sulphates can deposit on compressor blades and may result in stress corrosion attack and cause corrosion pitting. Filtration can capture the majority of these corrosive agents (15).

Sulphidation hot corrosion, as previously discussed is related to the deposition of alkali-rich sulphate salts. Na, Cl and K can combine with S to form a highly corrosive agent that will attack portions of the hot gas path. The principal corrosive compound associated with sulphidation corrosion is, as mentioned Na_2SO_4. The principal source of sulphate corrodents is sea salt, which is present in the air and has the potential to enter the gas turbine engine (13). Sulphates have limited solubility in water and are more likely to be found in the form of particulates in relatively dry climates (15). In general as the sea salt droplets pass through the low and high pressure compressor, the concentration of the salts increases as water evaporates from the surface, and the salts selectively precipitate on the high-pressure compressor (13). Nitrates are present in fertilizer products that can be released into the air by local agricultural activities. Solid particles are removed with selfcleaning pulse filters. Soluble alkali salts are removed with coalescing filters (15).

Alongside materials advancement there is a need to better protect the components from erosion and corrosion from unwanted species entering the engine. In order to meet expected maintenance intervals it is necessary therefore to remove solids and liquids that are considered harmful to the compressor and turbine flow path (15). Industrial gas turbine operating profiles are long, less cyclic, with fewer oscillating periods of operation compared with those for aircraft gas turbine engines. This results in creep, rather than thermal fatigue as the primary failure mechanism for hot-section components. In addition, an industrial engine operates in a harsher, less forgiving environment than an aero-engine because of the potential presence of the contaminants introduced continuously from the engine surroundings (13).

2.5 Coating of Superalloys

Blade coatings were originally developed by the aircraft industry for aircraft gas turbines, and are now well established as an important process in the manufacture of industrial gas turbines. Higher turbine combustion temperatures are desirable for increased engine efficiency but place severe demands on the physical and chemical properties of the material. Blade coatings are required to protect the alloy from hot corrosion, oxidation and mechanical property degradation. As superalloys have become more complex it has been increasingly difficult to obtain both the higher strength levels that are required and a satisfactory level of corrosion and oxidation resistance without the use of coatings. Corrosion can lead to a reduction in mechanical properties through diffusion of harmful species into the alloy. Therefore the trend towards higher temperature use increases the need for coatings. Coatings protect the substrate by forming extremely dense oxide scales at the surface which can then protect the substrate from damaging elements diffusing into the substrate. It is important that the coating is rich in oxide forming elements as the lifetime of the coating is limited by the content of these oxide formers. Superalloy coating processes are often divided into two main categories; those that involve alteration of the substrate outer layer by its contact and interaction with selected chemical species; a diffusion coating processes, and those that involve deposition of protective metallic species into the substrate surface, with adhesion provided by a much smaller amount of elemental interdiffusion; an overlay coating process (4).

2.5.1 Diffusion Coatings

The diffusion coating process consists of an alloy layer enriched with oxide formers, notably; Al, Cr, and Si. The elements combine with the primary constituents of the substrate alloy to form intermetallics with significant levels of the previously mentioned oxide scale formers. Methods of applying diffusion coatings include Pack Cementation, which is a type of vapour deposition process. The "Pack" contains mainly of an Al powder and a form of chemical based activator. The substrate and powder are then heated in an inert atmosphere. The Al and activator react then deposit a Al layer onto the component. Ni_3Al and NiAl are the likely phases to form during this process (4). Depending on the amount of Al in the pack the process is either "low activity/outward" or "high activity/inward". High activity diffusion occurs when the Al content in the powder is high, and the Al then diffuses inward faster than the nickel outward through the Ni-Al intermetallics that form at the surface (17). Low activity diffusion occurs when the opposite occurs and the Al content is low and Ni is favoured during the reaction. It is possible for both inward and outward coatings to be present on a single component. This is determined by the surface and substrate geometry (17).

2.5.2 Overlay Coatings

Overlay coatings are different from diffusion coatings as there is no interdiffusion required to generate the coating. Interdiffusion in this process is only required to ensure the coating stays attached to the substrate. The problem with diffusion coatings is that they are strongly dependent on the composition of the substrate. Overlay coatings however were developed to require very little interaction with the substrate as part of the coating process. Overlay coatings are normally of the form MCrAl(X), where M = Co/Ni and X = Y, Zr, Hf, Si (7). Overlay coatings provide high temperature protection by selective oxidation of Al to form a continuous external scale of Al_2O_3 at the surface of the bondcoat, and if present, the TBC interface. The coatings usually contain a small amount of reactive element which increases the adherence of the oxide scale to the metallic coating, the oxidation of overlay coatings will be discussed further in Section 2.5.6. In service environments both oxidation and coating substrate interdiffusion degrade the coating by reducing the Al content of the coating. Thermal cycling accelerates the loss of Al from the coating due to repeated Al_2O_3 spallation and reformation. The more severe the oxide spallation, the more rapid is the loss of Al from the coating (18).

Although land based turbines often operate in an isothermal mode for long periods, aero gas turbines undergo thermal cycling with each flight. This thermal cycling, primarily to ambient temperatures when the engine is shut down, can cause cracking and partial spalling of the protective Al_2O_3 scales. For aero engines loss of oxide is not catastrophic since selective oxidation of Al continues when the component reaches high temperatures again such that the damaged scale will effectively repair itself and grow (18). In addition to oxidation attack, overlay coatings are generally degraded by interdiffusion with the substrate, as the coating is higher in Al content than the substrate, Al diffuses from the coating into the substrate and becomes unavailable to support the growth of the protective alumina scale. This can be represented schematically as shown in Figure 2.2 (18). The Cr concentration in the coating is also typically greater than that in the substrate, resulting in the diffusion of Cr. In contrast Ni and other elements in the substrate diffuse into the coating. (18).

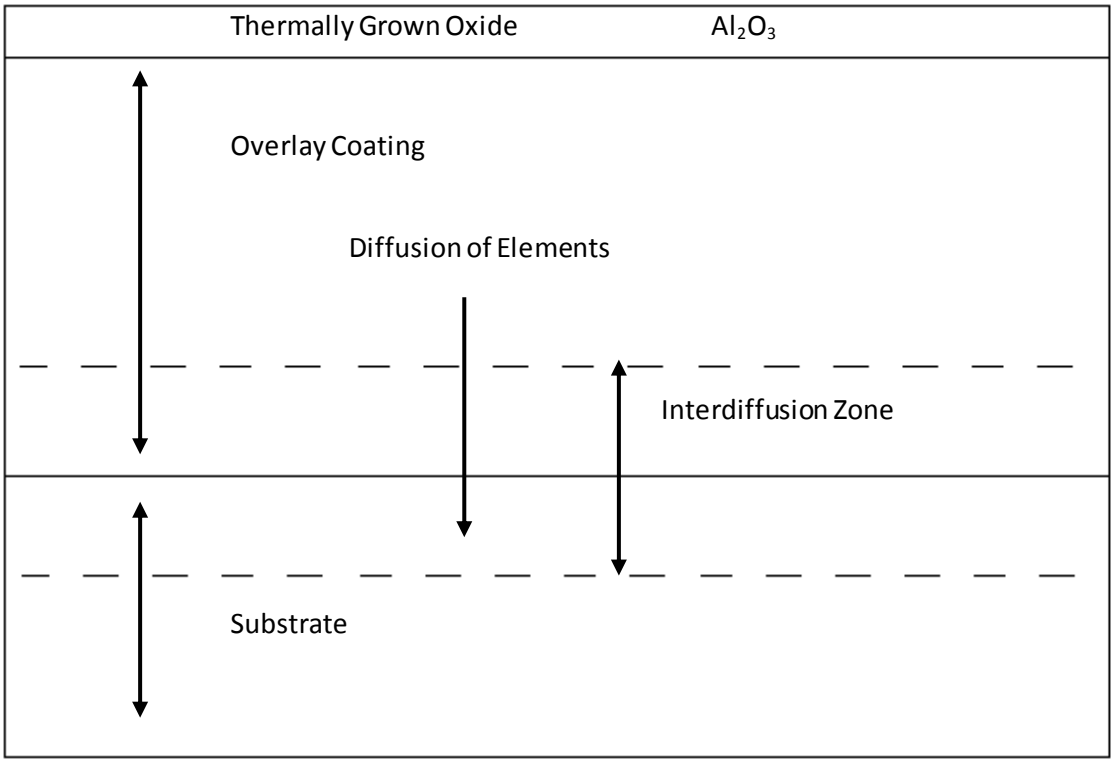

Figure 2.2 A simplified schematic showing an MCrAlY coating highlighting diffusion from within the MCrAlY layer into the substrate across the interdiffusion zone. The location of the thermally grown oxide layer is shown, both the interdiffusion zone and the thermally grown oxide layer are studied in this work.

2.5.3 Coating Application Methods

MCrAlY coatings may be applied by a number of processes, physical vapour deposition (PVD), plasma spraying and thermal spraying.

2.5.3.1 Physical Vapour Deposition

Electron beam physical vapour deposition (EBPVD), works by the vaporising of an ingot of coating material by use of an electron beam. The electron beam can be generated by thermionic emission, field emission or an anodic arc method. The beam is accelerated to a high kinetic energy and focused towards the ingot. The ingot melts and evaporates under a vacuum. The ingot itself can be enclosed in a copper crucible which is water cooled. As the vapour comes in contact with the component they react and the coatings is formed on the surface. A heat treatment will then be carried out which allows for some interdiffusion to take place between the coating and substrate which enhances the join.

2.5.3.2 Plasma Spraying

There are various forms of plasma spraying, including; low pressure (LPPS), vacuum plasma (VPS,) air plasma spraying (APS) and solution precursor plasma spray (SPPS). During plasma spraying the coating material, in a powder form, is fed into the plasma jet. The jet melts the coating material and propels it towards a substrate. Plasma spraying involves the injection of the required coating material in powder form into a high temperature plasma gas stream. On contact with the plasma the powdered coating material will proceed to melt and be accelerated towards the components surface. The parameters can be adjusted accordingly depending on the type of coatings required and the substrate upon which it will be applied.

2.5.3.3 Thermal Spraying

The principles of all thermal spraying processes are similar. A powder or wire is fed through a spray pistol, heated until molten or soft, and projected at speed onto a substrate to form a coating. A frequently used thermal spray method is High Velocity Oxy-Fuel (HVOF), where by the fuel gas and oxygen are fed into the combustion chamber where they are ignited and combusted continuously. A powder feedstock is injected into the expansion nozzle where the powder particles melt; the bonding of the powder to substrate by this method is predominantly mechanical. The density of the coating applied by HVOF is dependent on the material, the state of the particle on impact and the particle velocity. The bond between a sprayed coating and the substrate is primarily mechanical and not metallurgical. Adhesion of the coating to the substrate also depends on the condition of the substrate surface, which must be clean and roughened by grit blasting or machining prior to spraying (7).

The cheapest process to apply metallic coatings is APS, but it is does not provide a very dense coating. Better MCrAlY coatings can be obtained by HVOF or VPS. APS and HVOF have a similar application cost whereas VPS coatings are more expensive. PVD and specifically Electron Beam PVD is an alternative but at higher cost. HVOF therefore provides a coating similar in quality to VPS, which is better than APS, but at a lower cost. Interestingly for MCrAlY bond coats no improvement was found in a study by Wu and co-authors on spallation lives for the more expensive LPPS bond coats compared to the less expensive APS bond coats. In the particular study all APS bond coats outperformed the LPPS bondcoat. This suggests that the potential of the more expensive LPPS system has not yet been realised. Oxides on the LPPS bondcoat also grew faster than oxide on the APS bondcoat in general (19).

2.5.4 Thermal Barrier Coatings

Coating systems that include a TBC generally have four layers: substrate, bond coat, ceramic top coat and a TGO formed between the bondcoat and ceramic top coat during service, this is illustrated in Figure 2.3.

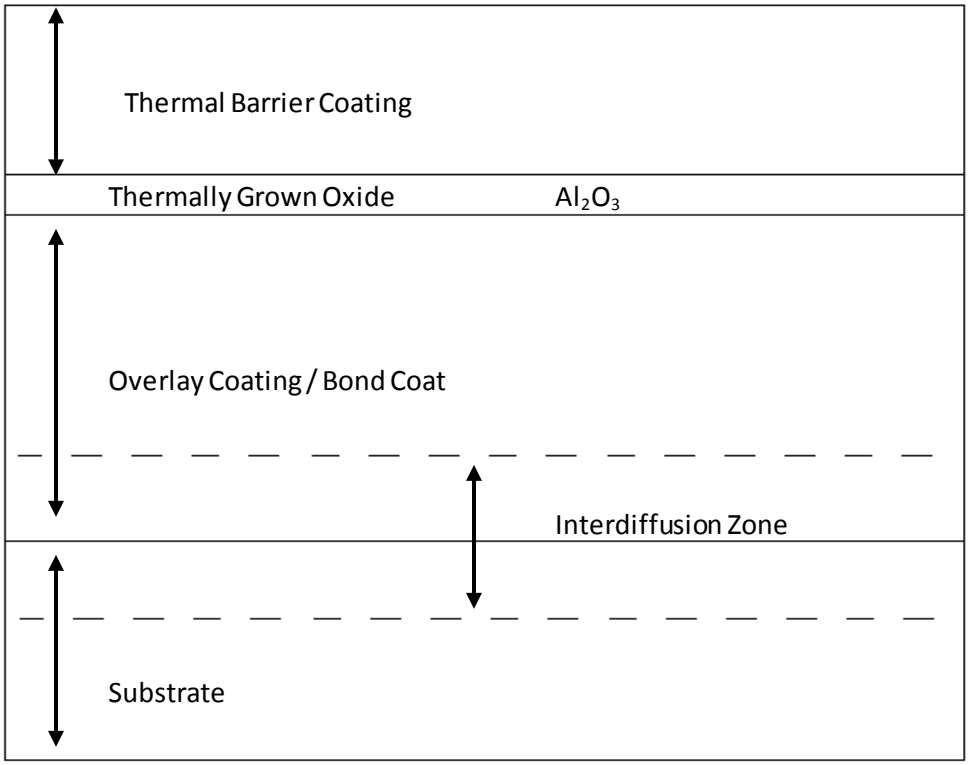

Figure 2.3 A schematic showing an MCrAlY + TBC coating highlighting Al diffusion from within the MCrAlY layer into the substrate across the interdiffusion and the thermally grown oxide layer that forms at the outer edge of the MCrAlY layer. The location of the YSZ ceramic layer is also shown.

TBC coatings have been widely used since the 1970s for the protection of components in gas turbine engines. The TBC system allows for an increase of the gas-inlet temperature without raising the base-metal temperature (20,21). Zirconia based coatings were commonly used as top coatings previously because of their low thermal conductivity and high coefficient of thermal expansion. As introduced previously, MCrAlY coatings are used as a bondcoat, they provide a good thermal expansion match between the top coat and substrate and to prevent oxidation of the base metal. TBC coatings are now commonly made of ZrO_2 partially stabilised with Y_2O_3, simply known as Yttria Stabilised Zirconia (YSZ). They are used to protect the substrate material from the high temperature environment. YSZ is a good thermal insulator which has a thermal conductivity of around 2.5 $Wm^{-1}K^{-1}$ at 1200^{o}C.

TBC coatings cannot be applied directly onto the substrate alloy but need a bond coat. The bond coat has the role of reducing the thermal expansion mismatch between the substrate and the TBC and to provide an oxidation resistance interface. There are a number of application methods for TBC coatings, including LPPS (low pressure plasma spraying), APS (air plasma spraying), EBPVD (electron beam physical vapour deposition) and SPPS (Solution Precursor Plasma Spray).

There are two main process routes for the application of TBC layers, which compete against each other on the basis of costs against high temperature environmental endurance benefits. These are plasma spraying (PS) and EBPVD. PS, specifically air PS, offers economic advantages and provides slightly better thermally isolating TBCs, however they show less tolerance against mechanical attack. EBPVD provides smooth aerodynamically attractive coatings with outstanding high temperature capabilities. The superiority of EBPVD TBC's is related to their columnar microstructure consisting of densely packed columnar crystals of 2-25µm diameter with high aspect ratios (22).

2.5.4.1 Solution Precursor Plasma Spray

The most recent development is a solution precursor plasma spray technique (SPPS). TBCs applied by this process demonstrated improved durability over a range of TBC thicknesses. However, failure methods experienced in SPPS coatings have been similar to those found in other TBCs. In previous studies TGO thickness has been shown to be important in controlling TBC durability. It was seen that although bond coat oxidation behaviour is expected to play an important role in determining the TBC durability, it was noted that the surprising effect of TGO growth rate on the TBC durability in SPPS coatings. It is reasonable that TGO growth rate should correlate with spallation life (19).

2.5.5 MCrAlY Coatings

MCrAlY coatings are a specific form of overlay coating and are widely utilised in high temperature applications. Operating temperatures are limited by the properties of materials at high temperatures. To avoid overheating structural components while increasing operating temperatures, heat flow in to the components is reduced by the use of TBCs. As discussed TBC systems typically consist of a ceramic insulating layer bonded to an oxidation resistant MCrAlY overlay coating. MCrAlY coatings have been designed that significantly outperform diffusion based aluminide coatings in oxidation tests. NiCoCrAlY compositions are the most widely used for oxidation protection (7). An MCrAlY coating is a combination of elements, where M is either Ni or Co, or a combination of both. Cr and Al are present in the MCrAlY composition because they form highly protective oxide scales, discussed in the following section.

MCrAlY coatings of the NiCrAlY, NiCoCrAlY form tend to consist of a mixture of the beta (NiAl) , gamma prime (Ni^3Al) and the gamma phases. Smart coatings have been developed in recent years to protect against hot corrosion and oxidation. The "smart" coating is a single coating that is able to respond to the environment to develop an optimum protective oxide layer, which can be either Cr_2O_3 or Al_2O_3. This aspect is useful in industrial engines where both different corrosion and oxidation conditions can occur across the surface of a single component due to variations in temperature. At temperatures around 600^oC it is preferential to have a Cr_2O_3 layer whereas at higher temperatures, above 800^oC an Al_2O_3 layer would be preferred. The smart coatings discussed in work by Evans and Taylor are formed by a combination of methods (23). The system is based on a NiCrAlY overlay coating deposited by plasma spraying which is heat treated and the coating aluminised by diffusion to produce a multi-layered coating, the heat treatment is currently proprietary information. The outer layer is rich in Al consisting of the beta phase, this will be the source of Al to form the Al_2O_3 layer. Underneath this Al rich layer is a Cr rich region, during hot corrosion at lower temperatures the outer Al rich layer will be consumed but will not penetrate beyond the Cr_2O_3layer (23).

2.5.6 Oxidation of Coatings

Coatings are needed to protect superalloys in aggressive operating environments. As discussed, overlay coatings provide high temperature protection by the selective oxidation of Al to form a continuous external scale of Al_2O_3 at the surface of the bondcoat and when isothermally aged will thicken at a parabolic rate (18).

There are generally three types of oxidation; uniform which occurs at the outer edge of the material, intergranular and internal. In this work the area of interest will be the outer edge of the MCrAlY coating, and when applied, at the MCrAlY/TBC interface. Oxidation is an environmental phenomenon in which metals and alloys exposed to oxygen at elevated temperatures convert some or all of the metallic elements into their oxides. The oxide can form a protective scale if it remains adherent, and reduces further oxidation, or may spall exposing metal, which can results in progressive metal loss. The scale formation over the MCrAlY surface is controlled by thermodynamic and kinetic factors which include both gas composition and temperature. Most metals oxidise readily because of the free energy change associated with the reaction. At high temperatures the oxidation rate is found to follow the parabolic time dependence behaviour which is described by Wagners theory.

The metal oxidation depends on the rates at which anion or cation transport can occur through the crystal lattice or along grain boundaries in the oxide. In alloys the most stable oxide is determined by the oxide dissociation pressure which is lowest for Al and Cr compared to other base elements used in superalloys. Cr_2O_3 can oxidise itself at temperatures greater than 850^{o}C to a volatile CrO_3 compound. Therefore, the use of Al for oxidation resistance is preferred at these temperatures for coatings that are the focus of the work in this research (24).

If the scale that forms were composed of a continuous scale of Al_2O_3, it would act as a diffusion barrier to suppress the formation of other detrimental oxides during the extended thermal exposure in service, therefore helping to protect the substrate from further oxidation and improving the durability of the system under service conditions.

When a coating is substantially depleted of Al during cyclic oxidation, it can no longer supply sufficient Al to heal the damaged protective scale. Less protective oxides such as NiO, FeO, CoO, Cr_2O_3 and nickel spinels can form, signalling the end of the protective life of the coating. The formation of less protective oxides can result in internal oxidation of Al in the coating. The failure to reform the Al_2O_3 scale and subsequently the formation of less

protective surface oxides is commonly referred to as breakaway oxidation and is associated with rapid consumption of the coating and eventually of the underlying superalloy (18, 25). The critical level of Al within the coating needed to form the Al_2O_3 scale can be used as a lifetime limiting factor of the coating. This Al level can indicate the time at which less-protective oxides begin to form on the surface or an earlier time, when the coating could be removed and a new one applied (18).

It has been found that other oxides such as Cr_2O_3, spinel $Ni(Cr,Al)_2O_4$ and nickel oxide (NiO), may form along with the Al_2O_3 TGO layer in air plasma spray (APS) TBC systems, which are discussed in Section 2.5.4 (26). These less protective oxides such as NiO, FeO, CoO, CrO_3 and nickel spinels can form signalling the end of the protective life of the coating. The protective Al rich scale that forms tend to form at a slower rate than Cr rich scale. Seo, Ogawa and Co-authors looked at the oxidation properties of coatings with various compositions. The TGO formation in the MCrAlY coatings studied was significantly influenced by the microstructure of the coating, the composition of the coating and the interdiffusion from the substrate. It was observed that wide interdiffusion zones up to 120µm from the interface were present (24).

In Figure 2.4 the relative oxidation and corrosion resistance of various different compositions of overlay coatings are shown. The forms likely to be of most interest for the purpose of this work are CoNiCrAlY and NiCoCrAlY as they offer a balance of protection to both oxidation and corrosion resistance.

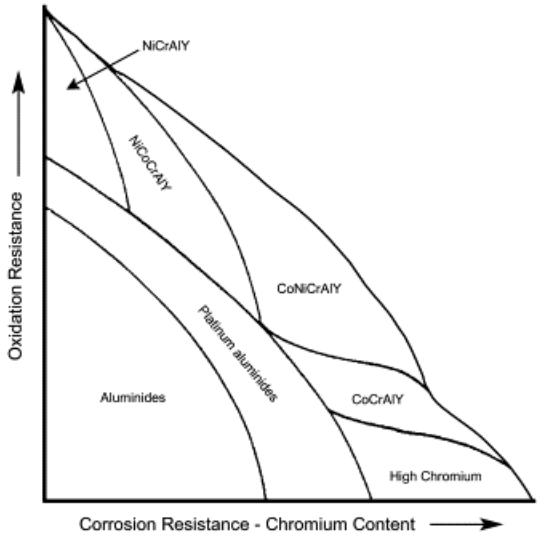

Figure 2.4 In this figure the relative corrosion and oxidation resistance of MCrAlY coatings with varying chromium content are shown. NiCoCrAlY and CoNiCrAlY coatings are the focus of this work (27).

Within this work an experimental coating applied to an ex-service component will also be studied, this coating had a small amount of the alloying element Re added to determine the effect of coating performance. The effect of various alloying elements on the performance of coatings has been carried out by a number of researchers. In work by Nicoll and Wahl it was found that the addition of Si and Ti improved cyclic oxidation resistance. The additions of Si promoted the formation of Al_2O_3 on a NiCrAlY alloy that would normally form a Cr_2O_3 scale (28). The downside to the addition of Si is that melting point of the coating falls.

The addition of Re to MCrAlY coatings has been investigated by Czech and co-authors, and it was found that Re improved oxidation resistance, it is suggested that Re effects the diffusion of Al to the surface of the coating slowing down the rate of oxidation (29). Czech also looked at the depletion of the beta phase at the outer layer of the MCrAlY and found that the depletion rate was dependent on the Al and Re concentrations within the MCrAlY. They observed that the effect on diffusion by the addition of Re to slow down the rate of formation of an Al_2O_3 scale which resulted in suppression of the beta phase depletion (29).

In its role as a bondcoat layer the MCrAlY performance was researched by Evans and Taylor and it was shown how the performance of the MCrAlY and resistance to oxidation has an effect on the TBC performance. It was shown how Al loss which results in the formation of non-protective oxides has a negative effect on TBC performance. Decohesion of the TBC layer at the MCrAlY interface occurs due to the nucleation and slow growth of small cracks. It is possible to predict the lifetime of the TBC system on the basis that failure will occur when the TGO reaches a critical value, but in previous work is has been found that there is no single failure process across all TBC systems (23).

Oxide spallation at the interface occurs due to the strain imposed on the outer later during changes in temperature. As the thermal expansion coefficient of Al_2O_3 is less than that of a typical MCrAlY coating the oxide layer experiences compressive stresses during cooling. The spallation process can occur by either buckling of the propagation of a crack along the coating/TGO interface.

In work by Evans and Taylor it was viewed that the key to understand the topcoat cracking is to recognise that the TGO grown on the MCrAlY bondcoat does so in an environment that is mechanically constrained by the ceramic TBC. This means that the volume increase occurring when the oxide is formed must be accommodated within the TBC system, mainly by a combination of bondcoat creep, deformation of the TBC or cracking. The volume

expansion pushes up against the TBC but any variation in displacement rates across the bondcoat surface will develop tensile stresses within the topcoat at elevated temperatures. These differences in displacement rates can develop even on a flat surface experiencing protective oxidation due to the variation in Al_2O_3 growth rates in localised areas. The variation in rates will become more pronounced if parts of the surface enter breakaway oxidation after there is not sufficient Al to form an Al_2O_3 scale (23). The failure of TBC's is discussed further in Section 2.5.7.

2.5.7 Failure of Thermal Barrier Coatings

The insulating characteristic of YSZ ceramic coatings and the oxidation/corrosion resistance of metallic bond coats provide an improvement in performance and efficiency for gas turbine engines. The major difficulty in the use of TBCs has been the spallation of the YSZ coating caused by thermal fatigue during cyclic oxidation exposure. Failure of TBCs is still largely due to the stresses generated by thermal expansion mismatch between the ceramic and the substrate, growth of the TGO, primarily Al_2O_3, and phase transformation within the YSZ ceramic coatings. TBC's will generally fail in their function when the ceramic topcoat spalls at this stage the MCrAlY bondcoat temperature will increase and the rate of oxidation of this layer will increase leading to premature failure of the component. The growth of the TGO as discussed previously is therefore a significant factor in the mechanisms of TBC failure and will be addressed in this work. It should be possible to predict the TBC lifetime on the basis that failure will occur when the TGO thickness reaches a critical value.

Work on ex-service blades by Sohn (30) has shown that serviced YSZ coatings appeared yellow, presumably due to the changes in oxygen concentration. Engine deposits, such as CaO, MgO, Al_2O_3, SiO_2, were found on the surface of the TBCs which could have been the cause of the yellowing of the surface. This was determined using EDS, and deposits of Ca, Mg, Al, Si and Fe were present. It should be noted that the deposits were found not to noticeably react with the YSZ TBC (30).

The same study also highlighted the fact that different areas of the blade can often experience varying degrees of failure. This is highlighted by the observation that TBC spallation was seen to be more severe near the leading edge than the trailing edge of the blade. The TGO primarily consisted of Al, with Ti, Ni, Cr, Co and Hf, suggesting that the oxidation products may consist of Al_2O_3, TiO_2, $(Al,Cr)_2O_3$, NiO, CoO and spinels such as $(Ni,Co)(Al,Cr)_2O_4$ (29). YSZ coatings have shown insufficient phase stability at temperatures >1200^{o}C. This was a driver for the development in the TBC material choice. A study by Schulz indicated that EBPVD TBCs are stable for up to 100 h at 1150^{o}C, but transform to a mixture of tetragonal (t) and cubic (c) + monoclinic (m) phases after exposure of 100 h at 1400^{o}C. The m-t phase transformation results in a volume change and subsequently high stresses. Therefore the m phase formed by phase transformations during temperature variation causes rapid spallation of the TBC. Not even a EBPVD, strain tolerant microstructure can accommodate these stresses (31).

For TBCs to be used in gas turbine engines it is critical that traces of m phases are detected after relatively short times at 1200^{o}C. However the m phase content increases slowly with time at a representative temperature level for the outer surface of a TBC. Stresses created with cooling during the t>m phase transformation will reduce the lifetime of the coating systems (31). TBC coating systems can fail by spallation during thermal fatigue/cyclic oxidation service. Various failure mechanisms that cause spallation of YSZ ceramic coatings are due to stress, thermal expansion mismatch, oxide growth stress due to bond coat oxidation, stress due to phase transformation of YSZ coating, stress due to sintering shrinkage of YSZ and damage due to molten salt deposits. Compositional development of TBC coatings and bond coats have shown that strain tolerant PVD YSZ coatings result in longer TBC life than plasma sprayed TBC's (32).

It has been found that oxidation of an NiCrAlY + YSZ TBC system is enhanced by the addition of water vapour to O_2 at 1050^{o}C. The study by Zhou et al.(32) showed that scales forming along the bondcoat and TBC interface in O_2 consisted of a continuous Al_2O_3 layer. The oxides that formed along the NiCrAlY/YSZ interface in O_2+5% H_2O consisted of a porous layer, which will not prevent oxidation, and were a mixture of Al_2O_3, Cr_2O_3, NiO and $Ni(Al,Cr)_2O_4$ (33). Recent work by Chen (26) investigated different bond coat application techniques; HVOF and APS, with a similarly applied APS top TBC to both. The APS CoNiCrAlY bond coat had lower Al content than the HVOF CoNiCrAlY bond coat; this was found to be due to the partial oxidation during the APS deposition process. Due to the low Al concentration in the APS CoNiCrAlY bond coat near the original TBC/bondcoat MCrAlY interface some other oxides in addition to Al_2O_3 formed.

For the APS bondcoat the TGO formed during the thermal cycling consisted of mixed oxide clusters and an unstable Al_2O_3 layer that eventually transformed to chromia + spinel. The HVOF bondcoat TGO developed during cyclic oxidation which contained less mixed oxide clusters and a stable Al_2O_3 layer. The TGO with a stable Al_2O_3 layer had a low growth rate and low tendency for crack propagation, which consequently led to an improved TBC durability. It may be noted that oxidation has been recognised as the cause for separation of the ceramic layer from the substrate, leading to TBC failure (26). Introduced earlier under Section 2.4 was the idea that NaCl vapour was detrimental to the life of a NiCrAlY bondcoat + YSZ TBC coating. It was shown in a study by Song and Zhou that non uniform porous layers of mixed oxide formed at the top-coat, bond-coat and interface of tested samples. TGO thickness increased with temperature and the failure of the TBC exposed to NaCl vapour

occurred within the top coat and close to the YSZ/TGO interface. After several cycles, depletion of Al in the coating surface occurred, due to this depletion of Al, Ni and Cr reacted with O_2 to form NiO and Cr_2O_3, these then reacted to from $NiCr_2O_4$ spinal. The thickness of the TGO increased when NaCl was present and the amount of Cr and Ni in the TGO increased (16,33,34).

As the TGO is thicker in the presence of NaCl than in air, the decrease in thermal cycling resistance for the TBC can be attributed to the increased TGO growth and the formation of $NiCr_2O_4$. The formation of non-protective oxide scales and the increased TGO therefore may be responsible for accelerated failure of the TBC, as it was found that the higher the temperature the shorter the oxidation life of coating and that the presence of water vapour accelerated the failure of the TBC in NaCl vapour and significantly enhanced the corrosion of the coating (16).

2.6 Advanced Microscopy

The characterisation of MCrAlY coatings and the microstructural evolution have been carried out using a range of conventional microscopy techniques. This work looks at developments in microscopy techniques that are allowing for the characterisation of material in three-dimensions (3D). The development of data acquisition techniques has allowed for improved representations of the change in microstructure during service exposure. There has been an increasing need for reconstruction techniques to reveal crystallographic information and to reduce/remove the ambiguities associated with two dimensional stereographic analysis.

The data acquisition steps are a key strength in the ability to collect information for a bulk region of a microstructure. Previous studies have shown that alongside qualitative visual representations, steps have been taken to make quantitative characterisation. The ability to extend this analysis into 3D can start to provide phase morphology and interconnectivity information that is highly desirable and can be achieved with recent developments of 3D combined EBSD/EDS.

A study by Xu et al. (35) discussed serial sectioning and EBSD mapping using a dual-beam focussed ion beam (FIB) and field emission scanning electron microscope (FEG-SEM). The work showed how sequential milling of submicron slices of material using the FIB and characterisation using EBSD can allow for a bulk region of material to be characterised. The milling technique to reveal a protruding rectangular volume section of interest has shown how it is a useful preparation method for serial sectioning (35). The slice and view technique, where by automated serial sectioning using a FIB and imaging using a FEGSEM is well established. This technique can be used to generate data that is mainly qualitative and provides very little crystallographic information. A process by generating crystallographic information involves combining FIB milling of a series of consecutive sections with EBSD. The process shown by Xu et al. highlights the importance of the communication between EBSD and FIB-FEG/SEM platforms. Using the technique it is possible to mill a series of slices and map the slices consecutively by EBSD. The spatial distributions of crystallographic features within the microstructure were observed during the study by Xu et al. Previous studies have used the technique to reconstruct deformation zones of a Fe_3Al intermetallic material in three dimensions (35).

A study by West and Thomson has shown how additional energy dispersive X-ray spectroscopy (EDS) data can be collected alongside EBSD information, using a fully automated process. The study focussed on the interdiffusion zone between an MCrAlY coating and a Ni-based superalloy substrate, characterising the chemical gradient, phase content and grain morphology changes within the interdiffusion region after aging. The paper detailed the data collection methodologies that allow for fully automated data acquisition in site specific areas of a microstructure. The EBSD/EDS information is collected in two dimensions and analysis carried out to enable the reconstruction of complex grain shapes (36).

The study by West and Thomson also identified the importance of sample preparation and setup for data acquisition. A dual-beam system was used to prepare the site specific area for characterisation. This involved using the ion beam to cut trenches to isolate the area of interest, in similar style to the work by Xu et al. (35) In this study the isolation of the area of interest was also used to prevent the re-deposition of material and eliminate shadowing effects which could restrict both the EBSD and EDS signals (36). During the study by West the size and morphology of recrystallised grains were studied. The size and morphology at the coating and substrate interface may have a significant effect on the interdiffusion phase formation. Therefore, the ability to generate accurate grain information could lead to improved models that can describe microstructural evolution. It was shown how reconstructing microstructures using EDS maps can reveal the relative connectivity of individual phases and how precipitates can be identified. It was found during the study that large data sets collected do result in 3D analysis issues; the size of the datasets collected was found to result in processing issues using conventional EBSD analysis software (36).

2.7 Summary

The literature review covered studies highlighting how the operation of gas turbine engines is dependent on the performance of the turbine components where the selection of materials is crucial to component performance.

The coating of superalloys to provide protection at elevated temperatures and in aggressive environments against hot corrosion and oxidation was researched. Various coating types were reviewed including diffusion and overlay coatings. The formation of a protective alumina scale during service for overlay coatings can protect the underlying substrate. The overlay coating is generally an oxide resistant MCrAlY coating, the MCrAlY is a combination of elements where M is either Ni or Co. The addition of Cr and Al is because they form highly protective oxide scales, NiCoCrAlY type coatings are the most widely used for oxidation protection. The alumina scale acts as a diffusion barrier preventing further detrimental oxides from forming. During high temperature service use an outer TBC can also be applied for high temperature protection to the overlay coating, where the overlay coating acts as a bondcoat layer. During service the diffusion of elements between the overlay coating layer and the substrate, this diffusion limits the lifetime of the coating system. A range of coating application techniques for MCrAlY and TBC coatings were researched, including HVOF thermal spraying for MCrAlY layers and air plasma spraying for TBC layers. Previous work has suggested how TBC's can fail during service due to thermal expansion mismatch between the ceramic layer and the substrate.

Developments in characterisation techniques were also researched, focusing on 3D microscopy techniques. The development in data acquisition techniques has allowed for improved representations of the change in microstructure during service exposure. Studies by Xu et al. (35) and West and Thomson (36) detailed techniques using a dual-beam FIB-FEGSEM. The established slice and view technique has been used to enable the collection of EDS and EBSD data using a fully automated process. Current limitations with 3D analysis were identified in the studies, including the size of data sets and the processing issues when analysing the data collected. The limitations and issues arising during data processing in previous studies will be addressed in this research.

3 Experimental Procedure

3.1 Introduction

In this work the microstructural evolution of a series of IN738LC coated samples and components was characterised. The microstructural evolution of the protective coating system consisting of both MCrAlY and TBC layers was investigated using a range of characterisation techniques, the different techniques used are detailed in this chapter.

The individual samples are listed in Section 3.2 and the relevant ageing treatments detailed. The samples characterised were selected to investigate the performance of an MCrAlY coating system after isothermal and service exposure. The effect of the addition of a thermal barrier coating (TBC) layer was also investigated. Isothermally aged material was used to benchmark a thermodynamic and kinetic model, developed within the research group, that is able to predict the microstructure after thermal exposure. The model was then used to predict the localised temperature experienced during service exposure for a range of service components.

In this chapter the experimental techniques used to characterise the isothermal and service exposed material are discussed, including macro and micro analysis and various forms of electron microscopy. The techniques used to prepare samples for macro and micro examination are also detailed. A new technique to reconstruct microstructures in three dimensions (3D) was also developed within this work, this technique forms a standalone section of work and is the focus of Chapter 7.

3.2 Materials

In this work the substrate studied across all samples is conventionally cast IN738LC. In order to provide protection against oxidation and corrosion and to minimise the risk of a service failure the alloy has a coating system applied. The system can be made of multiple layers of different compositions to maximise oxidation and/or corrosion resistance and a ceramic TBC to reduce the temperature that the base alloy is exposed to. A typical two-layered coating system comprises of a high temperature resistance Yttria Stabilised Zirconia (YSZ) TBC and an MCrAlY overlay coating. The MCrAlY coating can be applied as a standalone coating system or act as a bond layer for an outer coating and provides an increase in resistance to oxidation and corrosion. The MCrAlY coating was applied by a High Velocity Oxygen Fuel (HVOF) process and the TBC coating by an Air Plasma Spray (APS) method.

The composition of the substrate alloy is shown in Table 3.1, it was confirmed by EDS. The composition data for the substrate alloy was collected by Certified Alloy Products; part of the Doncasters group of industrial gas turbine material suppliers.

Table 3.1 The measured composition of unaged IN738LC. The composition of the substrate alloy was measured by Certified Alloys Inc., California, USA.

Element	Ni	Cr	Co	Al	Ti	W	Mo	Ta	C
Wt %	62.69	15.98	8.26	3.36	3.5	2.67	1.76	1.67	0.11

The bondcoat layers used in this work were AMDRY995; a CoNiCrAlY coating that was applied to isothermally aged disk samples and to the service exposed combustion chamber heat shield tiles, also a SC2464 NiCoCrAlReY coating was applied to a gas turbine stage 1 blade. The AMDRY995 composition was provided by the manufacturer of the coating powder and confirmed by energy dispersive X-ray spectroscopy (EDS), the SC2464 composition was measured using EDS after application, the composition of both coatings are shown in Table 3.2.

Table 3.2 The table shows the coating composition of both the AMDRY995 and SC2464 coatings, both compositions were confirmed by EDS after post coat heat treatment of 4 hours at 1080^{o}C.

	Element	Co	Ni	Cr	Al	Y	Re
AMDRY995	Wt. %	38.5	32	21	8	0.5	n/a
SC2464	Wt. %	26	45	18	9	n/a	2

In this research a range of substrate forms were used; including 7 mm diameter cylindrical bars that were sectioned to produce 5 mm thick disks, which form the samples discussed in Chapter 4. In Table 3.3 the isothermal ageing conditions are shown for all disk samples, there were two types of sample; one set had only a 50 µm AMDRY995 type MCrAlY layer applied and a second set had a 50 µm MCrAlY layer and an additional 250 µm outer protective ceramic TBC layer. In Chapter 5 a series of ex-service combustion chamber heat shield tiles are characterised, a sample tile, identical in coatings and preparation was sectioned and aged isothermally under the conditions shown in Table 3.4. Each sample had a 250 µm AMDRY995 type MCrAlY layer and an additional 250 µm ceramic TBC layer applied. In addition an ex-service stage 1 gas turbine blade was also characterised, the substrate of the blade was IN738LC, however, in contrast to the previous samples the component had a 250 µm Re rich SC2464 coating applied and an outer TBC layer.

Table 3.3 Isothermal ageing parameters for the disk samples; "MCrAlY" samples had only a 50 µm CoNiCrAlY layer applied by HVOF. "MCrAlY + TBC" samples had a 50 µm CoNiCrAlY layer applied and then an additional 250 µm APS YSZ TBC layer.

Time hours	Time months	850°C		900°C		950°C	
		MCrAlY	MCrAlY + TBC	MCrAlY	MCrAlY + TBC	MCrAlY	MCrAlY + TBC
2190	3	✓	✓	✓	✓	✓	✓
4380	6	✓	✓	✓	✓	✓	✓
6570	9	✓	✓	✓	✓	✓	✓
8760	12	✓	✓	✓	✓	✓	✓
10950	15	✓	✓	✓	✓	✓	✓

Table 3.4 Isothermal ageing parameters for tile sample; each sample had a 250 µm CoNiCrAlY and an additional 250 µm APS YSZ TBC layer.

Time hours	Time months	850°C	900°C	950°C
		MCrAlY + TBC	MCrAlY + TBC	MCrAlY + TBC
2190	3	✓	✓	✓
4380	6	✓	✓	✓
6570	9	✓	✓	✓
8760	12	✓	✓	✓
10950	15	✓	✓	✓

3.3 Coating System Application

In this work samples were prepared for isothermal and service exposure. Some materials and components were received in the as coated condition; therefore, the full coating preparation history is unknown. However, it is known that the MCrAlY layer was applied in each case using a HVOF spray method, the HVOF technique was detailed within Section 2.5.3.3.

The combustion chamber heat shield tiles were received before the protective coating system, that was the focus of this work, was applied. This allowed for controlled surface preparation and coating application. Before the MCrAlY layer was applied an abrasive grit blast of the substrate was carried out at 30-40 psi. The CoNiCrAlY layer was then applied by HVOF using multiple passes of the spray gun until a 250 µm layer was achieved. After the MCrAlY was applied a low

pressure compressed air clean of the surface was carried out. A further abrasive grit blast of the MCrAlY was carried out at 10-20 psi before a YSZ TBC was applied by APS. Each component and also every sample characterised in this work was given a post coating heat treatment at 1080°C for 4 hours before high temperature exposure to diffuse the MCrAlY layer to the substrate material.

3.4 Characterisation Techniques

In this work a range of experiential techniques including macro and micro analysis techniques were used depending on what information was required. When the heat shield tiles were initially removed from the combustion chamber the tiles showed signs of distortion. This distortion was characterised using freeform analysis techniques to map the tile surface. Following macro analysis, where required, all components and samples were then sectioned and the specific areas of interest mounted to allow for micro analysis.

The initial microscopy imaging was carried out using an Carl Zeiss (Leo) 1530 VP field emission gun scanning electron microscopy (FEG-SEM) with the aid of EDS for chemical composition analysis. An FEI Nova 600 Nanolab dual-beam focused ion beam (FIB) / FEG-SEM with the use of a solid state backscatter detector (BSD) was used to collect detailed imaging of the interdiffusion region and within the MCrAlY layer. Imaging using a BSD shows a clear contrast differential within areas of different chemical composition. This was particularly useful as it allowed for individual phases within the microstructure to be identified directly from images. The FEI Nova 600 Nanolab FIB/FEG-SEM was also integral to the work that is the focus of Chapter 7 where a technique was developed to analyse microstructures in 3D. The Electron back scatter diffraction (EBSD) technique and simultaneous EDS were carried out as part of the 3D data collection process.

3.4.1 Freeform Profile Analysis

The combustion chamber heat shield tiles that were studied in this work were observed to be distorted upon removal from the gas turbine engine. Therefore, a characterisation technique was required that would enable the level of distortion to be quantified. Initially a conventional contact co-ordinate measuring machine (CMM) was used. This technique uses a stylus that follows the profile of the component and collects measurements for a matrix of pre-defined points. A set of x,y,z co-ordinates were generated that could then be compared against a reference grid.

During analysis of the data is was observed that there were some difficulties in using a contact characterisation method at the edge of the component, where distortion is the greatest, as cracks were present and measurements could not be made. Further non contact techniques were required and initially laser CMM was used as a solution. The laser CMM technique was used to enable the reconstruction of single faces of the tile profile. As it was a non contact method data could be collected for all regions of the tiles including the edge regions where the tile showed cracking of the substrate. This technique was successful in mapping single faces of the tiles and comparisons were made.

Following analysis of the CMM data the distortion of the tiles was observed to occur in multiple planes, therefore data collected from a single plane did not show a full representation of the levels of distortion occurring during service. To enable a full 3D comparison more advanced techniques were required, a solution to this was the use of photogrammetry.

A GOM Atos system was used that is a high resolution optical 3D system. The system works by collecting a series of 2D datasets, the 2D datasets are made up of laser scanned CMM images and digital images. The component has a series of markers applied to all faces and edges, the markers are used reference points within each collected image. A series of digital images were collected at different angles, the series of images was then processed using dedicated software that uses the location of the markers within the laser scanned CMM and digital images to stitch together multiple 2D images to form a 3D model. The GOM system used is calibrated to enable a reconstruction of a freeform with a resolution +/- 50 µm.

The 3D models that were produced for each tile were then compared against a reference grid and the tile distortion measured. Surface maps were created that showed the regions and level of distortion. An example of a reconstruction output is shown in Figure 3.1, in this model the scale shows distortion +/- 2 mm and it can be seen how the edges of the tile show the greatest distortion. In Section 5.4.1 the individual tile results are compared.

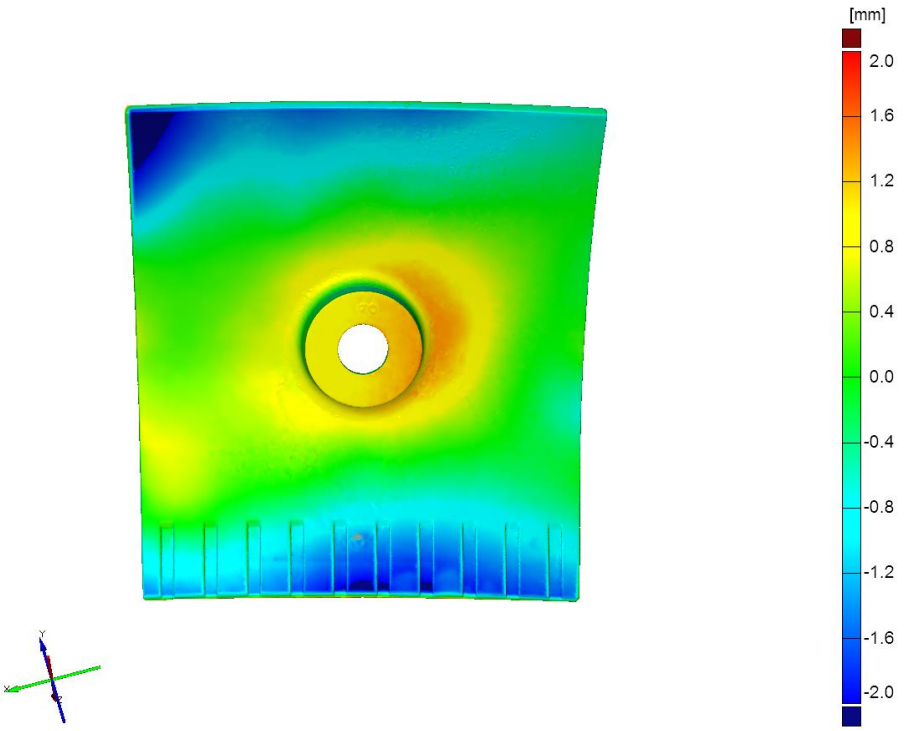

Figure 3.1 This figure is an example of a distortion map generated using photogrammetric data collected from an ex-service tile using the GOM Atos System and then compared with a reference tile. The scale in this figure shows distortion to +/- 2 mm. It can be seen how the greatest distortion is evident at the top and bottom edges of the tile.

3.4.2 Sample Preparation

This section details the sample preparation that was carried out prior to the characterisation of the microstructure. The sample preparation required was dependent on the characterisation technique carried out.

Sample preparation for microscopic examination using a FEG-SEM and FIB-SEM are detailed initially. The samples were sectioned using an Accutom-5 precision cutting machine, this was done at a cutting speed of 0.001 mm/s which would not cause deformation of the material, using a water cooled Al_2O_3 disk. The samples were then mounted using PolyFast conductive resin in an automatic mounting press; a Struers ProntoPress-10. After mounting the samples were then prepared for microstructural characterisation using a multi stage grinding and polishing sequence, this was carried out using a TegraPol-25 automated polisher, with the aid of a TegraForce-5 multiple specimen holder. Dosing of the polishing suspension was carried out using a TegraDoser-5, which is automated dosage hardware. The automated grinding and polishing processes allows for an improvement in repeatability of sample preparation and significantly reduces the time taken. Samples were initially ground using 200, 600 and 1200 grit grinding wheels, with water lubrication, to remove the surface layers. The samples were then polished using a combination of Struers Plan, Mol and Floc polishing cloth pads with 9 µm Plan, 3 µm Mol and 1 µm NapB diamond suspensions.

For EBSD characterisation a further polishing stage was required, Struers OP-S 0.04 µm colloidal silica suspension was used to get a flat finish, the technique combines mechanical polishing with etching and is known as chemo-mechanical polishing. This process removes any deformation in the surface that could have been caused from the abrasive grinding and diamond polishing stages and reveals the grain structure.

Cleaning of the samples was carried out immediately after each polishing stage using methanol to remove any foreign debris, samples were then mounted onto stubs using conductive adhesive, so that the samples could be held securely to the microscope stage.

3.4.3 Electron Microscopy

Within this work electron microscopy was the main technique used to characterise the microstructural evolution. A range of microscopy techniques were used, including; back-scatter imaging, EDS and EBSD. Within the microscope when the electron beam hits the sample it interacts in a number of ways; the different interactions are shown in Figure 3.2. The interactions in each sample are dependent on the material of the sample, the topography of the sample and the thickness. The different characterisation techniques use the different beam interactions in different ways to allow for a range of information about the microstructure to be acquired.

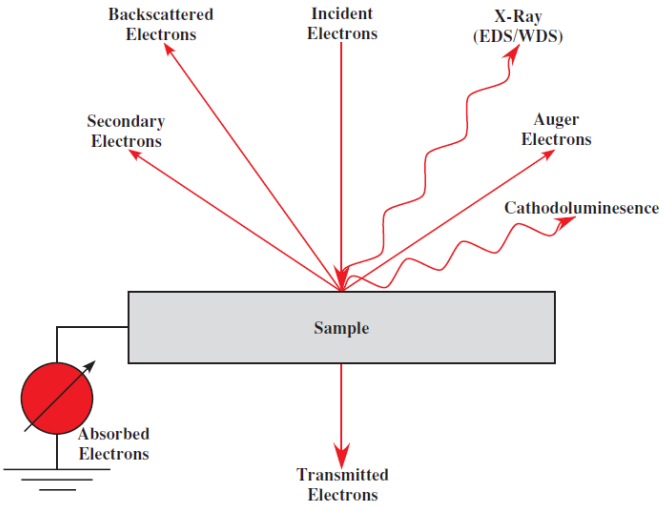

Figure 3.2 The different interactions within the sample during electron microscopy showing secondary electrons, backscattered electrons and the X-rays given off during EDS analysis.

3.4.3.1 Imaging Techniques

Initial examination of the samples was carried out using a FEG-SEM. The FEG-SEM was used to identify features at a resolution that is not possible using optical microscopy. The FEG-SEM also has a greater spatial resolution than standard SEM systems due to the higher current density of the electron beam produced; the FEG-SEM source is a thermally assisted field emission source with a tungsten tip. There were two different types of detector mode used during characterisation; a BSD and secondary electron detector (SE). Backscattered electrons consist of high-energy electrons originating in the electron beam that are reflected from deep within the specimen. Backscattered electrons may be used to detect contrast between areas with different chemical compositions, especially when the atomic number is different, the brightness of the back scattered image tends to increase with atomic number.

The SE mode was also used; electrons that are ejected from the surface of the sample with low energies are known as secondary electrons. It is, however, only possible to collect information about the very top region of the sample which means topography of the sample will affect the SE results. An operating voltage of 20 kV was used for imaging analysis, the working distance was dependent on operating mode, for imaging a target working distance of 6 mm was used. As working distance is reduced the demagnification of the electrons on the sample surface is increased; improving the focus.

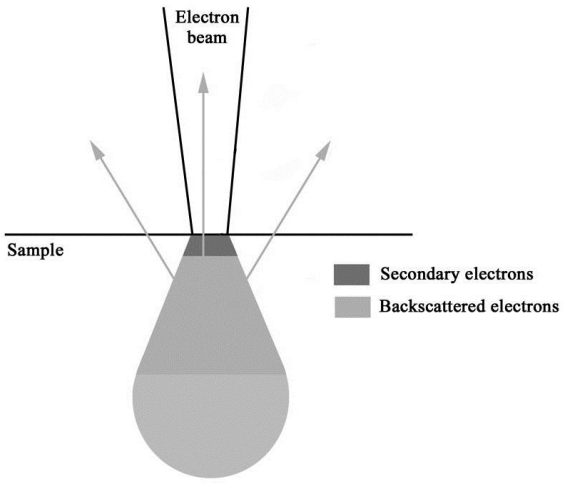

Figure 3.3 The different ınteractıon volumes of SE and BSE, it can be seen how the BSE are collected from a greater depth and SE only penetrate the top layer of the sample.

An Fei Nova Nano Lab 600 dual beam FEG-SEM/FIB system was also used to collect images of the samples. The dual beam uses an electron beam, the same as an FEG-SEM and a focused ion beam of gallium ions. FIB imaging was used as a technique to gain information about grain morphology. The ion beam is formed when gallium metal is placed in contact with a tungsten needle and then heated. The gallium then begins to wet the tungsten and the electric field causes ionisation and the field emission of gallium ions (37)

A major difference from an electron microscope is that ion beam imaging permanently effects the sample. When the gallium ions hit the sample, atoms are sputtered from the surface, etching away the sample each time an image is collected. This technique was not used significantly for collecting images for characterisation, however, for the 3D characterisation procedure the FIB milling was critical to the data collection as both electron and ion beam imaging can be carried out on a single sample in the dual beam microscope. The specific use and importance of the dual beam FIB including the settings and procedures used are detailed in Chapter 7 to show how a microstructure can be reconstructed in 3D.

3.4.3.2 Energy Dispersive X-Ray Spectroscopy

An EDAX Pegasus energy dispersive spectroscopy system was used in the FEG-SEM to gain chemical composition information from specific regions of the microstructure. EDS works by a high energy electron beam targeted at the sample, the electrons within the sample are excited by the beam, an electron within an inner shell is ejected and one from the outer shell then replaces it, when the vacancy is filled an X-ray is released. Each element has an X-ray energy that is characteristic of that element, and as such can be used to identify which elements are present within the area examined. Composition data is achieved by constructing an index of X-rays collected from a set area or spot. The EDS technique was used for collecting box compositions to characterise the coating composition initially and to confirm the quoted powder composition with the applied coating.

EDS spot analysis was used to determine the individual phases within the microstructure. EDS matrix and linescan techniques were also used extensively to characterise the change in chemical composition across a coating profile. This was particularly useful in identifying the coating/substrate interface which was key in various aspects of the microstructural characterisation techniques developed in this work.

There are some limitations with using the EDAX Genesis analysis software, it is possible for a number of different energy peaks to overlap and it must be noted that a penetration depth of the electron beam generating the X-rays can be up to 2 μm. The scale of this effect will depend on the microscope parameters and also the size of the phase that is characterised. When an unknown sample is examined with limited thermal history and composition, care should be taken in using the data collected when regions of composition are unknown. In this work, however, the technique was used as a discrimination tool where composition contrasts were present.

3.4.3.3 Electron Back-Scatter Diffraction

The EBSD technique was used to characterise the crystallographic nature of the microstructure within the coating and substrate components by collecting quantitative crystallographic information. In EBSD a stationary electron beam hits a sample tilted to 70^{o} and the diffracted electrons form a pattern on a phosphor screen, a Hikari charged coupled (CCD) camera was used to simultaneously acquire and index the patterns. The pattern formed is characteristic of the crystal structure and orientation of the sample region from the area it is collected. The diffraction pattern can be used to measure the crystal orientation, measure grain boundary misorientations and discriminate between different materials. When the beam is scanned across a polycrystalline sample and the crystal orientation measured at each point the resulting map can reveal the grain morphology, orientations and grain boundaries. A quantitative representation can be made of the sample microstructure.

Within this work the technique is limited in its ability to identify the individual phases without the use of combined EDS, this is due to the similarity in the lattice parameter of the gamma and gamma prime phases. However, the chemistry of the phases can be used to discriminate between gamma and gamma prime. The combined EBSD and EDS technique was developed within this work to derive a methodology for characterising microstructures in three dimensions. In Chapter 7 the technique and analysis of the collected data is discussed in detail.

3.5 Image Analysis

A series of image analysis procedures were used in order to quantitatively analyse micrographs of the microstructure. It was also desirable to identify the interfaces within the coating system in order to quantify the depletion of phases with changes in exposure conditions.

3.5.1 Interface Identification

During the application of the MCrAlY layer a grit blasting treatment of the substrate surface was carried out to aid in the adhesion of the layer, therefore, at the interface it was possible to observe Al_2O_3 grit. Observing the grit and voids present at the interface can be used as indicators to the location of initial MCrAlY/substrate interface which can be confirmed with EDS matrix scans. An EDS matrix scan used to characterise the interface region within a sample aged for 3 months at 850^{o}C is shown in Figure 3.4, the corresponding chemical analysis results are shown in Figure 3.5 and 3.6.

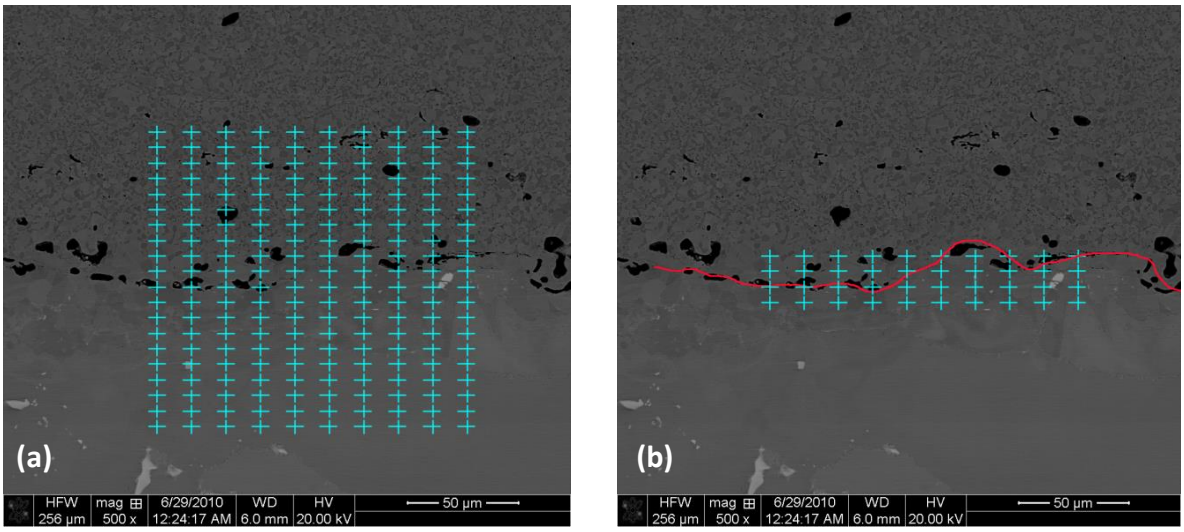

Figure 3.4 A back-scatter image of a sample aged for 3 months at 850^{o}C. EDS chemical analysis was carried out in the region shown in (a). A matrix of 10 x 20 EDS spot analysis points was carried out. Using the chemistry of the substrate and coating the interface was found to be within the region highlighted in (b).

In Figure 3.5 the mean chemistry of each of the 20 rows of the sampled matrix is displayed and shows how the chemistry changes as the distance from the first collected point changes, at the top left of the matrix in Figure 3.4a. The position of the substrate/coating interface can be identified using the known chemistry of the substrate and the coating. It can be seen within Figure 3.6a that the row of points 81-90 does show chemistry consistent with the MCrAlY coating. EDS point 87 suggests a composition consistent with the substrate, when locating this

point on the back-scatter image in Figure 3.6a it does appear that point 87 is situated within the substrate component of the system. Points 91-100 in Figure 3.6b suggests that the region examined is within the interface region as the chemistry appears to change from point to point. The Ni and Co concentrations can be used as an indicator of coating or substrate location. EDS points 101-110 in Figure 3.6c suggest a region that is substrate based on the measured composition. EDS point 104 appears to be within the coating region with locating this point within the back-scatter image, this is reflected in the chemistry notably the Co and Cr peaks.

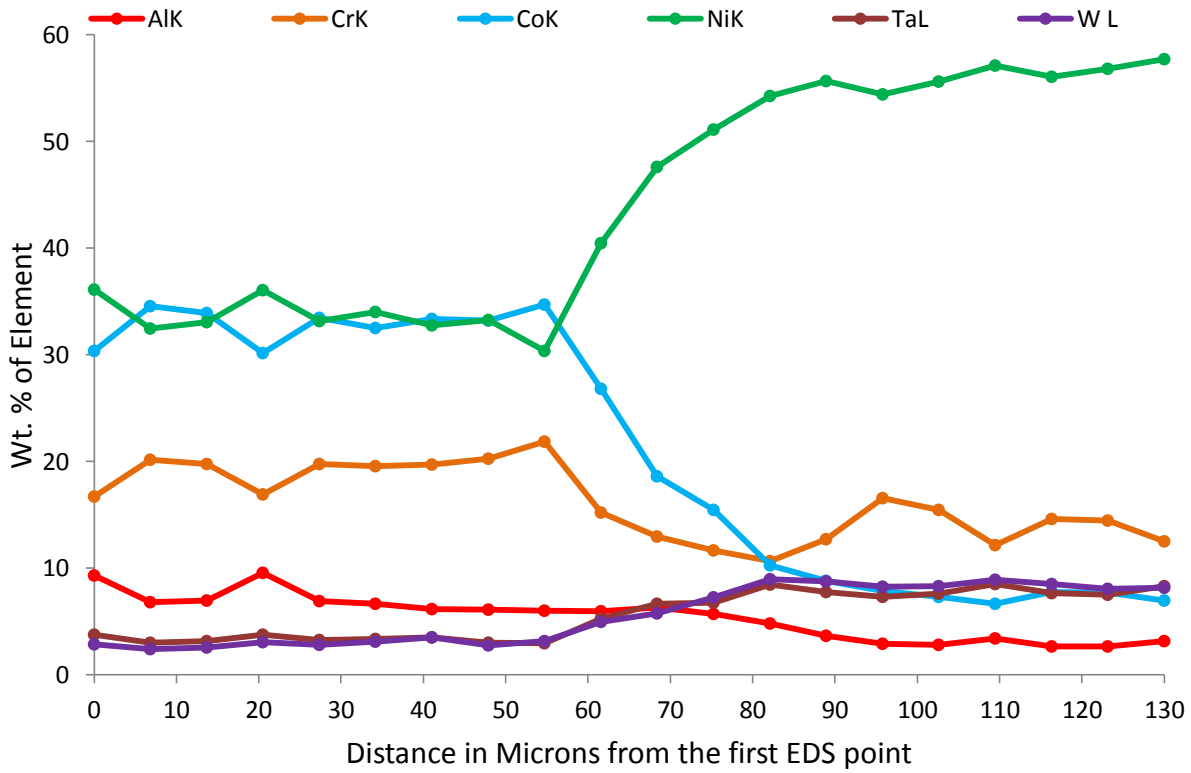

Figure 3.5 The graph shows the chemical profile of the mean chemistry of each row examined and the result expressed as a distance from the first data point collected, for a sample aged for 3 months at 850°C. The 20 rows of EDS data collected are converted to a distance measurement from the first data point. The data point for each row is the mean of 10 data points.

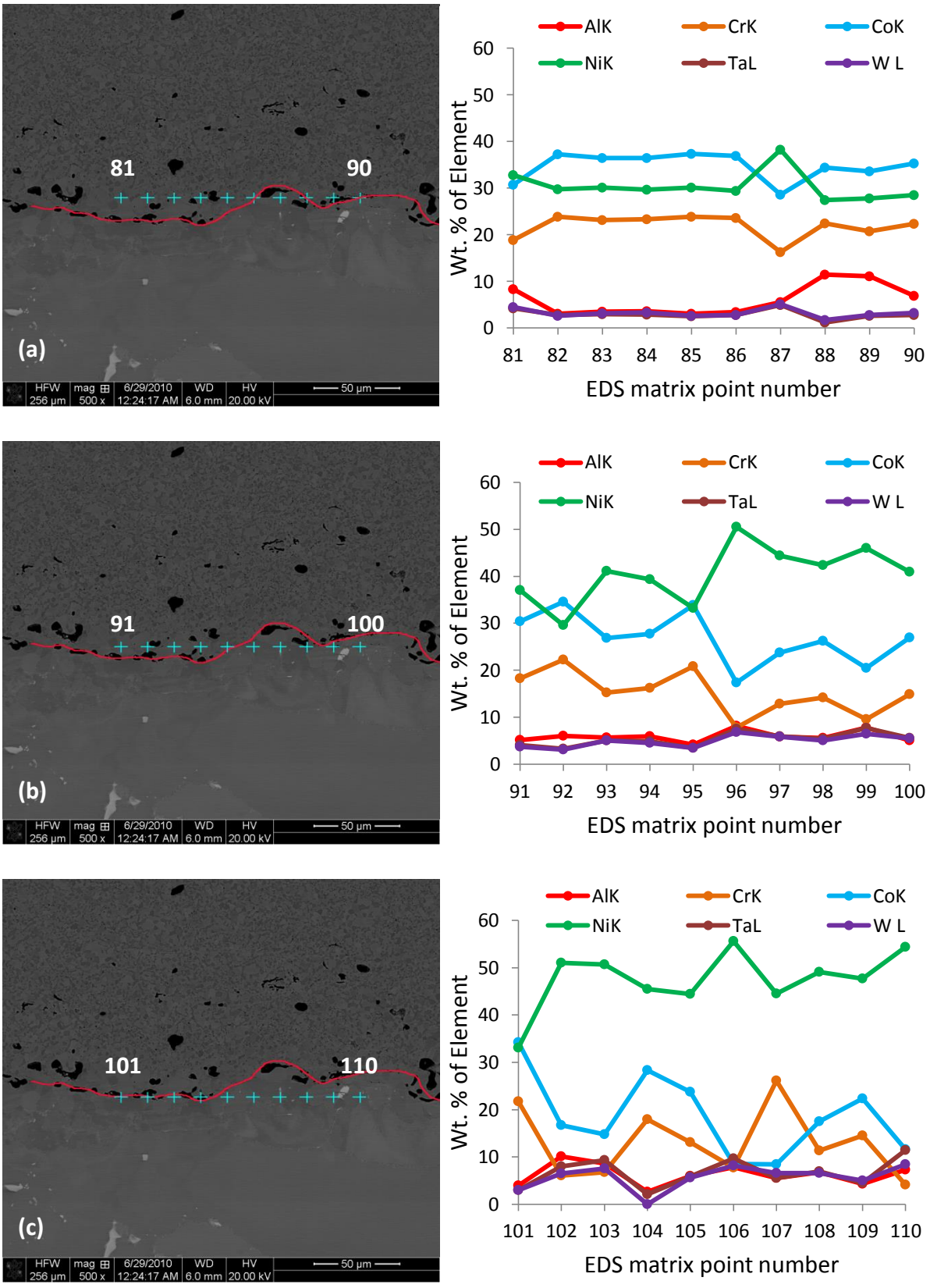

Figure 3.6 A series of back-scatter images showing the region of EDS analysis carried out and the resulting chemical profile of the series of EDS spots for a sample aged for 3 months at 850°C. The points show the relevant location from the 1-200 point matrix.

3.5.2 Oxide and Phase Identification and Quantification

A back-scatter detector was used when collecting micrographs for quantitative image analysis as it was found that due to the atomic number difference, phases and the oxide scale could be identified by using the brightness gradient. Figure 3.7 shows the beta and sigma phases within the MCrAlY and also the thermally grown oxide scale. By using a brightness segmentation tool within the software package ImagePro, developed by Media Cybernetics, it was possible to threshold out regions of interest and individual phases for quantitative analysis. The evolution of the oxide scale forming after exposure at elevated temperatures was investigated in this work and models were used to compare predicted results with experimental data from isothermal and ex-service material. The change in the thickness of the oxide scale was investigated; with a focus on the aluminium rich oxide scale. It was, therefore, desirable to identify the oxide region within the micrographs and also to be able to distinguish between different regions of the oxide layer. Figure 3.8 shows a series of EDS maps, the mapping was used to identify the regions of the oxide (a) that were rich in aluminium (b), chromium (c) and cobalt (d).

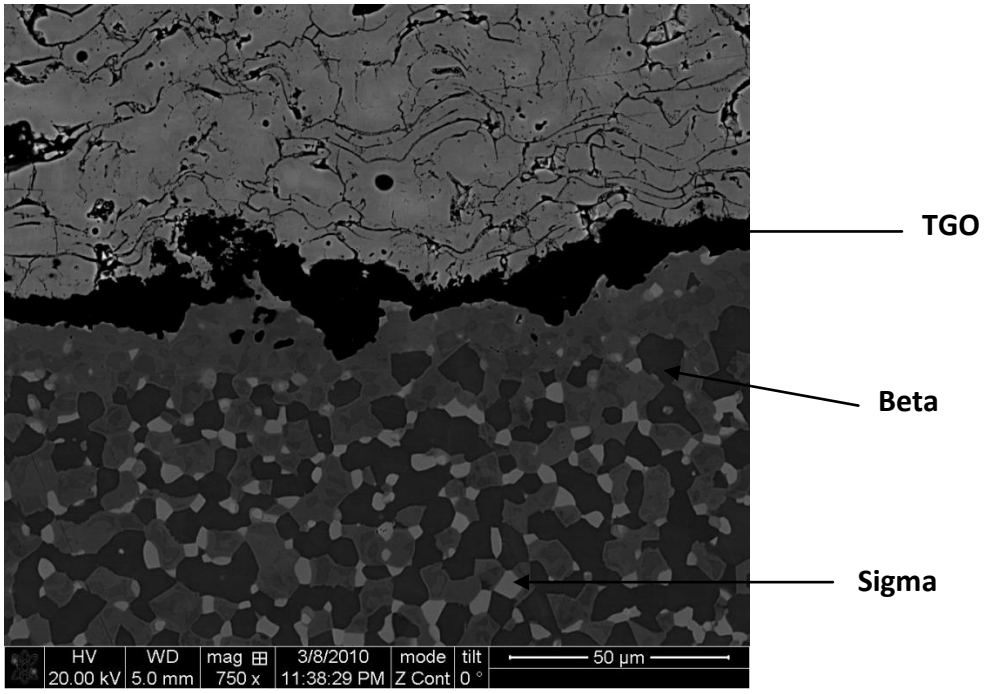

Figure 3.7 A micrograph taken at the outer edge of the Re containing MCrAlY layer from within a multiphase coating of an ex-service combustion chamber heat shield tile. The brightness gradient within the micrograph shows the individual phases.

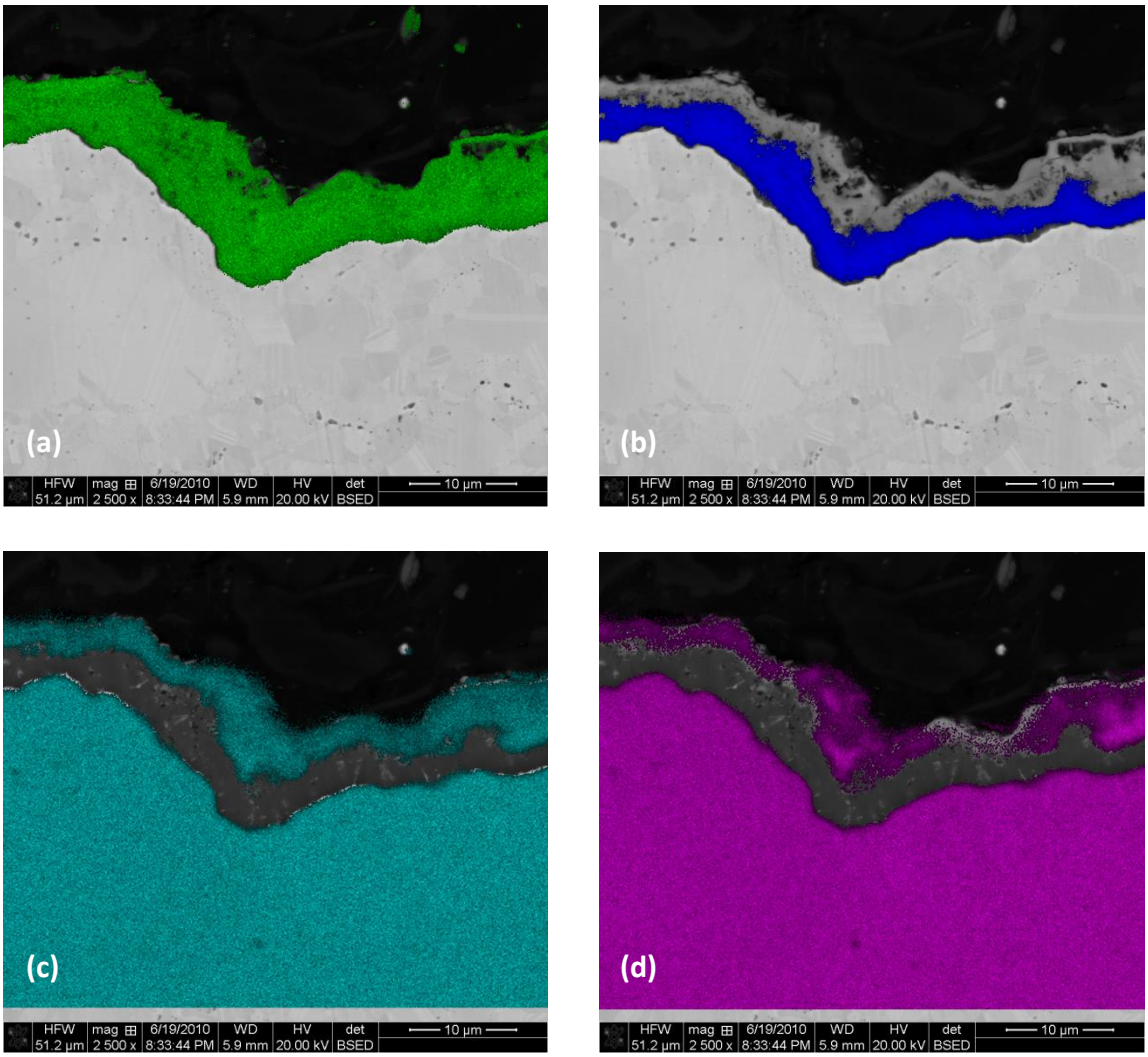

Figure 3.8 EDS analysis of a sample with only a 50 µm MCrAlY coating applied that was aged for 3 months at 950°C. The EDS results in (a) show oxygen concentration, (b) aluminium concentration, (c) chromium concentration, (d) cobalt concentration.

The aluminium rich region of the oxide scale that can be seen in Figure 3.8b scale was measured to determine a mean thickness. Within ImagePro a series of 100 linear measurements were taken from micrographs collected using a backscatter detector at a series of magnifications including 1000x, 2500x and 5000x with a working distance of 6.0mm. The measurements were taken by using a line trace tool that was able to select an interface using the contrast difference between two bordering regions to trace the interface. A mean measurement was taken for the thickness of the aluminium rich region of the oxide scale. This measurement was carried out for all samples, including isothermal and ex-service material. The measurements collected from the isothermally aged samples were used to benchmark existing oxide growth models.

In addition to the measurement of the oxide scale forming, the individual phases within the microstructure were also studied. The aim of the package of work was to derive a series of micrograph measurement tools that could then be used to estimate exposure temperature from a measurement taken from a micrograph. A feature of this work was the linear depletion of the beta phase, the depletion was investigated and the quantification of the changes in depletion used to benchmark a microstructural evolution model. Initially a backscatter image, as shown in Figure 3.9a, was compared with EDS mapping results. In Figure 3.9b, c and d the EDS mapping results for nickel, cobalt and chromium are overlaid onto the back scatter image.

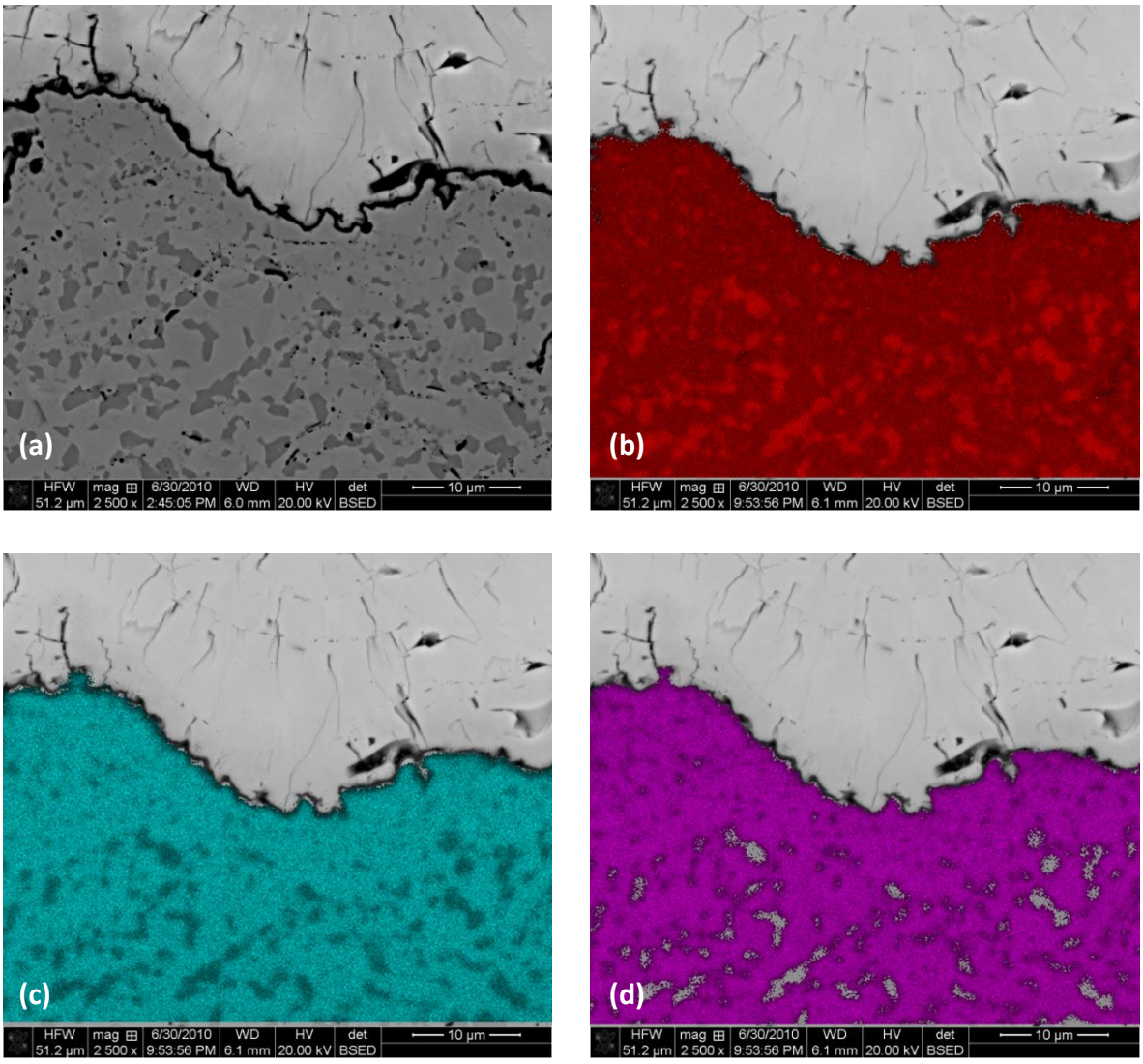

Figure 3.9 The series of micrographs show EDS mapping results for a MCrAlY + TBC coating after isothermal exposure for 6hrs at 900^{o}C. (a) shows the backscatter micrograph, (b) nickel, (c) cobalt, and (d) chromium.

Table 3.5 Phase concentration and chemistry results from thermodynamic calculations for the temperatures 900°C for an AMDRY995 CoNiCrAlY coating of the composition 38.5 Co, 32.5 Ni, 21 Cr, 8 Al Wt.%.

900°C	Co	Ni	Cr	Al
Beta (40%)	31.1	43.7	8.7	16.5
Gamma (60%)	43.4	25.1	29.1	2.4

The data in Table 3.5 shows the phase composition predictions for beta and gamma from thermodynamic calculations, these data were used when carrying out phase identification in addition to spot EDS to support the reliable use of micrographs collected using the back scatter detector in order to distinguish between the phases within the microstructure. The micrographs and EDS maps in Figure 3.9 show how the beta phase contains a higher concentration of nickel and a lower concentration of cobalt and chromium than the gamma matrix. The beta phase can be seen in Figure 3.9a as the darker phase within the MCrAlY layer.

By identifying the MCrAlY/substrate interface as discussed in section 3.5.1 it was then possible to measure the inner beta depletion. The same process was carried out at the outer edge of the MCrAlY layer, this outer depletion can be seen in Figure 3.7, it was measured from the edge of the oxide scale layer into the MCrAlY coating. By thresholding the image the beta phase can be identified as a single phase using brightness segmentation tools. Figure 3.10a and b show how the beta phase can be revealed as a single phase in a greyscale image. In addition to the linear measurements of both the oxide scale and the beta depletion it was possible to quantify the segmented images to calculate an area fraction of the phase present. The first 100μm of the MCrAlY was selected as the area of investigation, this was defined as the first 100μm from the MCrAlY/substrate interface out into the MCrAlY layer. In Figure 3.11a section of the micrograph is shown, this region was measured from the interface. By using the brightness segmentation tool it was then possible to calculate the area fraction of each of the individual phases present. In Figure 3.11b the sigma phase is segmented, this phase appears as the white spherical phase within 3.11a and in 3.11c the beta phase is segmented. The area fraction of the individual phases were calculated and compared with results from a thermodynamic and kinetic dynamic model. The model was previously benchmarked using isothermally aged material.

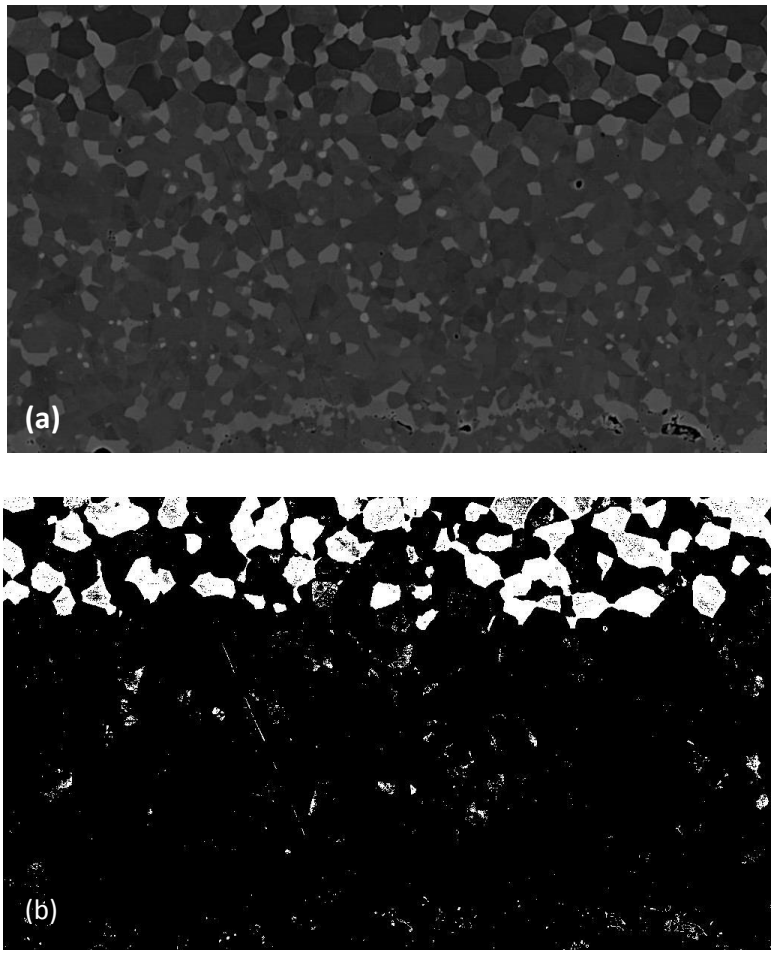

Figure 3.10 (a) A section of a micrograph shows the microstructure within an MCrAlY layer of an ex-service combustion chamber heat shield tile. (b) The beta phase is segmented using a brightness image analysis tool.

.

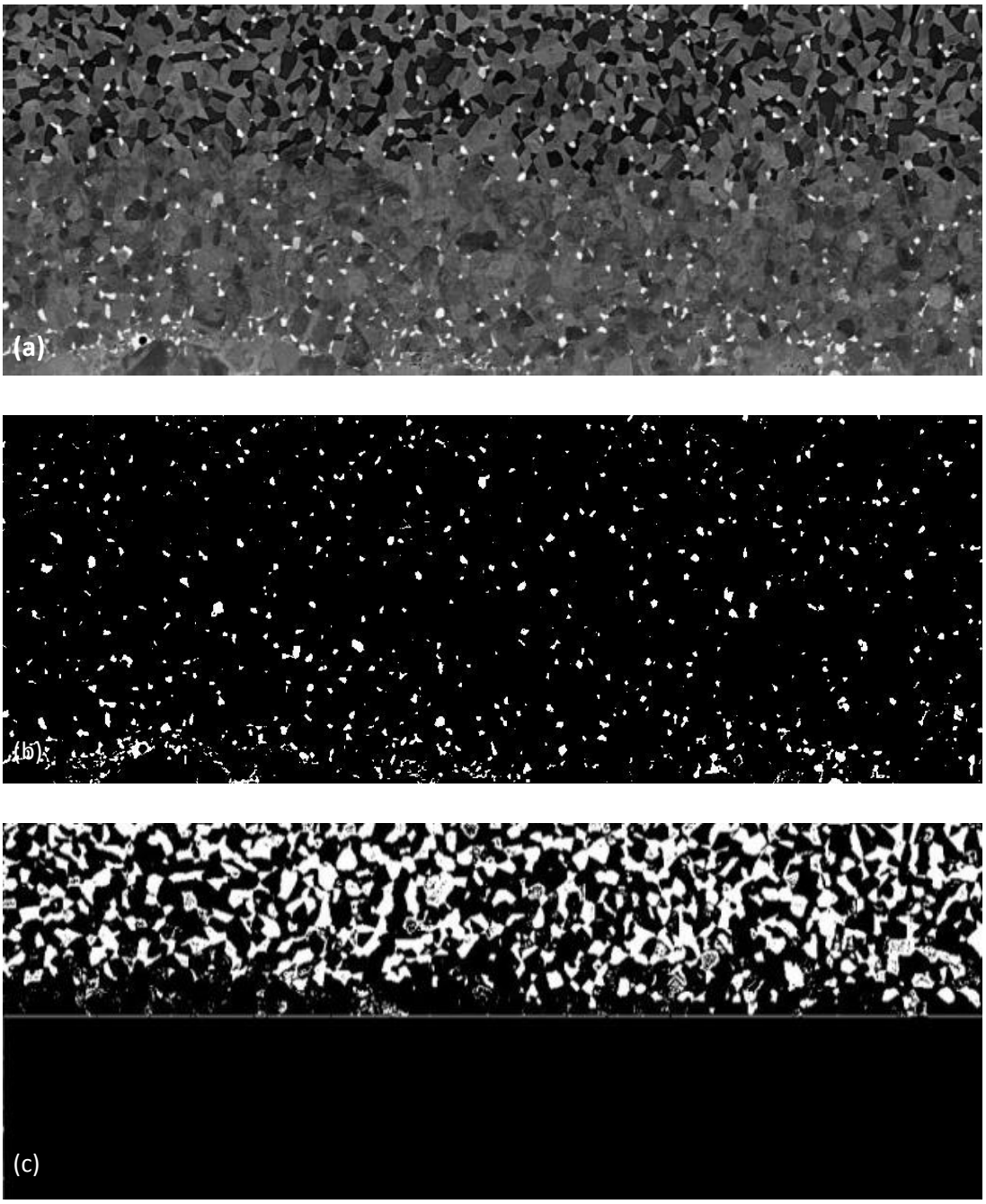

Figure 3.11 The series of micrographs and grayscale images show a section of the microstructure within an ex-service component. In (a) a section taken from a backscatter micrograph is shown, in (b) the sigma phase is segmented and (c) the beta phase.

3.6 Modelling of Microstructures

Thermodynamic equilibrium calculations were carried out initially using MTDATA, this allowed for a prediction of the phases present within each of the MCrAlY coatings and substrate to be made, and to investigate the likely effect of the exposure temperature on the phase composition. A coupled thermodynamic/kinetic model developed at Loughborough University was also used to predict the microstructural evolution after high temperature exposure. This model was used to develop a methodology to estimate the exposure temperature experienced during service; based on the ex-service microstructure.

3.6.1 Thermodynamic Calculations

Thermodynamic calculations were carried out for each of the substrate and coating compositions using the software package, MTDATA version 4.81. developed by the National Physical Laboratory (NPL) which was able to predict phases present, using specifically the superalloys database; Nidata3b1 and Nidata3b2. MTDATA allows for equilibrium to be calculated in a system containing multiple components and phases, the calculations are based on critically assessed thermodynamic data for simpler sub systems. It calculates equilibrium using true Gibbs free energy by finding the equilibrium volume fraction and the composition of the phases that are present. In order to predict the amount and chemical composition of the phases occurring in a system as a fraction of time and temperature at a given pressure it is necessary for accurate thermodynamic data for all the phases of interest to be available. Therefore, the data available for the components of interest and their interactions within a system are vital.

This data is stored in the form of assessed parameters for various models that describe thermodynamic properties of phases which are then assessed by an integral data management system. The software is able to predict the volume fraction and composition of phases present within a multi-component system. It is the change in time and temperature of the equilibrium that is important for this work. MTDATA allows for predictions in phase composition for the temperature range concerned with the area of work. The tool for this is called MULTIPHASE which allows for the solving of equilibrium problems involving many phases and components. The MULTIPHASE tool within MTDATA has been used, not only to get a prediction of compositions of the various phases but also to predict the amount of each phase present. Figure 3.12 shows the different software modules that are used to access the data and the series of calculations and processes that are carried out.

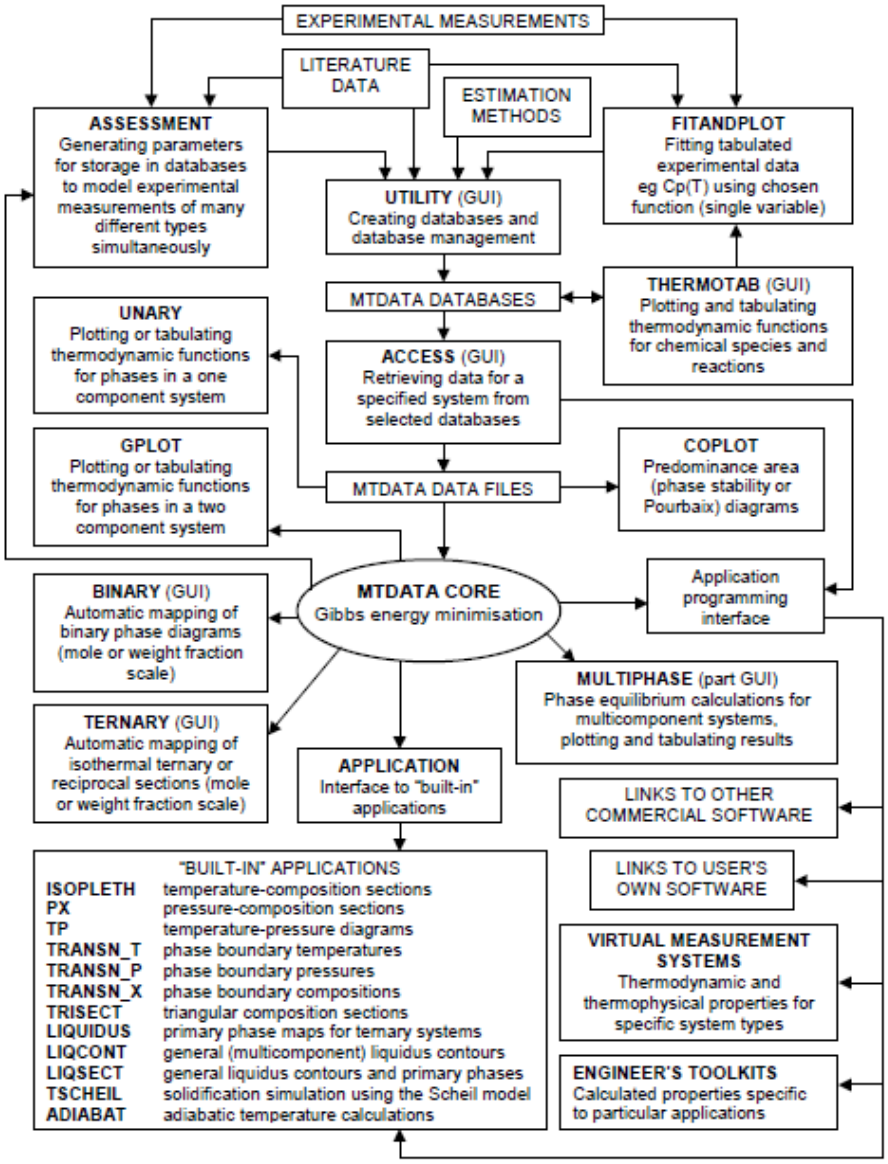

Figure 3.12 An overview of the MTDATA structure; showing the various calculations and processes that are carried out in order to complete an equilibrium calculation (38).

3.6.2 Diffusion Model

Alongside practical characterisation a coupled oxidation and diffusion based 1-d thermodynamic/kinetic model was used to predict the microstructure after isothermal and service exposure. The modelling was used as a tool to aid in the prediction of the experienced temperature during service. This technique is used in Chapters 5 and 6, showing how various model outputs can be compared with quantitative measurements made from isothermally exposed material and then the results used to predict the exposure temperature of ex-service material. The advantage of the diffusion model over the MTDATA thermodynamic calculations is that the diffusion of elements is accounted for and it is a dynamic model. The diffusion model enables a prediction of the phases present for a given exposure time and temperature. The quantity of each phase present can be calculated and this can be tested against the experimental results. The model interprets the substrate and coating as shown in Figure 3.13. The model assumes a phase mixture within the coating; this is currently homogenous in distribution, and that the oxide scale forming depletes the Al and Cr within the MCrAlY layer. Overtime, after thermal exposure, it is assumed that the oxide scale increases in thickness and the beta phase within the MCrAlY layer is depleted. At the substrate and coating interface an interdiffusion zone is assumed to form.

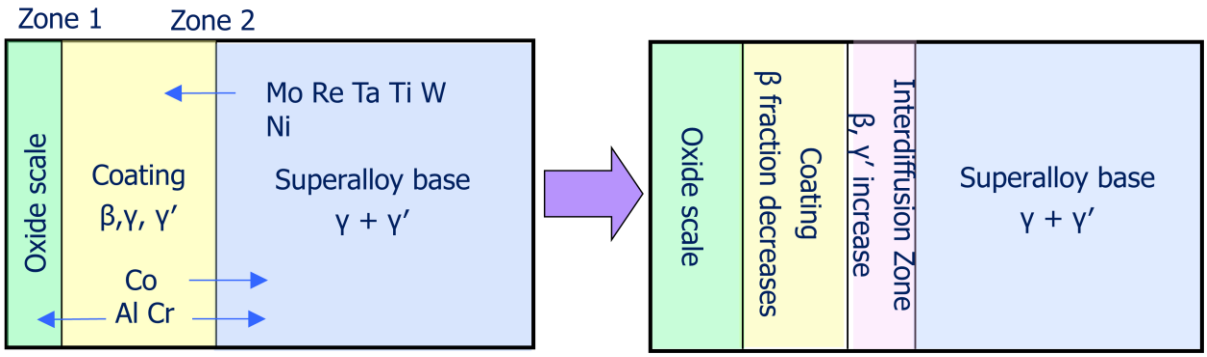

Figure 3.13 This figure illustrates how the thermodynamic and kinetic model interprets the substrate and coating components and how they are expected to evolve with time.

As assumptions are made about the homogeneity of elements throughout the material the areas of interest where diffusion is most likely to take place are concentrated on to help reduce the running time for the model. The region where the formation of the oxide scale occurs and the area of interdiffusion between bondcoat and substrate are where the gradient will be greatest, these areas are defined as Zone 1 and Zone 2, as highlighted in Figure 3.13. Each zone is split up into a grid of nodes, the calculations are carried out for each node. It is the combined results of each grid position that determine the next step size, which is the elapsed time for each calculation.

Over time Zone 1 will increase into the coating to account for the scale thickness increase and Zone 2 will expand as interdiffusion takes place further into both the coating and substrate. Model inputs are required to reflect the material and coating system of interest, the various inputs and the resulting model outputs are detailed in Figure 3.14. The composition of the coating and substrate are required alongside the thickness of the coating layer and thermal history, these parameters will affect the diffusion coefficients. The diffusion model is governed by Equation 3.1, where *D* is the interdiffusion coefficient, C_i the concentration of the element, *x* is the distance and *t*; time.

$$\frac{\partial C_i}{\partial t} = \frac{\partial}{\partial x} D \left(\frac{\partial C_i}{\partial x}\right)$$

Equation 3.1

The diffusion/kinetic model also uses an oxidation model, developed by Nesbitt (39). The model can then allow for the outward growth of the oxide scale at the edge of the coating layer which will result in a depletion of elements in this region. The oxidation model to predict thickness of the scale is defined by Equation 3.2, where δ is the scale thickness. Time in seconds is denoted by t, temperature in Kelvin by T, Q = 27777.4, T_o = 2423.7k and n = 0.332, of which all three are constants.

$$\delta = \left[exp\left\{Q\left(\frac{1}{T_0} - \frac{1}{T}\right)\right\} t\right]^n$$

Equation 3.2

The outputs of the model are in the form of concentration profiles for the elements present. A phase profile is also generated which shows how the various phases are predicted to be distributed as a volume fraction across the coating and substrate. The output profiles are both presented in terms of a distance from the edge of the oxide scale into the coating, an example output profile is shown in Figure 3.15. During high temperature exposure the oxide scale is assumed to increase in thickness, the thickness of this scale can be predicted by the model.

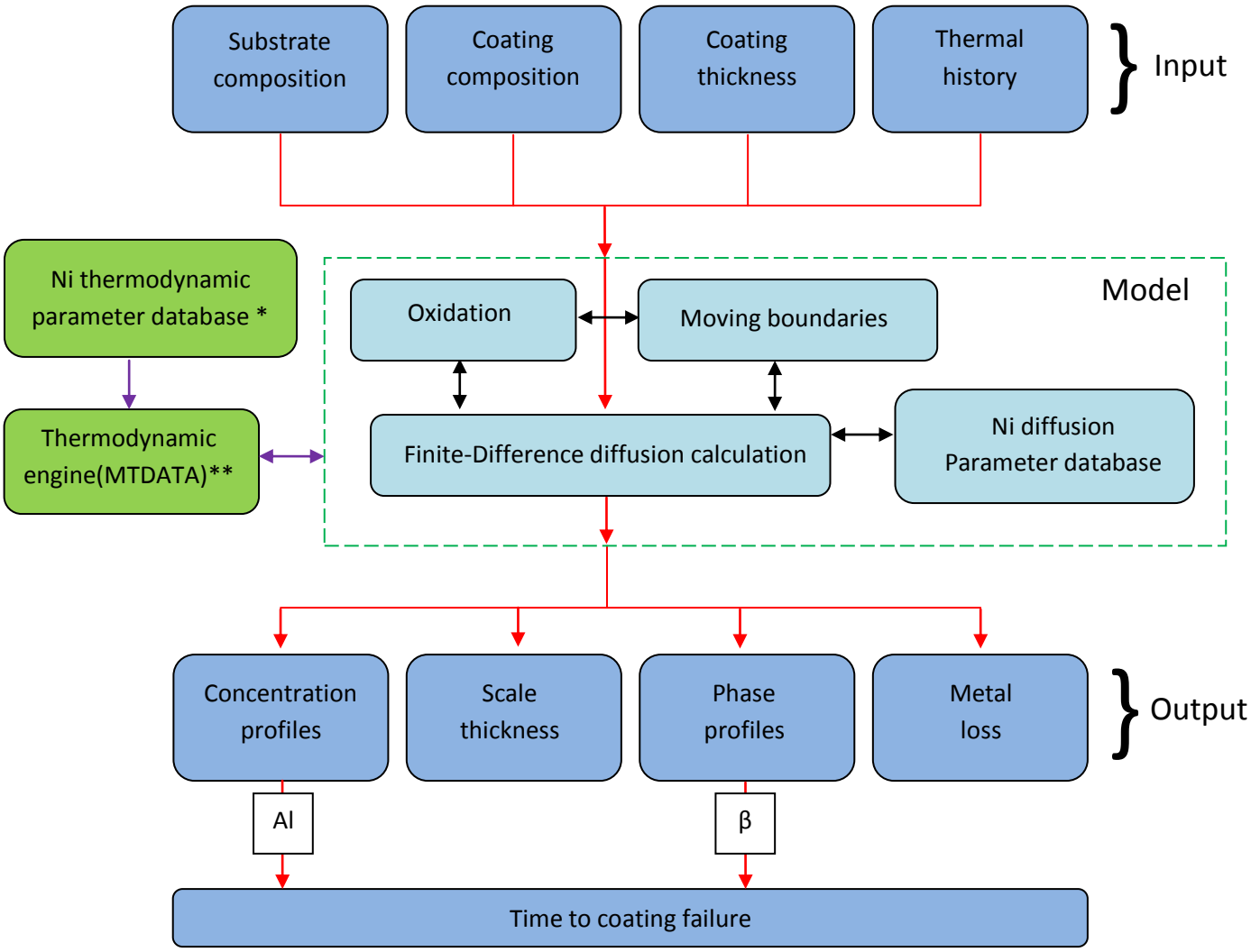

***Ni thermodynamic database**
****Thermodynamic engine (MTDATA)**

Figure 3.14 An overview of the model highlighting the various input parameters required, the individual components of the model and the model outputs.

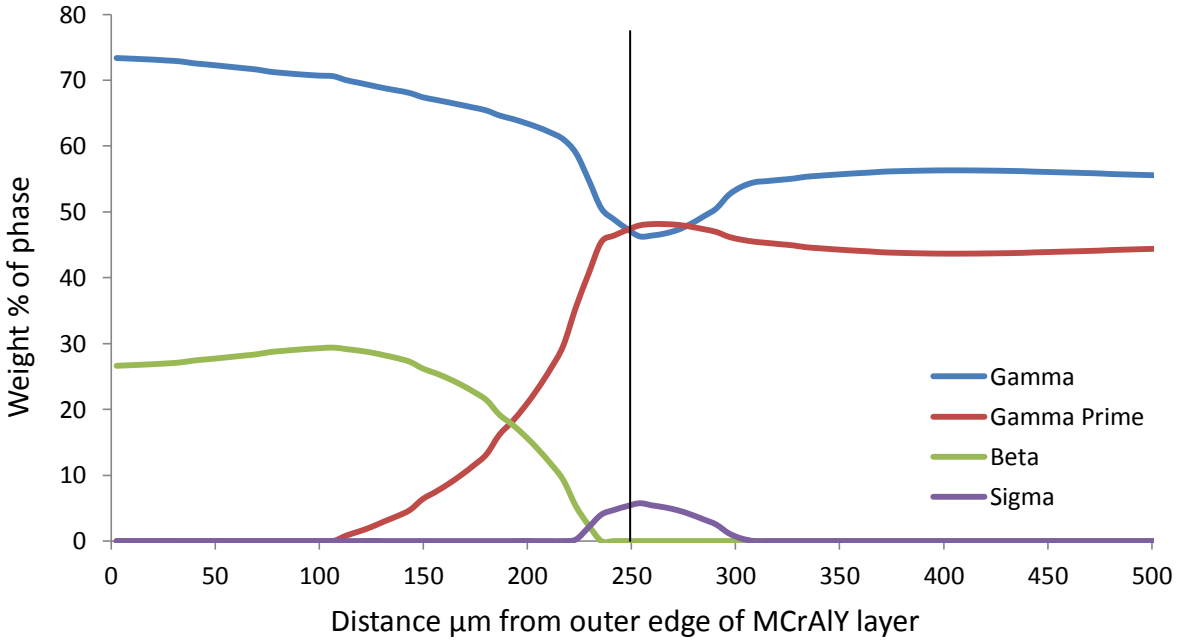

Figure 3.15 A kinetic/thermodynamic model result predicting the phases present within the microstructure of a 250 µm AMDRY995 MCrAlY layer applied to an In738LC substrate after exposure at 900°C for 5004 hours.

The actual model, as shown in Figure 3.14 is made up of a number of sub-steps that cycle to arrive at an output. For each node within a zone the series of steps are carried out. The first step is to determine the time step size; this is calculated by using the diffusion coefficient. As the gradient increases for diffusion the grid expansion will reduce so that the largest gradients are simulated over a shorter time period, which will produce an increased accuracy in the simulation result. After the time step is calculated the oxidation model is used to determine the effects of Al oxidation at the surface of the coating and the depletion of elements from within, this model assumes an Al only oxide scale. The next step of the model is using MTDATA for thermodynamic calculations, NiData3b1 and NiData3b2 Ni databases were used, MTDATA calculates the proportion of phases present at each node of the grid and the composition of each of the phases present. With the phase fraction of the node predicted a diffusion coefficient can be calculated, this is based on the interdiffusion of each element with Ni, the diffusion coefficient for each element forms the input for the diffusion sub section. At each node it is then possible to calculate the effective diffusion coefficient of each element within each phase using the phase fraction information from MTDATA. The difference in concentration of each element within a node can then be calculated for the new time step taking into account the interdiffusion due to time and temperature, the change in concentration effects the expansion of the grid and the position of the node for the next time step.

The diffusion of elements predicted by the model is tested against collected quantitative data from isothermally aged material. The combination of diffusion model prediction and sample results is used to enable predictions to be made about the exposure temperature experienced during service. Correlations between the isothermal characterisation and model predictions are highlighted in the results chapters.

3.6.3 Model Development

The thermodynamic and kinetic model used does make some assumptions that are currently in a position of refinement, the interface between the coating and substrate is assumed to be linear and the concentration of elements throughout the material is assumed to be homogenous. Other limitations mean that operating conditions concerning the effect of S in the fuel and NaCl ingested from air intake are not included; the model assumes that the material is cycled in air. Precipitated phases that form along grain boundaries can be modelled but there is no allowance for the amount of grain boundaries within the material as yet.

This initial model does not include the TBC coating into the calculations, within Chapter 4 the influence of a TBC layer on the performance of an MCrAlY coating system is shown, the results of this work will be used to help refine the accuracy of the microstructure models.

4 Microstructural Characterisation of MCrAlY Coated IN738LC Isothermally Aged Samples With and Without a Thermal Barrier Coating

4.1 Introduction

This chapter discusses the characterisation of a coated Ni-based superalloy system. The purpose of this work was to characterise the microstructural evolution of MCrAlY coated isothermally aged material and to study the performance effect of an additional thermal barrier coating (TBC). Thermodynamic calculations were carried out to predict the amount and the chemical composition of each phase present at equilibrium within the MCrAlY coating component of the system. The microstructure of the MCrAlY coating was characterised using a range of techniques. In this chapter backscatter imaging was used to show how the microstructure evolves with time at different temperatures, and to study the MCrAlY/TBC interface where oxide products form. Quantitative measurements of the microstructure were made, and where possible the measured results have been compared against combined kinetic/thermodynamic and oxidation modelling predictions. The substrate for all of the samples discussed in this Chapter comprises 7 mm diameter IN738LC bars sectioned to produce 5 mm thick disks. The samples had a 50 µm CoNiCrAlY coating applied by high-velocity oxygen fuel (HVOF) thermal spraying, and for each sample there was a comparable sample also with a 50 µm CoNiCrAlY layer applied and an additional 250 µm yttria-stabilised zirconia (YSZ) TBC, applied by an air plasma spray (APS) method. It should be noted that this 50 µm coating is typically a lot less than used on components for service, which can be in the range 150-200 µm thick. The composition of the MCrAlY coating powder provided by the powder manufacturer and the actual value measured in the coating, by EDS after spraying, are shown in Table 4.1.

Table 4.1 AMDRY995 CoNiCrAlY coating powder composition and the measured composition of a sample coated with an MCrAlY and TBC layer, measured after 4 hours at 1080^{o}C post coat heat treatment and before isothermal ageing.

Nominal Powder composition					
Element	Co	Ni	Cr	Al	Y
Wt.%	38.5	32	21	8	0.5
After post coating treatment - composition by EDS					
Element	Co	Ni	Cr	Al	Y
Wt.%	31.0	39.4	18.3	10.6	0.7

A discrepancy was observed between the nominal powder composition and the measured composition by EDS. A combined kinetic/thermodynamic model was used to predict the composition after post coating heat treatment. The predicted composition within the bulk of the MCrAlY and within the interdiffusion zone (IDZ) is shown in Table 4.2. It can be observed that the IDZ region is predicted to be a close match to the measured composition in Table 4.1. The MCrAlY in this work was a 50 µm layer, therefore, high temperature post coat heat treatments are likely to have a significant effect on the microstructure and phases present within the coating before isothermal exposure. Within a thin MCrAlY coating the IDZ is likely to represent a large proportion of the total MCrAlY thickness.

Table 4.2 Predicted coating composition in the bulk of the coating and within the interdiffusion zone. The prediction was made using a combined thermodynamic/kinetic model, which is detailed in Section 3.5.

model prediction in bulk coating after post-coat heat treatment					
Element	Co	Ni	Cr	Al	Y
Wt.%	38.4	32.7	21.1	7.8	x
model prediction within IDZ after post-coat heat treatment					
Element	Co	Ni	Cr	Al	Y
Wt.%	29.2	43.0	19.1	6.2	x

All samples were aged isothermally; the ageing time and temperatures are shown in Table 3.3. The temperatures were selected in order to provide an isothermal characterisation comparison with likely service conditions. Time intervals of 2190 hrs (3 months) were chosen to be able to characterise the microstructural evolution over a time period that would have reflected the likely service between inspections up to a maximum ageing time of 10950 hrs (15 months).

4.2 Thermodynamic Calculations

Thermodynamic equilibrium calculations were carried out for the CoNiCrAlY coating for a temperature range 500-1500°C, for a powder composition as shown in Table 4.1. The thermodynamic database used did not have an entry for Y, therefore the calculations were carried out using an adjusted Ni content of 32.5 wt.% incorporating the 0.5 wt.% Y content.

Figure 4.1 shows that, in the temperature window of interest for this work, the coating is essentially made up of two phases, gamma and beta. The gamma concentration increases from being thermodynamically unstable below 500°C up to a maximum concentration of 90 wt.% at 1330°C. The beta phase is shown to gradually decrease in concentration from 48 wt.% at 650°C to 10 wt.% at 1330°C. 35 wt.% sigma is predicted to be present at 500°C, however, as temperature increases the amount predicted falls until 840°C where 0 wt.% sigma is predicted above this temperature. The gamma prime phase is not stable above 640°C for this coating composition.

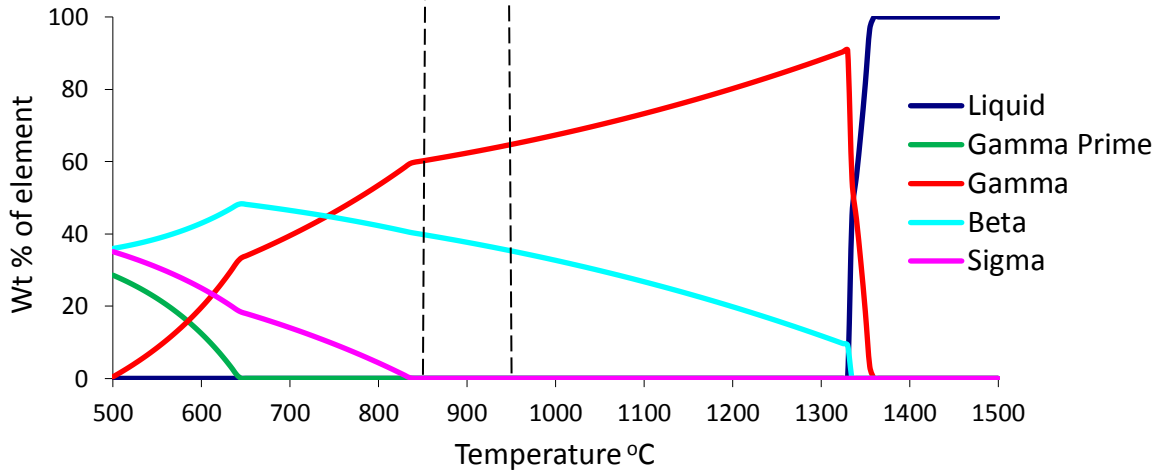

Figure 4.1 Thermodynamic calculation prediction for selected phases for the CoNiCrAlY coating. The calculation was carried out for the composition 38.5 Co, 32.5 Ni, 21 Cr, 8 Al wt % between 500-1500°C.

The phase composition for the bond coat changes from 60 wt.% gamma, 40 wt.% beta at 850°C to 65 wt.% gamma, 35 wt.% beta at 950°C as shown in Figure 4.1. Further calculations were carried out to determine the chemical composition of each phase predicted to be present at a specific temperature. The two temperatures used reflect two of the isothermal ageing temperatures used. Table 3.3 shows the composition of the phases present at 850°C and 950°C. It can be observed that the Al concentration is significantly different between the two phases; this therefore can be used as a factor to discriminate between phases using the backscatter imaging technique.

Table 4.3 Phase concentration and chemistry results from thermodynamic calculations for the temperatures 850°C and 950°C for an AMDRY995 CoNiCrAlY coating of the composition 38.5 Co, 32.5 Ni, 21 Cr, 8 Al Wt.%.

	Element wt.%			
850°C	**Co**	**Ni**	**Cr**	**Al**
Beta (40%)	31.1	43.7	8.7	16.5
Gamma (60%)	43.4	25.1	29.1	2.4

	Element wt.%			
950°C	**Co**	**Ni**	**Cr**	**Al**
Beta (35%)	30.5	43.8	9.0	16.7
Gamma (65%)	42.9	26.4	27.6	3.2

Figure 4.2 shows how the composition of the matrix gamma phase is expected to change with temperature. It can be seen that the phase is predominantly Co rich at 40-45 wt.%, 20-30 wt.% Cr and Ni are also present; the Cr and Ni concentration change as temperature increases. Figure 4.3 shows how the gamma prime phase elemental concentration does not change between 500 - 640°C, and it is not thermodynamically stable above 640°C. The gamma prime phase is of the composition Ni 65 wt.%, Co 20 wt.%, Al 10 wt.%, Cr 5 wt.%. Figure 4.4 represents the composition of the beta phase; a high Ni and Co content is observed alongside 14-16 wt.% Al and 4-8 wt.% Cr. Figure 4.5 shows the composition of the sigma phase, this phase is Cr rich, with above 50% wt.% Cr predicted with high concentrations (40-45 wt.%) of Co and 4-6 wt.% Ni.

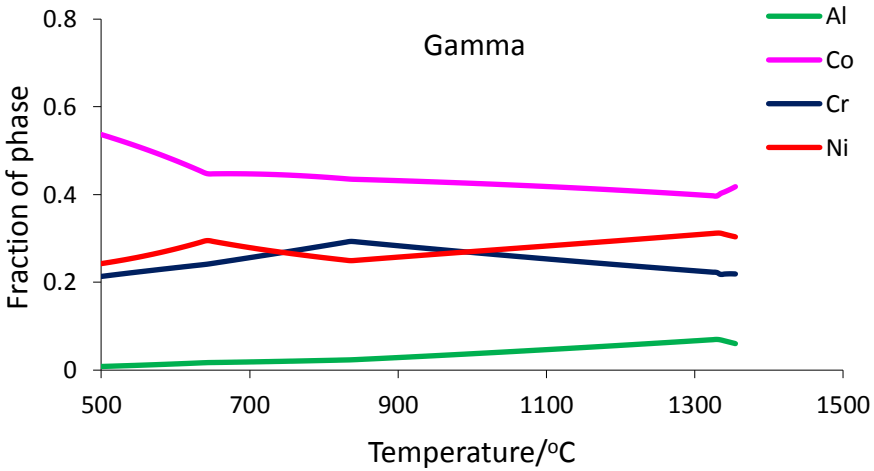

Figure 4.2 Thermodynamic prediction of the composition of the gamma phase in the CoNiCrAlY coating with composition 38.5 Co, 32.5 Ni, 21 Cr, 8 Al Wt.%.

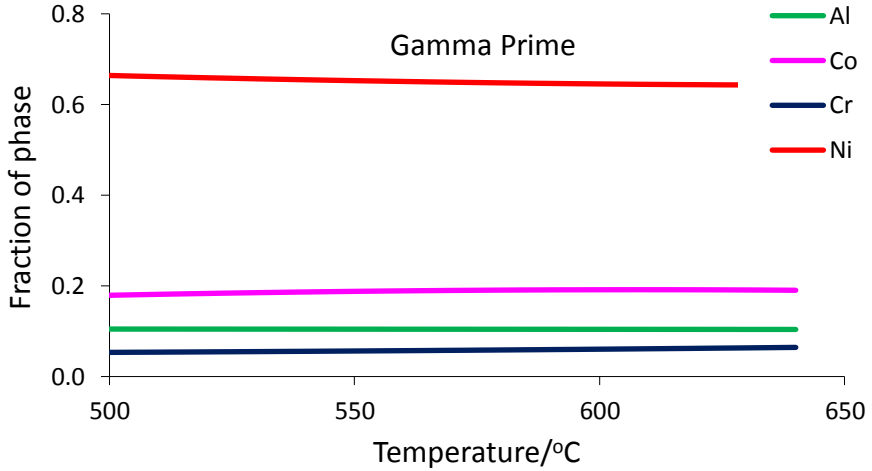

Figure 4.3 Thermodynamic prediction of the composition of the gamma prime phase in the CoNiCrAlY coating with composition 38.5 Co, 32.5 Ni, 21 Cr, 8 Al Wt.%.

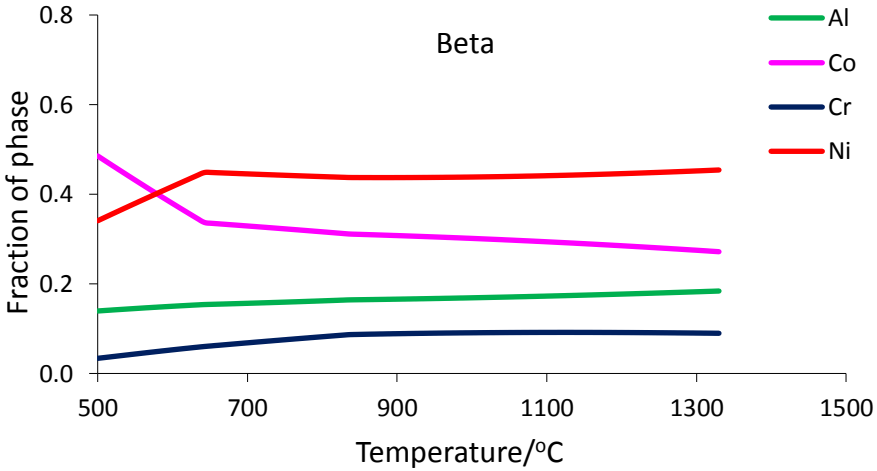

Figure 4.4 Thermodynamic prediction of the composition of the beta phase in the CoNiCrAlY coating with composition 38.5 Co, 32.5 Ni, 21 Cr, 8 Al Wt.%.

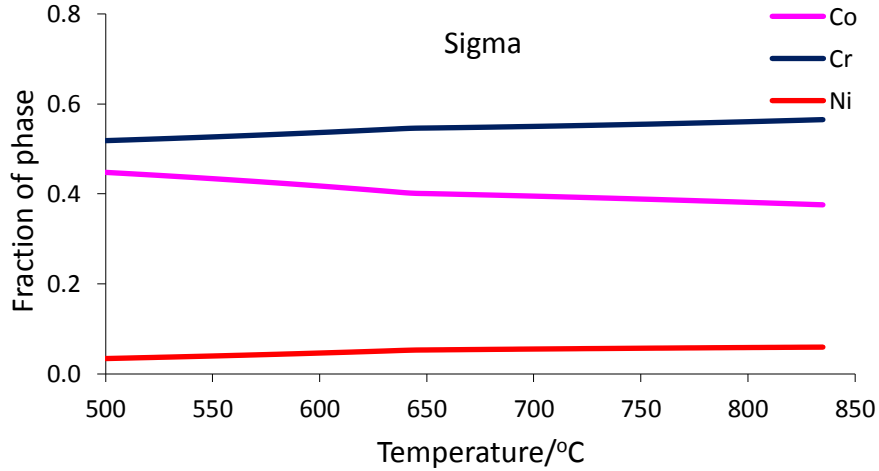

Figure 4.5 Thermodynamic prediction of the composition of the sigma phase in the CoNiCrAlY coating with composition 38.5 Co, 32.5 Ni, 21 Cr, 8 Al Wt.%.

4.3 Microstructure of CoNiCrAlY Coated IN738LC

The characterisation of the microstructure within the coating system is discussed in this section. The microstructure within an as received sample can be observed in the backscatter micrograph presented in Figure 4.6. The Al rich beta phase is highlighted in the bond coat layer. The outer TBC layer is present on top of a MCrAlY bond coat with a mean thickness of 55 µm. The degree of surface roughness of the MCrAlY layer can be observed in Figure 4.6; this is affected by the air plasma spraying parameters and coating surface treatments. The backscatter detector was used to collect images for quantification of the TBC, TGO and MCrAlY components of the coating system and to allow for thresholding of the phases within the micrograph. Measurements for coating thickness were made by using image analysis software so that over 100 measurements were taken from a single micrograph and a mean value calculated. The as-received sample comprised of the phases gamma (Ni), gamma prime (Ni_3Al) and beta (NiAl). By using EDS analysis of the chemistry of the beta phase, it was found to have the composition Al 21 wt.%, Cr 9 wt.%, Co 20 wt.% and Ni 50 wt.%. The beta phase can be observed in Figure 4.7 after 3 months ageing at 850^{o}C; it can be noted, however, that after only 3 months at 850^{o}C there is a large depletion region. The depletion of the beta at the substrate/MCrAlY interface and at the MCrAlY/TBC interface can both be observed. It is the depletion of the beta phase that is typically thought of as a lifetime indicator of the coating system, and the beta phase is crucial in the formation of a protective oxide scale at the TBC/MCrAlY interface as it is the source of the preferential protective oxide forming element Al. As the oxide scale forms the beta is dissolved, causing a depletion at the outer edge of the coating. This continues until the supply of Al ceases to be sufficient to form an Al rich TGO. As Al in the MCrAlY is consumed in the process of replenishing the oxide scale, it is also diffusing across the MCrAlY/substrate interface because of a lower Al concentration within the substrate. This forms an area of interdiffusion, known as the interdiffusion zone (IDZ), between the coating and substrate. Both oxide growth and interdiffusion result in the beta phase depleting at the inner and outer regions of the MCrAlY coating. Both the oxide scale and the beta depletion are microstructural features that it is possible to quantify as the microstructure evolves. Due to the thin MCrAlY coating applied in this case, the beta phase depleted during post coating heat treatments for all samples with only an MCrAlY layer present. The beta phase was only observed within samples that had an additional TBC applied which were aged at 850^{o}C. No beta was present after exposure at 900 or 950^{o}C when a TBC was applied.

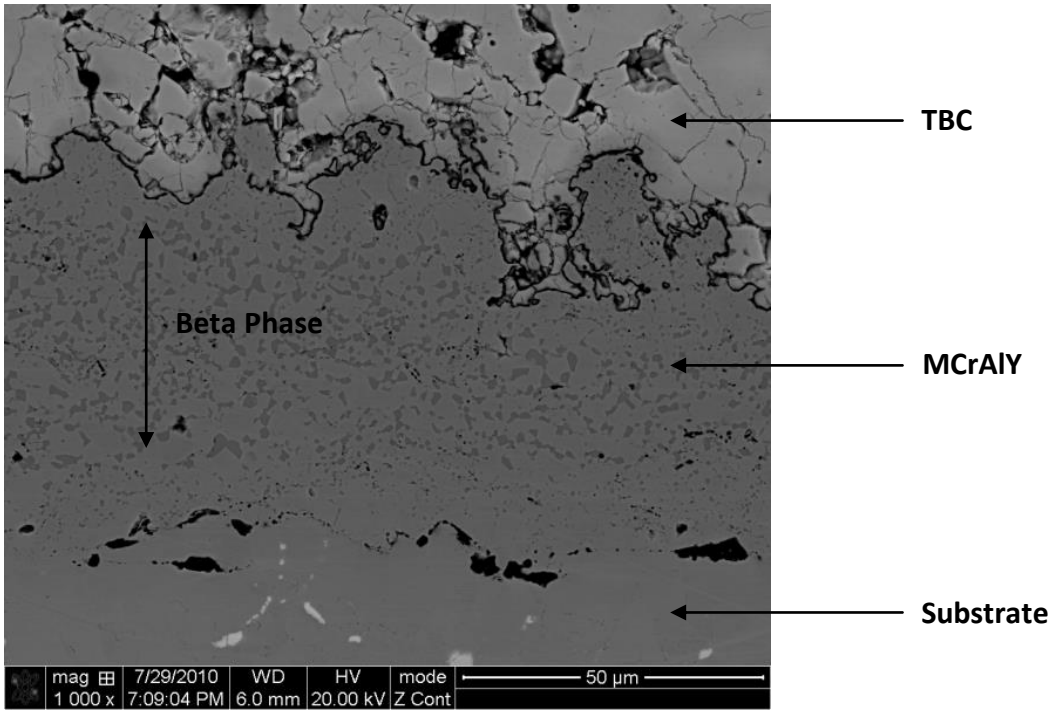

Figure 4.6 A backscatter micrograph showing the coating system components and substrate in the as received condition. Note the beta phase can be observed within the coating in the as received condition.

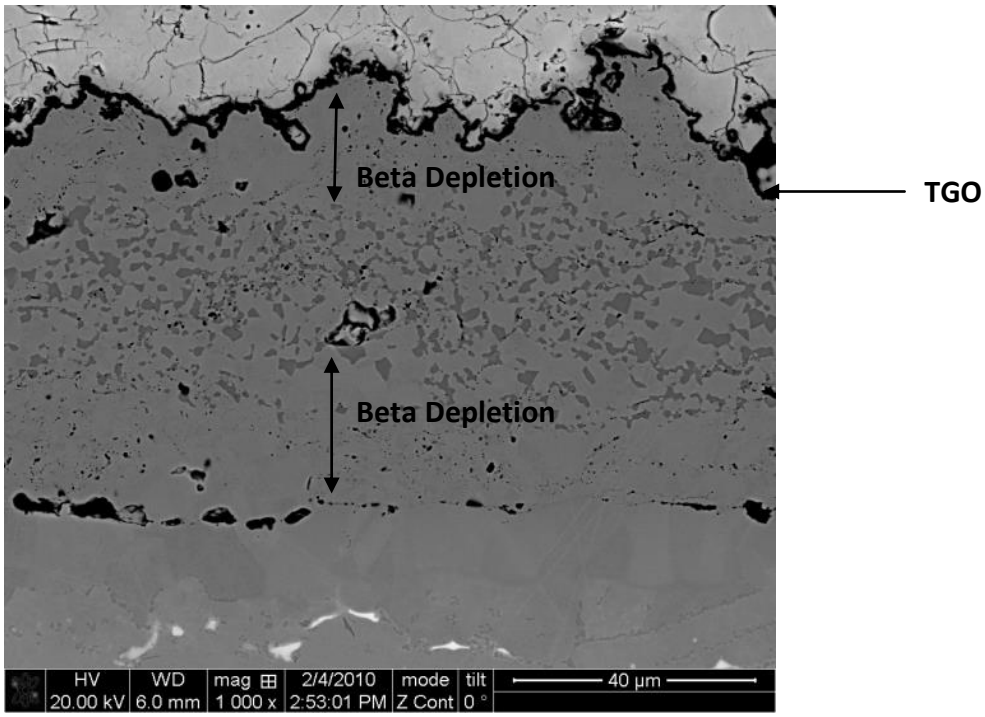

Figure 4.7 A dual-beam FIB FEGSEM BSD micrograph highlighting the depletion of the beta phase within the outer region of the MCrAlY coating in a sample with both an MCrAlY and TBC layer applied, after 3 months of ageing at 850^{o}C.

4.3.1 Oxide Case Study of Isothermally Aged Samples

Isothermally aged samples with and without a TBC were characterised after isothermal exposure between 3 and 15 months at 3 month intervals. Samples were aged isothermally at 850, 900 and 950^{o}C. In Table 3.3 the matrix shows the ageing time and temperature combinations for the samples characterised. The oxide layer was initially characterised to study the effect of ageing conditions on the thickness of the oxide forming. The oxide layer was measured by collecting a series of backscatter images and then using image analysis software to take a series of measurements to derive a mean oxide layer thickness.

In Figure 4.8 a series of backscatter images are shown for samples aged for 3 months and 6 months at temperatures of 850, 900 and 950^{o}C. The samples studied in Figure 4.8 had only a 50 µm MCrAlY coating applied. It can be seen within Figures 4.8a, c and e that the thickness of the oxide after 3 months appears to be very similar despite an increase in exposure temperature from 850 to 950^{o}C. There did, however, appear to be a variation in the surface roughness of the MCrAlY layer. Samples aged for 6 months, as shown in Figures 4.8b, d and f, show how the oxide thickness does not appear to show a correlation with an increase in the isothermal exposure temperature. In Figure 4.9 backscatter micrographs are presented for samples with only a 50 µm MCrAlY layer applied, aged for 9 months and 12 months at 850, 900 and 950^{o}C. The thickness of the oxide layer forming on all samples with only a 50 µm MCrAlY layer applied is shown in Figure 4.13. It can be seen how there does not appear to be a correlation between isothermal ageing conditions and the thickness of the oxide scale forming after isothermal exposure.

Alongside samples coated with only a 50 µm MCrAlY layer, there were also comparable samples with an additional TBC layer applied, as shown in Table 3.3. Figure 4.10 presents backscatter micrographs for samples aged for 3 months and 6 months at 850, 900 and 950^{o}C with both an MCrAlY and TBC layer applied. Figures 4.10a, c, and e show samples aged for 3 months; it can be seen how the oxide thickness appears to increase as the exposure temperature increases. Figures 4.10b, d and f shows samples aged for 6 months; it also appears that as the exposure temperature increases, the resulting oxide forming is also increasing in overall thickness. Figure 4.11 shows samples aged for 9 months and 12 months and the same relationship was observed; as the temperature increases, the oxide thickness increases in samples which have also had a TBC applied. Figure 4.12 shows that after 15 months, the samples still follow the same trend.

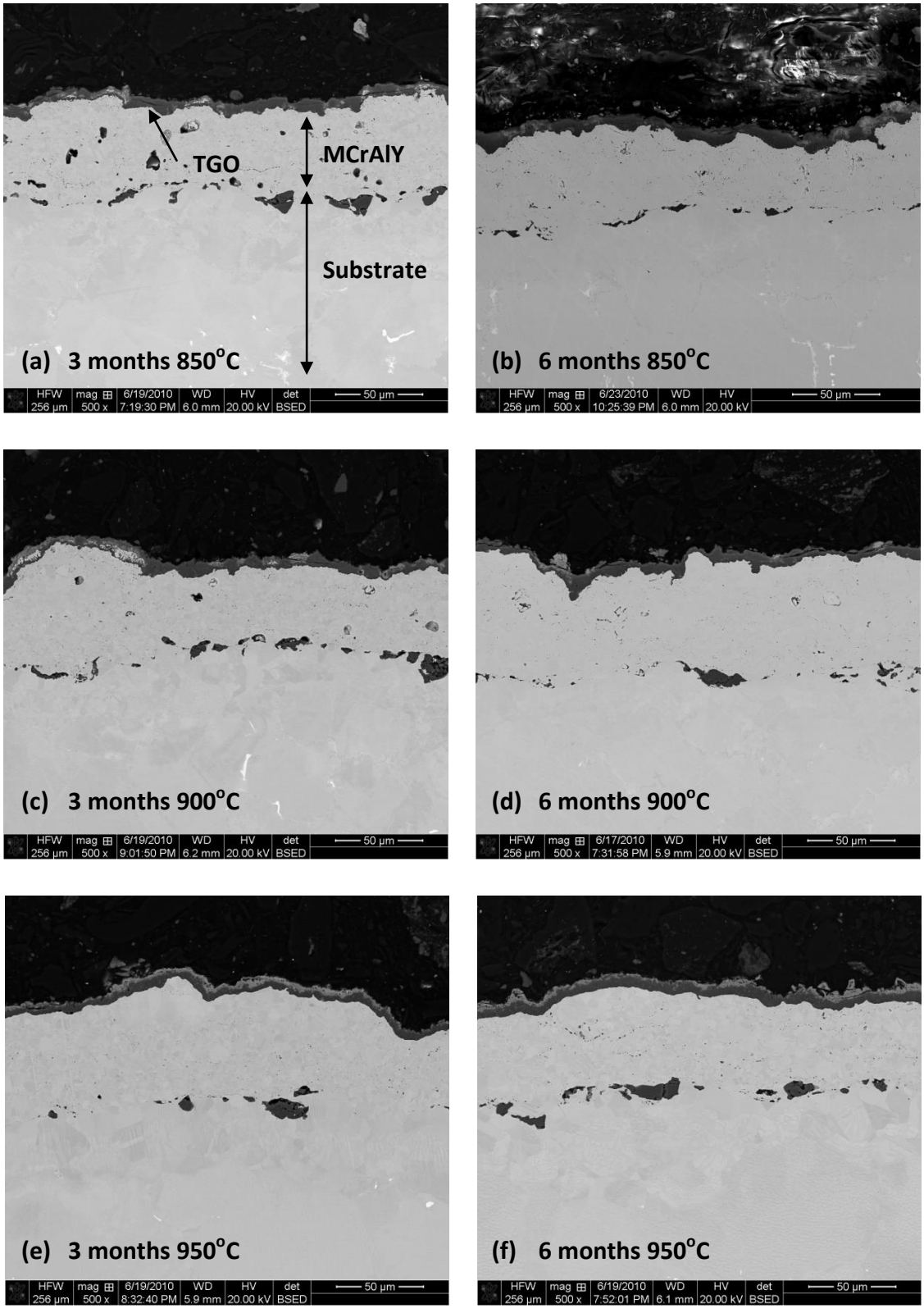

Figure 4.8 A series of backscatter images, after 3 and 6 months ageing at temperatures 850, 900 and 950°C. Images were collected using the same microscope settings for each sample.

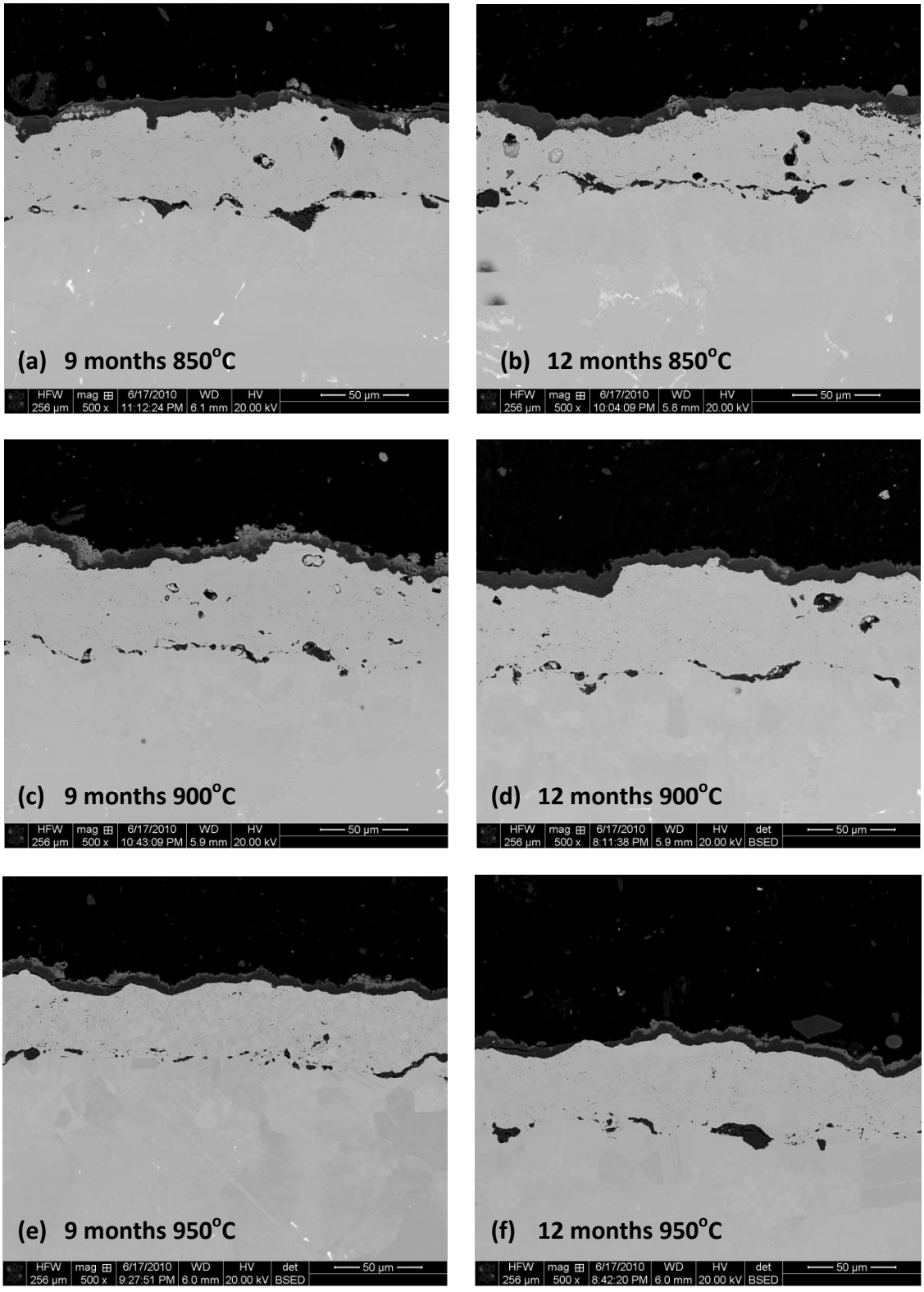

Figure 4.9 A series of dual beam backscatter images, after 9 and 12 months ageing at temperatures 850, 900 and 950°C.

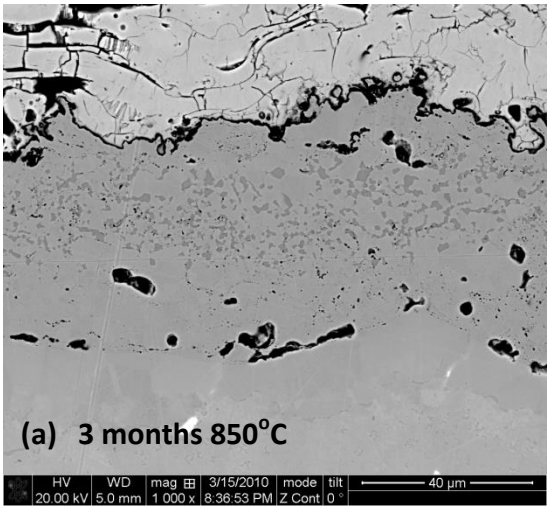

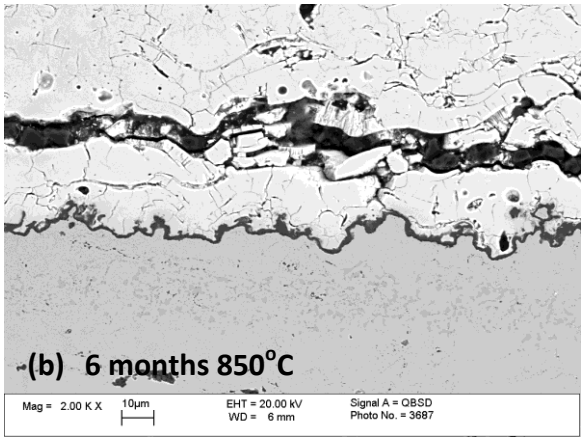

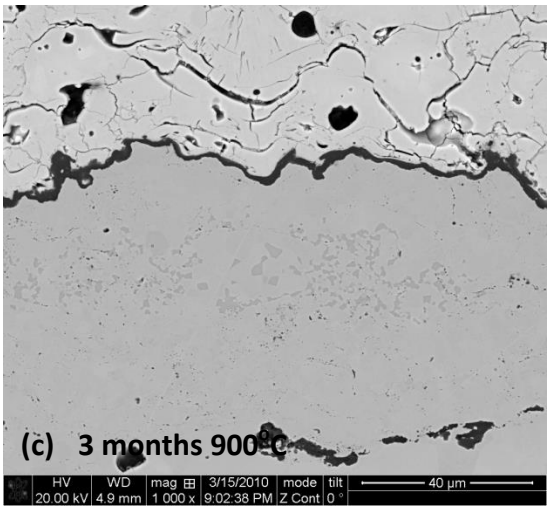

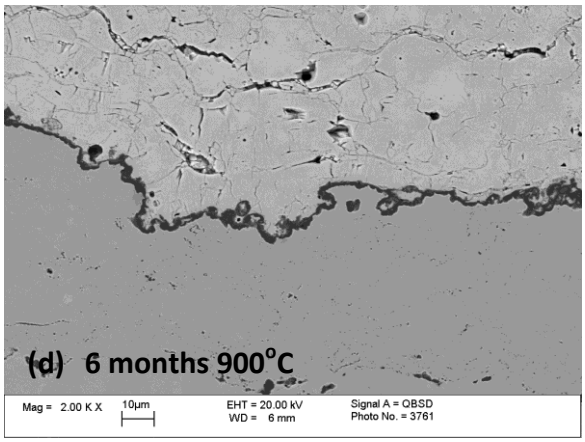

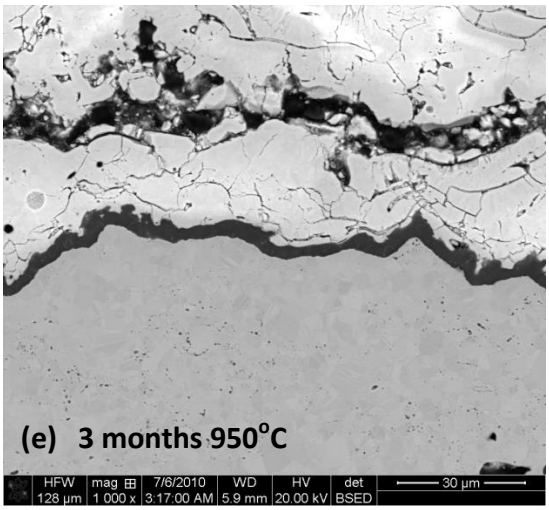

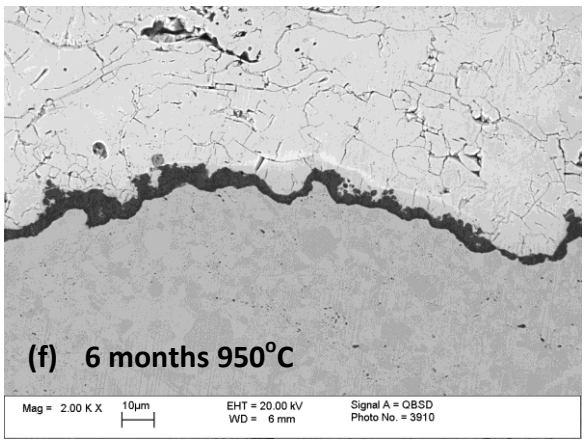

Figure 4.10 A series of backscatter images, after 3 and 6 months ageing at temperatures 850, 900 and 950°C. MCrAlY and TBC coatings were applied to each sample.

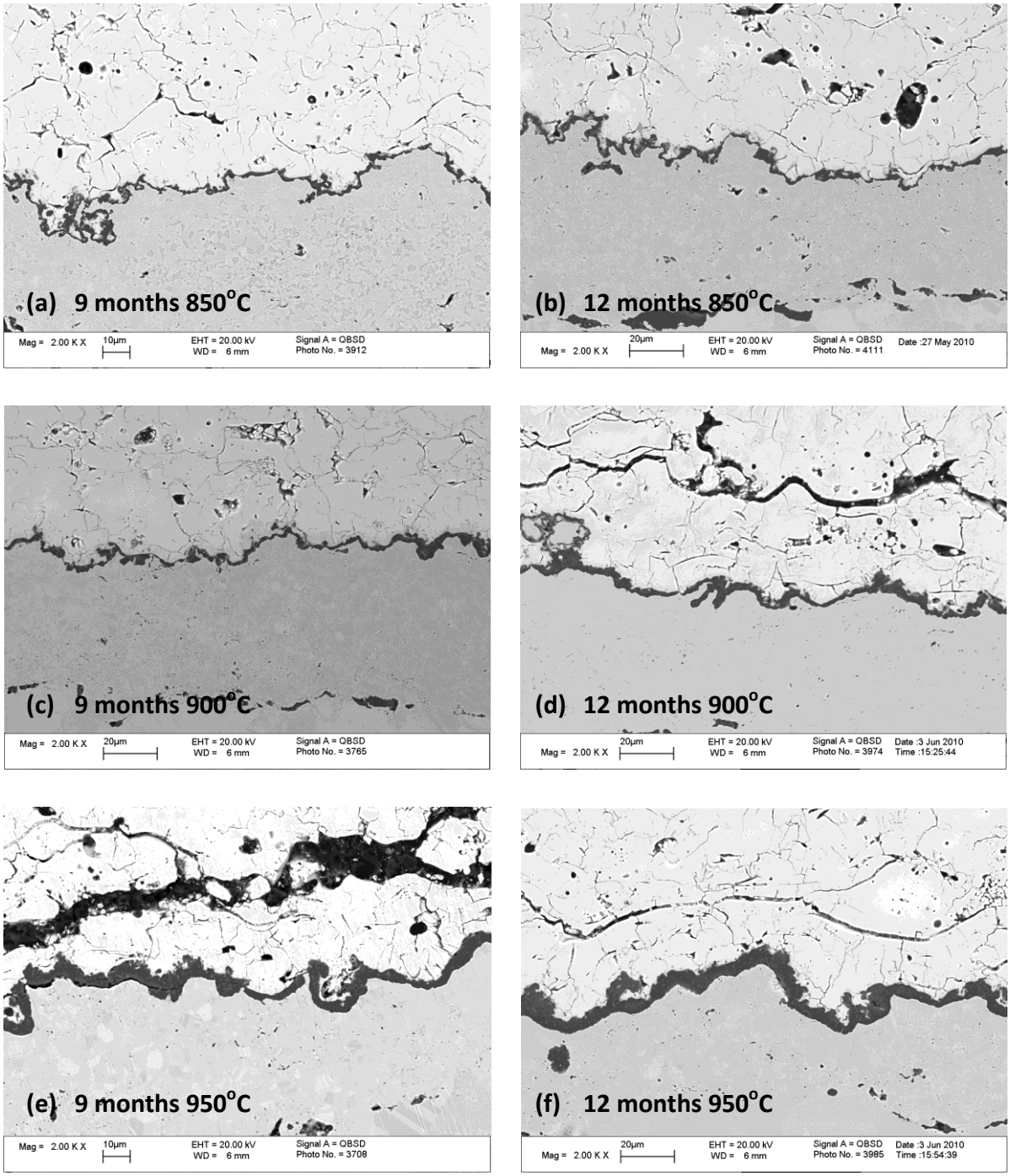

Figure 4.11 A series of backscatter images, after 9 and 12 months ageing at temperatures 850, 900 and 950°C. MCrAlY and TBC coatings were applied to each sample.

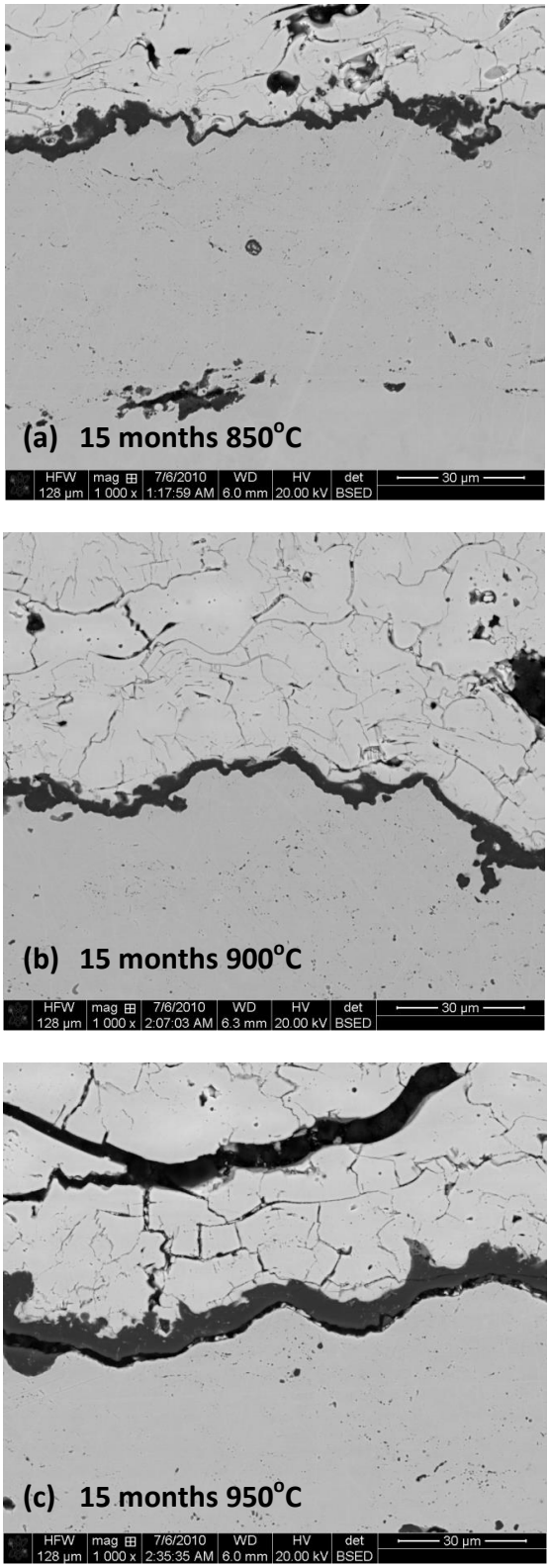

Figure 4.12 A series of backscatter images, after 15 months ageing at temperatures 850, 900 and 950°C. MCrAlY and TBC coatings were applied to each sample.

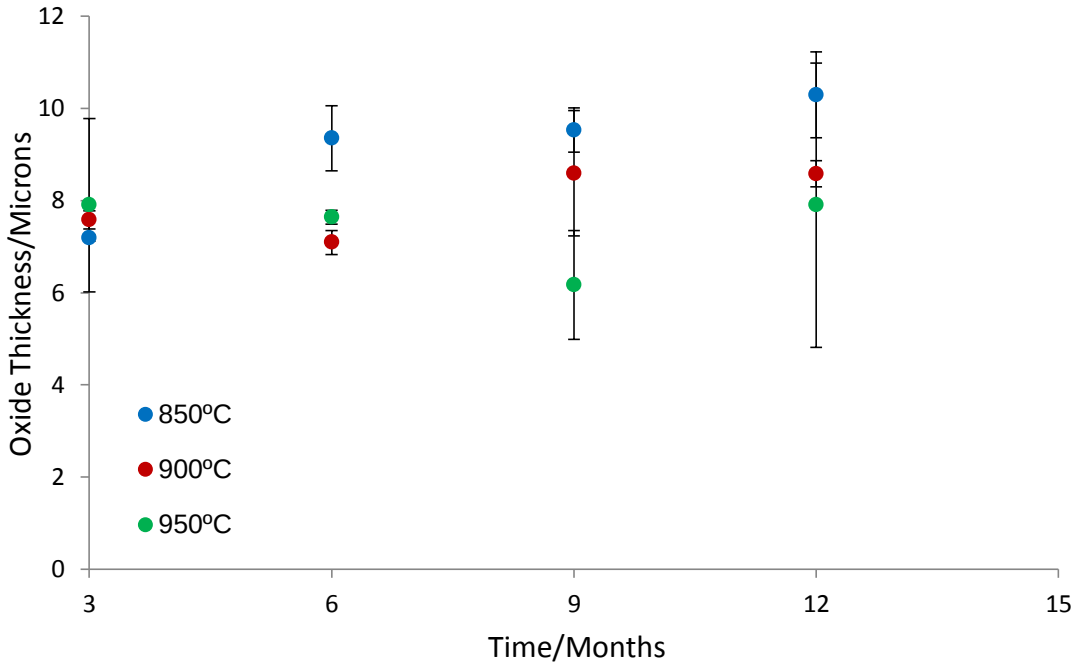

Figure 4.13 Experimental results showing the oxide thickness for isothermally aged samples and the standard deviation. The samples were aged for 3, 6, 9 and 12 months at 850, 900, 950°C. Each sample had only a 50 µm MCrAlY layer applied. The measurements were taken using image analysis software and the mean oxide thickness measurement is shown.

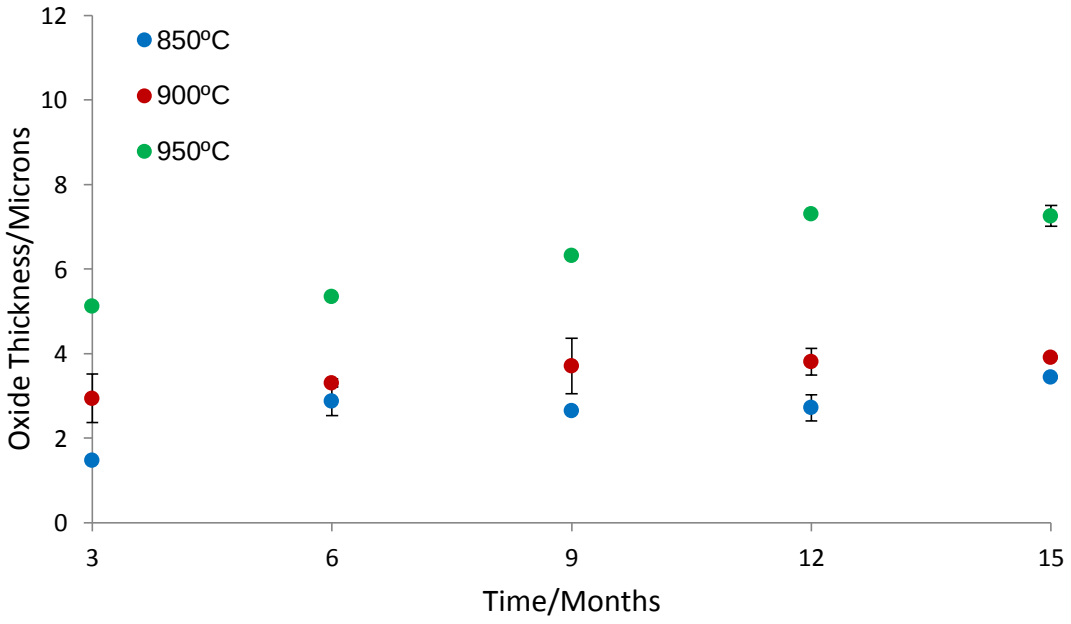

Figure 4.14 Experimental results showing the measured oxide thickness for 15 isothermally aged samples and the standard deviation. The samples were aged under the same conditions and measurements taken as those highlighted in Figure 4.13.The samples shown in this figure had an MCrAlY layer applied and an additional 250 µm YSZ TBC coating applied on top of the MCrAlY layer.

The thickness of the oxide layer forming after isothermal exposure when both an MCrAlY and TBC layer were applied was measured using image analysis software. The results for samples aged from 3-15 months at temperatures 850, 900 and 950^{o}C are plotted in Figure 4.14. It can be seen how there is a relationship between the isothermal ageing conditions and the thickness of the oxide forming. What is apparent from the thickness results is that there is a significant difference between the results in Figure 4.13, when only an MCrAlY layer was applied and Figure 4.14 when an additional TBC layer was applied. The samples with only an MCrAlY layer applied do not appear to have a correlation between oxide thickness and the isothermal ageing conditions. Where there is an additional TBC in place the results in Figure 4.14 show that there does appear to be a correlation in this scenario; when the exposure temperature is increased from 850 – 900^{o}C the oxide thickness does appear to increase. The increase in temperature to 950^{o}C shows a more significant increase in the oxide thickness. There is also a correlation observed between the length of isothermal ageing and the resulting oxide thickness when a TBC layer is applied.

The presence of a TBC layer is seen to suppress the growth of an oxide scale during isothermal exposure. When no TBC layer is applied, the oxide thickness ranges from 6.2 – 10.3 µm. However, when an additional TBC layer is applied, the oxide thickness ranges from 1.4-7.3 µm. Comparable isothermal aged samples in this work with and without a TBC always show a thicker oxide forming when the TBC is not applied, at all time and temperature combinations. The difference in thickness, of two to three times is more apparent at the lower ageing temperatures of 850 and 900^{o}C. The effect of the additional TBC layer could be influenced by the oxygen permeability of the zirconia layer, which is a result of the porosity of the coating. Using a water permeability test it was found that the TBC layer appeared to be of open porosity. However, the addition of this layer was shown to have a direct effect on the thickness of the oxide forming.

4.3.2 EDS Chemical Analysis of the Oxide Scale

After initially measuring the thickness of the oxide layer that had formed after thermal exposure and observing that the additional TBC layer was influencing the thickness of TGO forming, the chemistry of the oxide product was characterised. The chemistry of the oxide layer was characterised using EDS analysis.

EDS results within Figures 4.15a and b show how a sample that had only a 50 µm MCrAlY layer applied and was aged for 3 months at 850^{o}C had a TGO forming that is rich in Al throughout. When an isothermal sample was aged at 900^{o}C it can be seen in Figures 4.15c, d, e and f that there was also an oxide forming that was predominantly Al rich, however, there are also clusters of Cr and Co rich areas within the oxide. For a sample aged at 950^{o}C for 3 months as shown in Figure 4.16a-f it can be seen that there is an inner oxide layer that appears to be rich in Al. Alongside this inner oxide layer there appears to be a second oxide layer that at 950^{o}C is Co, Cr and Ni rich. This can be seen in Figures 4.16d, e and f. It does appear that the outer layer rich in Co, Cr and Ni is of a consistent thickness. This is in contrast to the oxide observed after 3 months at 900^{o}C shown in Figure 4.15e and f showing clusters of Cr and Co rich oxide. It does also appear that the Al rich oxide layer is thinnest on the sample aged at 950^{o}C compared to samples aged at 850 and 900^{o}C.

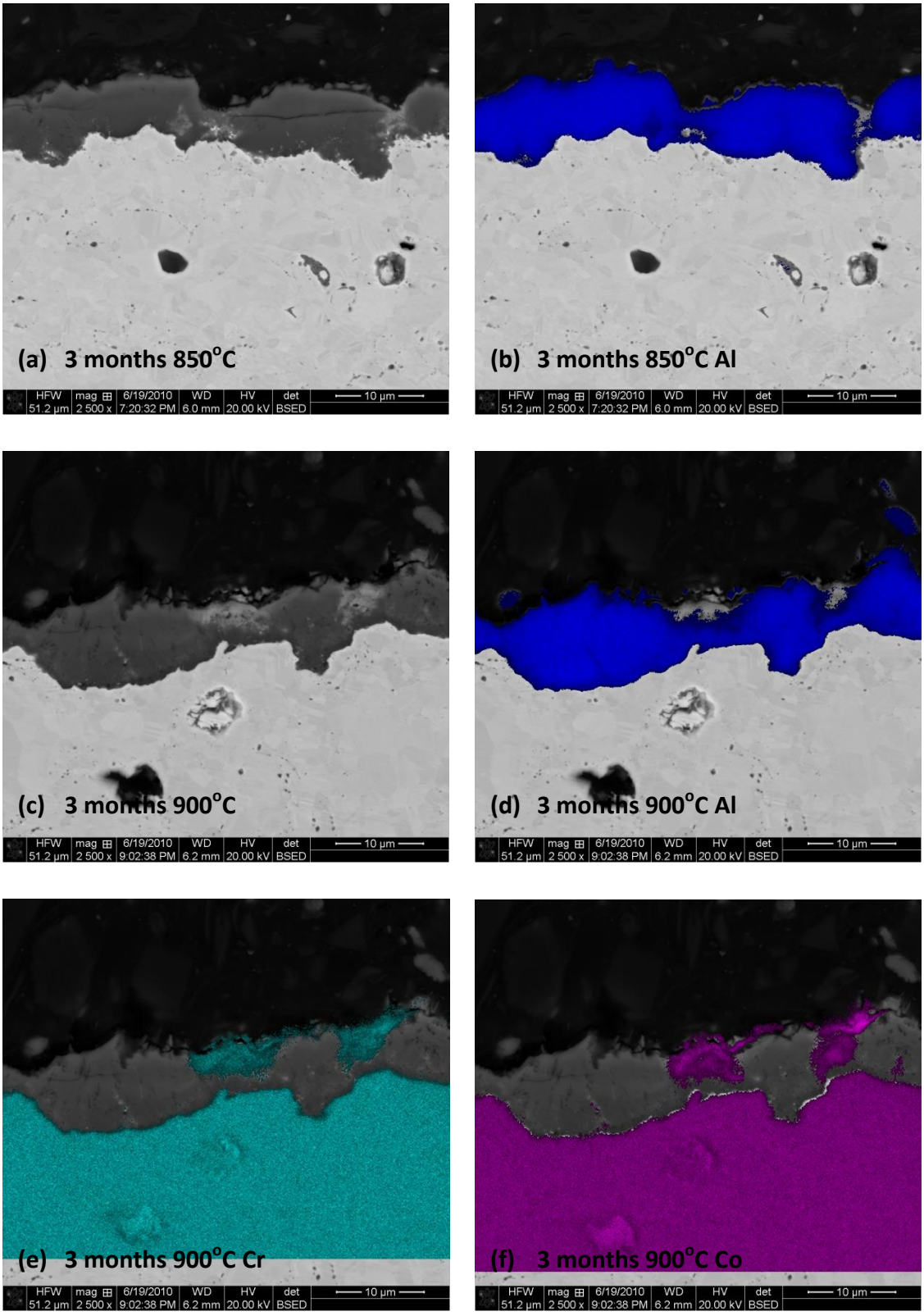

Figure 4.15 Experimental results showing EDS analysis of two samples, one sample was aged for 3 months at 850°C, in a and b. A second sample in c, d, e and f was aged for 3 months at 900°C.

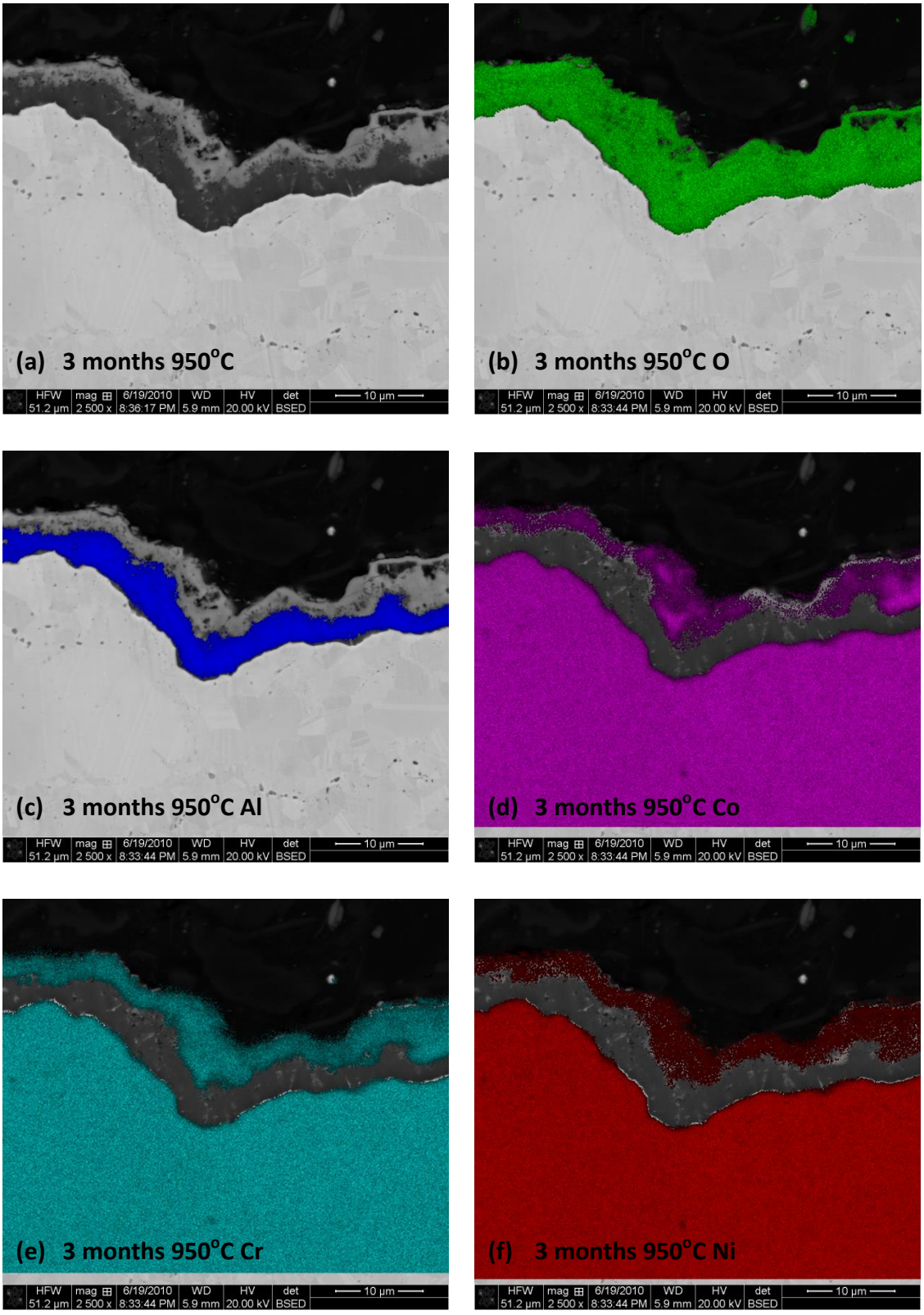

Figure 4.16 Experimental results showing EDS analysis of a sample with only a 50 µm MCrAlY coating applied that was aged for 3 months at 950°C.

Samples aged for 6 months were also characterised; the results for samples aged at 850 and 950^{o}C are shown in Figure 4.17. It can be seen within Figure 4.17b how the oxide forming after exposure at 850^{o}C appears to be rich in Al across the full oxide region. A sample aged for 6 months at 950^{o}C, presented in Figure 4.17c, d, e and f shows how there is an Al oxide layer present and an additional outer oxide layer rich in Co and Cr.

The sample aged for 9 months at 850^{o}C formed an oxide layer that consisted only of an Al rich region, as can be seen in Figure 4.18. When a comparable sample was characterised that was aged for the same time period, 9 months, but at 900^{o}C, shown in Figure 4.19, localised oxide regions rich in Cr, Co and Ni are present. These localised oxide regions can be seen in Figures 4.19d, e and f. When characterising a sample aged for 9 months at 950^{o}C, as shown in Figure 4.20, it was found that the oxide layer that formed consisted of an Al rich layer and a very thin layer rich in Cr, Co and Ni. This contrasts with a sample aged for 3 months at 950^{o}C where a substantial layer rich in Cr, Co and Ni was present.

Samples aged for 12 months were characterised using EDS analysis to study the chemistry of the oxide layer; the results are shown in Figure 4.21 and 4.22. Figure 21 shows how after exposure at 850^{o}C the oxide layer that forms appears to be only rich in Al. The sample aged at 950^{o}C for 12 months is shown in Figure 4.22; it can be seen how there also an Al layer forming, but as seen previously in samples aged at 950^{o}C there is a thin outer oxide layer rich in Cr, Co and Ni. This is similar to samples aged for 3, 6 and 9 months at 950^{o}C. In Table 4.4 a summary of the EDS analysis is shown for samples which have only a 50 µm MCrAlY layer applied.

Table 4.4 Summarising the characteristics of oxide scales present after isothermal ageing of "MCrAlY" samples which have only a 50 µm CoNiCrAlY layer applied by HVOF, after ageing between 3-12 months at 850-950^{o}C

	Temperature/^{o}C		
Time months	**850^{o}C**	**900^{o}C**	**950^{o}C**
3	alumina layer	alumina layer with localised Cr, Co rich cluster regions	thin inner alumina layer and Ni, Cr, Co rich outer layer
6	alumina layer	alumina layer with localised Cr, Co rich cluster regions	inner alumina layer with thin outer layer rich in Co and Cr
9	alumina layer	alumina layer with localised Ni, Cr and Co regions	alumina layer and thin outer layer rich in Ni, Cr and Co
12	alumina layer	alumina layer with localised Ni and some Cr, Co regions	alumina layer with thin outer layer rich in Ni, Cr and Co

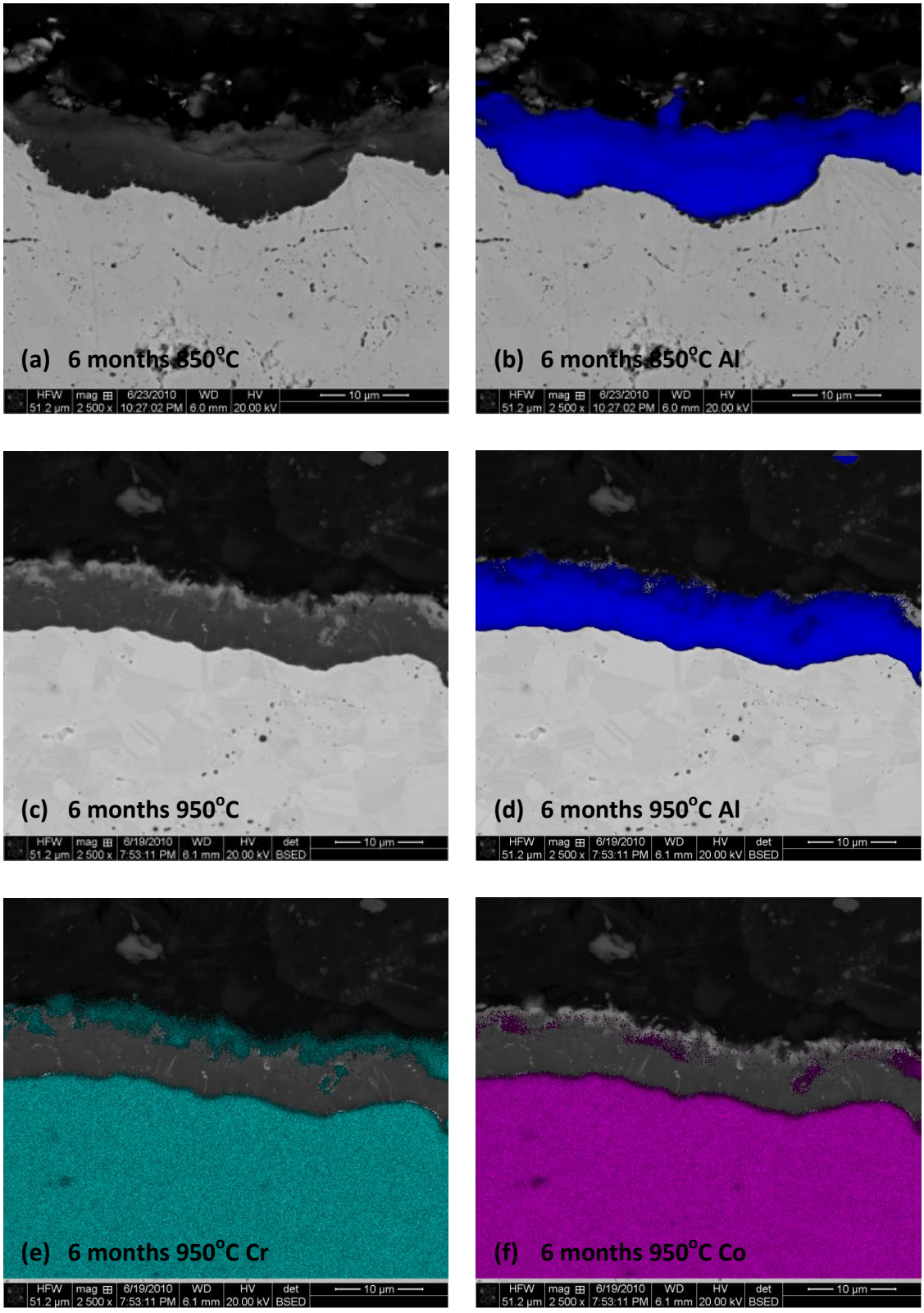

Figure 4.17 Experimental results showing EDS analysis of two samples with only a 50 µm MCrAlY coating applied. One sample was aged for 6 months at 850°C, shown in a and b and a second aged for 6 months at 950°C, shown in c, d, e and f.

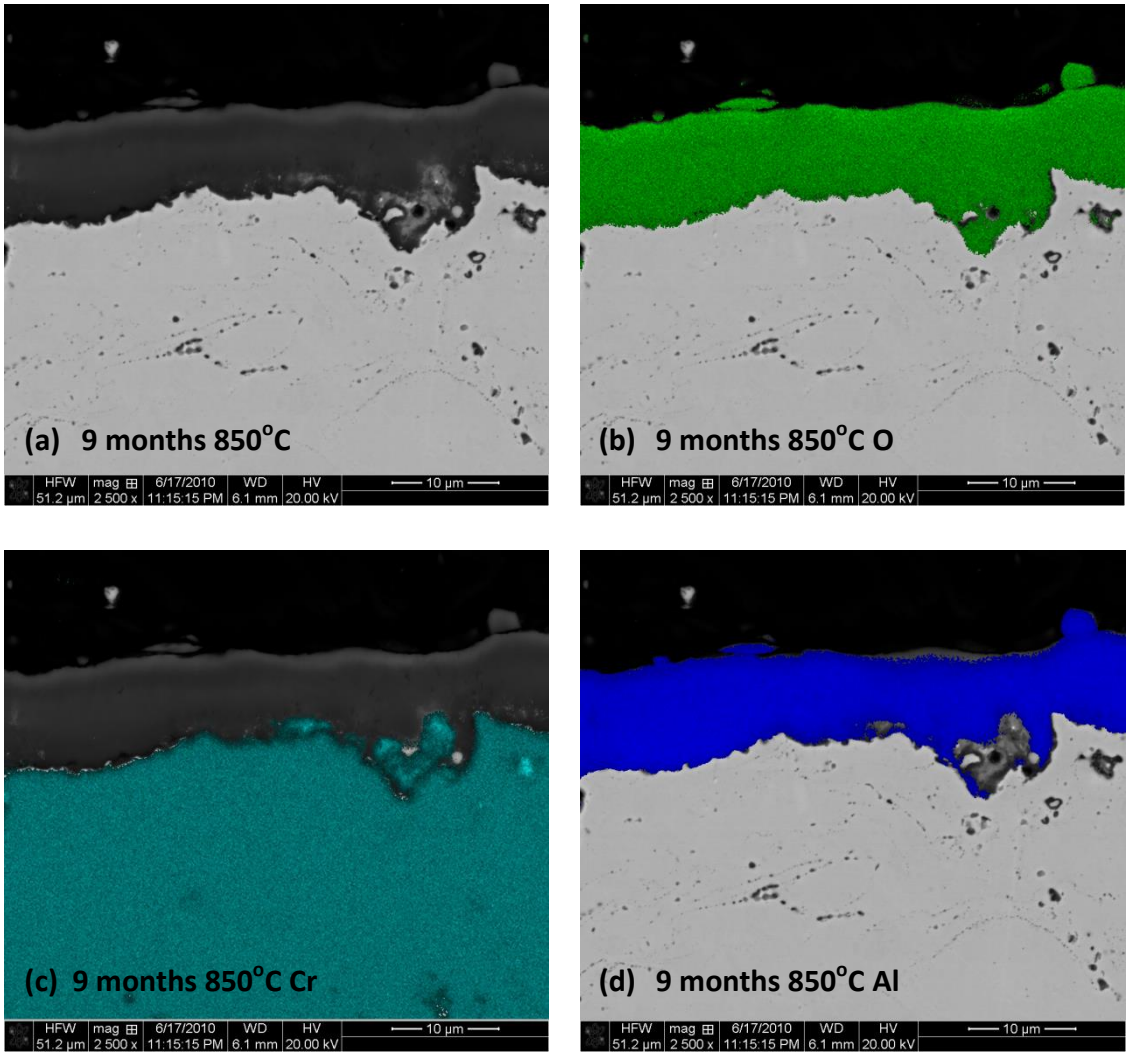

Figure 4.18 Experimental results showing EDS analysis of a sample with only a 50 µm MCrAlY coating applied that was aged for 9 months at 850°C.

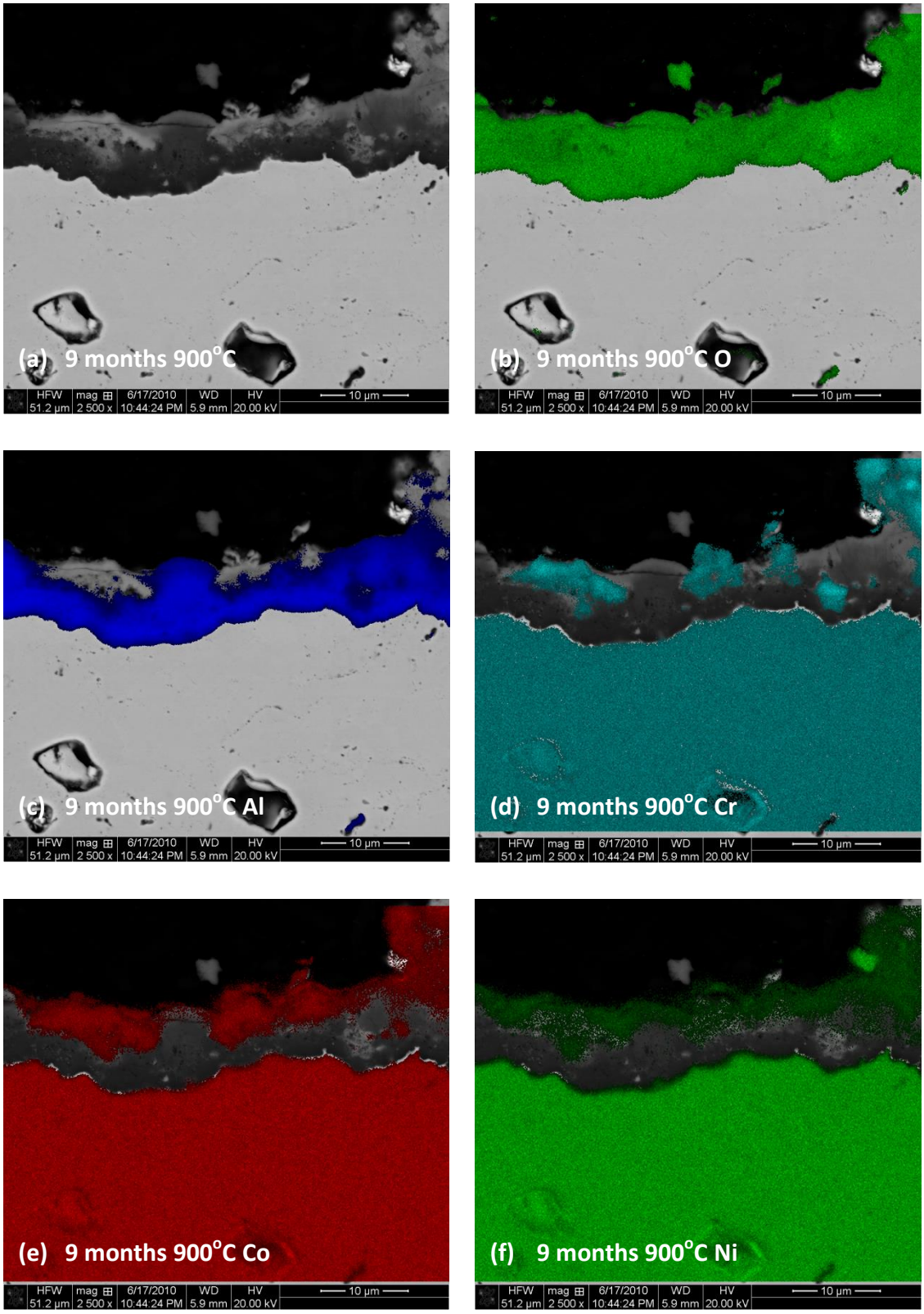

Figure 4.19 Experimental results showing EDS analysis of a sample with only a 50 µm MCrAlY coating applied that was aged for 9 months at 900°C.

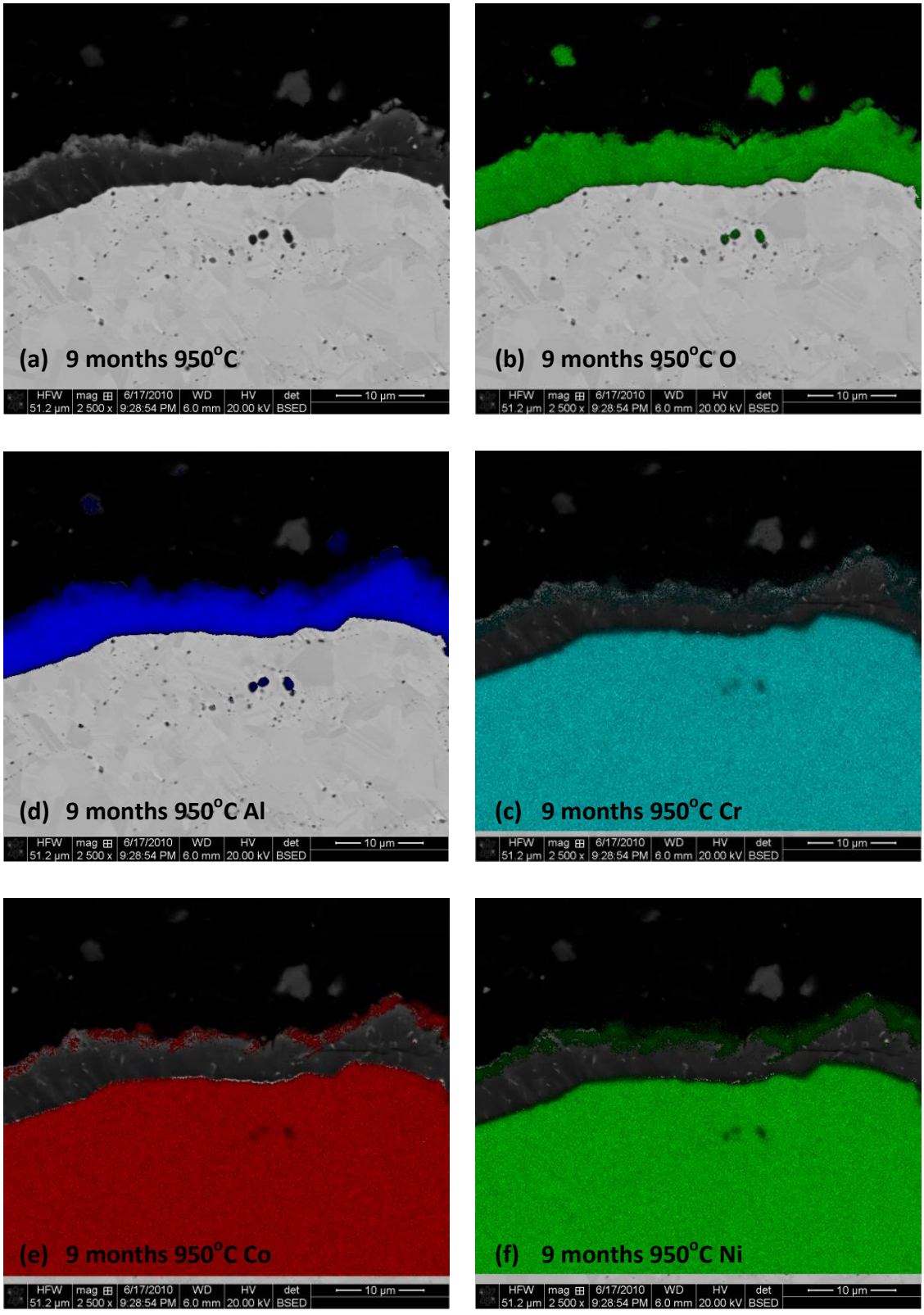

Figure 4.20 Experimental results showing EDS analysis of a sample with only a 50 µm MCrAlY coating applied that was aged for 9 months at 950°C.

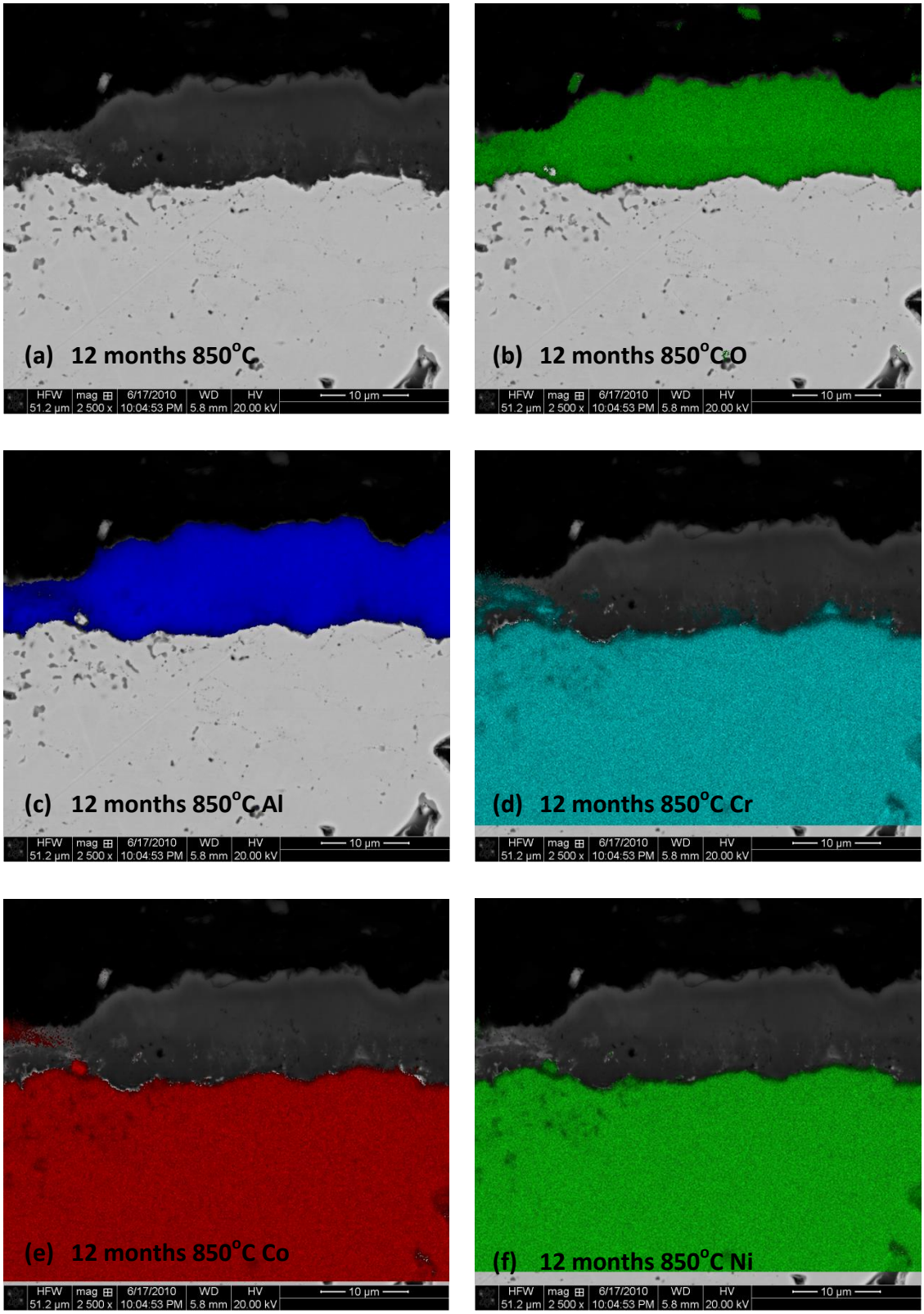

Figure 4.21 Experimental results showing EDS analysis of a sample with only a 50 µm MCrAlY coating applied that was aged for 12 months at 850°C.

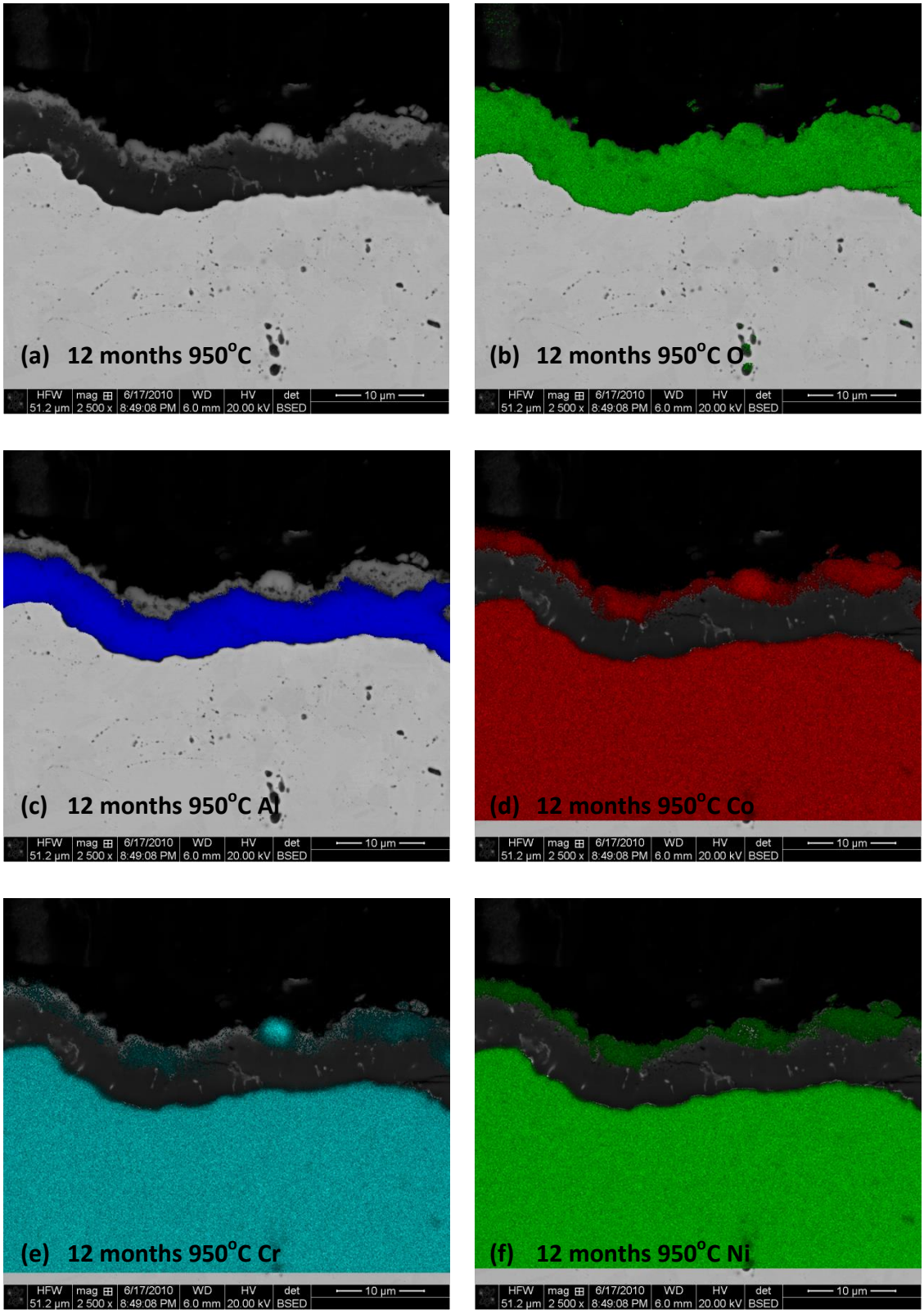

Figure 4.22 Experimental results showing EDS analysis of a sample with only a 50 µm MCrAlY coating applied that was aged for 12 months at 950°C.

In addition to studying samples with only an MCrAlY layer applied, comparable samples with a 50 µm MCrAlY coating and also a 250µm TBC were also characterised. Figure 4.23 shows a sample aged for 3 months at 950^{o}C. The comparable sample with only an MCrAlY layer applied in Figure 4.16 had an inner oxide layer that was Al rich and also an outer oxide region rich in Cr, Co and Ni. It can be seen in Figure 4.23 that the addition of a TBC has an effect on the chemistry of the oxide layer forming after isothermal ageing. With a TBC layer present the oxide forming is rich in Al throughout the whole of the oxide layer; Figures 4.23b and c show this from the EDS results. There does not appear to be any regions of the oxide rich in Cr, Co or Ni as shown in Figures 4.23d, e and f.

In Figure 4.24 EDS results are shown for a sample that was aged for 15 months at 950^{o}C with the TBC layer present. It can be seen how the oxide layer that formed after isothermal exposure is only rich in Al. The EDS maps in Figures 4.24d, e and f show how the oxide layer does not appear to be rich in Cr, Co or Ni. e and f.

Comparing the EDS analysis of the oxide with the isothermal conditions does reveal some trends. When an additional 250 µm TBC layer is applied on top of the 50 µm MCrAlY layer the oxide that forms on all samples aged for 3-15 months at 850-950^{o}C appears to be only rich in Al. When comparing the chemistry with the measurement of the oxide thickness it was found that the samples with a TBC present had thinner oxides forming compared to samples with only an MCrAlY layer applied. When only an MCrAlY layer was applied it was found that at the lower isothermal ageing temperature of 850^{o}C, only an Al rich oxide layer was present, this occurred at all the ageing time periods from 3-12 months at 850^{o}C. At 900^{o}C and 950^{o}C localised oxide clusters rich in Cr, Co and Ni were present, when only an MCrAlY layer was applied.

As variations in the oxides forming were discovered, mainly concerning the presence of oxide layers rich in Cr, Co and Ni, the thickness of the region only rich in Al was measured. This was due to the fact that the current oxidation model, introduced in Chapter 3, predicts the thickness of an alumina layer only. Figure 4.25 shows how the Al rich oxide changes with temperature. The significant difference compared to the total oxide thickness was found to be for samples aged at 950^{o}C. At 950^{o}C a Cr, Ni and Co rich layer formed, the Al rich oxide layer was measured to be thickest at 850^{o}C, and to decrease in thickness as exposure temperature increased for the majority of sample ageing times.

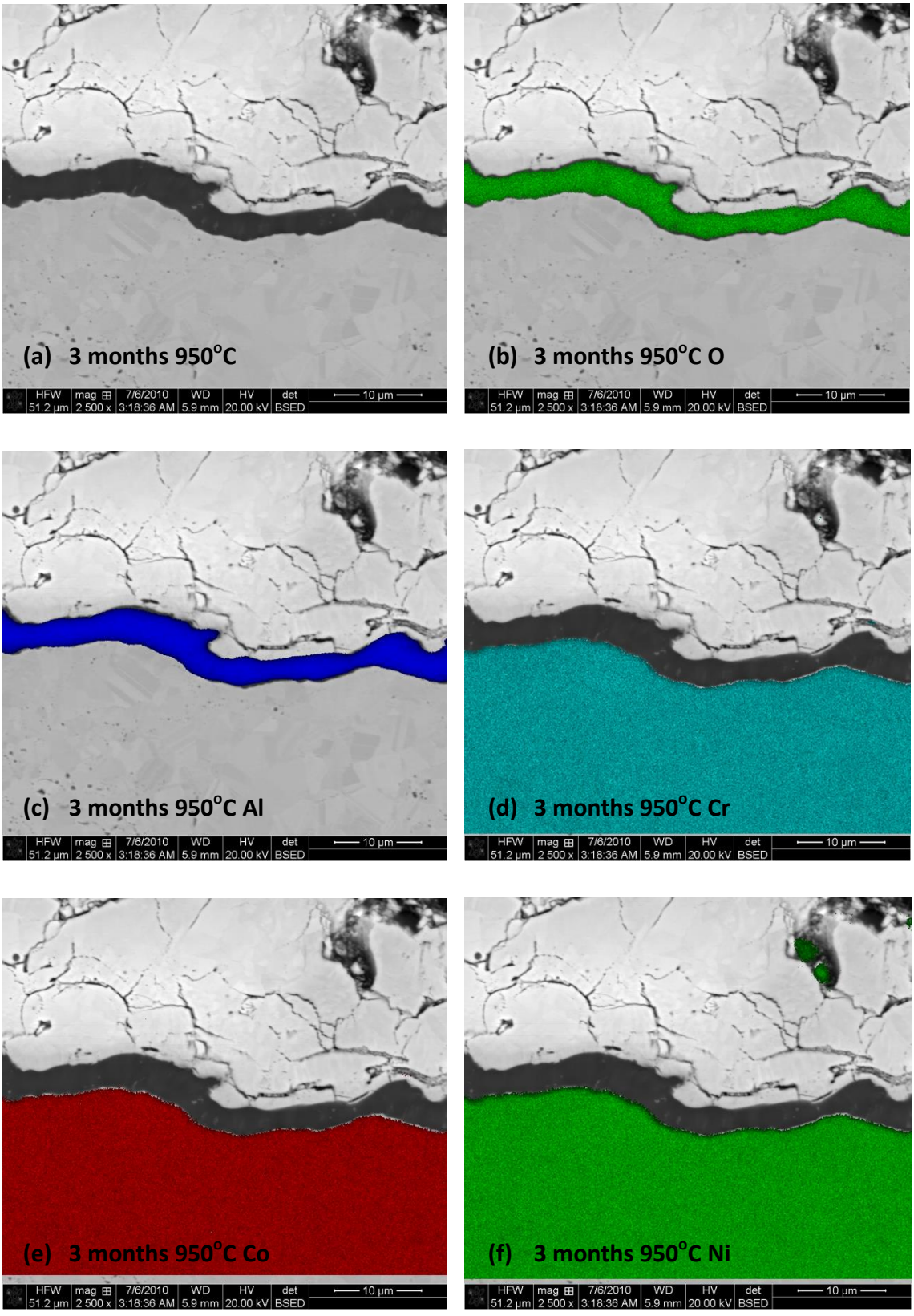

Figure 4.23 EDS map results showing how the oxide layer that has formed on a sample aged for 3 months at 950°C with both an MCrAlY bond coat and TBC layer applied.

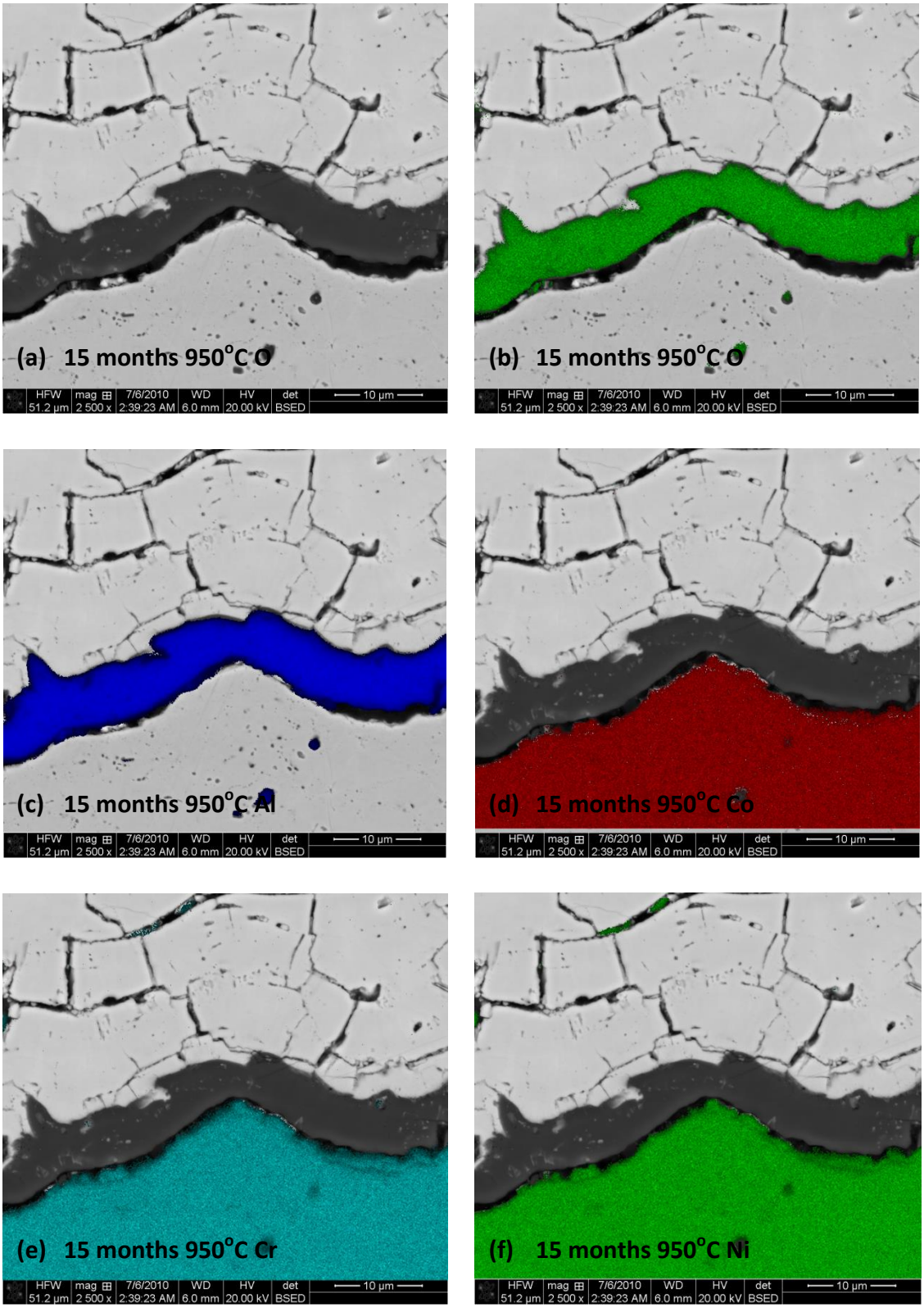

Figure 4.24 EDS map results showing how the oxide layer that has formed on a sample aged for 15 months at 950°C with both an MCrAlY bond coat and TBC layer applied.

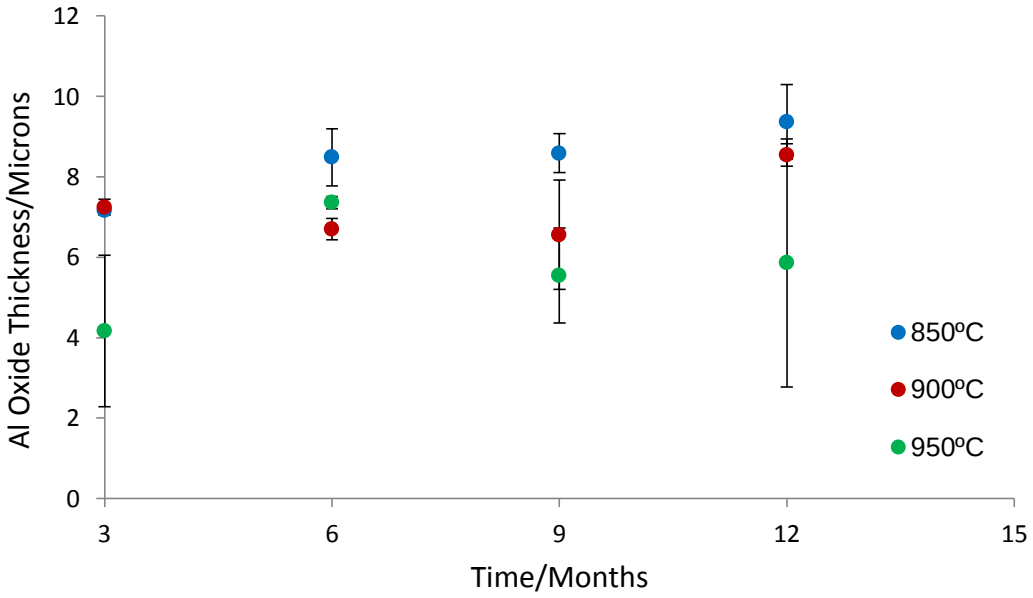

Figure 4.25 Experimental results showing the oxide thickness for isothermally aged samples and the standard deviation, for only the Al rich portion of the oxide. Samples were aged for 3, 6 and 9 months at 850, 900, 950^{o}C. Each sample had just the 50 µm MCrAlY layer applied.

4.3.3 Image Reconstruction of an Oxide Scale in 3D

After studying the oxide scale forming after isothermal ageing using a series of two-dimensional micrographs, further techniques were sought to be able to characterise the surface of the oxide scale. The EDS maps presented within section 4.3.2 have shown that there appears to be an outer oxide layer forming during isothermal exposure at 900 and 950^{o}C on samples with only an MCrAlY layer present. After ageing for 3 months at 950^{o}C an outer layer was present rich in Cr, Co and Ni. As the exposure time increased the thickness of the outer oxide layer reduced. After ageing at 850^{o}C there was no consistent outer layer present, and after exposure at 900^{o}C localised clusters of oxide rich in Cr, Ni and Co were present. By studying the surface of the oxide that has formed after isothermal ageing and using EDS analysis the surface chemistry of the oxide was characterised. Figure 4.26 shows the oxide surface of a sample aged for 15 months at 850^{o}C. It can be seen how there appears to be distinct chemical differences across the surface of the oxide layer; this is evident from the brightness gradient within a backscatter micrograph. EDS was used to analyse the surface and the results are presented in Figure 4.27. It can be seen how there appears to be a predominantly Al rich region with localised Cr, Co and Ni rich regions. The bright regions within Figure 4.26 were found to be rich in Cr and Co.

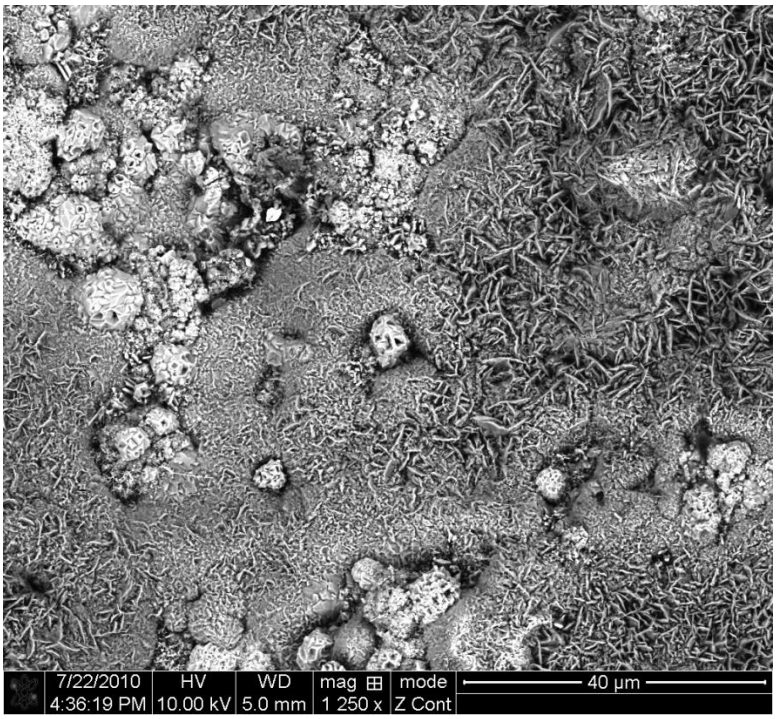

Figure 4.26 A backscatter micrograph showing the surface of the oxide scale that formed after isothermal ageing for 15 months at 850^{o}C when only an MCrAlY layer is applied.

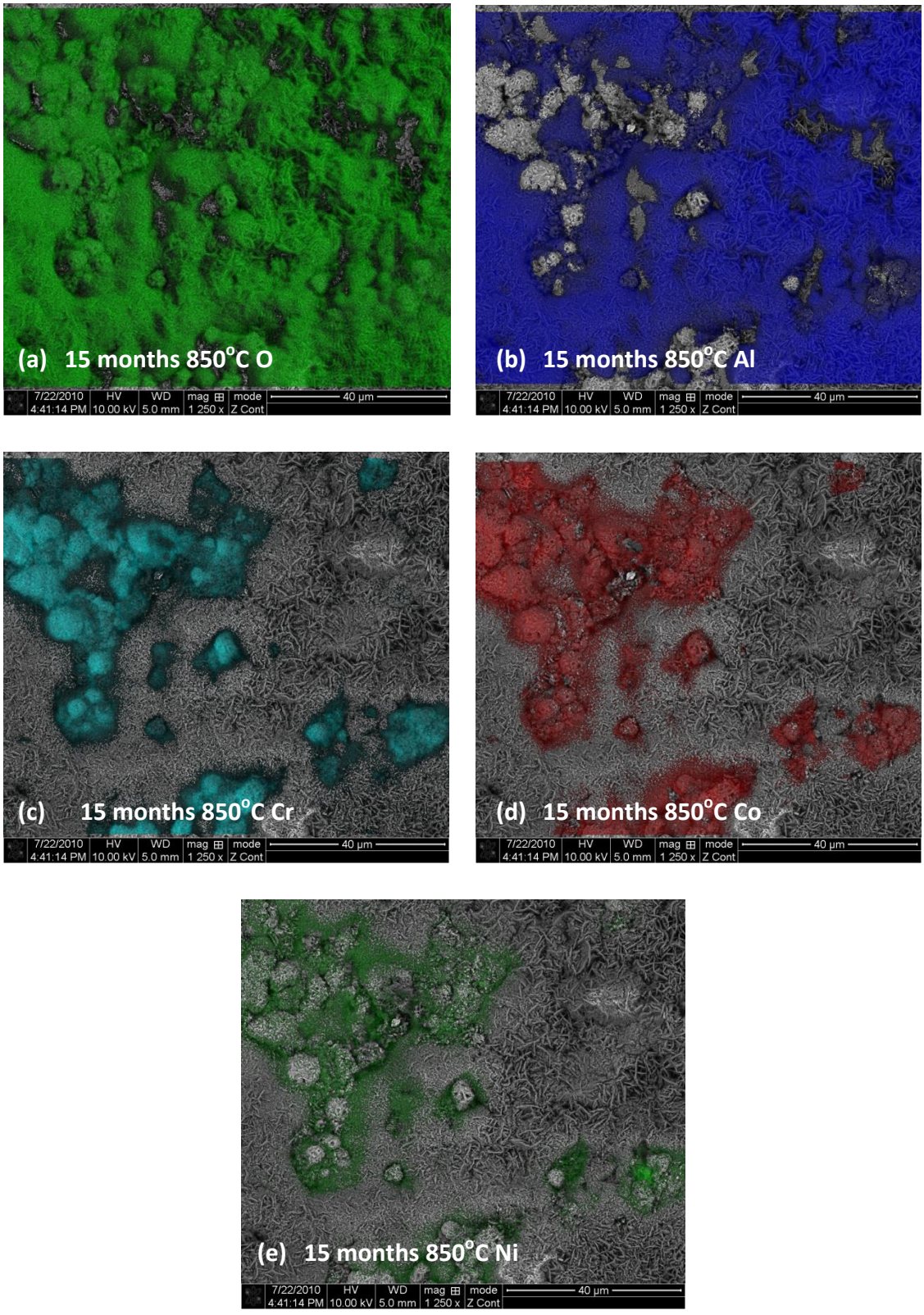

Figure 4.27 A series of EDS maps overlaid onto backscatter images showing the chemistry of an oxide scale formed during isothermal ageing for 15 months at 850°C.

After studying the chemistry of the surface of the oxide layer, the surface roughness was also investigated. Using dedicated software a series of images were collected at pre-defined tilt angles and were then processed to reconstruct a single image showing the surface roughness of the oxide scale. It can be seen within Figure 4.28 how the oxide scale roughness is defined by the oxides present. The Al rich region seen within Figure 4.27 is present with a whisker type morphology, where as the protruding clusters are rich in Cr and Co. Previously all quantification of the oxide was carried out using a series of 2D slice images, whereby one specific region of the oxide was characterised. The study of a greater region of the oxide surface shows that the oxides present vary across the sample surface. It was found that the 2D analysis does correlate with the 3D reconstructions. At 850^{o}C the oxide forming consists of a majority Al rich region, at 900^{o}C, localised regions of Cr, Co and Ni oxide are present. Previously it was observed that after long term ageing at 950^{o}C the oxide forming was found to have only an Al rich oxide layer present after 12 months exposure. It was found when studying the surface of the oxide scale that after ageing at 950^{o}C no Cr, Co or Ni oxide regions were present at 15 months exposure.

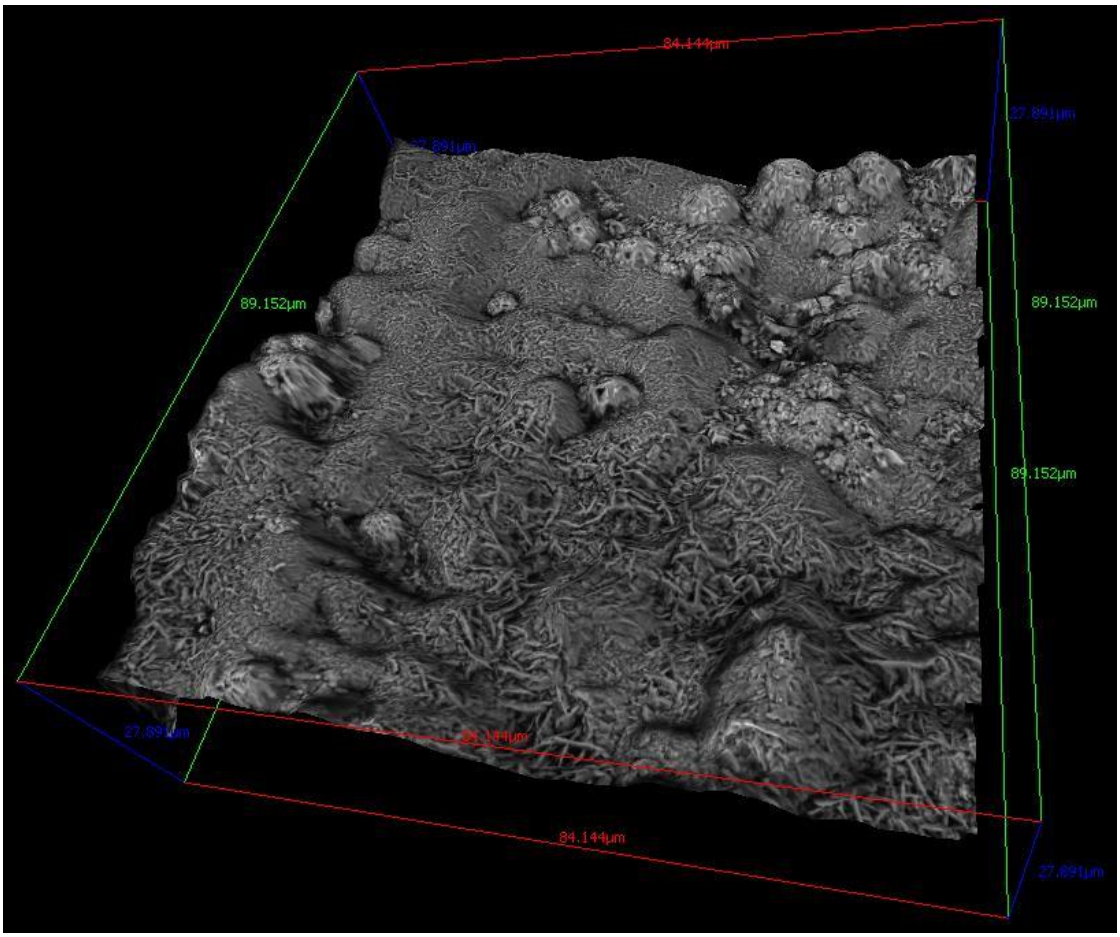

Figure 4.28 A 3D construction of the oxide morphology of a sample aged for 15 months at 850^{o}C. The reconstruction was carried out using Alicona digital imaging software.

4.3.4 Short Term Oxidation Study

In order to understand what the drivers are for the formation of the Al rich layer and the localised regions of mixed oxide, short term ageing of samples, both with and without a TBC, was carried out. Four samples were aged for 6 hours, as highlighted in Table 4.5.

Table 4.5 The type of coating and temperature parameters for four samples aged isothermally for 6 hours at two temperatures.

	Temperature °C	
Coating	**900**	**950**
MCrAlY	✓	✓
MCrAlY + TBC	✓	✓

The oxide thickness and oxide chemistry were characterised for each sample using backscatter imaging and analysis software, and also EDS chemical analysis. A backscatter micrograph in Figure 4.29a, shows the oxide layer forming after 6 hours when only an MCrAlY layer is applied. EDS mapping results shown in Figure 4.29b, c, d, e and f confirm that the oxide formed is only rich in Al. When an additional TBC layer was applied, shown in Figure 4.30, the oxide that formed was also only rich in Al, this can be seen in Figures 4.30b, c, d, e and f. The oxide was measured to be of 1 µm average thickness when a TBC layer was applied and without the additional TBC layer, the oxide was measured to be 3 µm. In both cases the oxide was not found to be rich in Co, Cr and Ni. This does also show that the first oxide to form is the Al rich layer. Comparable samples aged at 900°C were also characterised, and a similar relationship to the samples aged at 950°C was observed; the initial oxide was only rich in Al. A difference was observed in the thickness of the oxide forming at 900°C. The sample with only an MCrAlY layer applied had an oxide thickness of 0.8 µm, and the sample with a TBC applied 0.5 µm. The difference in TGO at 900°C and 950°C correlates with the longer term isothermally aged sample TGO thickness measurements shown in Figures in 4.13 and 4.14.

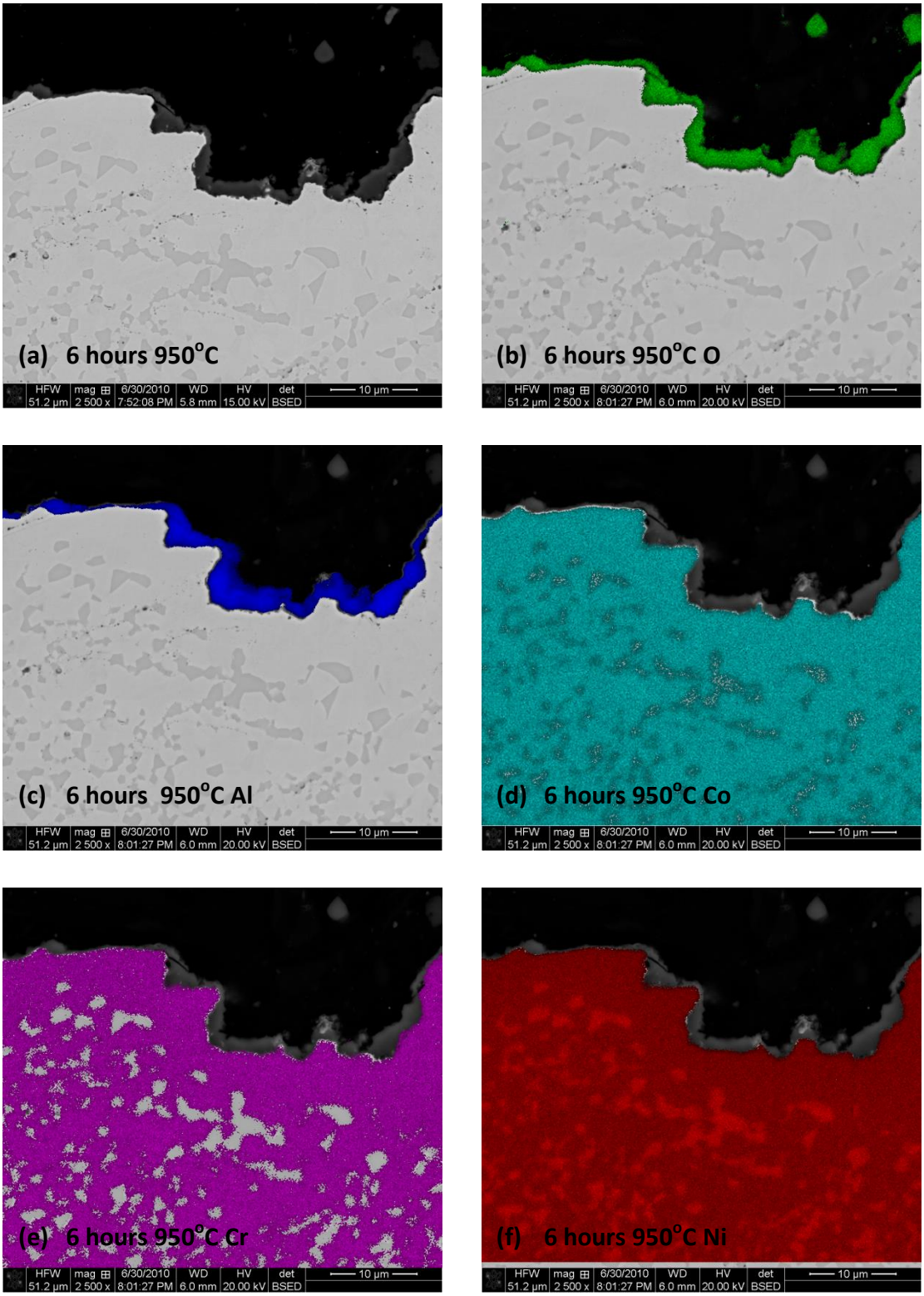

Figure 4.29 A backscatter image and EDS map results showing the oxide layer that forms after 6 hours ageing. The sample was aged for 6 hours at 950°C and had only an MCrAlY coating applied.

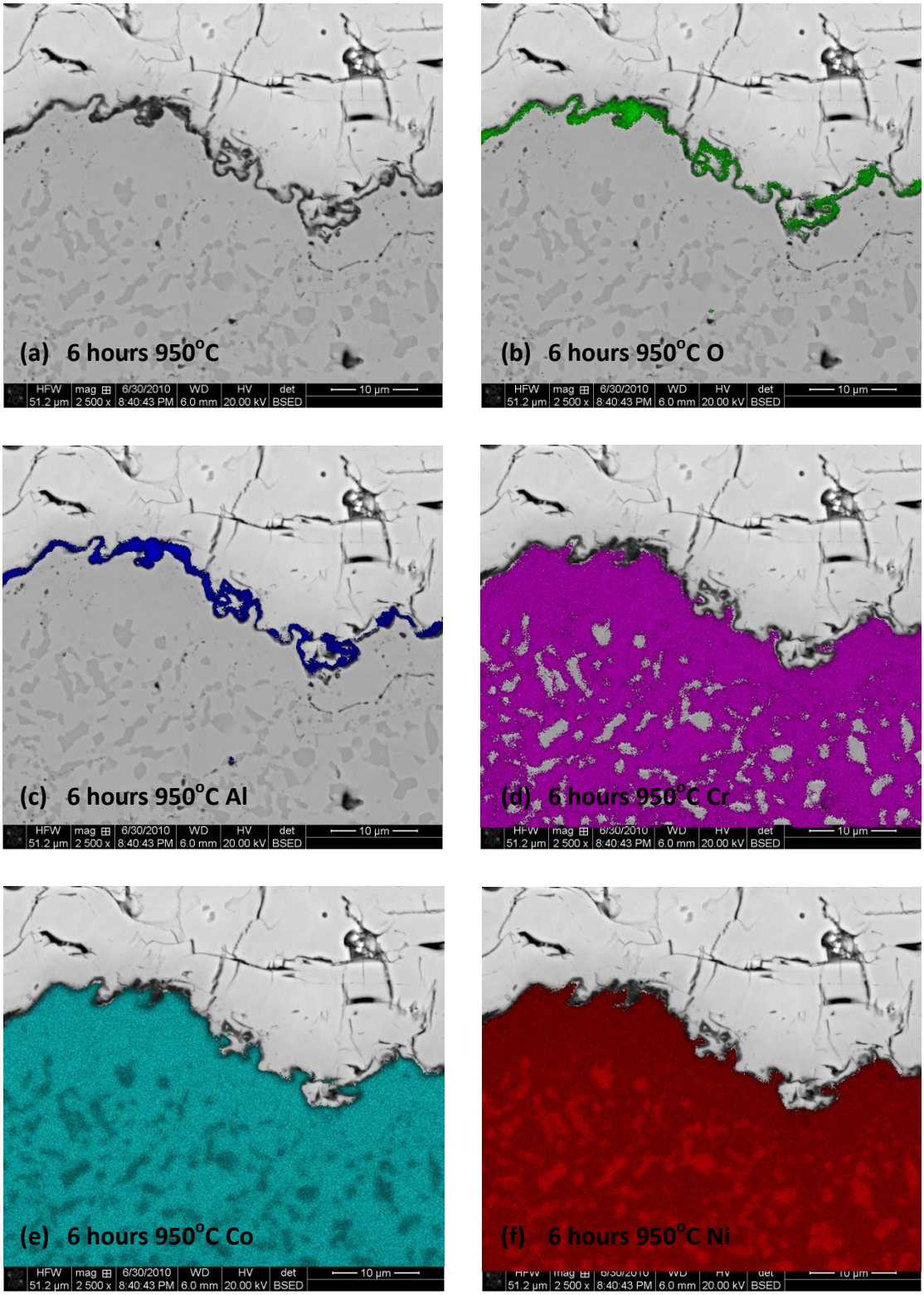

Figure 4.30 A backscatter image and EDS mapping results showing how the oxide layer that forms after 6 hours is a consistent layer of Al rich oxide. The sample was aged for 6 hours at 950°C and had an MCrAlY coating and a 250 µm TBC layer applied.

4.4 Modelling of the Oxide Scale

After characterising the oxides forming on the samples, a comparison was then made with a model prediction, discussed previously in Chapter 3. The oxidation model by Nesbitt (39) was used to compare the measured oxide thickness data with the predicted oxide thickness, δ in µm given by Equation 4.1. where t is the time in seconds, T is the exposure temperature in K, T_o, Q and n are constants with values $T_0 = 2423.7$, $Q = 27777.4$ and $n = 0.332$.

The predicted oxide thickness results after ageing for 3 and 12 months are shown in Figure 4.31. It can be seen how the thickness of the oxide is predicted to increase as the exposure temperature increases. For samples exposed for 3 months at 850°C, the oxide is predicted to be 2.3 µm, at 900°C it is predicted to be 3.3 µm and at 950°C the thickness is predicted to be 4.6 µm. After 12 months exposure the thickness is predicted to be 3.7µm at 850°C, 5.3 µm at 900°C and 7.3 µm at 950°C. The oxidation model used was developed for a coating system that consists of an MCrAlY layer and an additional TBC coating (39).

$$\delta = \left[\exp\left\{ Q\left(\frac{1}{T_0} - \frac{1}{T} \right) \right\} t \right]^n$$

Equation 4.1

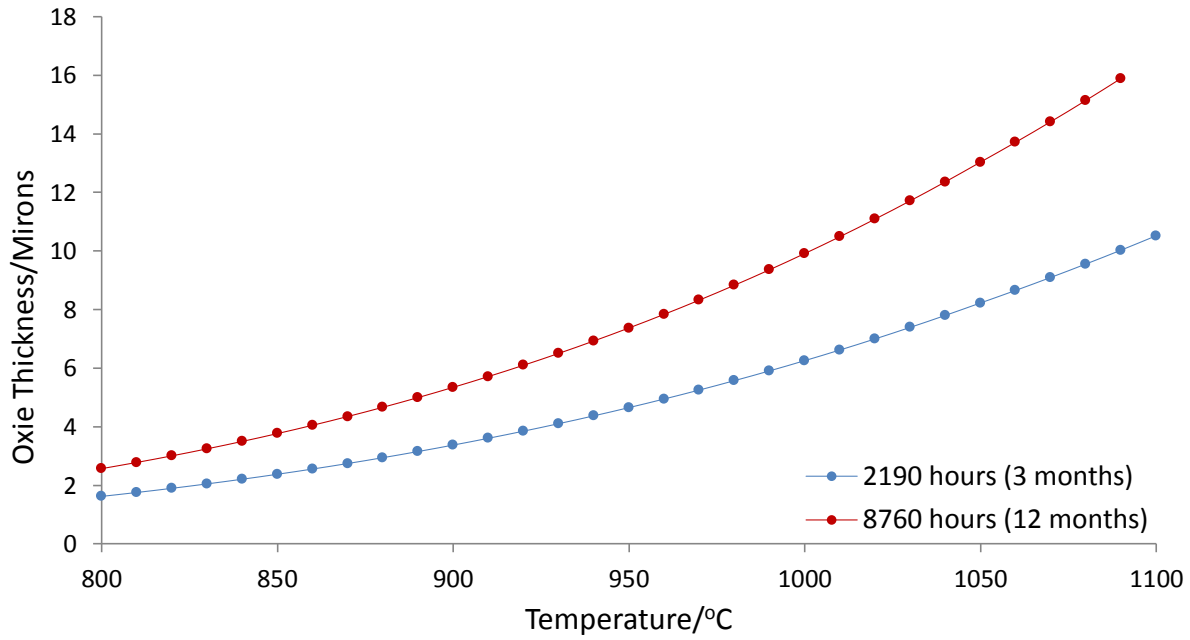

Figure 4.31 Modelling results showing the predicted Al_2O_3 oxide thickness for a sample aged for 2190 hours, 3 months and 8760 hours, 12 months. The graph illustrates how the predicted oxide thickness will increase as the temperature the samples are exposed at increases.

4.5 A Comparison between Modelling of Oxide Thickness and Experimental Results

The prediction of oxide thickness can be compared to the measured oxide thickness for samples with and without the application of a TBC layer. Figure 4.32 shows a graphical representation of the predicted thickness and the comparable sample measured thickness, at 850°C. It can be seen how the samples without an additional TBC layer appear not to be consistent with the oxidation model predictions. The measured oxide thickness displayed is for the thickness of an Al oxide layer only. The samples that had a TBC layer applied do show a correlation with the predicted oxide thickness, as seen in Figure 4.33 and 4.34. At 850°C the maximum discrepency for the measured oxide when a TBC is applied was 0.9 µm. Figure 4.34 shows the correlation at 900°C. It can be seen how when a TBC layer is applied the oxidation model used is able to predict the thickness of the oxide scale forming.

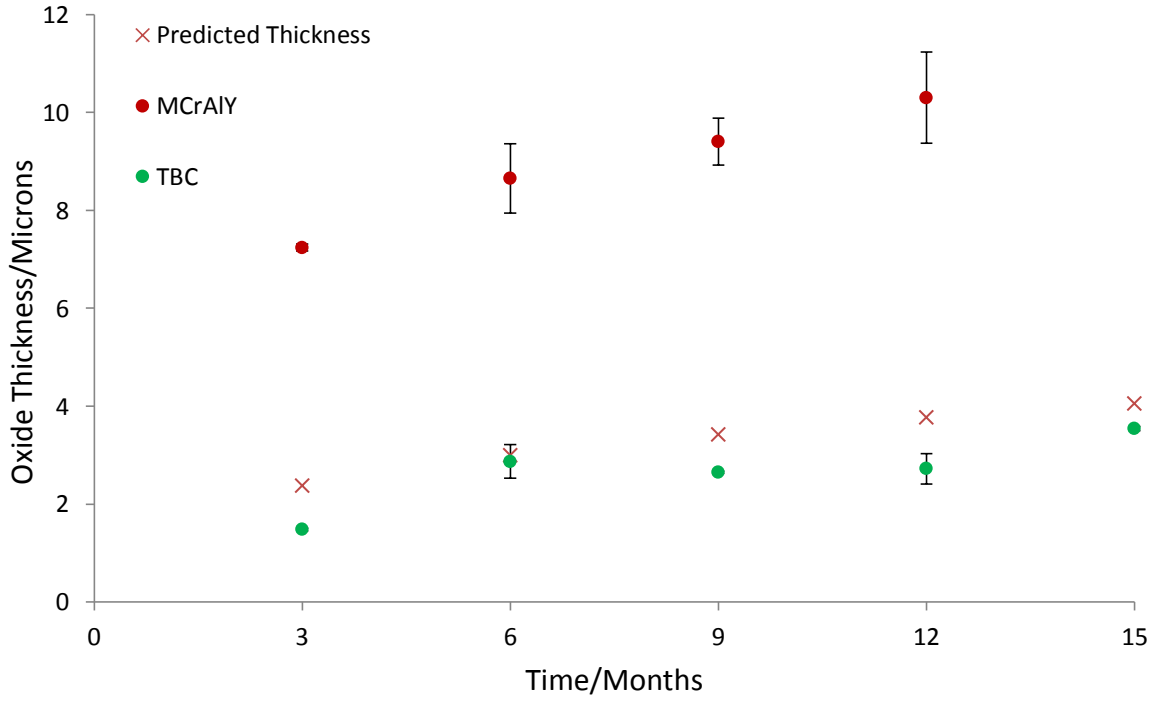

Figure 4.32 The predicted oxide thickness results from Equation 4.1 and measured oxide thickness results and the standard deviation from samples aged for 3, 6, 9, 12 and 15 at 850°C both with and without a TBC on top of the MCrAlY layer.

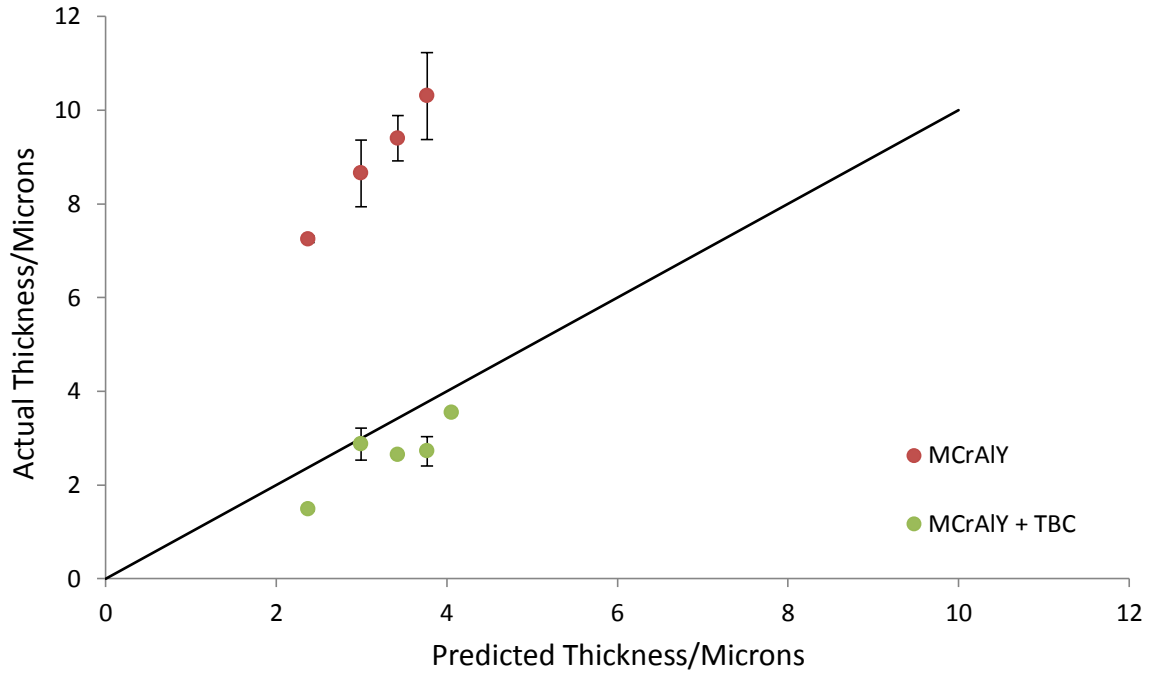

Figure 4.33 The predicted oxide thickness from the oxidation model in Equation 4.1 against the experimental results and the standard deviation measured for samples aged for 3-15 months at 850°C.

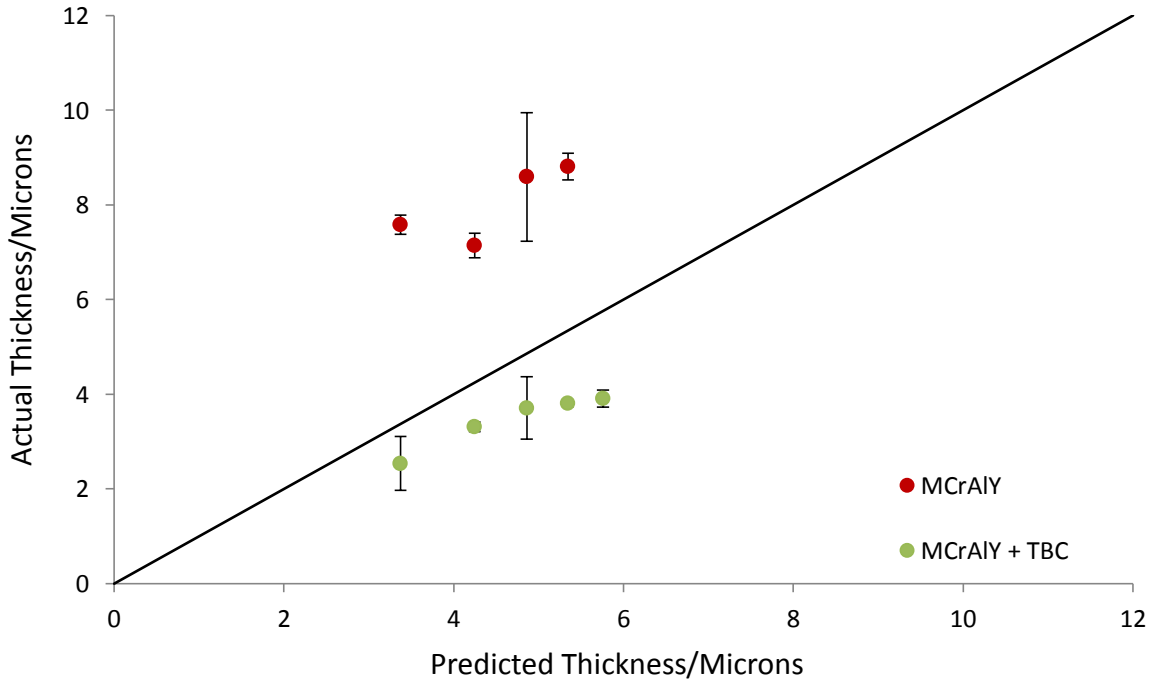

Figure 4.34 The predicted oxide thickness from the oxidation model against the experimental results and the standard deviation for samples aged at 900°C for 3-15 months.

4.6 Conclusions

Within Chapter 4 isothermally aged samples that had only a 50 µm MCrAlY coating and comparable samples with an additional 250 µm TBC layer were characterised. The thickness of the oxide forming after isothermal exposure when only an MCrAlY layer was applied did not correlate with a change in isothermal conditions. However, when an additional TBC layer was applied oxide thickness was found to be dependent on the ageing temperature; the oxide thickness increased as the exposure temperatture increased. The beta phase was identified within the microstructure after post coating heat treatments and before isothermal ageing. However, after isothermal ageing at 900 and 950^{o}C the beta phase was not observed within any of the samples, with either an MCrAlY layer or with both an MCrAlY and TBC layer.

EDS map analysis was carried out and was used to study the chemistry of the oxide forming. It was observed for samples with only an MCrAlY layer applied that at 850^{o}C the oxide present after isothermal exposure was rich in Al, and after exposure at 900^{o}C clusters of Cr, Co and Ni oxide were present. When isothermal samples with a MCrAlY layer were aged at 950^{o}C an outer layer of oxide was observed, this layer was found to be rich in Cr with small amount of Ni and Co present. It was also observed that the thickness of the Cr rich layer decreased as ageing time increased. The surface of the oxide scale was characterised for samples aged isothermally for 15 months. It was observed how the oxides forming at 850 and 900^{o}C consisted of an Al rich layer with localised regions of Cr rich oxide. After 15 months at 950^{o}C only small traces of a Cr rich layer were present suggesting that the Cr rich oxide was subliming after long term exposure. It may be that at the higher temperatures volatilisation of the chromia layer is occuring. At temperatures normally associated with above 1000^{o}C a chromia layer can continually oxidise to form CrO_3 which evaporates from the surface (40).

Short term oxidation for samples aged for 6 hours at 900 and 950^{o}C, with and without a TBC were carried out. It was found that only an Al rich oxide scale was present after short-term ageing with only an MCrAlY layer present. This suggests that the Cr, Co and Ni layers observed in long term aged samples formed as a secondary layer. An oxidation model was used to predict the alumina oxide thickness for isothermally aged samples, and the predictions were compared with the measurements of the Al rich oxide region that had formed after isothermal exposure. It was observed that the model correlation with experimental results was strongest when a TBC coating was applied. The study into isothermal samples with and without a TBC present after ageing shows that the TBC layer, although of open porosity, does affect the rate of oxidation of the MCrAlY coating and the chemistry of the oxides formed.

5 Microstructural Characterisation of MCrAlY Coated IN738LC Ex-service Combustion Chamber Heat Shield Tiles and Comparable Isothermally Aged Samples

5.1 Introduction

The aim of this chapter is to compare the microstructural evolution of MCrAlY coated IN738LC superalloys that have experienced service conditions with samples that have been isothermally aged. The isothermal samples are identical in chemical composition to the service exposed material, and both sample sets were prepared under the same conditions. The MCrAlY coating thickness applied to the isothermal samples studied in this chapter is of a more conventional thickness than the samples studied in Chapter 4. The characterisation of isothermal material has been used to validate oxidation and diffusion based thermodynamic and kinetic models that have then been used independently to derive estimations for the exposure temperature experienced by components during service. Combustion chamber heat shield tiles that line the chamber of a SGT5-4000F gas turbine were studied. The engine has an annular combustion chamber with 24 hybrid burners around the circumference of the chamber that can operate on both liquid and gaseous fuels. For this study five tiles were entered into service and removed after 5004 hours operation. The position of the tiles within the industrial gas turbine engine is highlighted in Figure 5.1.

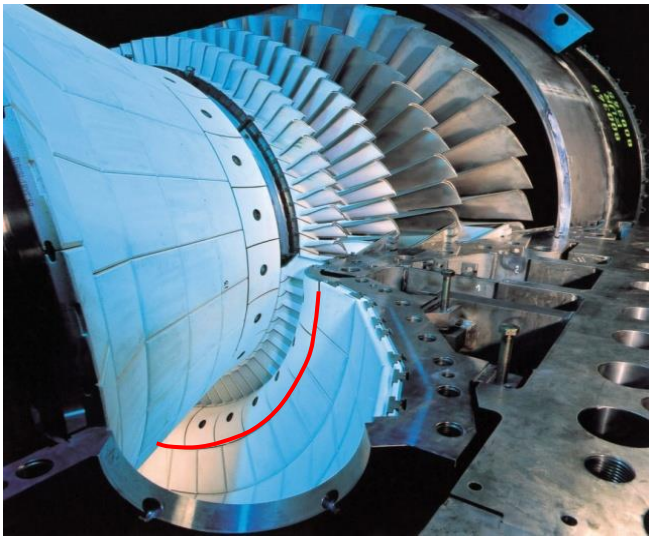

Figure 5.1 Photograph of a Siemens SGT5-4000F gas turbine engine, with the outer casing removed revealing the combustion chamber and turbine blades; the combustion chamber tiles are highlighted in red.

In Chapter 4 a protective coating system, consisting of an MCrAlY bondcoat and a TBC layer was introduced and characterised for a series of isothermally aged samples. The samples discussed in this chapter have a significantly thicker MCrAlY layer, and are not directly comparable with the samples discussed in Chapter 4, although the coating applied has the same nominal composition. The isothermally aged tile samples characterised in this chapter were coated with a High Velocity Oxy-Fuel (HVOF) sprayed MCrAlY at the same time as a series of heat shield tiles were prepared for service. All coating pre treatment and processing were identical for both the isothermal samples considered in this chapter and heat shield tiles that were entered into service. Before the MCrAlY coating was applied, an abrasive grit blast of the substrate was carried out at 30-40 psi and after the MCrAlY was applied, a low pressure compressed air clean of the surface was carried out. All samples were then sprayed with a 250 µm CoNiCrAlY coating, the powder composition of which is shown in Table 5.1. A further abrasive grit blast of the MCrAlY was carried out at 10-20 psi before an yttria-stabilised zirconia (YSZ) thermal barrier coating (TBC) was applied by an air plasma spray (APS) method. Each sample/component was then given a post coating heat treatment at 1080^{o}C for 4 hours. The measured coating composition after post coating treatments is shown in Table 5.1. Post coating heat treatments are typically carried out to increase the bond coat adhesion (11). A combined thermodynamic and kinetic model was used to predict the coating composition after heat treatments but before isothermal ageing experiments were carried out. The predicted composition is shown in Table 5.1, and the isothermal ageing conditions used for samples in laboratory air are shown in Table 3.4.

Table 5.1 (a) AMDRY995 CoNiCrAlY coating powder composition, provided by the coating manufacturer, and (b) the measured composition in the bulk of the coating by EDS after post coat heat treatments and (c) the predicted composition by a combined kinetic and thermodynamic model.

Element	Co	Ni	Cr	Al	Y
(a) Nominal powder composition					
Wt %	38.5	32	21	8	0.5
(b) After post coating treatment - measured composition					
Wt %	36.5	33.3	19.6	9.7	0.9
(c) Thermodynamic and kinetic model coating prediction after 4 hr post-coat age heat treatment at 1080^{o}C					
Wt %	38.5	32.7	21.1	7.6	x

5.2 Thermodynamic Calculations

Thermodynamic equilibrium calculations were carried out for the CoNiCrAlY coating which was applied to the tiles and isothermal samples. Although the coating thickness applied differs from the samples studied in Chapter 4 the coating composition of the powder is the same. The thermodynamic calculation results can be found in section 4.2 as the results are identical; this is due to the fact that coating thickness is not an input for equilibrium calculations. The calculations were carried out for a temperature range 500-1500^{o}C. The thermodynamic calculations for this coating show that in the temperature window of interest for this work; 850-950^{o}C, the coating is essentially made up of two phases, gamma and beta.

5.3 Characterisation of Isothermally Aged CoNiCrAlY Heat Shield Tile Samples

The characterisation of the microstructure of the CoNiCrAlY coated IN783LC isothermally aged samples are discussed in this section. A micrograph taken from an as received test specimen is shown in Figure 5.2a. The samples also had an additional 250 µm YSZ TBC layer applied, a micrograph taken from a test sample showing both MCrAlY and TBC components of the coating system is shown in Figure 5.2b.

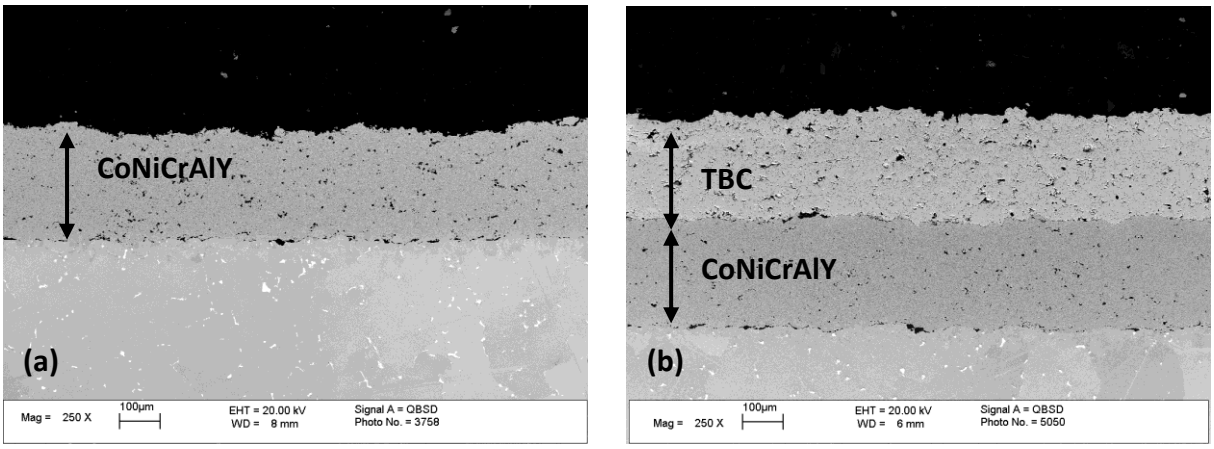

Figure 5.2 (a) A back-scatter electron micrograph showing just an MCrAlY coating applied to a test specimen and (b) a similar micrograph showing both MCrAlY and TBC coatings present on a second test specimen.

The as-received sample with only an MCrAlY coating is shown in Figure 5.3a, a sample with an MCrAlY and a TBC is shown in Figure 5.3b; cracks can be seen within the TBC and the surface roughness of the MCrAlY can be observed. Both samples were given a post coating heat treatment of 4 hours at 1080^{o}C.

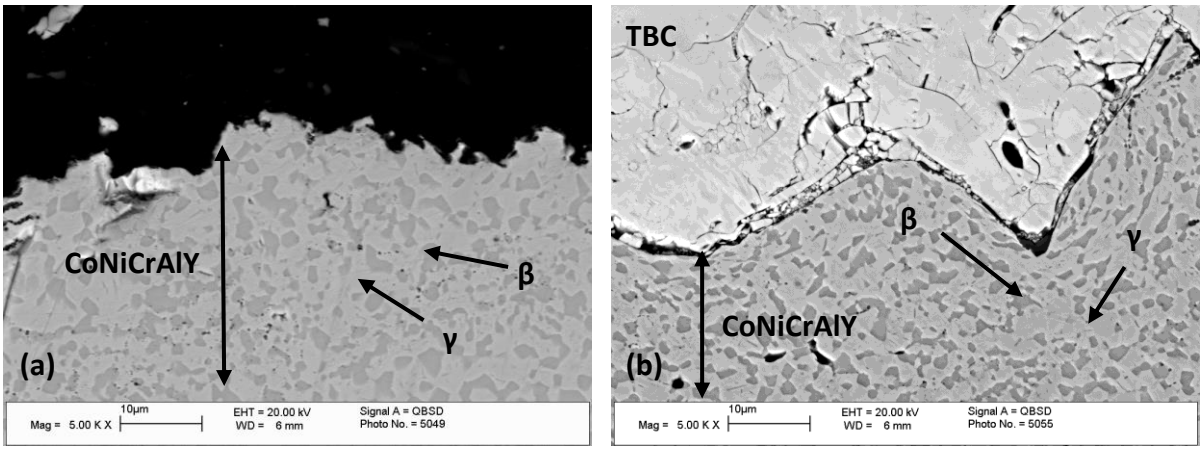

Figure 5.3 Back-scatter images showing the top of a MCrAlY layer without (a) and with (b) a TBC layer applied in the unaged condition. Within the coating the gamma and beta phases can be observed.

The beta phase can be observed within the unaged test samples; as dark grey, it was identified by electron back-scatter diffraction (EBSD) and energy dispersive spectroscopy (EDS). Using thermodynamic calculations the coating was predicted to be two phase, beta and gamma. The predicted composition for each phase is shown in Table 4.4 in the previous chapter as the coating is of the same nominal composition. The mean beta and gamma composition within an unaged tile was measured using EDS and the result is shown in Table 5.2. The relationship can be observed showing that the concentration of elements can be used to identify the phases present.

Table 5.2 Composition of the beta and gamma phases measured using EDS on a test sample before isothermal ageing, but after post coat heat treatments.

Phase	Element wt%	Co	Ni	Cr	Al
Beta		25.1	45.9	9.9	19.1
Gamma		41.0	30.6	22.6	5.8

Combined EBSD and EDS maps were used to identify the phases present by using both crystallographic and chemical information independently. An EBSD/EDS map scan was carried out on a sample that had both an MCrAlY and TBC layer applied. The area scanned was in the centre of the MCrAlY coating to avoid any areas affected by post coating heat treatments. The resulting scan image quality map is shown in Figure 5.4a. The small grain size within the MCrAlY coating is evident from this figure, showing a maximum grain diameter of 2.7 µm. Figure 5.4b shows the phase map of the coating based on crystallographic information. Figure 5.4b shows that there are two phases present, beta and gamma. The beta phase is shown in red and gamma in green.

Alongside EBSD data, simultaneous EDS data were also collected for the same region. These data enable selected elements to be identified and the resulting maps show areas of high and low concentrations of the collected elements. The results for the elements Al, Co, Cr and Ni are presented in Figure 5.5. Figure 5.5a shows in red high concentrations of the element Al and in green low concentrations. Comparing the Al EDS map with the phase map in Figure 5.4b it can be seen that the beta phase appears to have a higher concentration of Al than the gamma phase. This can be compared with thermodynamic predictions in Figure 4.2 and 4.4 which suggest that the beta phase will have a higher Al content. The relationship of concentrations of Co, Cr and Ni within the beta and gamma phases is shown in Figures 5.5b, c, d and the results correlate with the thermodynamic predictions in Figures 4.2 and 4.4.

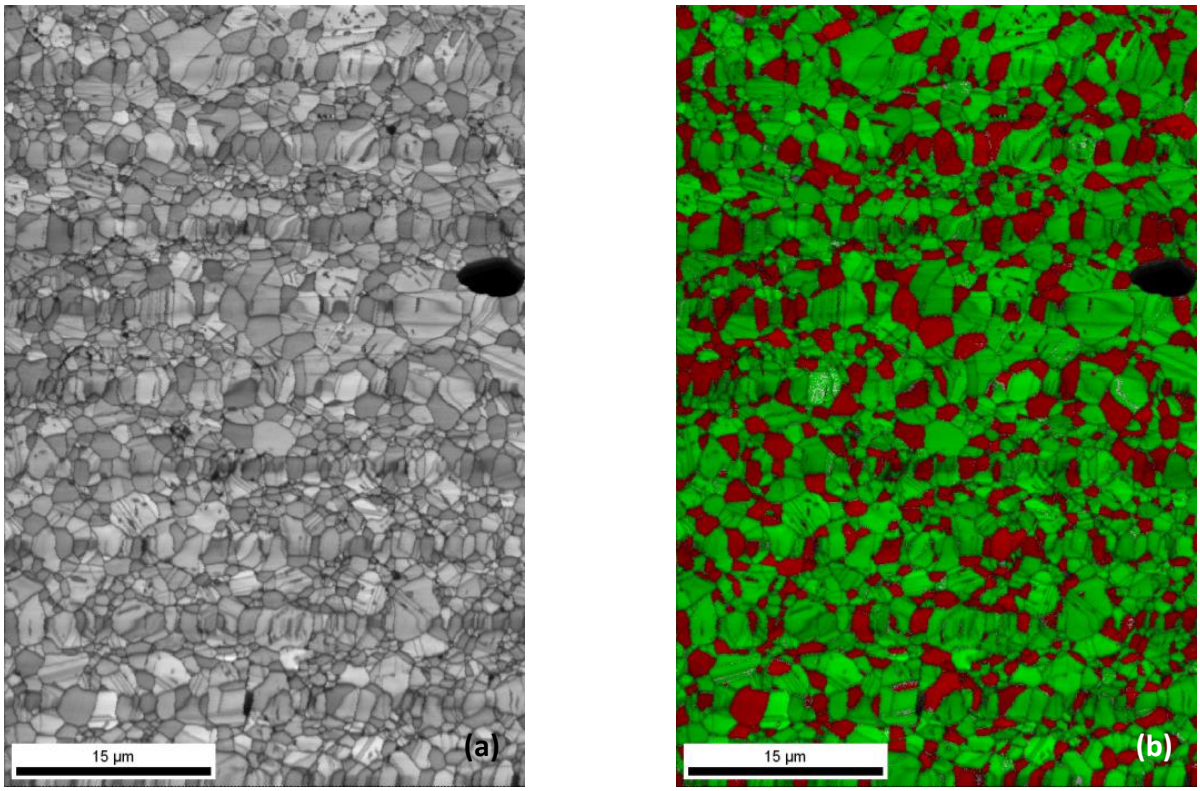

Figure 5.4 EBSD results from an unaged test sample showing the image quality map and a phase/image quality composite map highlighting the two phases present. Using the crystallography data collected the phases can be identified showing the red region as the beta phase and the green region the gamma matrix.

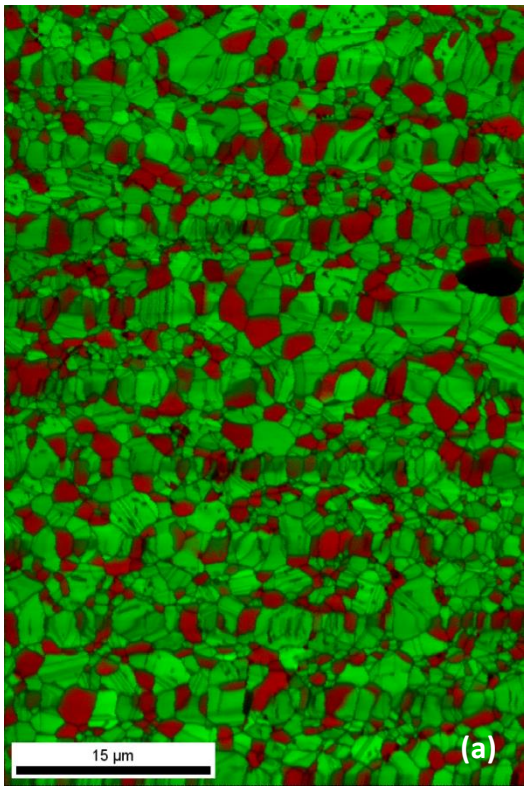

Al

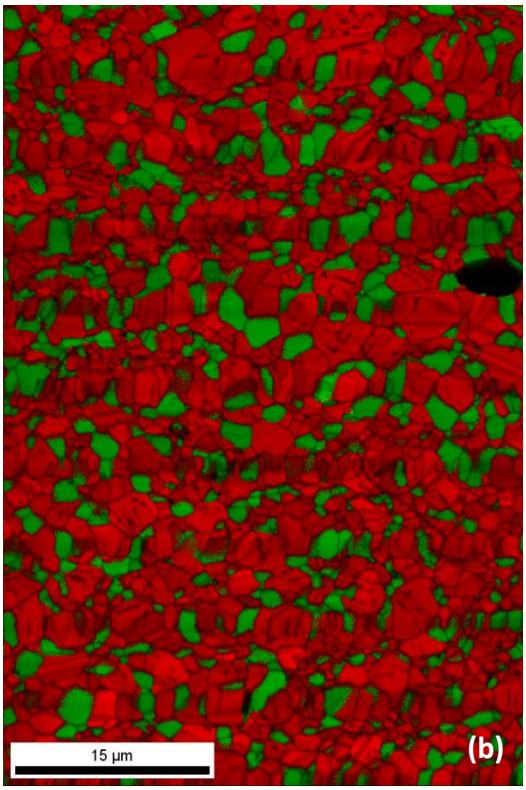

Co

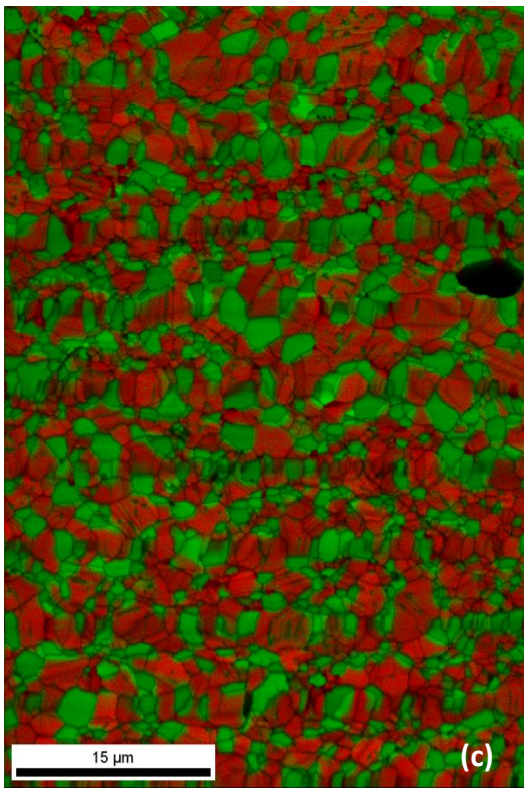

Cr

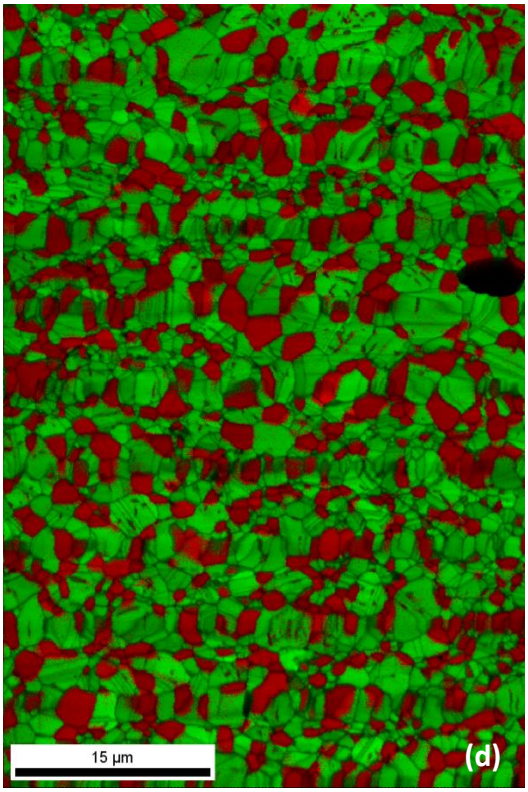

Ni

Figure 5.5 Individual EDS map results for Al, Co, Cr, and Ni collected within the MCrAlY layer of an unaged sample. Images show areas high in concentration of the element in red and low concentrations in green.

5.3.1 Oxide Case Study of Isothermally Aged Tile Samples

Isothermally aged samples were removed from furnaces at three monthly intervals to provide samples at the ageing time and temperature conditions shown in Table 3.4. Initially micrographs were collected to study the oxide scale that forms at the outer edge of the MCrAlY layer. The oxide scale that forms at the interface is limited by the supply of oxide forming elements within the coating (41,42). The relationship between the supply of Al and the change in the oxide scale was discussed in Chapter 4. The oxide forming on all isothermally aged samples was then studied and the thickness of the oxide scale measured.

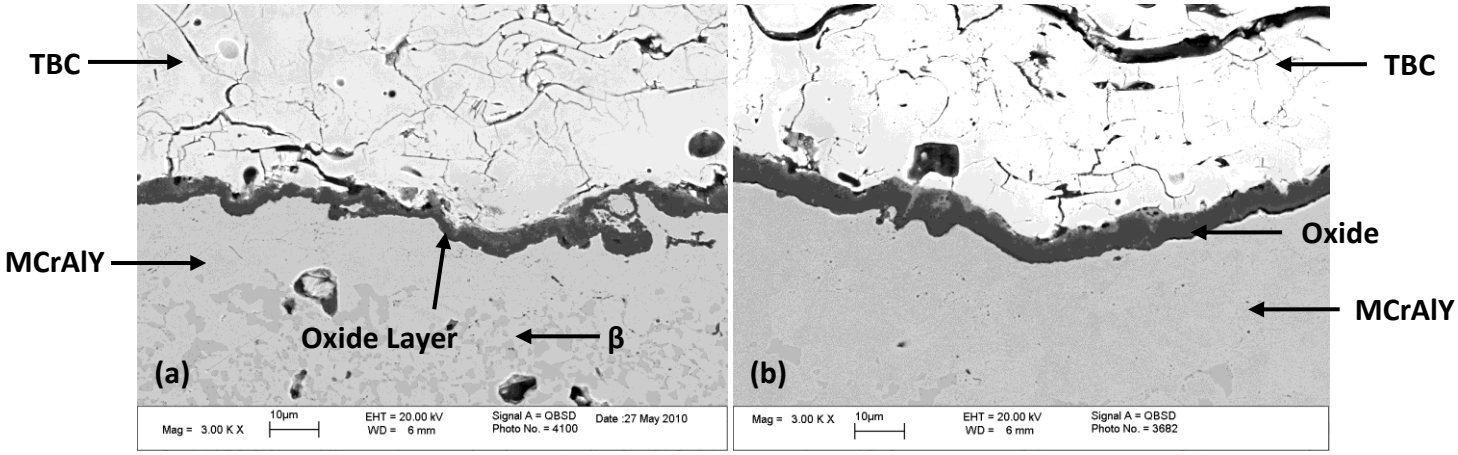

Figure 5.6 (a) A back-scatter image of a sample aged for 12 months at 850^{o}C and (b) 3 months at 950^{o}C. Under both conditions the TGO that has formed at the MCrAlY interface can be observed.

A selection of images were taken, consisting of images at x 2k and x 3k magnification in multiple positions; two positions were selected and using image analysis software the mean oxide thickness was determined. In Figure 5.6a the oxide was measured to be 4.6 µm and in Figure 5.6b; 5.5 µm. The sample in Figure 5.6b has been aged for 3 months at 950^{o}C, compared to 12 months at 850^{o}C for the sample in Figure 5.6a. The difference in oxide thickness suggests that the temperature increases the oxidation rate (43). Results for samples aged for 3-15 months at 850, 900, 950^{o}C are shown in Figure 5.7. Samples aged at 850^{o}C had an oxide thickness range 3.1-4.7 µm and samples at 900^{o}C; 4.5-6.9 µm. The oxide thickness increased for samples aged at 950^{o}C to range between 5.5-9.3 µm.

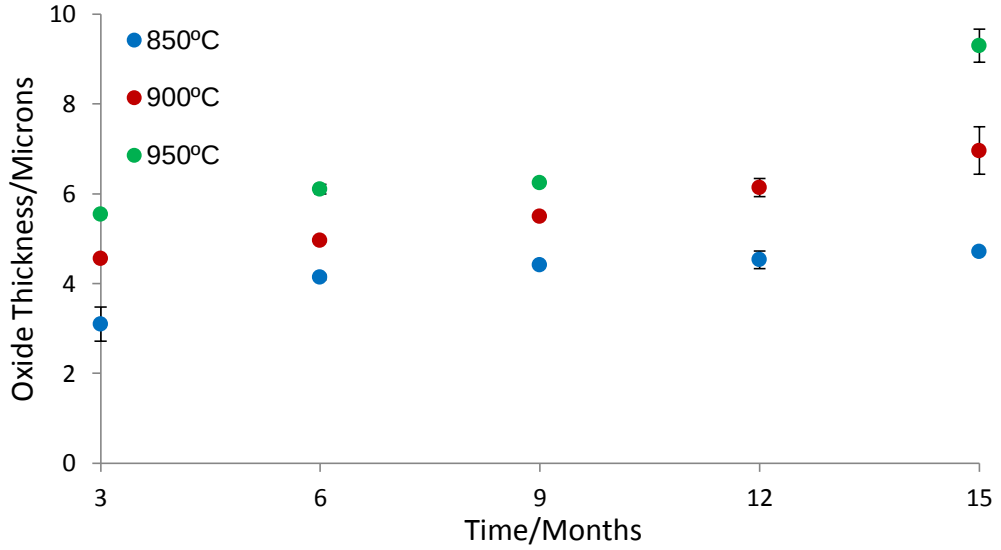

Figure 5.7 The measured mean oxide thickness and the standard deviation, calculated from measurements on a number of micrographs for isothermally aged samples as a function of ageing time and temperature.

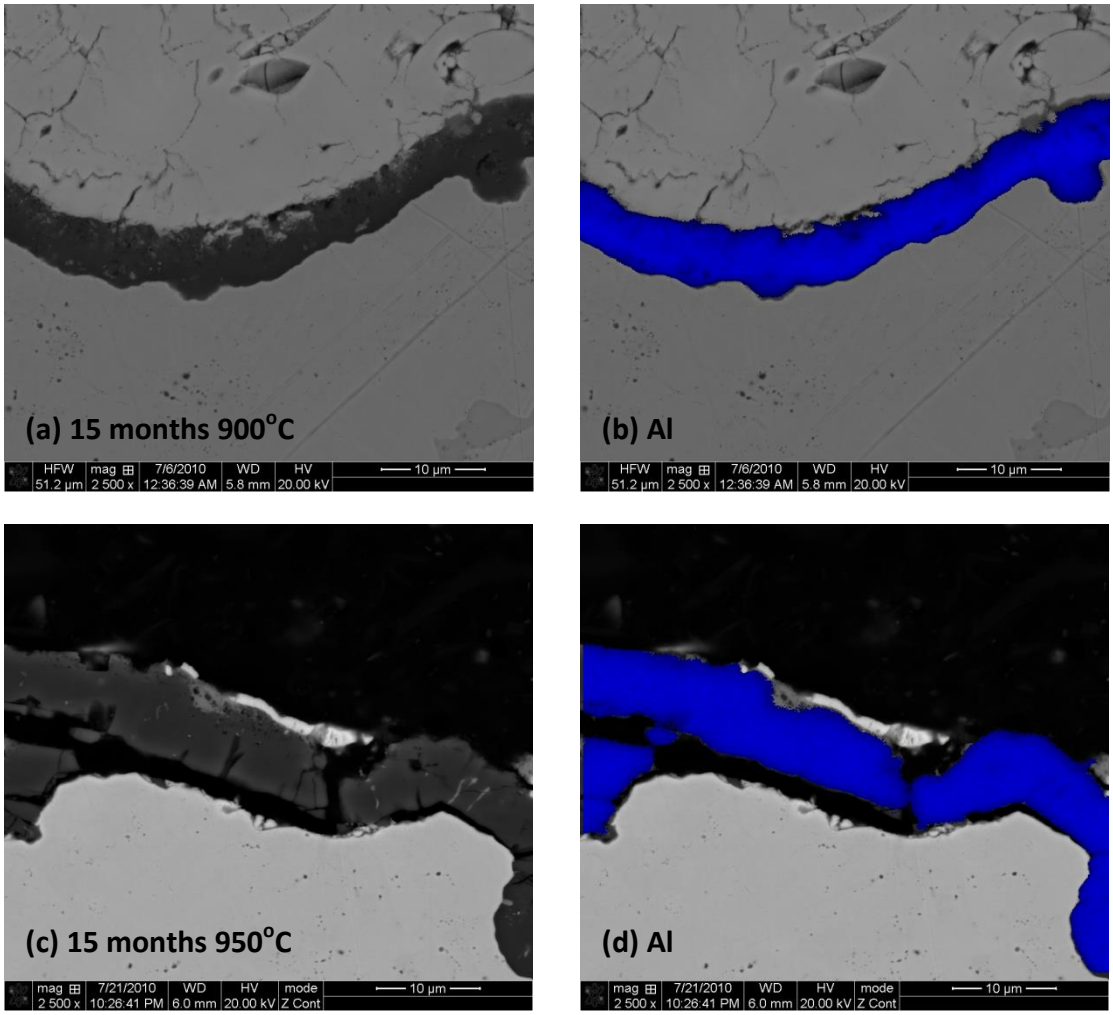

Figure 5.8 Back-scatter electron images (a, c) and EDS maps overlaid onto EDS back-scatter electron images (b, d) show two samples aged for 15 months at 900°C (a, b) and 950°C (c, d). The sample aged for 15 months at 950°C shows spallation of the TBC layer during the isothermally ageing process.

The chemistry of the oxide was studied in the isothermal tile samples in this chapter and at the highest temperature, longest ageing time it was found that the oxide forming was only Al rich. This can be seen in Figure 5.8 where two samples are presented, in Figure 5.8a and 5.8b a sample aged for 15 months at 900^{o}C is shown. In Figure 5.8c and 5.8d a sample aged for 15 months at 950^{o}C is presented. In both cases the Al EDS map shows that the whole oxide layer is rich in Al. The EDS maps for Cr, Co and Ni did not show any areas of the oxide which were rich in these elements. A continuous alumina TGO can itself act as protection against the formation of other detrimental oxides including chromia and spinel (44). In Chapter 4 the oxide chemistry was studied and it was also found that when a TBC layer is applied the oxide that formed consisted of only a consistent Al rich alumina layer.

5.3.2 Study of the Beta Phase within Isothermally Aged Tile Samples

The outer beta depletion zone can be observed in Figure 5.9a, and this can be compared with an unaged sample in Figure 5.3b where no depletion of beta is present. It is assumed that the alumina scale forming initially is dependent on the supply of Al within the coating, specifically within the beta phase (23). Al is consumed to form an oxide from the edge of the beta zone initially, therefore, as the oxidation rate increases the beta will begin to deplete (41).

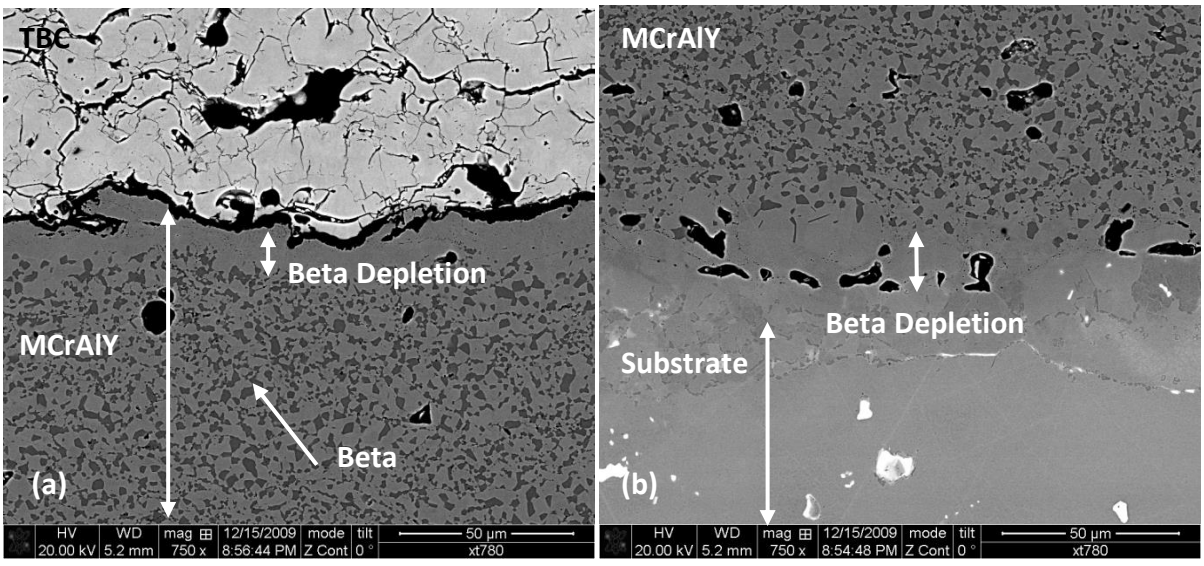

Figure 5.9 Back-scatter micrographs showing a sample that has been aged for 3 months at 850^{o}C. The depletion of the beta phase can be observed in both the outer (a) and inner (b) regions of the MCrAlY layer.

The width of the beta depletion region was measured at the outer edge of the MCrAlY coating; this zone can be seen in Figure 5.9a, and it was measured to be 10.64 µm. Within this sample the microstructure did show signs of beta depletion symmetry, for example as Al diffuses to form an oxide scale at the outer edge of the MCrAY layer, Al is also diffusing across the substrate/coating interface as there is a mismatch in the composition between coating and substrate (41). In Figure 5.9b, inner depletion of beta within the MCrAlY was observed, and measured to be 10.17 µm. The coating/substrate interface was identified using EDS line scans across the interface region and using the known chemistry of the coating and substrate each component of the system could be identified.

The extent of the inner and outer beta phase depletion of the MCrAlY coating was measured within all samples. The inner depletion occurs at the substrate/MCrAlY interface and the outer depletion occurs at the MCrAlY/TBC interface. The inner depletion measurement results can be seen in Figure 5.10. The sample aged for 15 months at 950^{o}C had no beta remaining within the MCrAlY microstructure and the TBC was found to have spalled. The TBC layer was found to have spalled after overnight natural cooling; this desktop spallation phenomenon has been investigated by Smialek and he observed that the moisture content in the ambient environment is critical (45). It could not be established whether the TBC had failed during high temperature ageing or due to water vapour induced spallation during cooling, therefore the sample was not used within the isothermal characterisation comparison. Figure 5.11 shows the measurements for thickness of the outer beta depletion zone. It can be noted that there is a correlation between the extent of outer and inner beta depletion and the isothermal ageing conditions. In Figure 5.12 both the outer and inner depletion results are plotted, which shows that the depletion of the beta phase appears to be symmetrical. There are likely to be differences in the oxidation and beta depletion between isothermally aged samples and service exposed samples due to the operating conditions. Within service components there are thermal gradients across the tiles as a result of impingement cooling systems in the back of the tiles designed to limit the exposure temperature of the component.

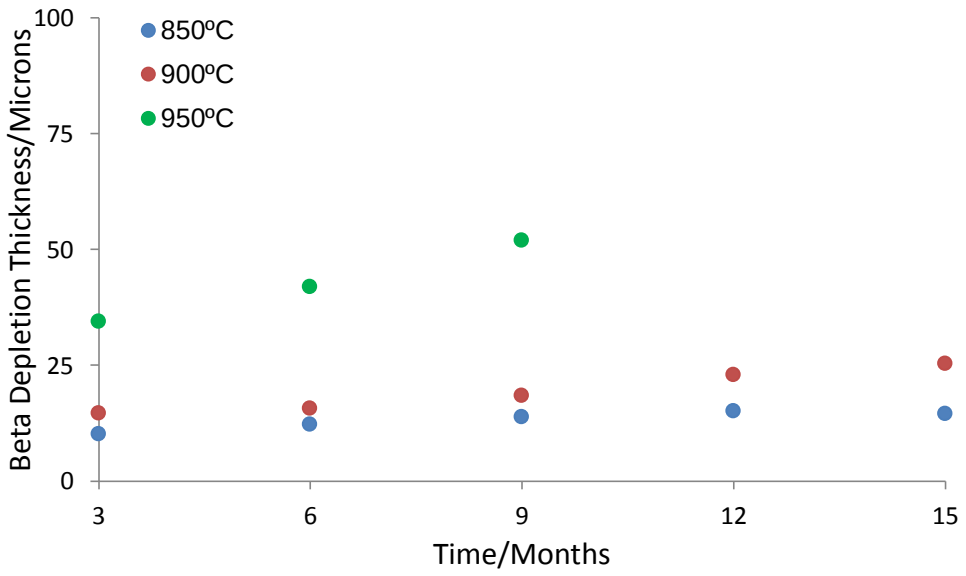

Figure 5.10 Experimental results showing the measured inner depletion of beta. The measurements were taken from the edge of the beta phase to the MCrAlY/Substrate interface within isothermally aged samples at temperatures of 850°C, 900°C and 950°C for times up to 15 months.

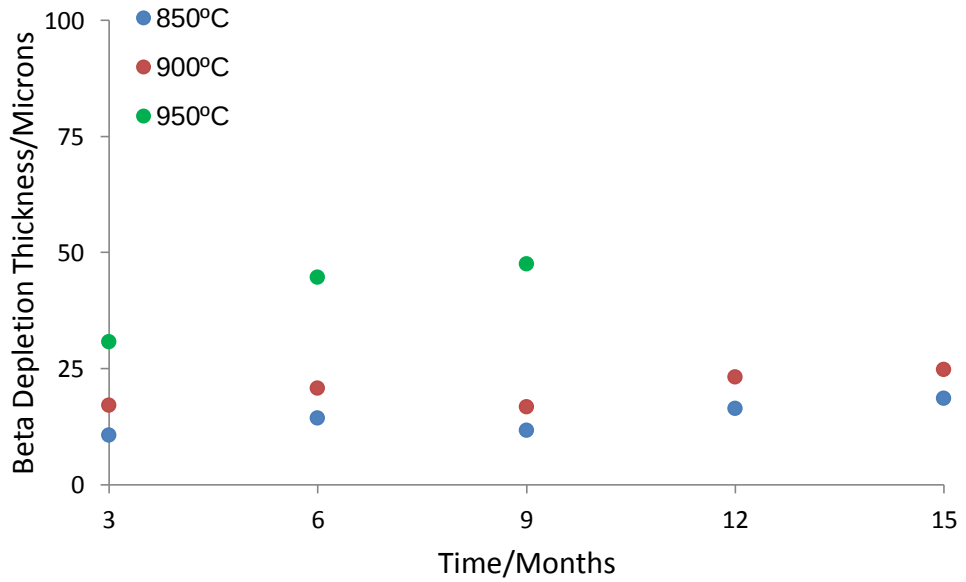

Figure 5.11 Experimental results showing the measured depletion of outer depletion of the beta phase within isothermally aged samples. The depletion measurements were taken from the edge of the beta phase to the MCrAlY/TBC interface.

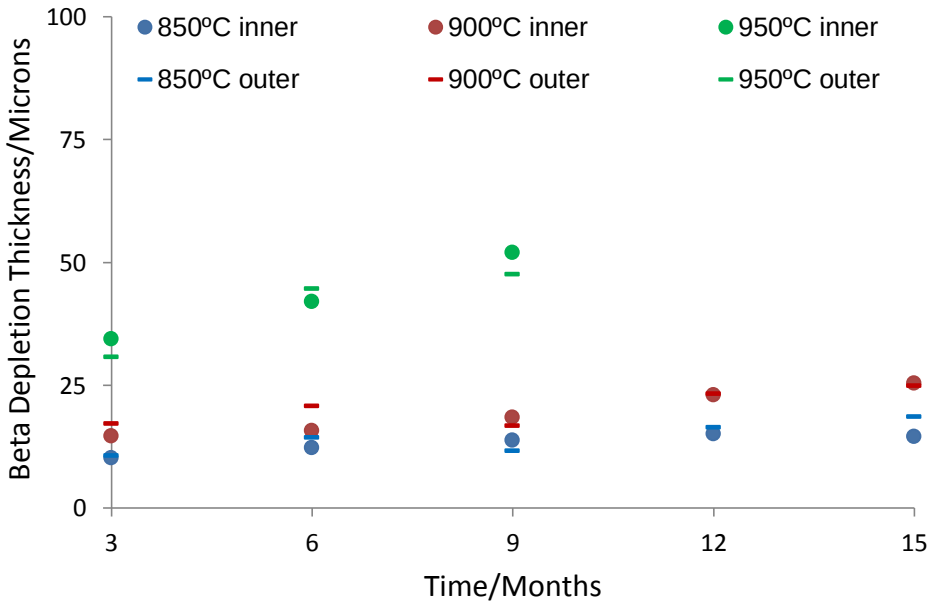

Figure 5.12 Experimental results showing the measured inner and outer beta depletion results. The results were derived from measuring the beta depletion from a series of micrographs with the aid of image analysis software. The TBC layer had spalled on the sample aged for 15 months at 950^{o}C, the sample was characterised and no beta was found to be remaining within the coating suggest it has been exposed to an elevated temperature, which correlates with TBC spallation.

5.3.3 Deriving Beta Depletion Measurement Predictions from Microstructure Models

Using a combined thermodynamic and kinetic model detailed in section 3.5.2 it is possible to predict the extent of the beta depletion based on the diffusion of elements within the MCrAlY layer into the substrate material. The model predicts the amount of each phase present after thermal exposure and from this is it possible to derive a prediction of the depletion of the beta phase at the substrate/MCrAlY interface.

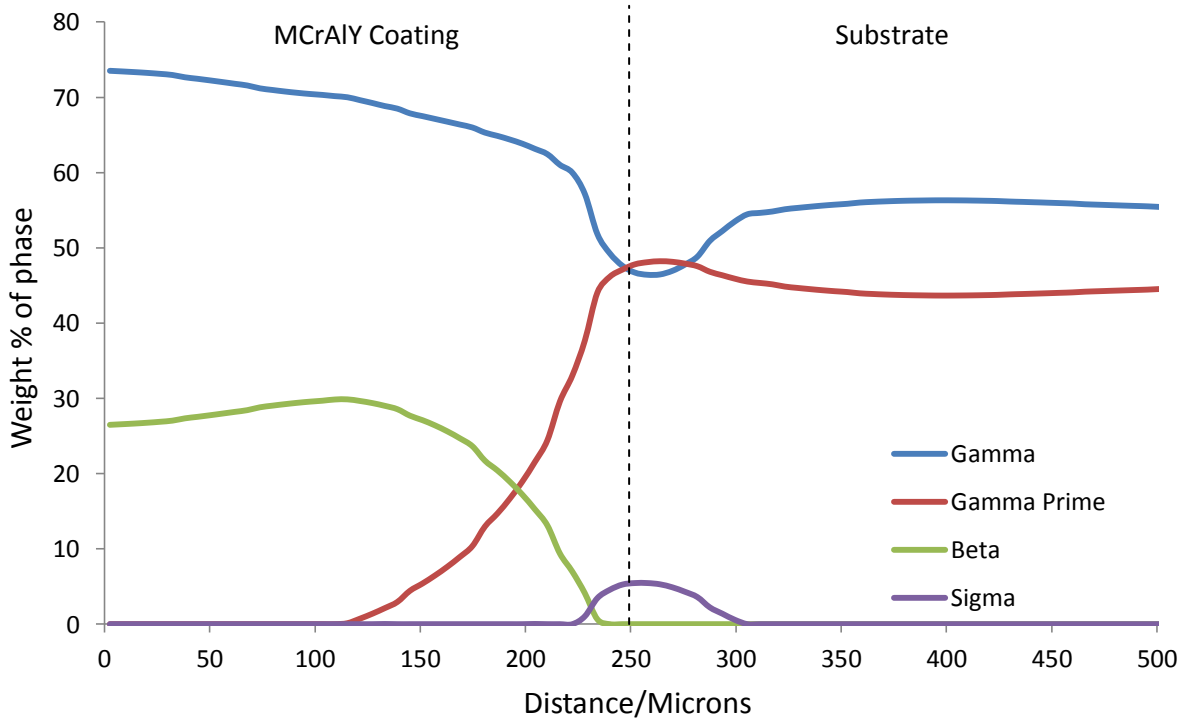

Figure 5.13 A kinetic and thermodynamic model prediction of the phases present within the microstructure of a tile with a 250 µm AMDRY995 MCrAlY layer applied to an In738LC substrate after exposure at 900°C for 6 months. The x-axis distance is the distance from the edge of the MCrAlY interface into the tile.

Figure 5.13 shows a thermodynamic and kinetic model prediction after exposure for 6 months at 900°C. The result is for the wt. % of phase at a distance from the TGO interface into the coating. The coating thickness is an input parameter. It is possible to measure the linear depletion of the beta phase at the MCrAlY/substrate interface from the simulation result. In Figure 5.13 the linear beta depletion is predicted to be 16 µm. By carrying out multiple simulations at different ageing times and temperatures, a graph can be constructed as shown in Figure 5.14. The graph shows the model predictions of inner beta depletion for samples aged at 850, 900, 950°C for 3, 6, 9, 12 and 15 months.

The predicted linear beta depletion from the multiple simulations and linear beta depletion measurements within the isothermally aged samples are compared in Table 5.3. It can be seen how at 850 and 900°C there is a good correlation but at the higher temperature of 950°C the measured beta depletion is far greater than predicted. It was discussed previously how TBC spallation had occurred for selected samples aged at 950°C so no comparison is available for this specific case.

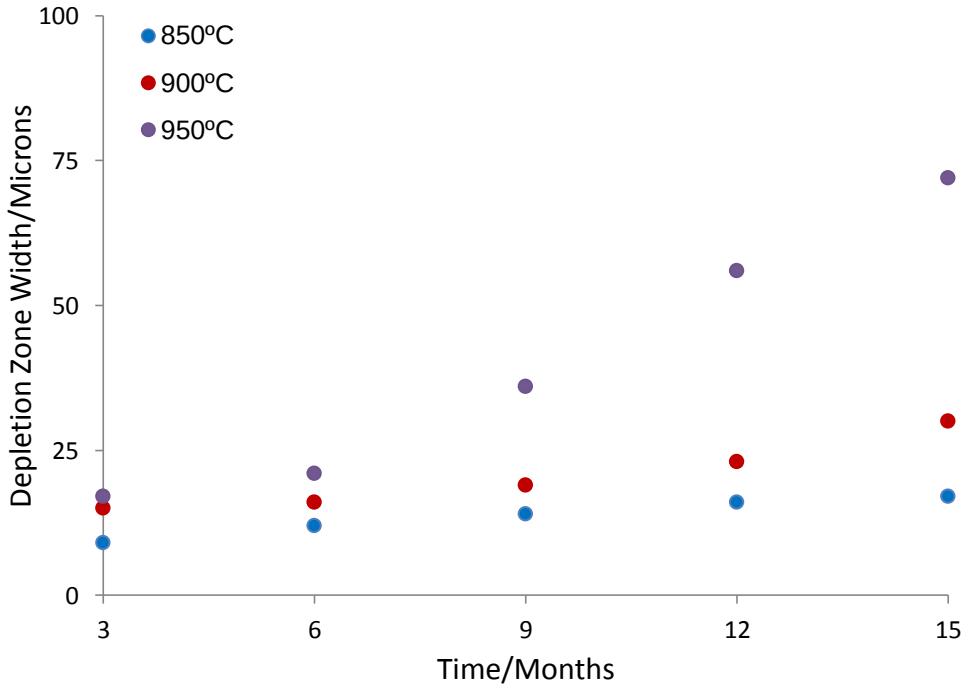

Figure 5.14 Predicted inner beta depletion derived from a series of simulations carried out using a combined kinetic and thermodynamic model to predict microstructural evolution.

Table 5.3 Predicted inner beta depletion derived from a kinetic and thermodynamic model and actual measured inner beta depletion results for isothermally aged samples.

Predicted Inner Beta Depletion (µm)

Temp	3 m	6 m	9 m	12 m	15 m
850°C	9	12	14	16	17
900°C	15	16	19	23	30
950°C	17	21	36	56	72

Measured Inner Beta Depletion (µm)

Temp	3 m	6 m	9 m	12 m	15 m
850°C	10.2	13.3	13.9	15.2	14.6
900°C	14.7	15.7	18.4	23	25.4
950°C	34.4	42	52	x	x

5.4 Characterisation of Ex-Service Combustion Chamber Heat Shield Tiles

In the previous section the microstructure was studied within a CoNiCrAlY coating applied to isothermally aged test specimens. The isothermal test samples were prepared at the same time as a set of five combustion chamber tiles were sprayed with the same MCrAlY/TBC coating system, and the five tiles were entered into service in a commercial industrial gas turbine. Upon inspection of the engine after 5004 hours the tiles showed signs of coating failure and were removed from service. The tiles located within the engine are shown in Figure 5.15. The location of the tiles is significant; previously combustor pressure oscillation has been a problem within this SGT5-4000F engine. This causes vibrations within the turbine and within the casing and bearings. A solution is to control the convective time lag, which is time lag for the fuel/air mixture to enter the combustion chamber. To make it possible to adjust this parameter a cylindrical burner outlet (CBO) is welded onto the burner nozzle, and they are visible within the engine in Figure 5.16 (46).

Figure 5.15 A photograph taken from within the engine combustion chamber showing the tiles in their specific locations. The five tiles characterised within this piece of work are highlighted, numbered 136, 137, 138, 139 and 140.

Figure 5.16 A photograph taken from within the engine combustion chamber showing the modified burner rings; this is the location directly opposite the five test tiles.

The engine that the tiles were entered into service within this work has had previous combustion chamber heat shield tile failures. The original tiles that failed were from the row 1 position adjacent to the burners. The investigation suggested one tile failed initially due to overheating. The tiles also showed evidence of thermal distortion, which was attributed to overheating. The tile design was changed to increase the cooling air flow, by manufacturing a series of slots present on the underside of the tiles, and this can be seen within one of the five tiles removed from the engine in Figure 5.17 (47).

Figure 5.17 A photograph showing the underside of the tile and the updated tile design with additional cooling slots to try and prevent tile overheating.

During service the component and the coating are exposed to hot combustion gas on the TBC face and cooling air on the underside of the tile. The effective temperature at the interface between the coating system components can be calculated from Equation 5.1 by calculating the effective cooling throughout the coating system and component substrate. Figure 5.18 highlights the coating system and substrate properties and environment parameters which have been used to calculate the effect of TBC thermal protection and air cooling.

$$h_{hot}(T_{g1} - T_1) = k_{TBC}\frac{(T_1 - T_2)}{t_{TBC}} = k_{MCrAlY}\frac{(T_2 - T_3)}{t_{MCrAlY}} = k_{Metal}\frac{(T_3 - T_4)}{t_{Metal}} = h_{cold}(T_4 - T_{g2})$$

Equation 5.1

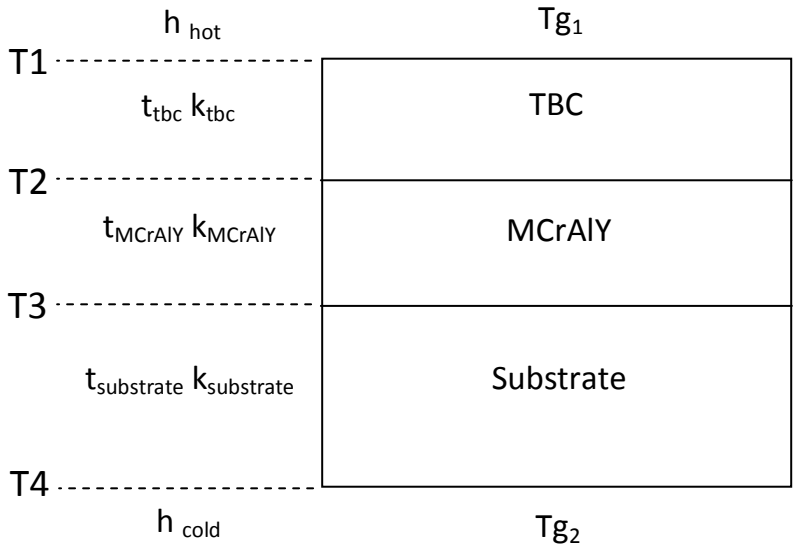

T1, T2, T3, T4 = temperature at interface

Tg_1 = gas entry temperature

Tg_2 = cooling air

k = thermal conductivity

t = thickness

h = heat transfer coefficient

Figure 5.18 A diagram to illustrate the parameters used to calculate the interface temperature assuming exposure to the combustion gas temperature and cooling of the tile from the underside. The thermal gradient within the coating system and substrate of the tiles can be used to calculate a temperature at each interface.

By using approximate values for the gas entry temperature and the cooling air provided by the engine operator it was then possible to calculate the interface temperatures. The values used to calculate the temperatures are shown in Table 5.4. By inputting these values into equation 5.1 it was possible to derive a series of temperature predictions at each interface. The interface predictions are shown in Table 5.5. It can be seen how the application of a TBC introduces a significant thermal gradient within the component. At the TBC/MCrAlY interface the temperature is predicted to be 909^{o}C which represents a 125^{o}C temperature change across the TBC layer. This drop is consistent with literature suggesting the addition of a TBC layer allows for inlet temperatures to be raised by 93-148^{o}C (54). The temperature drop across the MCrAlY is predicted to be only ~10^{o}C, but the temperature drop across the tile is 200^{o}C due to the forced cooling on the underside of the tile.

Table 5.4 The parameters used to calculate the cooling effect of the TBC and MCrAlY components of the coating system. The values used are from the engine operator for the hot and cold gas temperatures and from literature for the specific coating system component and substrate.

Tg_1 = 1350^{o}C (48)	Tg_2 = 450^{o}C (48)	
k_{tbc} = 1.2 W/m/K (49)	k_{MCrAlY} = 15 W/m/K (50)	$k_{Substrate}$ = 22 W/m/K (51,52)
t_{tbc} = 250 µm	t_{MCrAlY} = 250 µm	$t_{Substrate}$ = 6.5 mm
h_{hot} = 1939 W/(m^{2}K) (53)	h_{cold} = 2273 W/(m^{2}K) (53)	

Table 5.5 Temperature predictions at the interface positions within the TBC/MCrAlY coating system calculated from the parameters in Table 5.4 and Equation 5.1.

Interface	**Temperature**
T1- surface of TBC	~1036^{o}C
T2 -TBC/MCrAlY	~909^{o}C
T3 – MCrAlY/Substrate	~898^{o}C
T4 – underside of tile	~718^{o}C

One of the heat shield tiles, Tile 136, was sectioned initially. A micrograph showing where the TBC had spalled is shown in Figure 5.19. It was found upon removal of the tiles from the engine that some of the tiles appeared distorted, therefore, prior to microstructural characterisation of the microstructure, macro characterisation techniques were carried out. The macro characterisation is presented in section 5.4.1

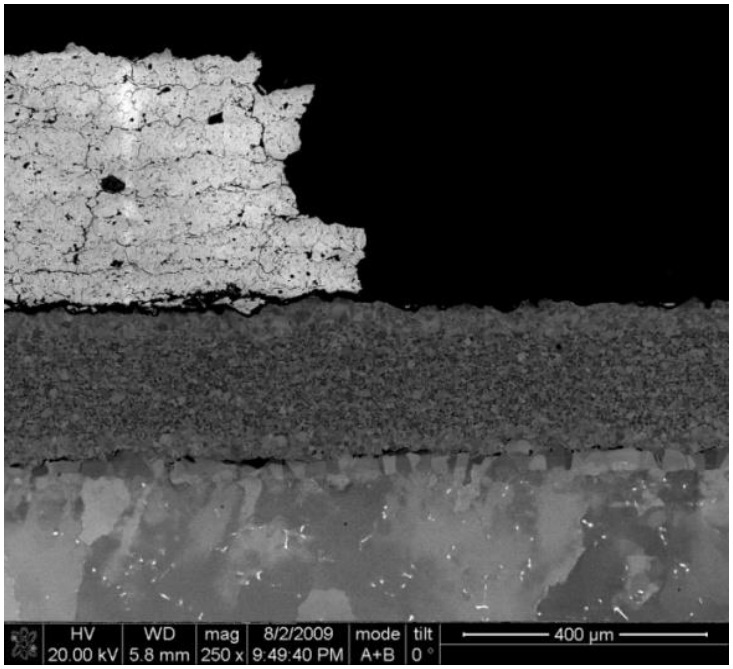

Figure 5.19 A back-scatter electron beam image showing the spallation of the TBC layer after 5004 hours in service within Tile 136. Cracking can be observed along the TBC/MCrAlY interface.

The condition of the remaining MCrAlY on this tile, including the oxide interface and the extent of beta depletion suggested that the TBC layer spalled during the shutdown cooling of the engine. (55)There are generally two sources of stress build up within the coating systems; firstly the growth of the TGO layer under the TBC and the second due to the thermal expansion mismatch between the TBC and MCrAlY which will occur when components are cooled (56).

When the engine is operating at temperature the bondcoat is likely to be under a tensile stress, however, during cooling this will be compressive. The presence of a TGO will influence the stress within the TBC. The thermal expansion behaviour of the MCrAlY and TBC is important, because of a large variation in the thermal expansion coefficient between the two components a tensile stress is imposed on the TBC layer during the operation of the engine at the elevated temperature. During service the components are held at temperature for a

significant period of time; in this research the time was 5004 hours. During this period the MCrAlY is assumed to relax by creep. When the engine is then shutdown and the components begin to cool the same thermal expansion mismatch now causes a compressive stress to be present within the TBC layer. It is these compressive stresses that can contribute to crack propagation and then to spallation of the TBC as shown in Figure 5.19. Alongside the five tiles characterised in this study with a CoNiCrAlY coating applied, two tiles with an SC2453 NiCrCoAlReY coating were also characterised and a micrograph of the SC2453 coating is shown in Figure 5.20. The two SC2453 tiles showed very little signs of substrate distortion and TBC spallation. This coating applied is routinely used within industrial gas turbines and is the coating applied to the remaining heat shield tiles within the engine that is the focus of this research. The two tiles were characterised as a benchmark study to compare the performance of a coating system that is routinely used in a service environment with the CoNiCrAlY coating system.

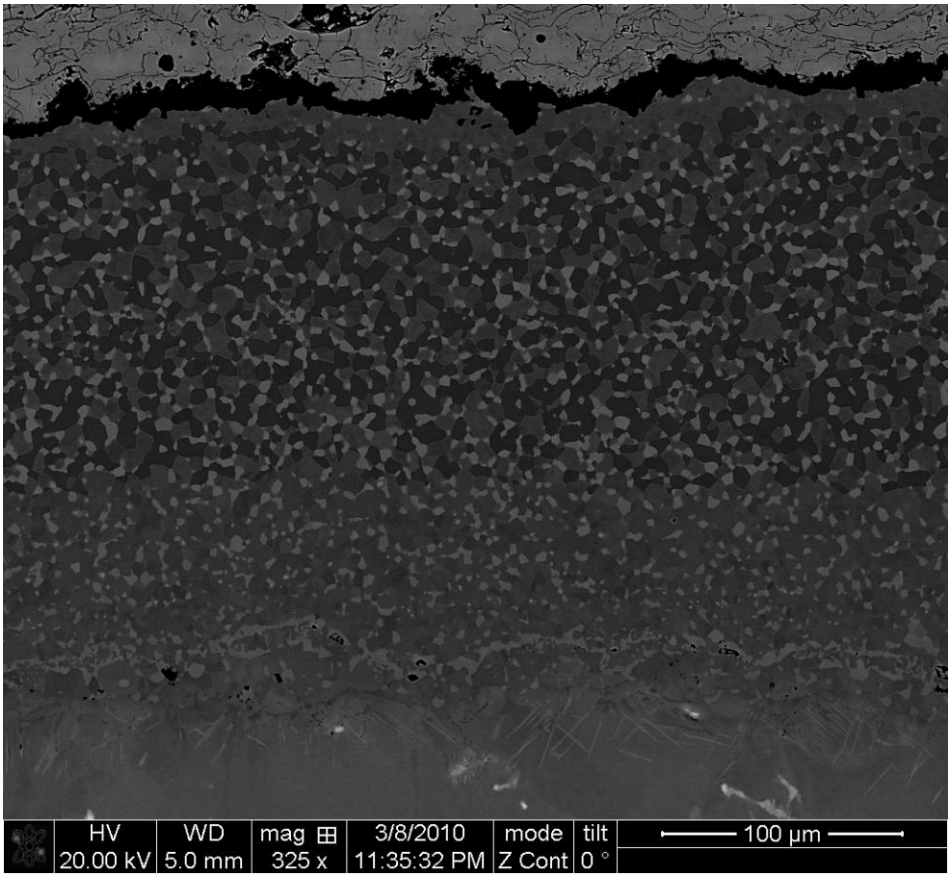

Figure 5.20 A back-scatter micrograph showing the sigma and beta rich SC2453 coating that is applied to the remaining heat shield tiles within the combustion chamber. These tiles are routinely used for long term service so were used as a benchmark for the performance of the CoNiCrAlY coating system.

5.4.1 Characterising the Distortion of Ex-Service Heat Shield Tiles

An examination of the thermal distortion of the tiles is presented in this section. Thermal distortion of combustion chamber heat shield tiles was investigated previously by engine operators due to tile failure and a maximum of 1.5mm distortion was measured in the worst case (47).

Within this work initially a co-ordinate measuring mechanism (CMM) was used, and a result from this technique is shown in Figure 5.21. Contact CMM allowed for a mesh to be constructed for each tile for data collected from a series of predefined coordinates. This technique was used to get an overview of the distortion levels within the tiles characterised, and showed how the tiles changed in relation to a series of predefined locations. This was, however, not suitable to study distortion of the substrate at the edge of the tile, where the tiles show the greatest distortion, because it is a contact method and where cracks are present it is not possible to record a measurement. For this reason additional characterisation methods were required. Laser scanning CMM was then used to enable a full mesh reconstruction, including the edges of the tiles. This is a non contact method and therefore allowed for a mesh of the tile face to be constructed, as shown in Figure 5.22. There were also limitations with this technique and in particular, it is difficult to reconstruct the full freeform including both faces and all edges of the tile. A full 3D mesh construction was therefore required and a technique capable of constructing a photogrammetric dataset was used.

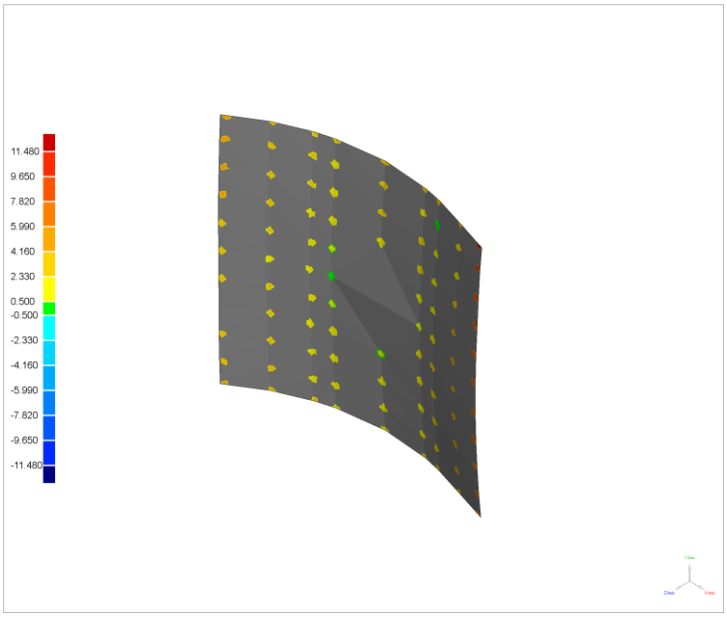

Figure 5.21 A mesh construction of one face of Tile 139 compared with a reference tile with no distortion using a contact CMM method. The spots highlighted are the data points collected in a matrix of 11 x 9.

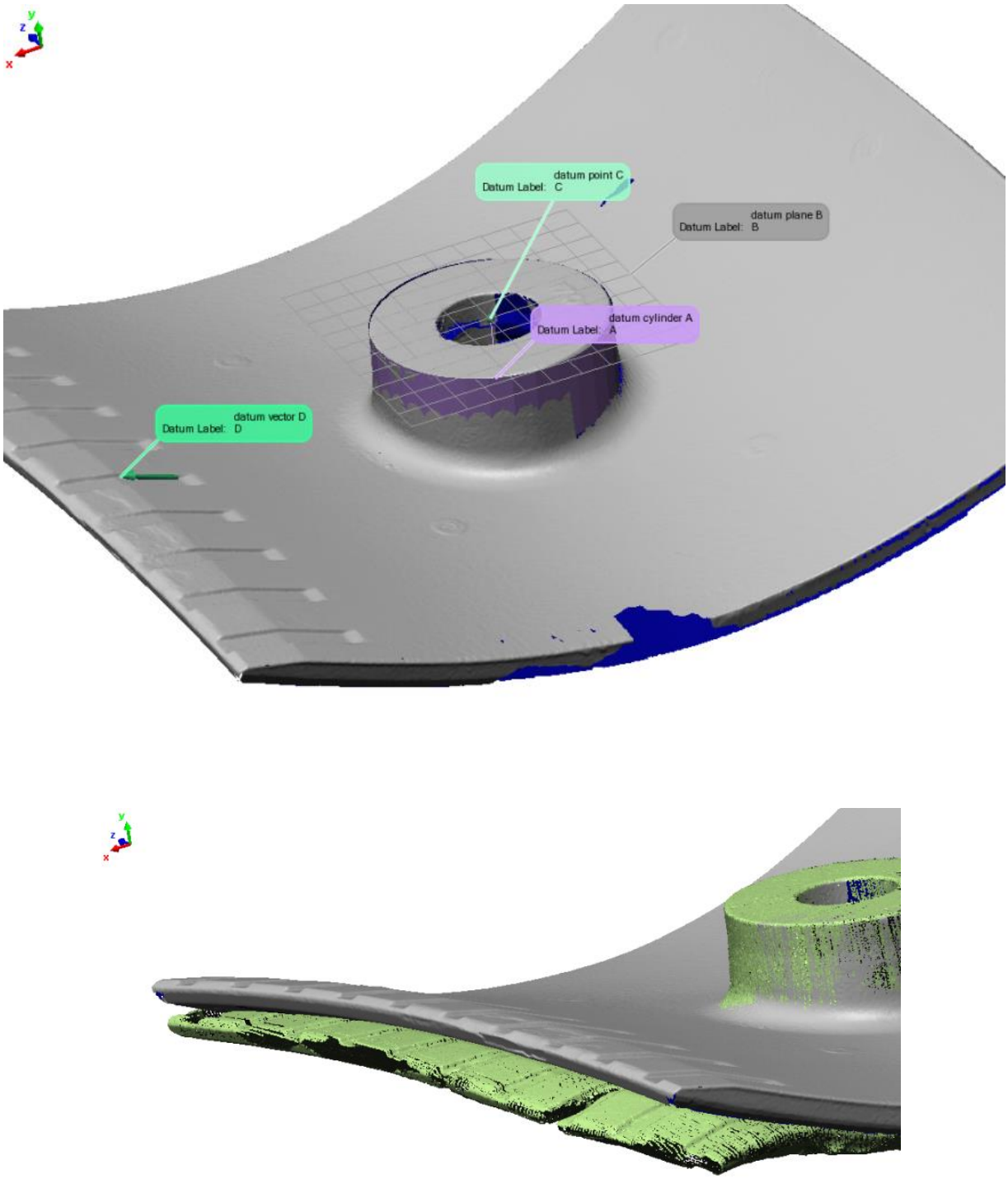

Figure 5.22 A mesh construction of one face of Tile 139 compared with a reference tile using a laser scanning CMM method. The mesh of Tile 139 was compared to the reference tile by using a series of datum points to align both meshes. These are highlighted in the top reconstruction and included the plane of the mounting section, the centre of the bolt hole and the edge of the cooling grooves.

Figure 5.23 shows how tiles with an SC2453 coating applied, a coating that is routinely used in service, show very little distortion of the tile substrate. Small areas of TBC spallation around the bolt hole in the centre are present in (b) The mesh construction for Tile 137, which has an AMDRY995 coating applied, is compared against a reference tile and the resulting distortion is shown in Figure 5.24. Two scales were used to present the distortion results; +/- 10 mm and +/- 2 mm, the 10 mm scale was used to show large areas of distortion. The top face of Tile 137 shows large areas of TBC spallation in (b) around the centre of the tile and the bottom left corner. When comparing the TBC spallation with the back of the tile it can be seen that the areas of greatest distortion do correlate with the region of greatest TBC loss.

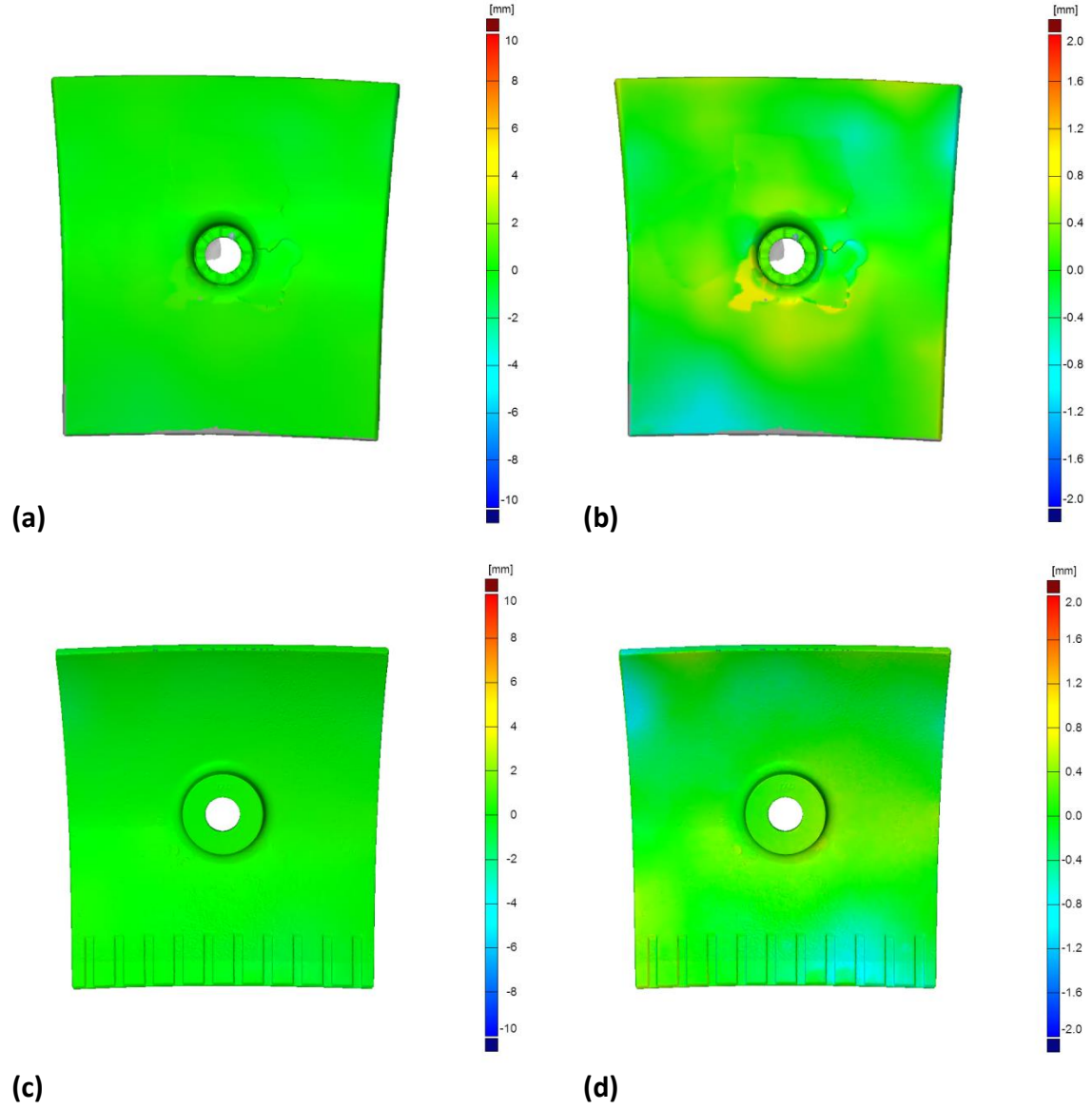

Figure 5.23 A mesh construction of the front and back faces of two Tiles 134 and 145, which had an SC2453 coating applied, the tiles were used as a reference and showed very little sign of distortion.

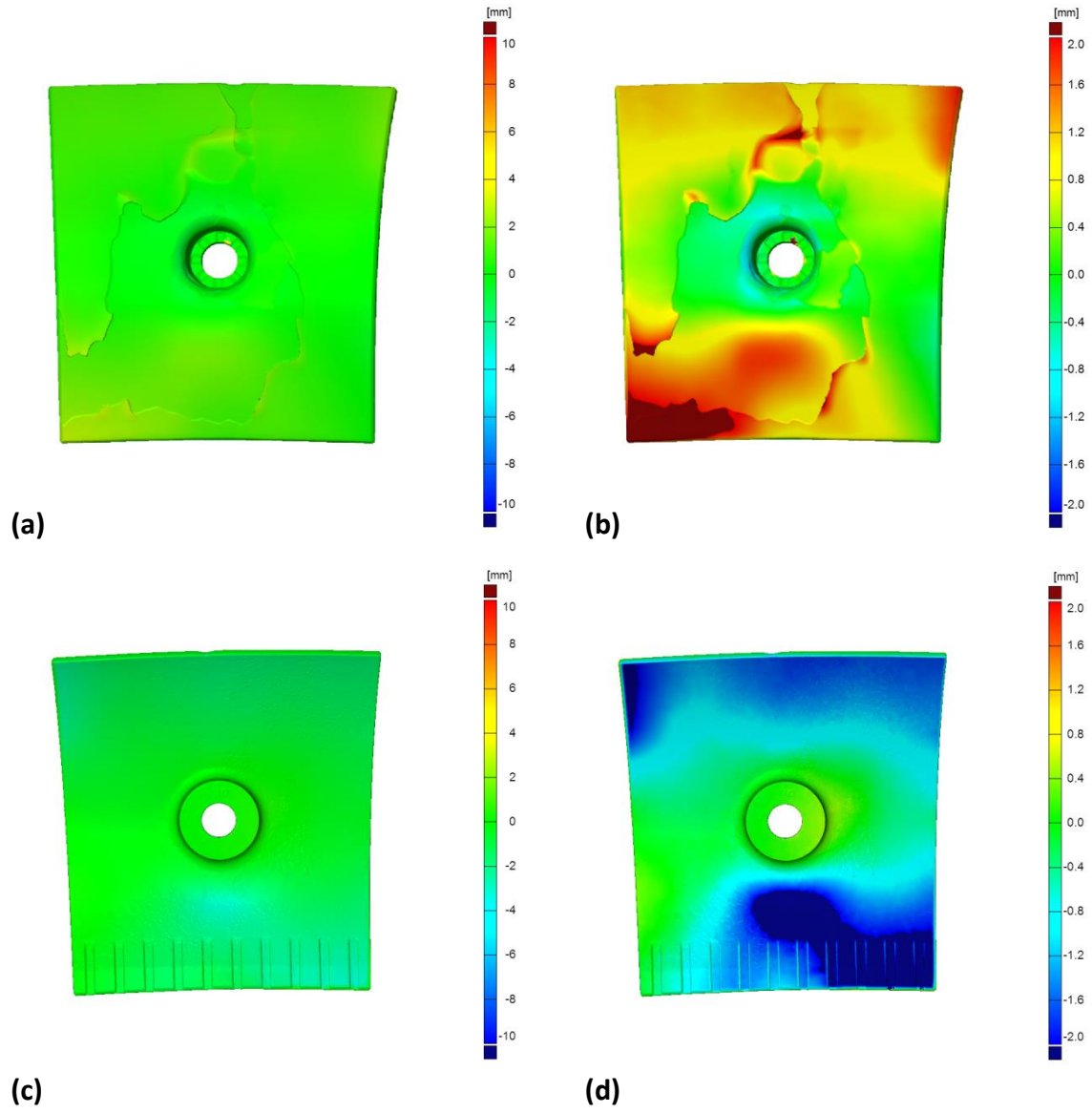

Figure 5.24 A mesh construction of front and back faces of Tile 137, using two scales +/- 2 mm and +/- 10 mm.

A mesh was reconstructed for Tile 138 as shown in Figure 5.25. Significant distortion of the substrate appears to be present within this tile. The back of the tile shows the location of greatest distortion along the edge where the cooling channels are present. The distortion map with a +/- 2 mm scale, Figure 5.25d, shows that the tile has distorted greater than 2 mm for the majority of the tile away from the centre. The tile is mounted to the engine casing by a single bolt through the centre of the tile. This region of the tile is, therefore, unlikely to show any distortion as it is fixed to the casing. From Figure 5.25c it appears that the bottom edge of the tile has distorted by ~6-8 mm. The edge along which cooling channels are present appears to show the greatest distortion. Some small tears also appear along the edges of the tile, as shown in Figures 5.25a and c.

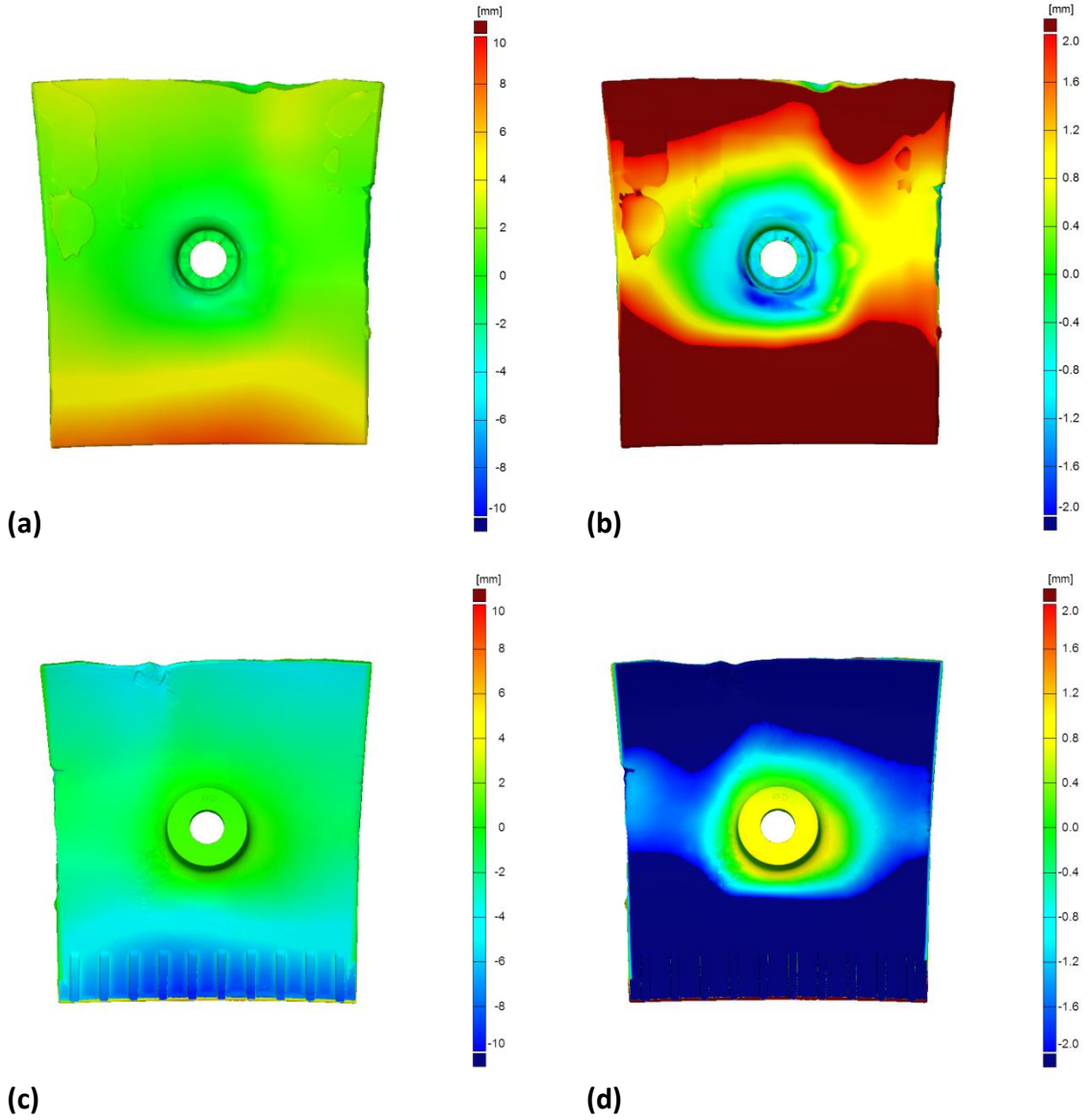

Figure 5.25 A mesh construction of front and back faces of Tile 138, using two scales +/- 2 mm and +/- 10 mm.

The mesh construction of Tile 139 is shown in Figure 5.26 and shows how this tile had distorted the most. Figure 5.26d shows the majority of the tile, excluding the centre mounting section which is fixed in place, has distorted by more than 2 mm. When studying Figure 5.26c it can be seen from the back of the tile that the bottom edge has distorted by approximately 12 mm. Tearing of the substrate of the tile is evident in the bottom right corner, and is thought to be due to overheating. In Figure 5.26a it can be seen that large areas of the TBC have spalled and the remaining TBC is only present in the top left and top right corners. This tile shows signs of severe failure and excessive overheating and degradation of the coating system and substrate.

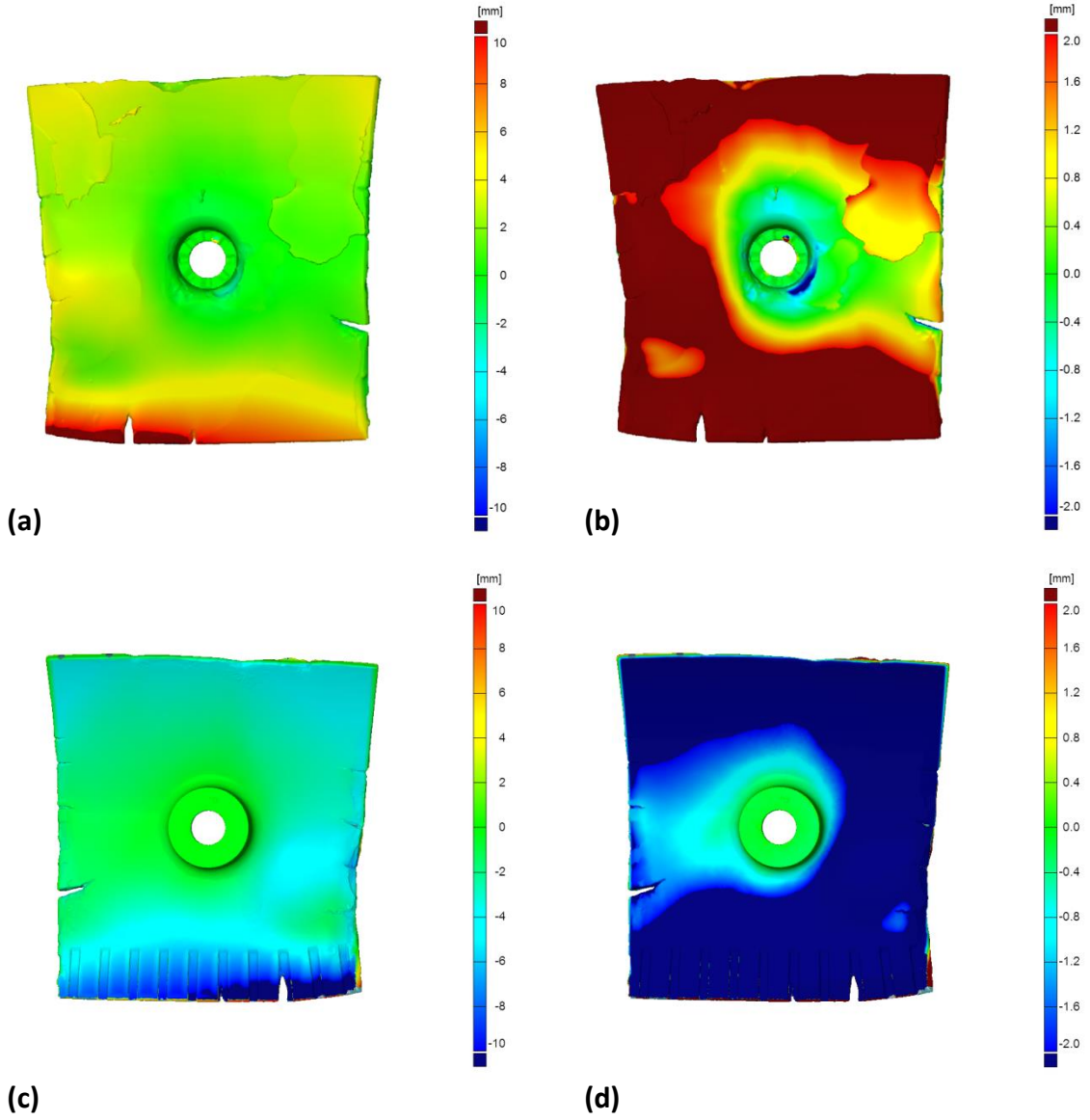

Figure 5.26 A mesh construction of front and back faces of Tile 139, using two scales +/- 2 mm and +/- 10 mm.

Tile 140 shows significantly less distortion than Tiles 138 and 139. Figure 5.27c shows how there did not appear to be any regions of the tile that have distorted greater than 10 mm. Figure 5.27d shows that there are areas of the tile with a distortion greater than 2 mm; on the back face of the tile, in the top right corner and along the edge where cooling channels are present. Figure 5.27a shows that the TBC has spalled within the centre of the tile around the bolt hole; this appears to be a consistent area of TBC failure across the set of tiles characterised. The tiles coated with a SC2453 coating also showed small areas of TBC failure in this region. When comparing Figure 5.23 with 5.26 it can be seen that there is a difference in coating performance, and comparing Figures 5.25, 26, 27, the location of the tiles within the engine appears to affect the performance of identical MCrAlY coatings.

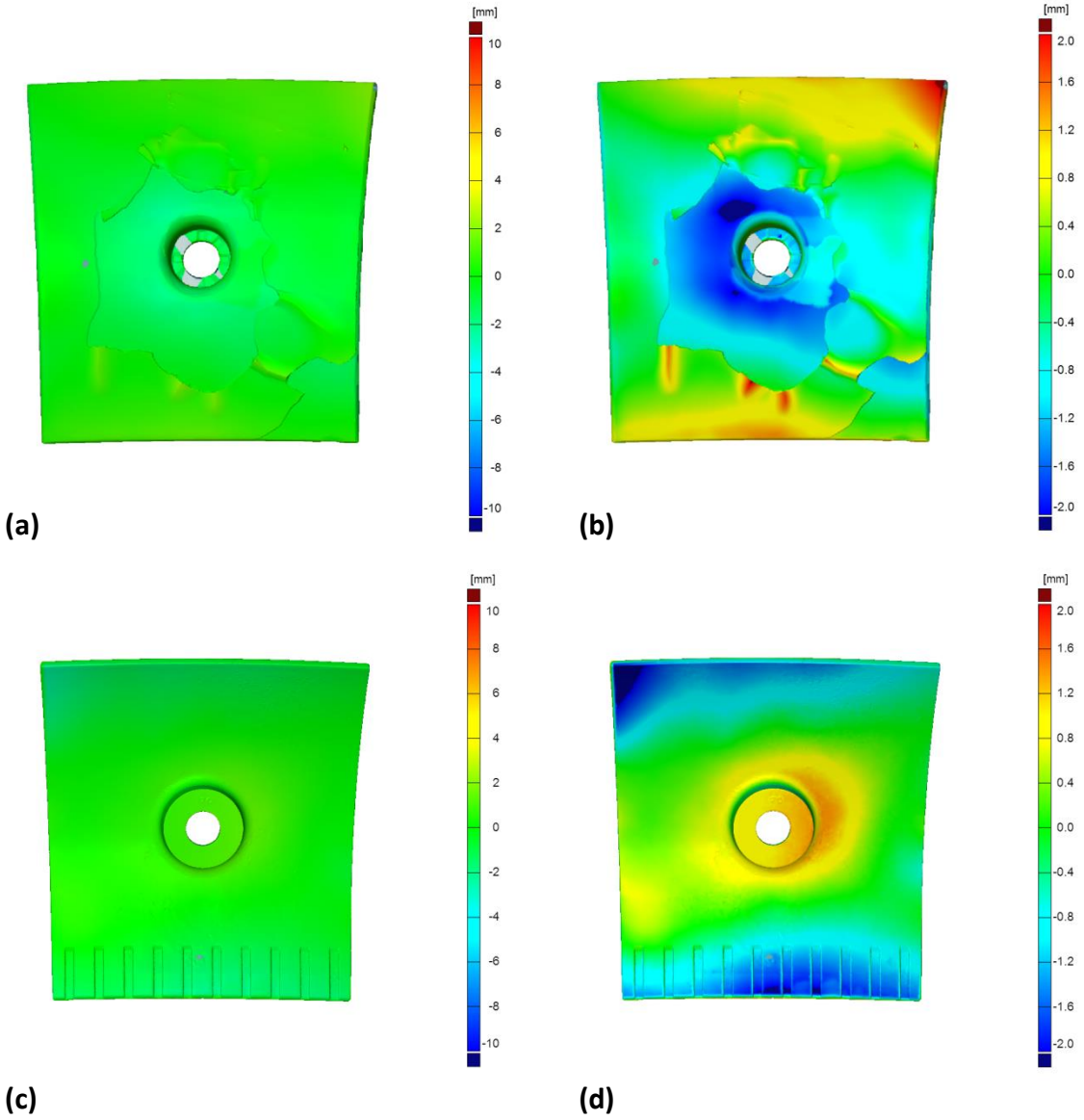

Figure 5.27 A mesh construction of the front and back faces of Tile 140, using two scales +/- 2 mm and +/- 10 mm. The maximum spallation is shown in red in (b), which occurs at the corner of the tile.

5.4.2 Measurements of the Spallation of the TBC

Spallation of the TBC on each tile was quantified before microstructural characterisation. Measurements were carried out using image analysis software to calculate an area percentage of TBC loss, a spallation map is shown in Figure 5.28. The tiles with a SC2453 coating applied were also characterised to enable a comparison with a coating system that is routinely used during service. The SC2453 coating showed small amounts of TBC spallation in the centre of the tile. The tile is mounted in this region and is the area of the tile with the greatest geometrical complexity and the TBC was found to have spalled in this region on all tiles. One reason for this could be that during the TBC application process complex geometries often have a coating applied that is of a greater thickness than specified as for a complex component multiple passes of the spray gun are required. Figure 5.19 shows how the TBC layer applied was 400 µm, whereas the specified thickness was 250 µm. This can cause micro-cracks within the TBC and in severe cases coating delamination if adhesion is poor (57). Table 5.6 shows the area fraction of TBC loss for each of the tiles. Tiles 138 and 139 show a significant increase in spallation compared to the other tiles characterised.

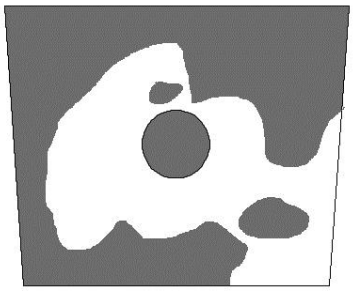

Figure 5.28 Spallation map of Tile 140, the image was constructed and analysed using image analysis software. The white area shows a region of TBC loss, an isolated region can be seen in the bottom right-hand corner.

Table 5.6 The table shows the measured spallation of the TBC after service exposure for 5004 hours.

Tile Number	TBC Loss %	Rank Order	Tile Number	TBC Loss %
134	2.70	**6**	**134**	2.70
137	44.17	**5**	**145**	3.54
138	87.50	**4**	**140**	39.92
139	81.95	**3**	**137**	44.17
140	39.92	**2**	**139**	81.95
145	3.54	**1**	**138**	87.50

5.4.3 Microstructural Evolution of Combustion Chamber Heat Shield Tiles

After studying the ex-service tiles using macro analysis techniques, the tiles were then sectioned and the microstructure characterised. Each tile was sectioned to allow for characterisation in a comparable region, which is highlighted in Figure 5.29. The reason for taking a sample from this section was to allow for a study of the microstructure when the protective TBC coating is still in place on as many of the tiles as possible. The MCrAlY microstructure in regions where the TBC had spalled is likely to be exposed to greater temperatures without the TBC layer in place. In the previous chapter, the application of the TBC was shown to be significant in the microstructural evolution of an MCrAlY coating system after isothermal ageing. The focus of the work in this section was to characterise the microstructure of the MCrAlY layer within an MCrAlY + TBC coating system on ex-service components and compare and contrast the performance with isothermally aged material.

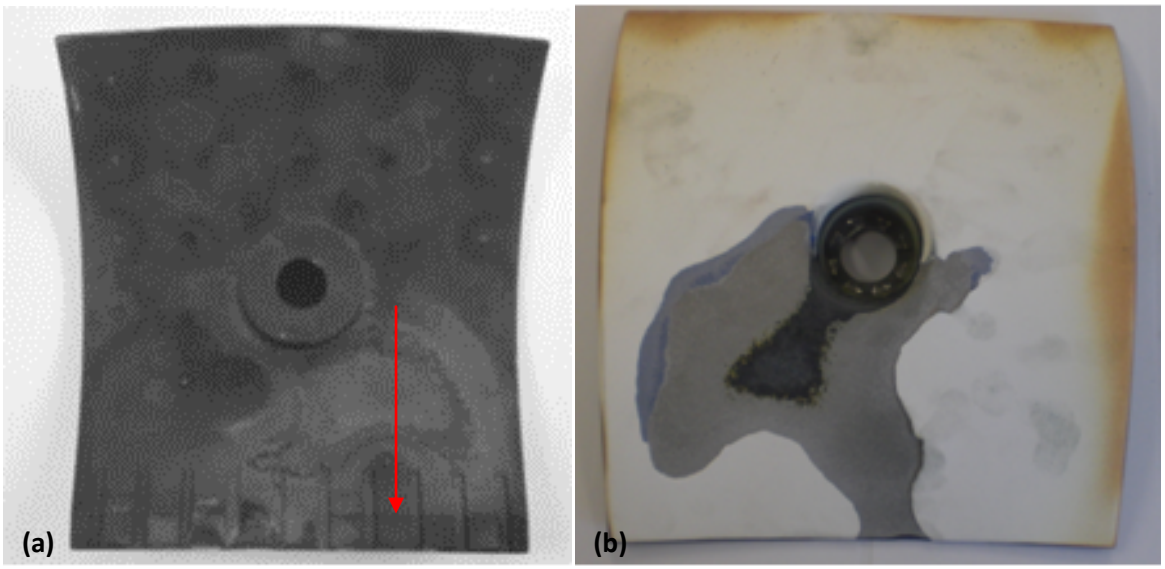

Figure 5.29 Photographs of the front (a) and back (b) of Tile 136 after service. The location of the sample studied is shown. The spallation of the TBC can be observed in the front image (b), a region of oxide can be observed on the left hand side of the tile, and a blue oxide product suggests a Ni rich oxide layer.

5.4.4 Study of the Thermally Grown Oxide Scale

The oxide scale that forms at the MCrAlY/TBC interface was characterised on all five tiles. Within previous sections it was discussed how the alumina thickness changes as the isothermal ageing conditions change. Within this section the specific temperature conditions for the tiles are unknown. Figure 5.30 shows back-scatter images collected for each tile focusing on the alumina scale. The same microscope settings and magnification were used to enable a comparison across the set of tiles. In Figure 5.30a, Tile 136 has an oxide layer that appears to be of uniform thickness. In Figure 5.30b Tile 137 appears to have a thermally grown oxide scale that is less uniform than Tile 136, however, there also appears to be a greater surface roughness of the MCrAlY layer.

The TBC layer applied to Tile 138 had spalled in 87.5 % of the area applied during service and the oxide layer that had formed also shows signs of spallation in Figure 5.30c. It is possible that the spallation of the TBC occurred in this region during the cool down after the engine was shutdown. However, as the tile appears to have an oxide thickness greater than Tiles 136 and 137 it is more likely that the TBC failed during service and the resulting oxide was formed. Where the oxide scale was still present at the interface, a back-scatter image was collected, as shown in Figure 5.30c, and within this figure a small region of the TBC is visible attached to the oxide scale. In Figure 5.30d, Tile 139 shows a similar oxide thickness to the oxide present on Tile 138. The TBC has also spalled on this tile, however, a large region of oxide scale was still in place on this tile suggesting that the TBC failed at the TBC/oxide interface. In Figure 5.30d small regions of what appeared to be a thin outer oxide layer had spalled from the main oxide layer. Chemical analysis, in section 5.4.6, of this area was used to determine if the spalled area was TBC or an oxide rich in Cr, Co, Ni which was routinely present on the samples characterised in Chapter 4. In Figure 5.30e, Tile 140 appears to have an oxide thickness consistent with Tiles 136 and 137. The TBC is also still present on this tile. Taking into account the distortion results in section 5.4.1 and the spallation results in 5.4.2, it can be seen that there is a correlation between the loss of TBC and the oxide thickness forming. Measuring the thickness of the oxide and studying the chemistry will give a quantitative evaluation of this relationship. Within the isothermally aged samples, the oxides forming after ageing were Al rich, whereas the oxides forming on tiles without a TBC layer present appear to be very thick and may not be only alumina scales, therefore characterisation of the chemistry of the oxide was used to reveal if any additional oxides were present.

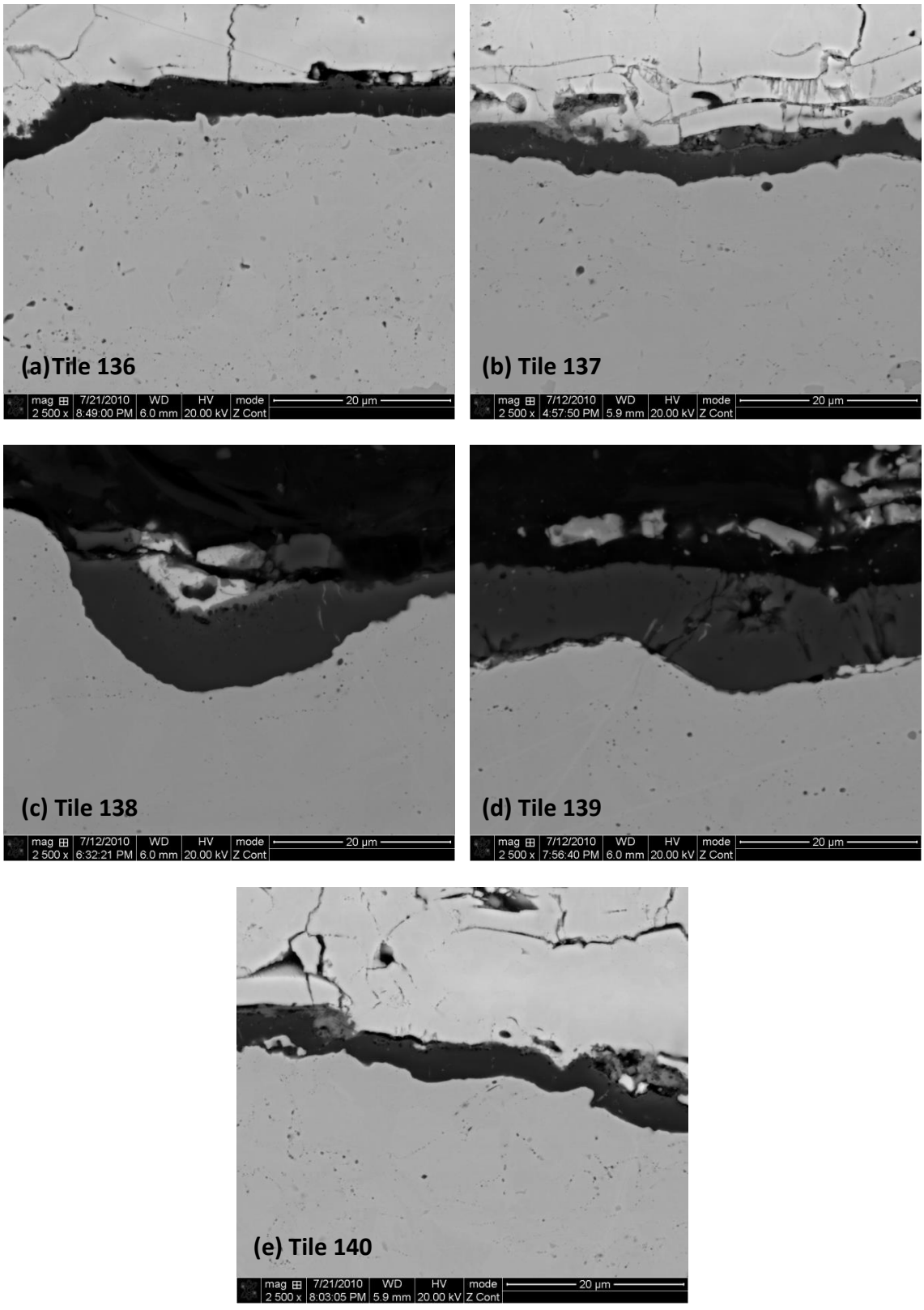

Figure 5.30 Back-scatter images of Tiles 136, 137, 138, 139, and 140 showing the oxide scale at the MCrAlY / TBC interface. All images were collected at the same magnification using the same microscope settings.

5.4.5 Study of the Thickness of the Thermally Grown Oxide Scale

The thickness of the oxide product that formed during service that was highlighted in Figure 5.30 was measured using image analysis software. The aim was to characterise the oxide growth during service in different positions within the combustion chamber. Comparisons could then be made with the isothermally aged samples studied that had the same coating composition and coating thickness applied. Figure 5.31 shows that the location of the tile within the engine affected the thickness of the oxide scale forming during service. In Chapter 4 it was shown how the oxide thickness can be critical in the performance of the coating system. The result in Figure 5.31 could represent a variation around the engine in operating conditions. A mean oxide thickness is plotted, and it can be seen that the five tiles appear to be in two distinct groups, Tiles 136, 137 and 140 show very similar oxide thickness measurements; this was seen previously in Figure 5.30. Tiles 138 and 139 showed significantly thicker scales in Figure 5.30.

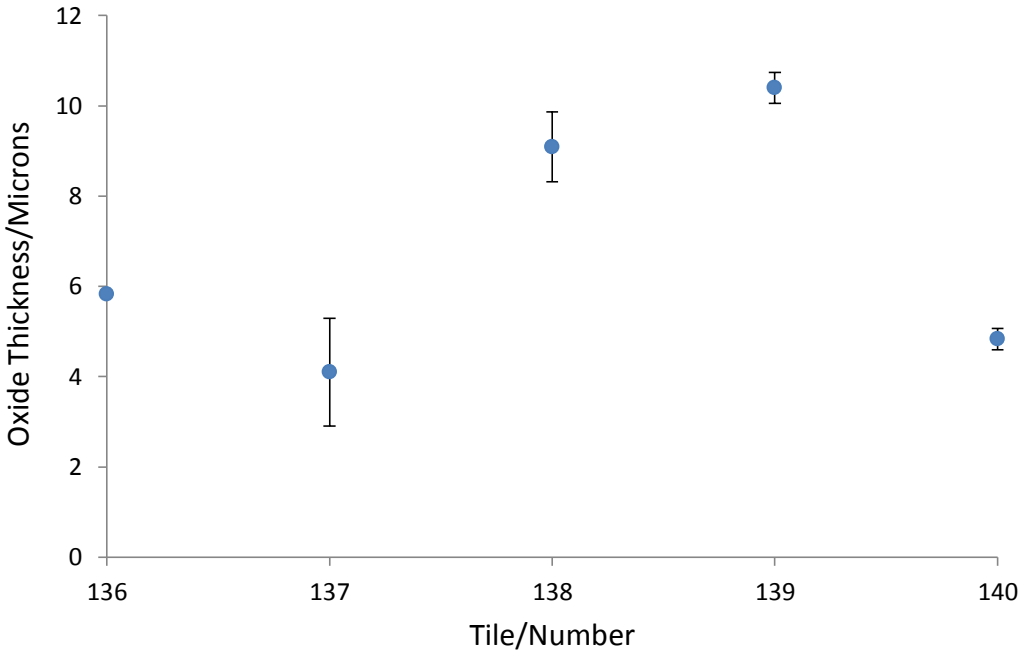

Figure 5.31 A graph showing the measured thickness and the standard deviation of the oxide scale across the heat shield tiles characterised. The measurements were made using image analysis software and a mean measurement is plotted.

5.4.6 Study of the Chemistry of the Thermally Grown Oxide Scale

After measuring the thickness of the oxide scale, the chemistry of the oxide forming after service exposure was studied. This was carried out using EDS mapping analysis. EDS maps were collected for all tiles; it was found that the results were grouped into two categories. The tiles that had the thinner oxide scale and the TBC layer present, which were Tiles 136, 137 and 140 showed very similar oxide chemistry results. This consisted of an Al rich layer forming underneath the TBC; as shown in Figure 5.32b and c for Tile 136. Figure 5.32b shows the area rich in oxygen suggesting an oxide scale and 5.32c shows the area rich in Al; it can be seen that the two regions are identical, suggesting the scale is alumina. Notably, Figures 5.32d, e and f do not show regions of high concentrations of the elements Cr, Co and Ni within the oxide scale present on Tile 136. This was also the case for Tiles 137 and 140.

EDS analysis of Tiles 136, 137 and 140 suggested an oxide that was only Al rich. The EDS analysis of Tile 139 showed there to be an Al oxide layer that formed the bulk of the oxide scale formed. However, at the outer edge of the oxide layer forming on Tile 139 there appears to be a spalled region of Cr, Co and Ni rich oxide, which can be seen in Figure 5.33d, e and f. In section 5.4.5 only the dense dark region within the back-scatter micrographs was measured, as back-scatter imaging indicates chemical differences based on contrast the Al rich scale could be measured.

In Chapter 4 when no additional TBC layer was applied oxides rich in Cr, Co and Ni were also present. This suggests that the TBC has spalled during service and not during the engine cooling during the shutdown, as the component would need to be exposed at temperature without a TBC layer present for the oxides rich in Cr, Co and Ni to form. It is likely that the thin outer region of the oxide layer in Figure 5.33spalled during the hot mounting process as it is present within the mount. On Tile 138 the TBC had also spalled, however, the oxide present on this sample was only Al rich. The result of this is inconclusive as Figure 5.30c shows that there is only a small region of oxide present on the tile suggesting that both the TBC and oxide layer had spalled. The results within Chapter 4 did suggest that if no TBC layer is present the oxidation rate will increase significantly and the oxide present is likely to be rich in the elements Ni, Co and Cr depending on the exposure temperature.

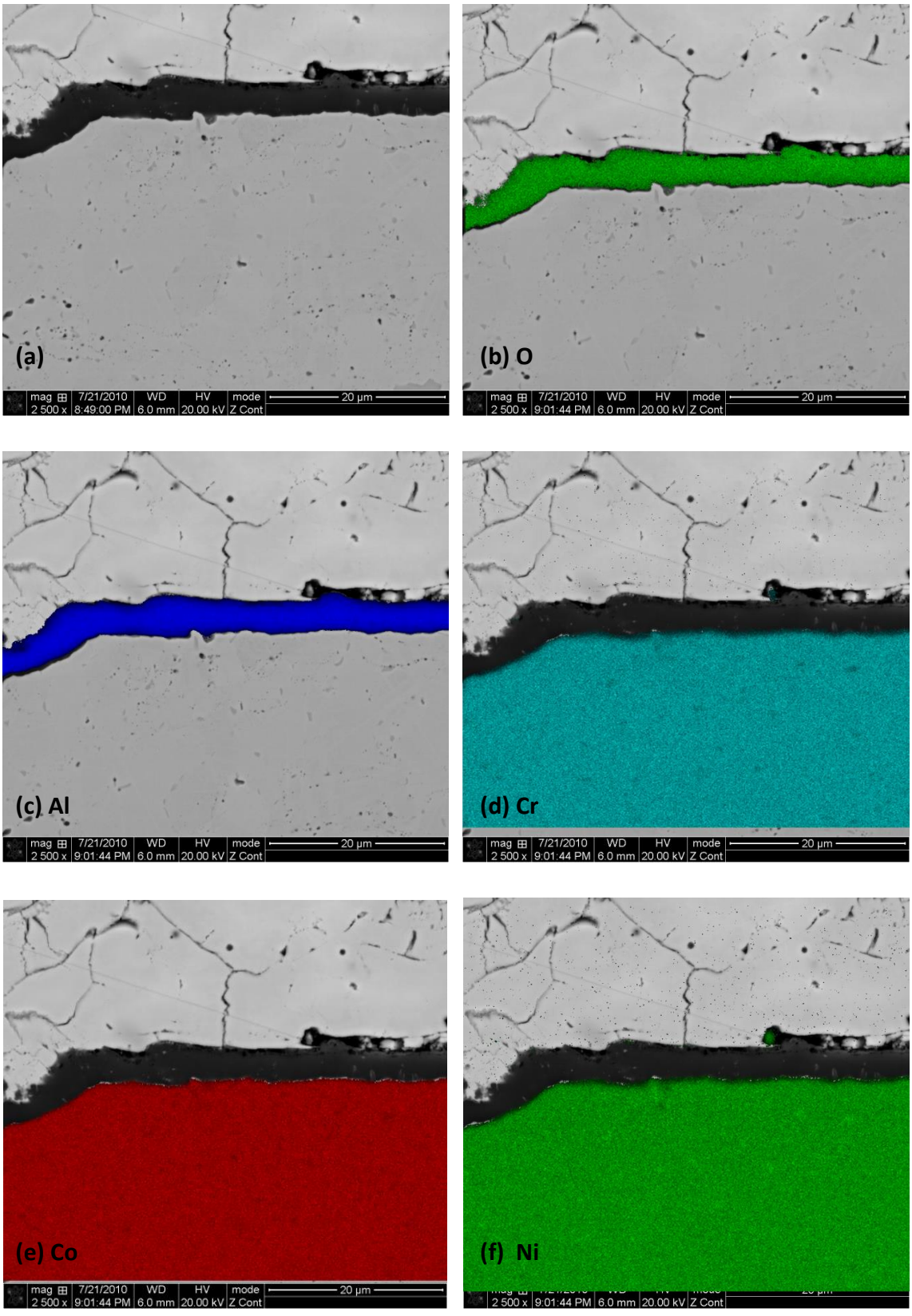

Figure 5.32 Results for EDS analysis of the chemistry of the oxide scale for Tile 136, showing elemental maps for O, Al, Cr, Co and Ni overlaid onto back-scatter electron images.

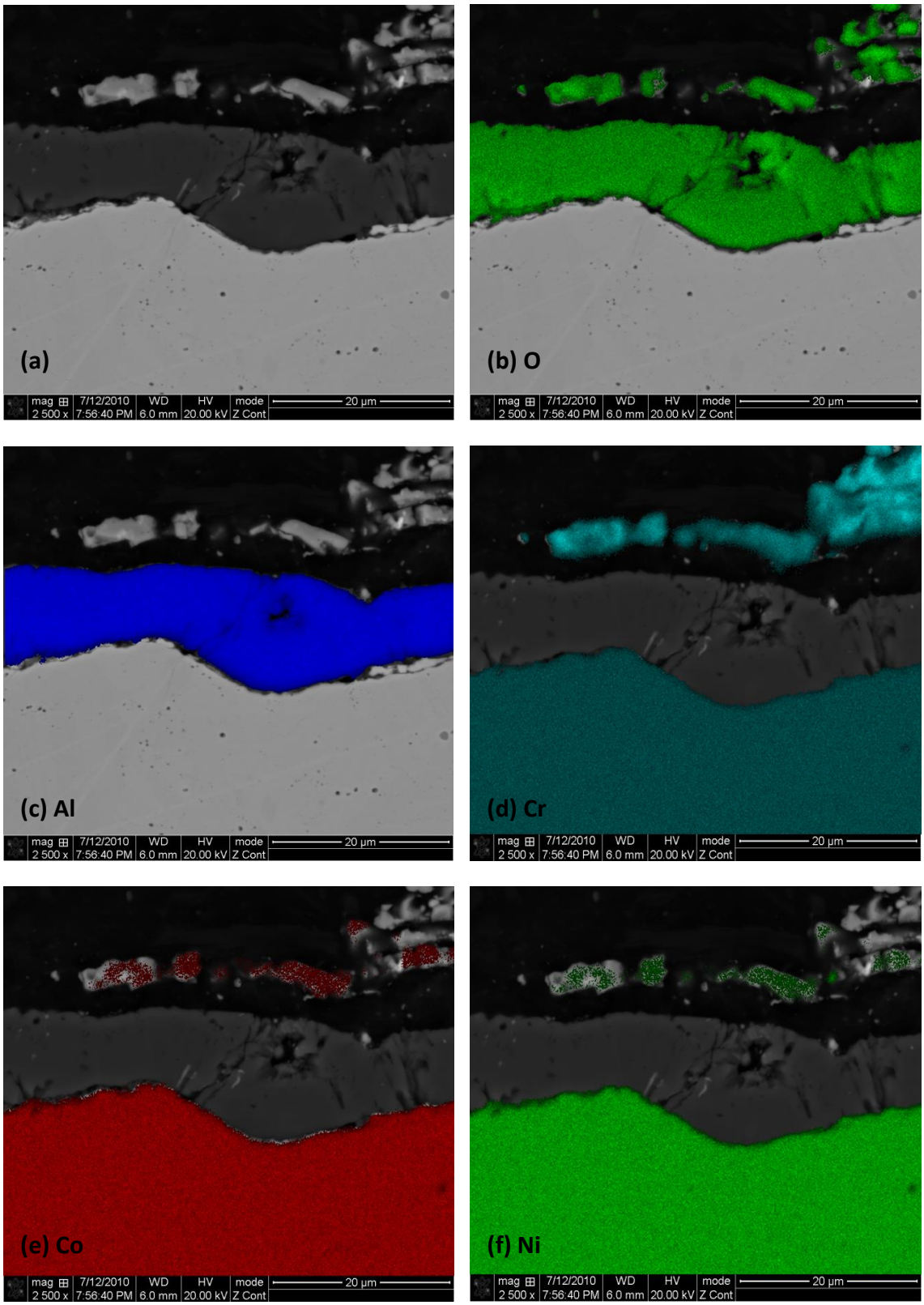

Figure 5.33 The EDS map results for analysis of the chemistry of the oxide scale for Tile 139, showing the elemental maps for O, Al, Cr, Co and Ni.

5.4.7 Quantitative Study of Beta Phase

After studying the oxide that had formed during service, the beta phase was also characterised. Beta was identified by EBSD and EDS analysis as shown in section 5.3. Back-scatter imaging was used as the brightness of each phase within the images is a direct result of the phase chemistry. Therefore, within the MCrAlY coating it is possible to distinguish between the beta and gamma phases using back-scatter imaging. Figure 5.35a shows the depletion of the beta within Tile 136 where it can be seen that there is depletion at the TBC/MCrAlY interface and also at the MCrAlY/substrate interface. In this work in addition to outer beta depletion characterisation the inner linear beta depletion has been characterised. Previously isothermally aged material had shown significant surface roughness, and when measuring the outer beta depletion the surface roughness of the MCrAlY was found to have an impact on the linear measurement of beta depletion. A cross-section image from a region with significant surface roughness will introduce localised measurement errors as 2D image analysis is used to characterise the linear beta depletion. Within this work, the MCrAlY layer applied to the tiles in an unaged condition had undulations with ~20 µm height, as shown in Figure 5.34. A study by Gil et al. (43) observed that for an as-sprayed MCrAlY the surface roughness was R_a = 10 µm but localised undulations measured up to 80 µm. The characterisation of isothermally aged material in section 5.3.2 shows how after 9 months ageing at 850 and 900^{o}C the maximum linear beta depletion is 19 µm and therefore in a location with undulations of 20 µm this value could be increased significantly. Therefore, in this work in addition the inner linear beta depletion was also studied as a comparison.

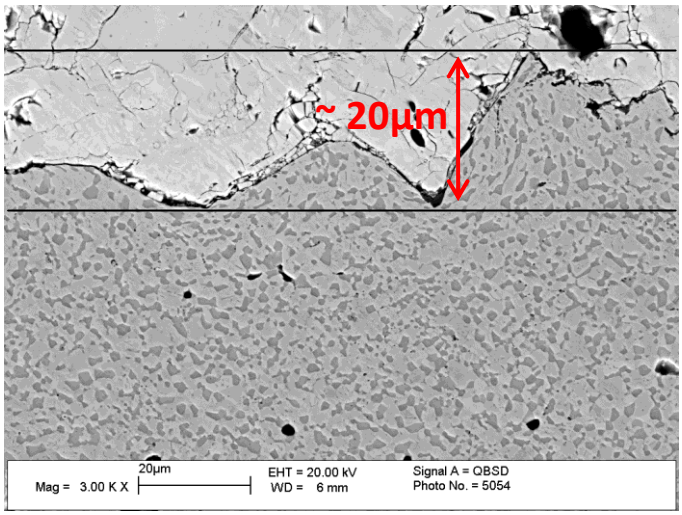

Figure 5.34 A back-scatter micrograph showing the surface roughness in the as-sprayed condition of the MCrAlY layer applied to the heat shield tiles by HVOF, a 20 µm undulation can be observed.

Figure 5.35b shows the extent of the beta depletion and the inner and outer regions of the MCrAlY coating in Tile 137. The depletion does appear to be greater in both regions for Tile 136 compared to Tile 137. In Figure 5.35c there is no beta remaining within the MCrAlY coating for Tile 138. The TBC had also spalled during service on the region characterised within this tile. Tile 139, shown in Figure 5.35d also showed no sign of any beta remaining within the MCrAlY coating. The TBC layer applied to this tile had also spalled during service. The depletion of the beta phase within Tile 140 can be seen in Figure 5.35e, and appeared to be very similar to the depletion within Tile 136 in Figure 5.35a.

Measurements were made for the two beta depletion zones, using the same procedure as described for measuring the oxide thickness. The images collected for beta depletion were also in the same location as the images used for characterising the oxide. The inner beta depletion was defined as the region up to the MCrAlY/substrate interface. It was shown in section 5.3.2 how the interface can be defined by EDS matrix scans. The outer depletion was measured from the outer edge of the MCrAlY to the edge of the beta phase. In Figure 5.36 the outer depletion zone measurements are plotted. Tiles 138 and 139 had no beta remaining within the MCrAlY coating. Figure 5.37 shows the inner beta depletion measurements. Both sets of data for inner and outer depletion show similarities, it can be seen that Tile 137 has an inner depletion width of 22.0 µm and an outer beta depletion width of 22.5 µm. The inner and outer beta depletion measurements for Tiles 136 and 140 are similar; however, the outer depletion zone appears to be of a slightly greater thickness for both tiles.

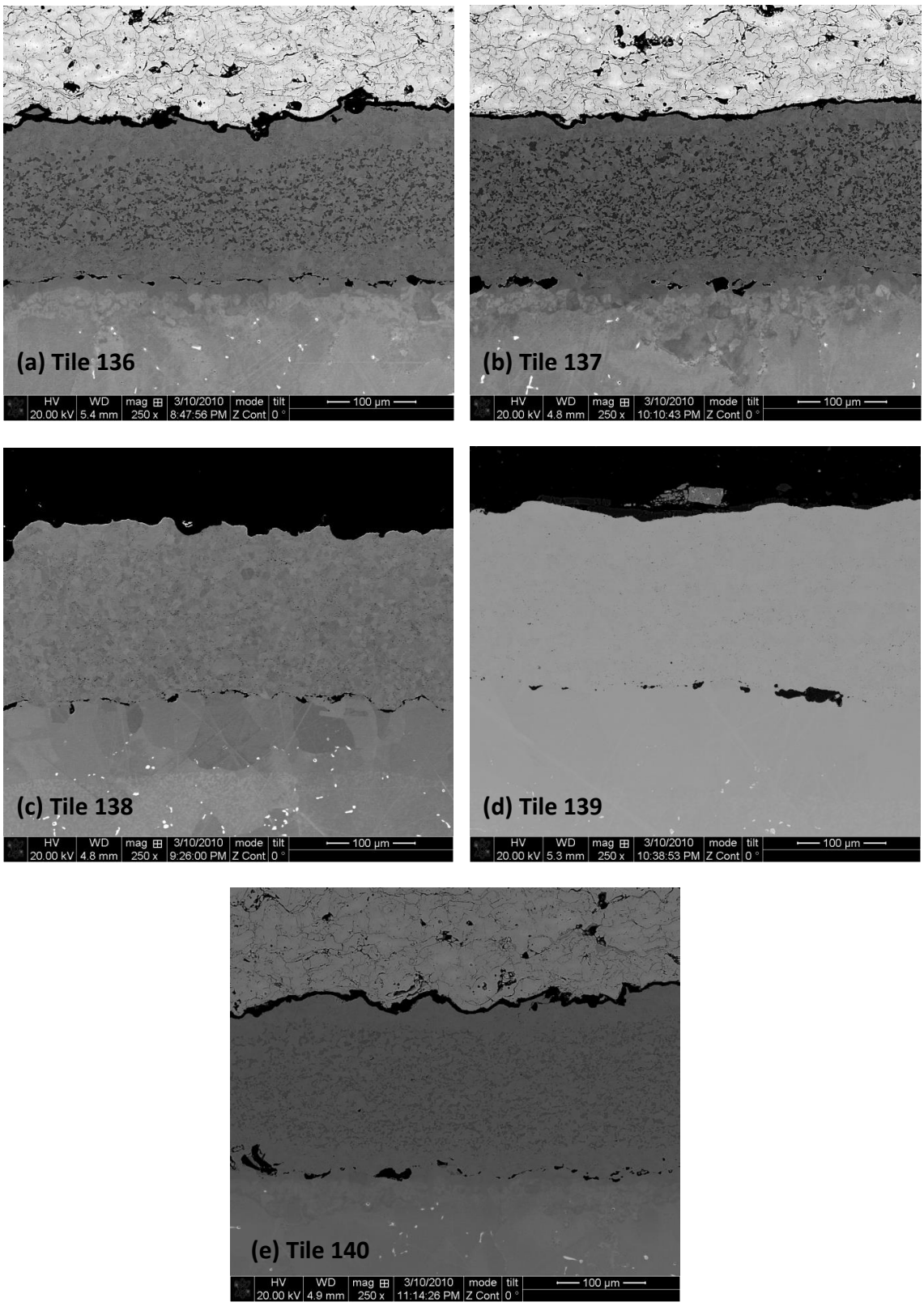

Figure 5.35 A series of back-scatter images for Tiles 136, 137, 138, 139 and 140. Each image was collected at the same magnification and using the same microscope settings to enable a direct comparison between tiles.

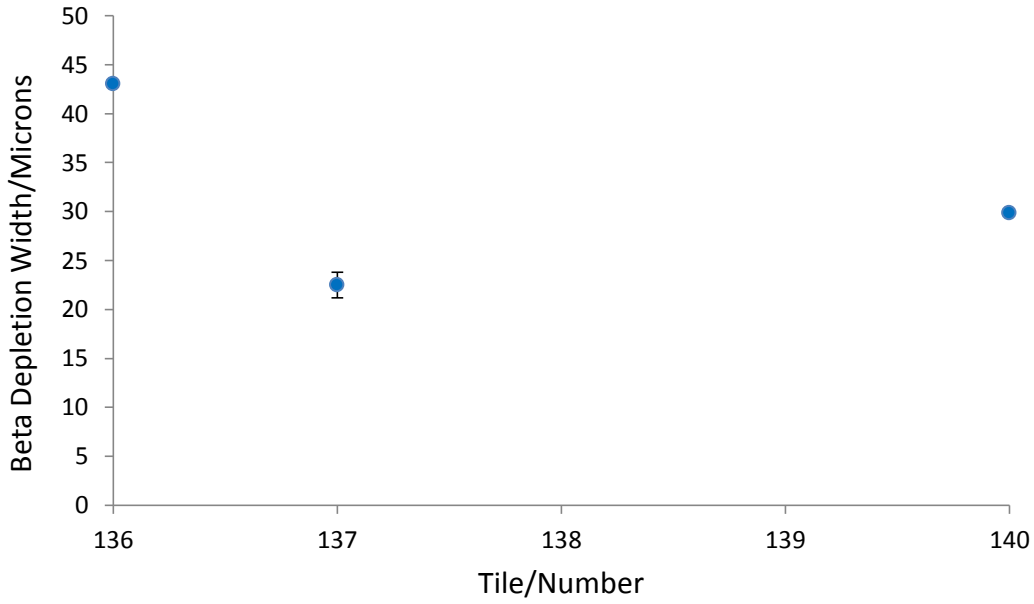

Figure 5.36 The graph shows the results for the width of the outer beta depletion zone and the standard deviation of the ex-service Tiles 136, 137, 138, 139 and 140.

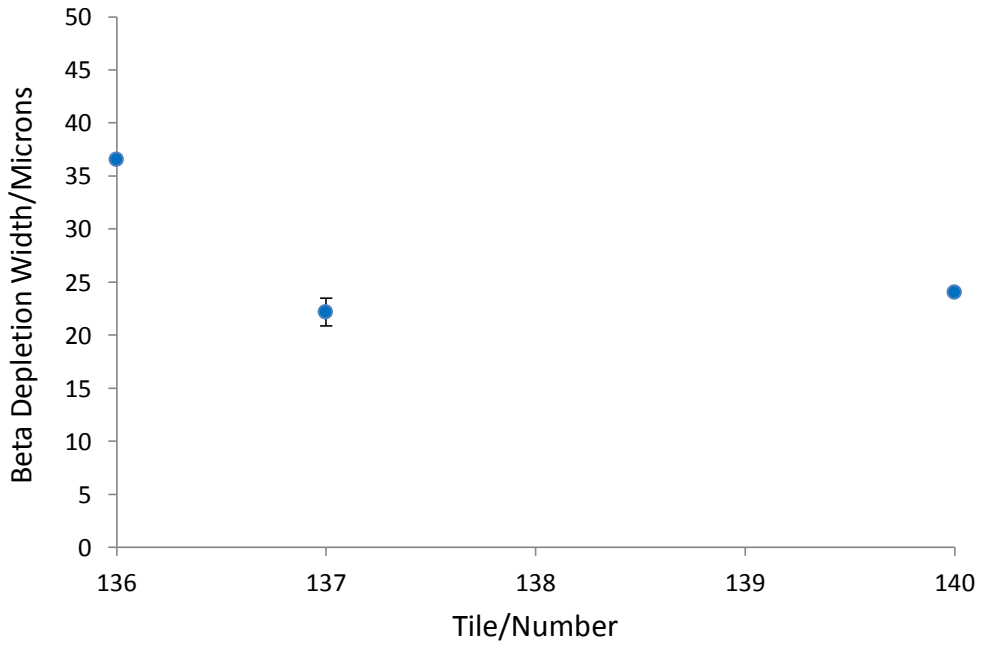

Figure 5.37 The graph shows the results for the width of the inner beta depletion zone and the standard deviation of the ex-service Tiles 136, 137, 138, 139 and 140.

5.5 Comparison of the Microstructures of Ex-Service Tiles and Isothermally Aged Tile Samples with Microstructural Modelling Techniques

Measurements for thermally grown alumina thickness and beta depletion within isothermally aged and ex-service material can be compared. Approximate service temperature estimations have been derived based on the results from the isothermal characterisation. Refined temperature predictions have been carried out using both oxidation and diffusion based thermodynamic and kinetic models, using alumina thickness and linear beta depletion as an indicator for likely service temperature exposure.

5.5.1 Comparison between Oxidation Model and Characterisation

Comparing the results from an oxidation model with experimental results in Chapter 4 showed how the model was representative of the actual alumina layer forming when a TBC layer was applied. It has been used in this chapter to compare the alumina thickness forming on isothermal and ex-service components. The tiles were in service for 5004 hours and the alumina thickness prediction after this time is shown in Figure 5.38. The alumina thickness prediction after 6 months isothermal ageing is also shown, which is the isothermal ageing time for comparable samples. As the ex-service tiles have an unknown exposure temperature the graph for 5004 hours has been used to predict the temperature at the MCrAlY interface during service using the measured alumina thickness to indicate exposure temperature.

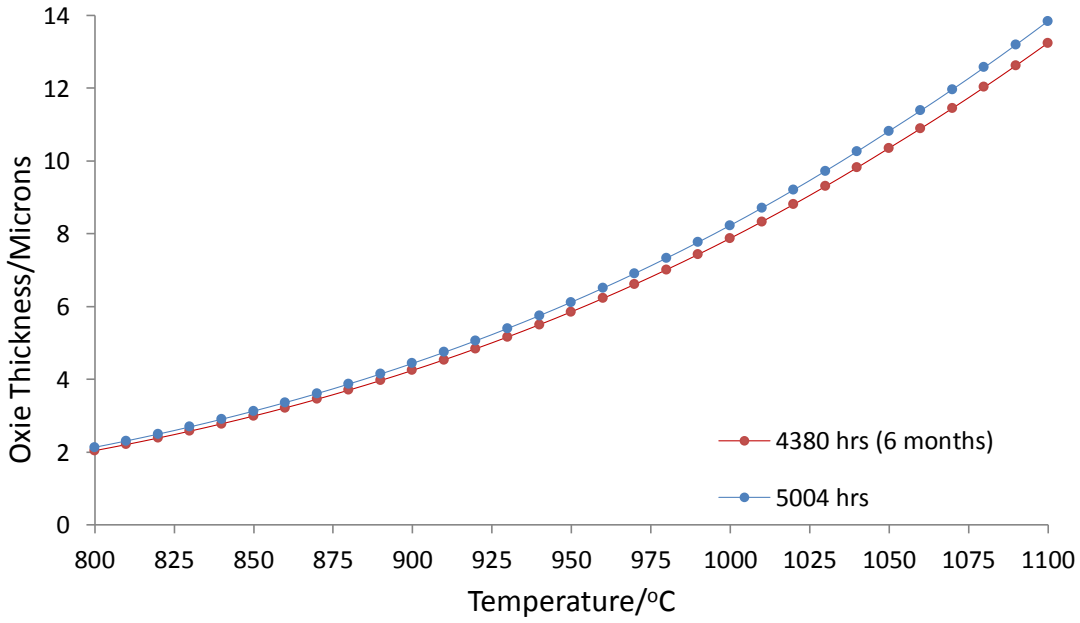

Figure 5.38 A prediction of the thickness of the alumina scale as a function of temperature after 4380 (6 months) and 5004 hours (service exposure); the oxidation equation is detailed in Equation 4.1.

Table 5.7 shows the predicted temperature based on TGO measurements. It can be seen how the thickness of the alumina on Tiles 136, 137 and 140 suggests a temperature range of 900 – 940^{o}C. However, Tile 138 and 139 have TGO scales present that are consistent with elevated exposure temperatures and in this case they are predicted to be 1015 and 1040^{o}C respectively.

It is known that the hot gas entry temperature to the turbine is ~1350^{o}C and the peak flame temperature is ~1800^{o}C (48). The gas temperature in contact with the tile is assumed to be in the region of the gas entry temperature. As the TBC layer had spalled during service on Tiles 138 and 139 the MCrAlY interface is likely to have been exposed to a greater temperature than the remaining tiles as the thermal protection from the TBC layer is no longer provided. The TBC has been shown to provide a thermal gradient of ~120^{o}C between the edge of the TBC layer and the TBC/MCrAlY interface in Table 5.5.

The cause for TBC spallation could be due to Tiles 138 and 139 having been exposed to a higher temperature within the engine which resulted in the onset of coating failure. It must be noted that the TBC may have actually spalled during the engine shutdowns due to the thermal expansion mismatch when the different components of the coating system cool down. Taking into account the results for the distortion of the substrate in section 5.4.1 and the area fraction of spallation of the TBC shown in 5.4.2 it is likely that the TBC was not present during exposure at temperature which resulted in the unprotected MCrAlY interface to be exposed to the gas temperature. The location of Tiles 138 and 139 next to each other suggests that the position of the tiles within the combustion chamber has influenced the performance of the coating system; this is consistent with previous tile failings within the same engine series (47).

Table 5.7 The table highlights the measured results for the oxide thickness present on each heat shield tile and the derived temperature based on the oxidation model result in Figure 5.38.

Tile	Measured Oxide	Temperature derived from oxide thickness prediction
136	5.82 µm	940^{o}C
137	4.47 µm	900^{o}C
138	9.09 µm	1015^{o}C
139	10.4 µm	1040^{o}C
140	4.83 µm	910^{o}C

By using the oxidation model to derive a predicted exposure temperature for the ex-service tiles, a comparison could then be made with the isothermally aged sample results. It can be seen in Table 5.7 that Tile 136 had an oxide thickness that is associated with an exposure temperature of 940^{o}C based on a model prediction. A comparable isothermally aged sample was available for comparison that was aged for 4380 hours, 6 months, at 950^{o}C. While the time of exposure is of a shorter duration than service exposure it was seen for the measurement results in section 5.3.1 that the exposure temperature influences the oxidation rate to a greater degree than the time of exposure. Figure 5.39 shows the difference in predicted alumina thickness when the exposure time is increased from 4380 hours, (6 months), to the service exposure time of 5004 hours; at 850^{o}C the thickness increases by 0.19 µm, at 950^{o}C; 0.26 µm and at 1050^{o}C; 0.47 µm. Figure 5.39 shows how the oxidation model predictions compare with the actual measured values for isothermally aged samples aged at 950^{o}C for 3 – 15 months. The results show a maximum prediction error of 1.4 µm between measured and predicted oxide thickness. The measurement showing this discrepancy was for a sample aged isothermally for 15 months at 950^{o}C. The TBC had spalled during ageing for this sample and also a significant area of oxide had also spalled, therefore the measured oxide thickness on this sample should be treated with caution.

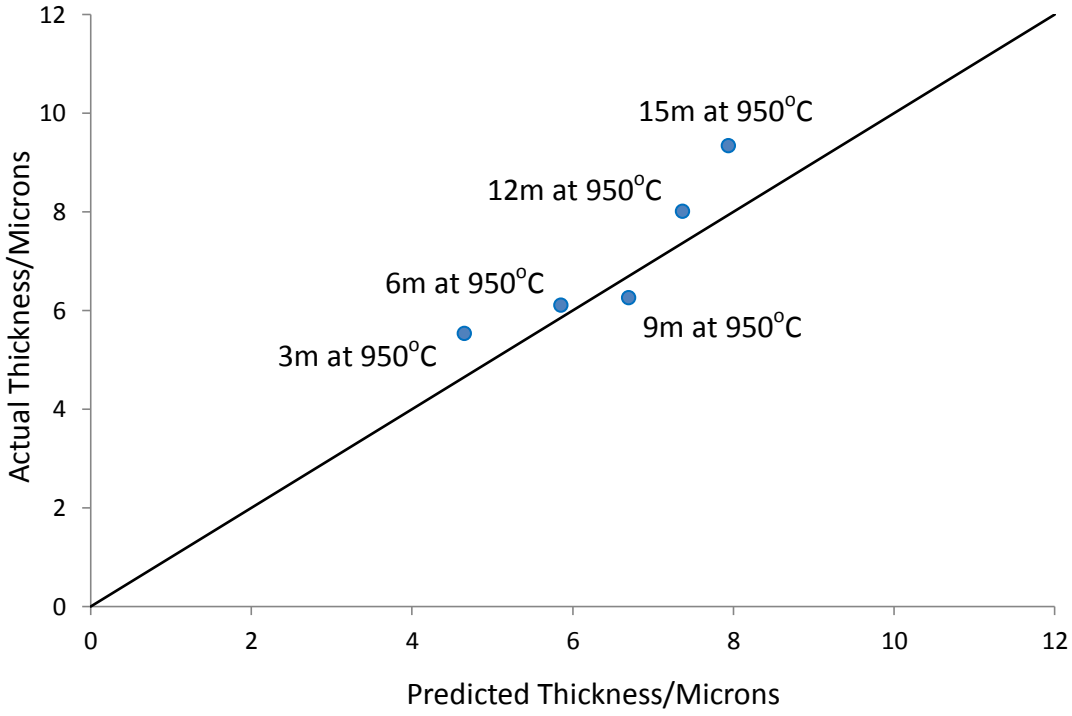

Figure 5.39 The predicted alumina thickness using an oxidation model compared to the measured oxide thickness of isothermally aged tile samples after exposure at 950^{o}C. The measured results are plotted and show the prediction after 3, 6, 9, 12 and 15 months.

Figure 5.40 shows a series of back-scatter images from the heat shield tiles and comparable isothermally aged samples. Tile 136, shown in Figure 5.40a, has an alumina scale thickness of 5.82 µm. By using the oxidation model, after 5004 hours exposure an alumina thickness of 5.7 µm suggests an exposure temperature of 940^{o}C. A comparison can be made with an isothermal sample as shown in Figure 5.40b. This sample was aged for 4380 hours (6 months) at 950^{o}C. The measured alumina thickness after exposure was 6.0 µm. The oxidation model can be used to predict the alumina thickness expected after 6 months exposure at 950^{o}C, which was 5.9 µm.

Tile 137 had a measured alumina thickness of 4.1 µm after 5004 hours exposure, and the oxidation model prediction suggested a tile exposure temperature of 900^{o}C. Figure 5.40d shows a sample aged isothermally for 6 months at 900^{o}C. The oxide thickness was measured to be 4.94 µm, this can be compared with a model prediction of 4.24 µm.

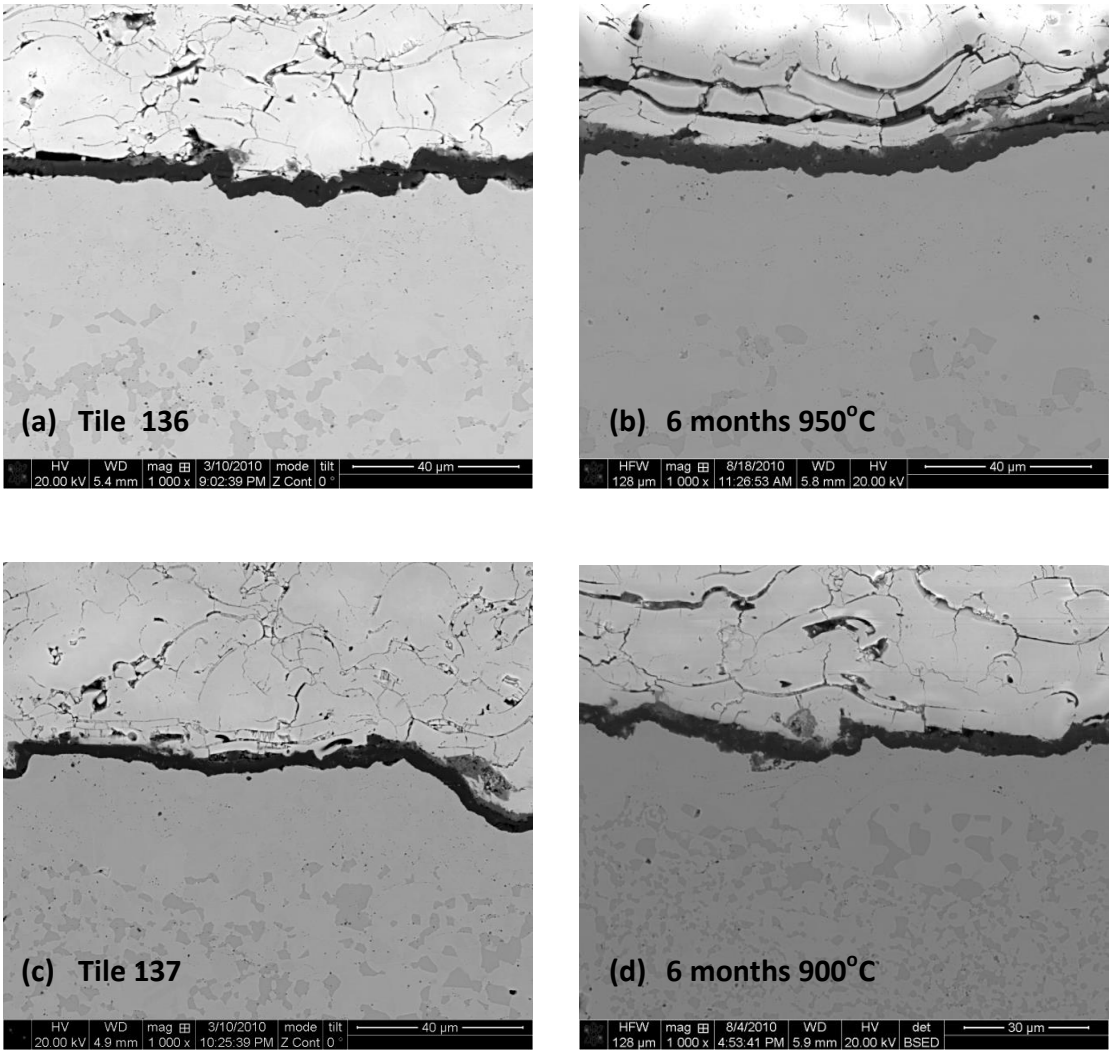

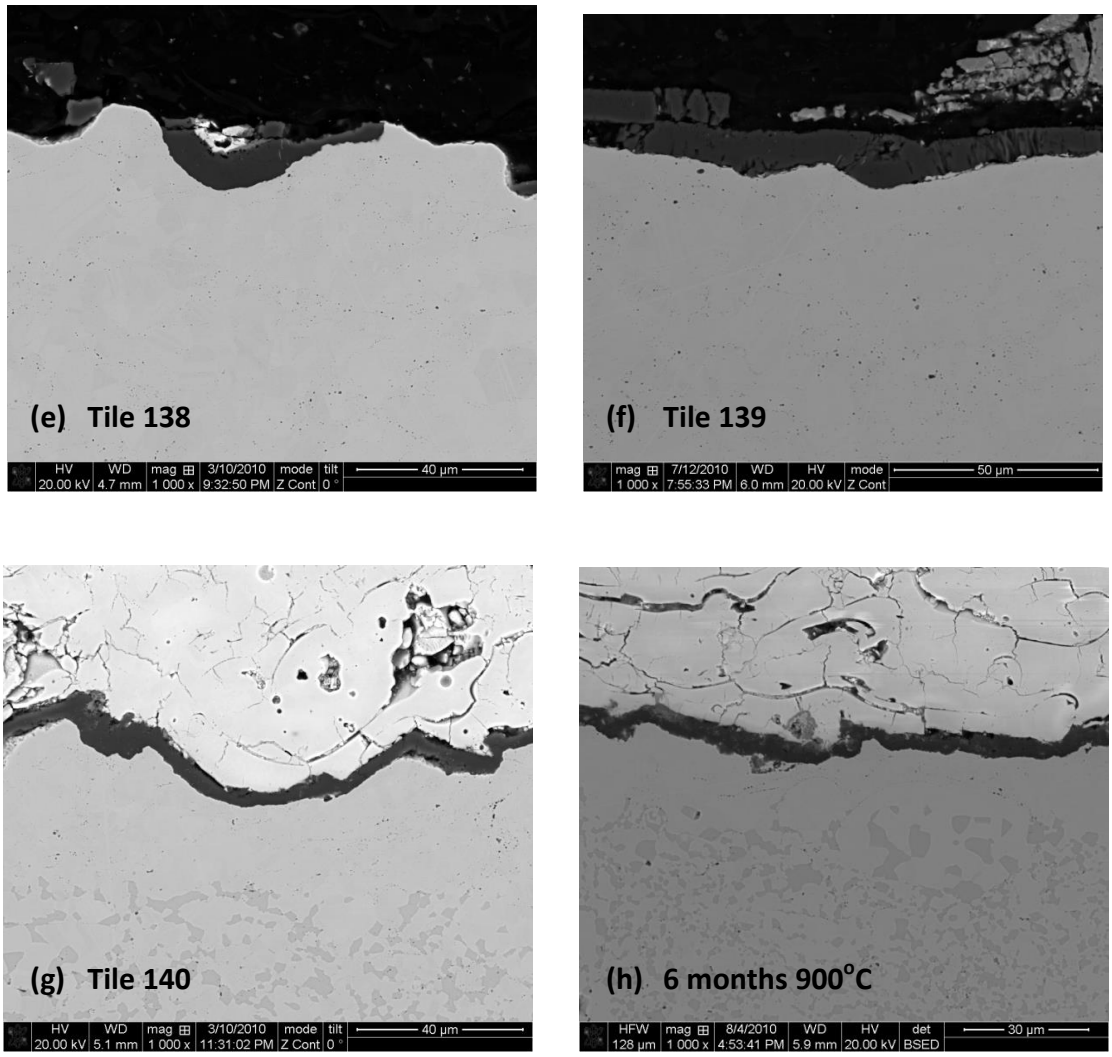

Figure 5.40 A series of back-scatter images, (a-h), collected from ex-service tiles 136, 137, 138 and 140 and comparable isothermally aged samples at specific time and temperature conditions as detailed. All images were collected at the same magnification using the same microscope settings.

Tiles 138 and 139 both had measured alumina thicknesses that were significantly greater than the other tiles characterised. On Tile 138 the oxide scale was measured to be 9.09 µm and on Tile 139, 10.4 µm. The oxidation model was used to make exposure temperature predictions for both Tiles 138 and 139 and the predicted temperatures were 1015°C and 1040°C respectively. Tile 140 had an oxide measured to be of 4.83 µm and the oxidation model predicted an exposure temperature of 910°C for such an oxide thickness to form after 5004 hours exposure. An isothermally aged sample, aged for 4380 hours at 900°C, had an oxide thickness of 4.94 µm.

5.5.2 Comparison between Predicted and Experimentally Measured Beta Depletion and Characterisation

A comparison could also be made between the extent of beta depletion within isothermally aged samples and ex-service components. The inner and outer depletion of the beta phase was previously measured within isothermal samples and the results were shown in section 5.3.2. The beta depletion within ex-service heat shield tile samples was also determined and the results were presented within section 5.4.7. In Figure 5.41a the inner beta depletion region of Tile 136 is visible. This was measured to be 36.5 µm, which can be compared to an isothermally aged sample for 6 months at 950^{o}C showing an inner beta depletion zone width of 42.0 µm, as shown in Figure 5.41b.

The inner beta depletion within Tile 137 was also studied and compared with an isothermally aged sample. Tile 137 had a measured inner beta depletion region of 22.2 µm. A comparison can be made with an isothermally aged sample that has been aged for 6 months at 900^{o}C, in which the inner beta depletion was measured to be 15.7 µm. The inner beta depletion present within tile 140 is shown in Figure 5.41e. The depletion is very similar to Tile 137 and was measured to be 24.1 µm, which similarly can be compared to a tile aged isothermally for 6 months at 900^{o}C. Tile 140 showed an inner beta depletion of 24.1 µm.

The combined thermodynamic and kinetic model, which was used to compare isothermal inner depletion measurements with model predictions in section 5.3.2 and the predictions presented in Figure 5.14, was used to enable a prediction of the beta depletion after service exposure for a range of temperatures. In Figure 5.42 a thermodynamic and kinetic model prediction is shown for an AMDRY995 coating and an IN738LC substrate system, with the amount of each phase after ageing at 900^{o}C for 5004 hours predicted. The inner depletion occurs at the coating/substrate interface, and for each simulation a 250 µm coating thickness was assumed. Therefore, the last position of a prediction of beta phase to be present can be used to derive a prediction of the width of the beta depletion zone. Section 5.3.3 detailed the method used because the same principle was applied to predict the depletion within isothermally aged material. The width of the inner beta depletion zone after 5004 hours at 900^{o}C was predicted to be 18 µm. This enables an approximate estimation of the exposure temperature experienced by Tile 137, in Figure 5.41c as the inner beta depletion was measured to be 22.2 µm. An isothermally aged tile aged for 6 months at 900^{o}C, shown in Figure 5.41d had an inner beta depletion of 15.7 µm, the model prediction for 6 months at 900^{o}C was 16 µm, showing a good correlation.

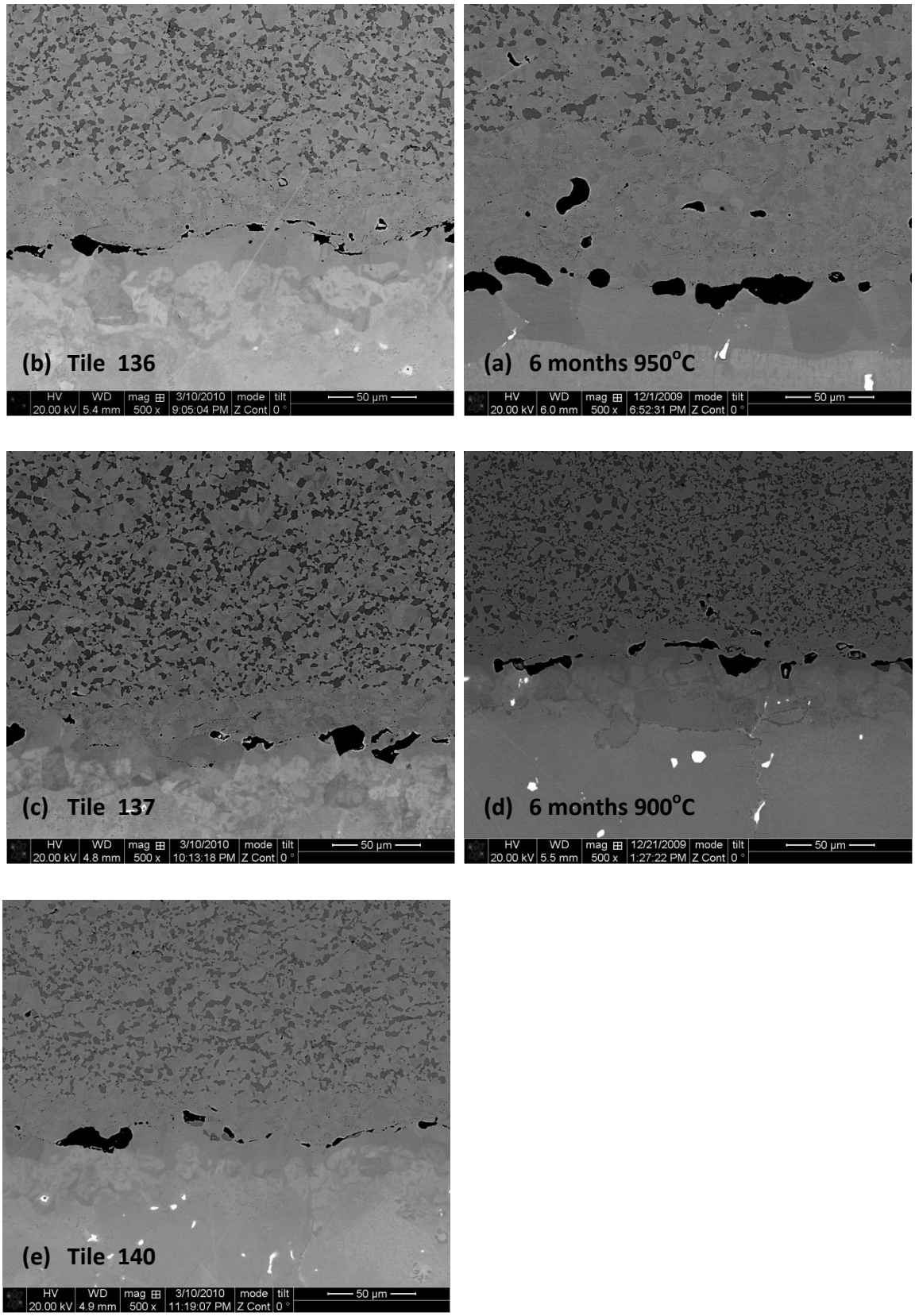

Figure 5.41 A series of back-scatter images (a-e) collected from each ex-service tiles 136, 137 and 140 and also comparable isothermally aged samples aged for 6 months at 900 and 950°C showing the inner beta depletion region.

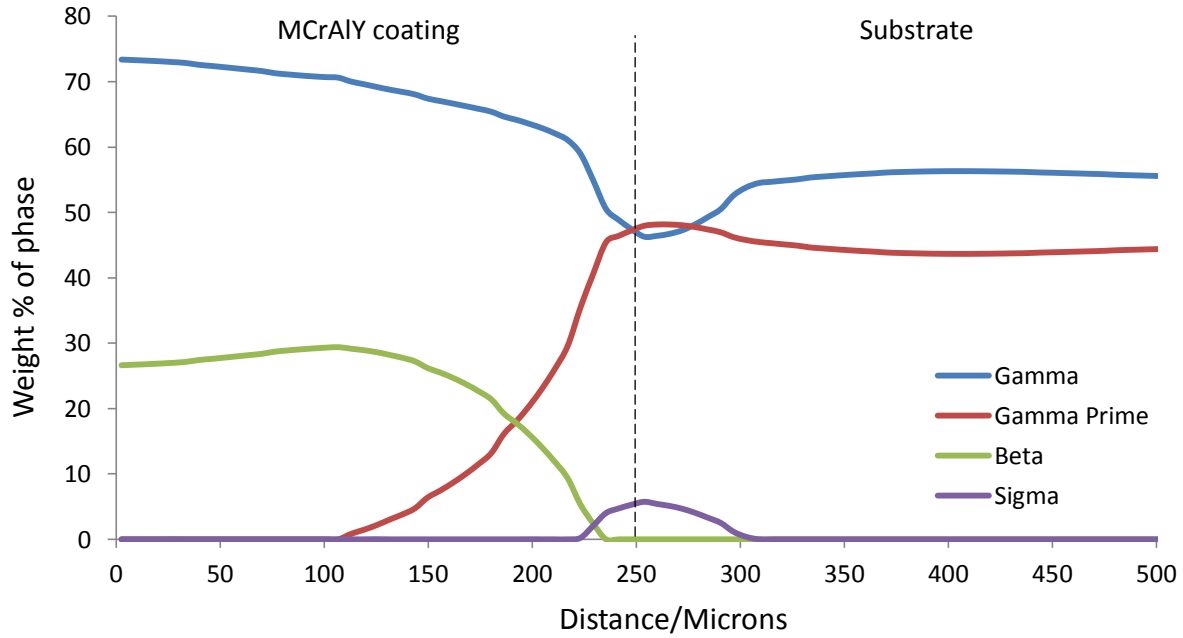

Figure 5.42 A kinetic and thermodynamic model result predicting the phases present within the microstructure of a tile with a 250 µm AMDRY995 MCrAlY layer applied to an In738LC substrate after exposure at 900°C for 5004 hours. The x-axis distance is the distance from the edge of the MCrAlY interface into the tile.

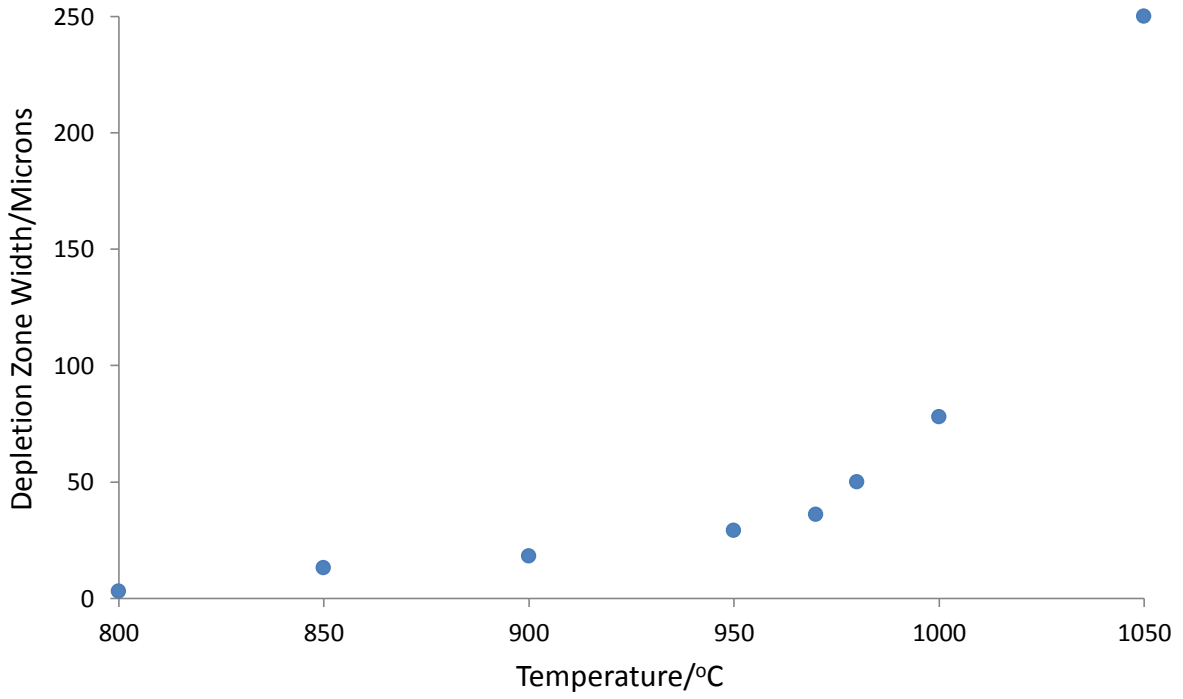

Figure 5.43 The graph shows the predicted inner beta depletion zone width after 5004 hours exposure at a range of temperatures. The predictions were derived from a series of thermodynamic and kinetic model simulations.

In Figure 5.43, a graph is presented that has been constructed from a series of thermodynamic and kinetic model simulations at different temperatures. The graph shows how the inner beta depletion is expected to increase as the isothermal exposure temperature increases for an AMDRY995 MCrAlY layer applied to an IN738LC substrate aged for 5004 hours. It is possible to use the graph as a temperature estimation tool. This was carried out by taking the measured inner beta depletion results from the ex-service components and using the beta depletion graph to derive an estimated exposure temperature for each ex-service tile. The predicted exposure temperature for each ex-service tile where beta depletion was measured is shown in Table 5.8. Tiles 138 and 139 had no beta remaining and from Figure 5.46 this suggests an exposure temperature between 1000-1050^{o}C.

Table 5.8 An estimation of exposure temperature of the MCrAlY coating during service for each heat shield tile. The temperature has been derived from a series of thermodynamic/model simulations.

Tile	Inner Beta Depletion	Temperature Estimation
136	36.5 µm	970^{o}C
137	22.2 µm	920^{o}C
138	N/A	N/A
139	N/A	N/A
140	24.1 µm	930^{o}C

The outer beta depletion was also measured, as shown in section 5.4.7. Tiles 138 and 139 did not have any beta remaining within the microstructure after service exposure. Therefore, outer beta depletion measurements could only be made for Tile 136, 137 and 140. The outer depletion of the beta phase within Tile 136 was measured to be 43.0 µm, this could then be compared with an isothermally aged sample that was aged for 6 months at 950^{o}C, as shown in Figure 5.44b, in which the outer beta depletion within the isothermal sample was measured to be 44.6 µm. Tile 137 had an outer beta depletion measured to be 22.5 µm, this can be compared to an isothermal sample in Figure 5.44d aged for 6 months at 900^{o}C where the outer beta depletion is measured to be 20.8 µm. Tile 140 had an outer depletion zone width of 29.9 µm. Based on the isothermally aged samples this would suggest a service temperature of approximately 920-930^{o}C, and the model prediction estimated the exposure temperature to be 930^{o}C.

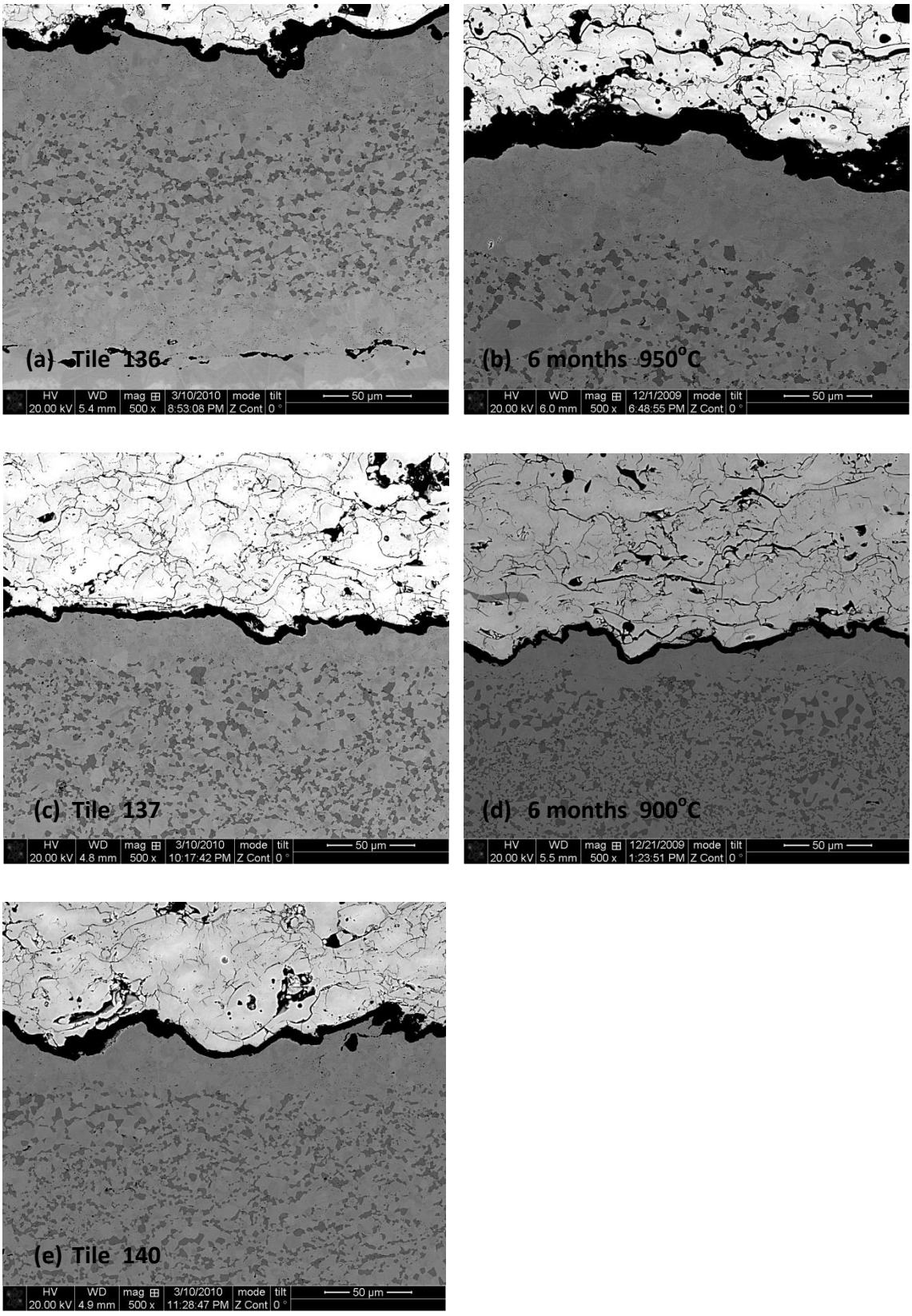

Figure 5.44 A series of back-scatter images collected from ex-service tiles 136, 137 and 140 and also comparable isothermally aged samples that were aged for 6 months at 900 and 950°C showing the outer beta depletion region.

5.5.3 Comparison of Temperature Estimation Methods

A comparison can be made between the various characterisation methodologies used to estimate the exposure temperature experienced during service. It can be seen in Figure 5.45 how the independent methods for predicting the exposure temperature during service, including alumina scale thickness and linear beta depletion, correlate. The location of tiles 138 and 139 does appear to be significant within the engine as they show a microstructure associated with high temperature exposure, including significant TBC spallation, full depletion of the beta phase and a thick oxide scale that consists of a Cr, Ni and Co rich layer. From Figure 5.45 a correlation can also be observed between spallation of the TBC layer and the predicted exposure temperature, as expected, the two tiles that showed significant spallation of the TBC layer (138 and 139) were exposed to increased temperatures. Table 5.9 also shows that there is a correlation between the distortion of the tile substrate and TBC spallation. Due to the repeated shutdowns the component is likely to have experienced it is possible that the TBC did spall during engine shutdown due to the thermal expansion mismatch and when the engine was restarted again the tile began to overheat as no thermal protection was provided and the MCrAlY was exposed to elevated temperatures, resulting in complete depletion of the beta phase and non-preferential Ni, Cr and Co rich oxide formation.

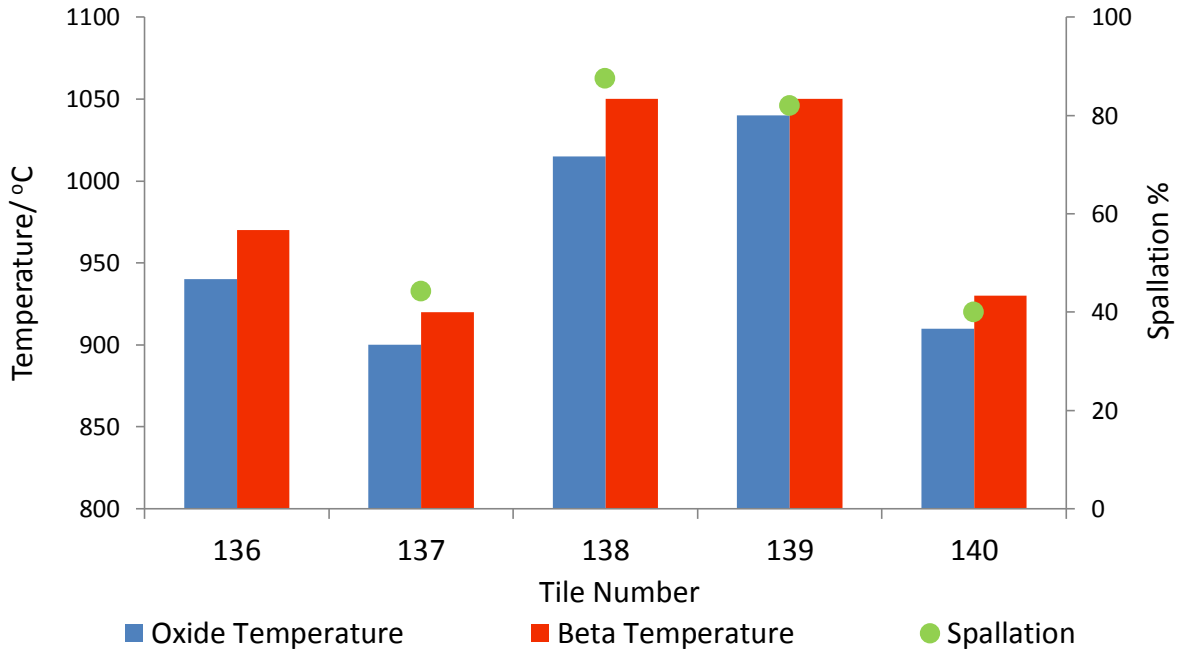

Figure 5.45 The graph shows how the oxide thickness and inner beta depletion temperature estimation compare with TBC spallation.

Table 5.9 The table shows the rank order of tiles in terms of TBC loss and also substrate distortion. Tiles 134 and 145 that have an SC2453 coating applied and this coating is applied to the remaining tiles within the combustion chamber and is used as a benchmark for CoNiCrAlY coating performance.

Tile Number	TBC Loss %	Rank Order	Tile Number	Distortion Rank Order
134	2.70	6	**134**	5
137	44.17	3	**137**	3
138	87.50	1	**138**	1
139	81.95	2	**139**	1
140	39.92	4	**140**	4
145	3.54	5	**145**	5

5.6 Conclusions

The performance of a CoNiCrAlY coating system applied to isothermally aged and service components has been investigated in this chapter. Microstructural features including alumina scale thickness and linear beta depletion zone thickness have been measured.

It was shown in section 5.3.1 how the alumina scale that forms during isothermal ageing is expected to increase in thickness as time and temperature increase. A TBC was applied to the isothermally aged samples in order to provide thermal protection to the MCrAlY layer. Studying the chemistry of the oxide forming showed that only alumina formed when a TBC was present. The depletion of the beta phase was quantified within the isothermally aged samples and it was seen in Figure 5.12 how at the higher ageing temperature of 950^{o}C, the beta depletion at the inner and outer regions is significantly greater than at 850 and 900^{o}C. For all time and temperature combinations it was found that the inner and outer beta depletion regions showed a symmetrical diffusion effect, as evident in Figure 5.12 for the isothermally aged material.

The ex-service microstructure within combustion chamber heat shield tiles was subsequently compared with the isothermally aged material. Initially the tiles were measured for substrate distortion and TBC spallation and it was shown that there was a link between the location of the tile within the engine and the level of distortion, which correlated with the area fraction of TBC loss. The oxide layer forming on the tiles was also characterised and it was found that the thickest alumina scale occurred on the tiles that showed the greatest distortion and TBC spallation. Oxides rich in Cr, Ni and Co were also present within two tiles where the TBC layer had spalled. The isothermally aged samples were used to compare oxide thickness measurements with the oxide scale that formed on the tiles during service. The beta depletion zones were also measured where possible within the tiles, and a comparison also made with isothermally aged samples. An approximate service exposure temperature estimate could then be made based on the characterisation of the microstructure, comparing isothermally aged material with ex-service material.

A combined thermodynamic and kinetic and an oxidation model were both used to derive predicted microstructural evolution results including alumina scale thickness and inner and outer beta depletion zone widths. The inner beta depletion interface was studied as it was found that the outer beta depletion interface was susceptible to measurement distortion by the severity of surface roughness. The model predictions were validated against isothermally aged

sample measurements. The models were then used to make a refined prediction of the exposure temperature experienced by the ex-service tiles during service at the MCrAlY interface. It was found that there was a variation in predicted tile exposure temperature depending on the position of the tile within the engine. This technique has shown that it is possible to measure microstructural features within a complex coating system and to derive a predicted exposure temperature during service. Independent measurements for alumina scale thickness and linear inner beta depletion show a good correlation and the predictions correlate well with TBC spallation and tile substrate distortion.

The difference in the microstructure within the tiles characterised suggests that there is a variation in service conditions around the combustion chamber; it was known that the tile location correlated with a position of a cylindrical burner outlet (CBO), which is welded onto the burner nozzle to reduce engine vibration, visible within the engine in Figure 5.16. The performance of the CoNiCrAlY coating system showed signs of coating failure, TBC spallation was a significant factor; surrounding tiles that had a SC2453 MCrAlY coating applied later showed very little TBC spallation. However, the specific locations of the tiles could have had an important effect on the coating performance and the temperature individual tiles were exposed too.

6 Microstructural Characterisation of an MCrAlY coated IN738 Ex-Service Blade

6.1 Introduction

This chapter discusses the characterisation of the microstructure within an MCrAlY coated Ni-based superalloy ex-service industrial gas turbine stage 1 blade, that was in service for 18,477 baseload hours within a SGT5-4000F engine. The component had a NiCoCrAlReY SC2464 coating applied to an IN738LC substrate and an additional yttria stabilised zirconia (YSZ) thermal barrier coating (TBC) layer applied on top. The composition of the MCrAlY coating was measured using energy dispersive spectroscopy (EDS) in a Scanning Electron Microscope (SEM), and the result is shown in Table 6.1.

Table 6.1 The measured coating composition of the MCrAlY coating applied to an ex-service stage 1 blade. The composition was measured by EDS in an SEM in the central region of the coating.

Element	Ni	Co	Cr	Al	Re
Wt. %	48.4	24.2	15.7	9.9	1.8

The ex-service microstructure of the gas turbine blade was characterised in this work to determine how the service conditions experienced around the profile of the blade affect the microstructural evolution. An additional aim of this work was to characterise a component after long term service exposure, and by using the post service microstructure, provide validation for a model of microstructural evolution developed in parallel with this research. An accurate prediction of localised temperatures based on microstructural evolution is also required, in order to develop remaining useful lifetime time prediction methodologies to enhance performance and extend the life of existing components in operation, which include gas turbine blades. Chapter 5 illustrated how the microstructural characterisation of isothermally aged material can be used to estimate the service exposure temperature of ex-service components. This chapter presents an experimental and simulation based approach to aid in predicting the service temperature experienced within sections of an ex-service gas turbine stage 1 blade.

The component was sectioned initially as shown in Figure 6.1. A section 187.5 mm from the root of the blade was examined and this was sectioned as shown in Figure 6.2 to produce samples from within the leading and trailing edge regions and from the suction and pressure sides in the centre of the blade profile.

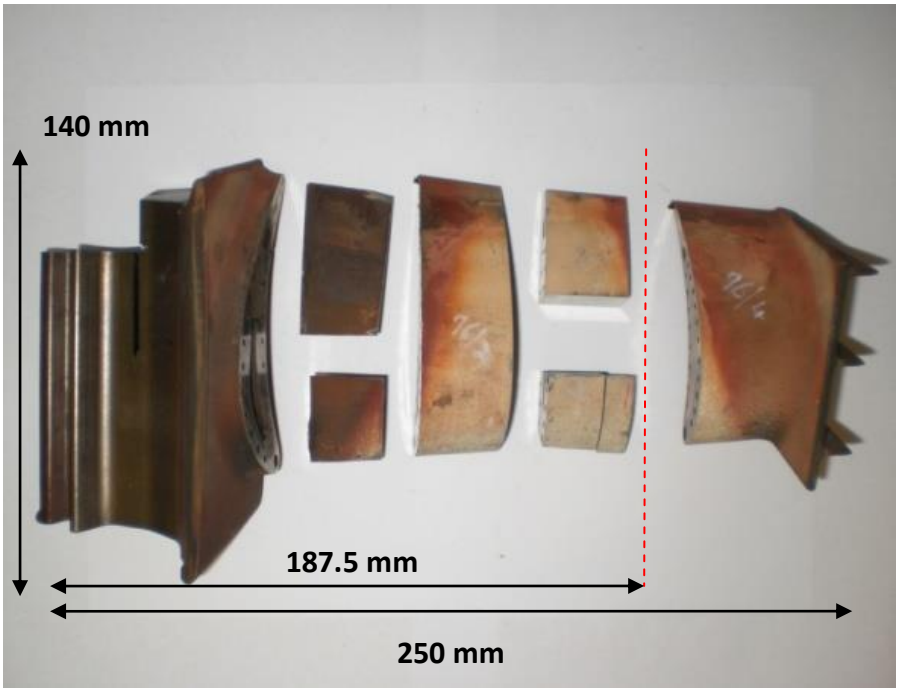

Figure 6.1 The ex-service stage 1 blade sectioned 187.5 mm from the root of the blade, the inner face of the section characterised is highlighted in red.

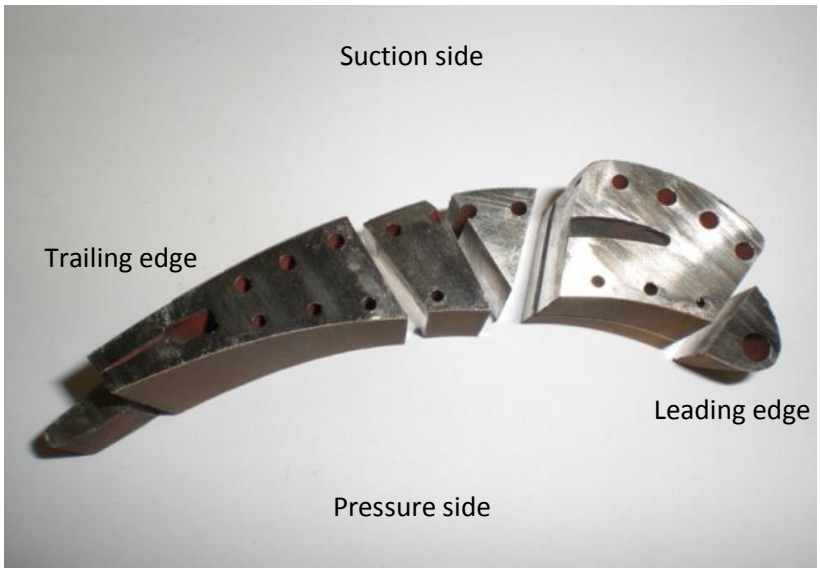

Figure 6.2 The region sectioned in Figure 6.1 was then sectioned to allow for the examination of the leading and trailing edges, and the pressure and suction sides of the blade.

6.2 Thermodynamic Calculations

Thermodynamic calculations were carried out for the NiCoCrAlReY coating across the temperature range 500-1500°C, and the composition used is shown in Table 6.2. In Figure 6.3 it can be seen how the thermodynamic prediction suggests that in the temperature range 700-900°C multiple phases are present, and that the predicted phases change as temperature increases. Above 900°C the coating is predicted to be a two phase, gamma, beta coating. The sigma phase is not predicted to be stable above 890°C, and above 820°C gamma prime is not predicted to be present. The service temperature of the component was unknown but it was expected to be within a temperature range 800 - 1100°C. Due to the predicted change in the amount of each phase and the number of phases present within the coating it is therefore, possible in the simplest case, to use the presence or absence of a specific phase within the microstructure as a temperature indicator. The amount of phase present can also be an indicator of exposure temperature.

Table 6.2 The coating composition used for thermodynamic calculations, the coating composition was provided by the industrial user of the service component and it was confirmed by EDS analysis as shown in Table 6.1.

Element	Ni	Co	Cr	Al	Re
Wt. %	48	25	15.5	10	1.5

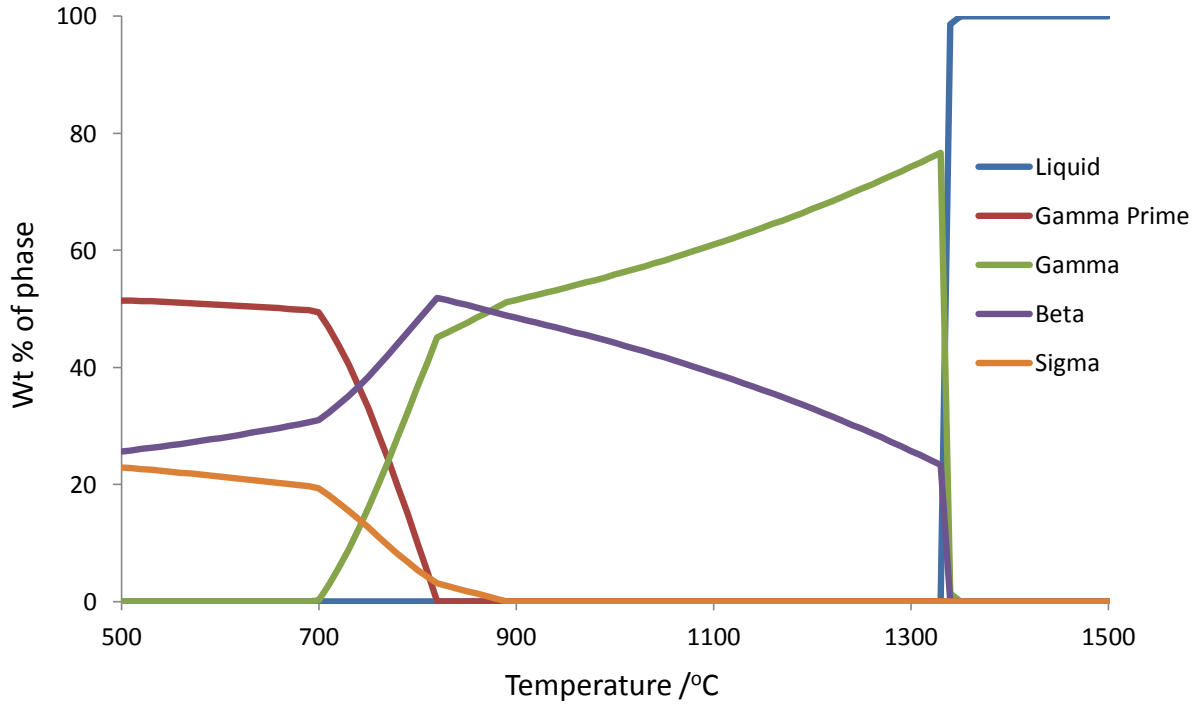

Figure 6.3 The thermodynamic calculation for selected phases for the NiCoCrAlReY coating. The calculation was carried out for the composition 48 Ni, 25 Co, 15.5 Cr, 10 Al, 1.5 Re Wt. %.

Figure 6.4 shows how the composition of the gamma matrix is expected to change with temperature. It can be seen that the phase is predominantly Ni rich with 32-45 wt %; 40 wt. % Co predicted at 700^{o}C, falling to 30 wt. % as the temperature increases to 750^{o}C, 18-23 wt. % Cr is also predicted. The Al concentration within gamma is predicted to increase from 2 wt. % at 700^{o}C to 8 wt. % at 1330^{o}C. Figure 6.5 highlights how the gamma prime phase does not change significantly with temperature and is not thermodynamically stable above 810^{o}C. It is predicted to be 65-70 wt. % Ni rich with 13-16 wt. % Co. The Al concentration is approximately 10 wt. % between 500-810^{o}C and between 4-7 wt. % Cr is predicted in the same temperature range. In Figure 6.6 it can be seen that the beta phase is rich in Ni, predicted to contain 42-57 wt. %. Beta is also predicted to contain 37 wt. % Co, falling to 18 wt. % as temperature increases above 850^{o}C. Approximately 16 wt. % Al is predicted across the temperature range and also 4-7 wt. % Cr is predicted to be present. Figure 6.7 shows how the sigma phase is predicted to be Cr rich, with 53 – 42 wt. %. 36 wt. % Co is predicted at 500^{o}C, falling to 21 wt. % as temperature increases towards 890^{o}C. The sigma phase is also predicted to be rich in Re, with 6 wt. % at 500-600^{o}C, rising to 27 wt. % between 600 and 890^{o}C. Sigma is not thermodynamically stable above 890^{o}C.

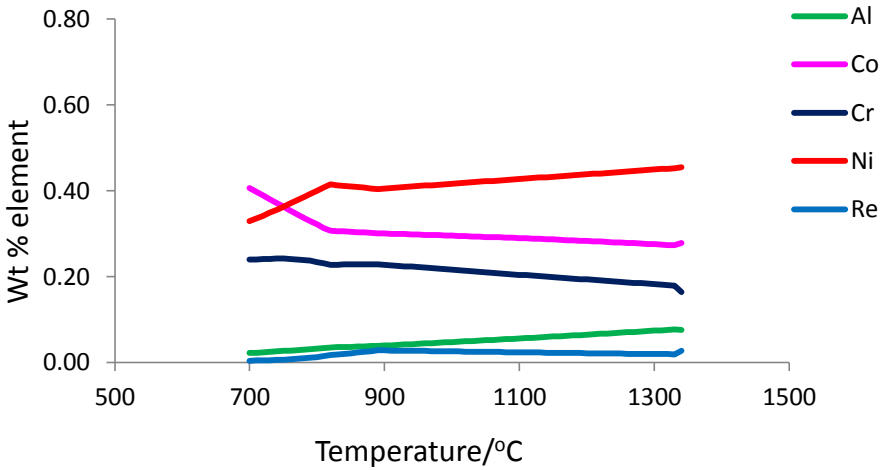

Figure 6.4 Thermodynamic prediction of the composition of the gamma phase in the SC2464 coating with composition 48 Ni, 25 Co, 15.5 Cr, 10 Al, 1.5 Re Wt. %.

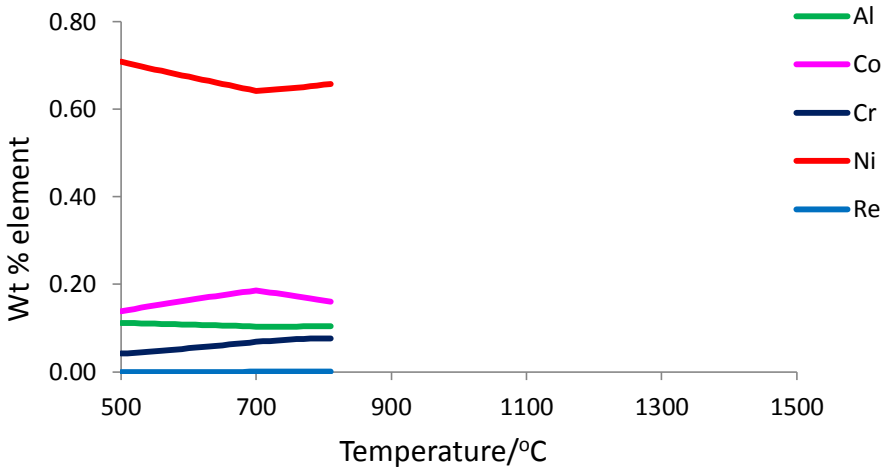

Figure 6.5 Thermodynamic prediction of the composition of the gamma prime phase in the SC2464 coating with composition 48 Ni, 25 Co, 15.5 Cr,.10 Al, 1.5 Re Wt. %.

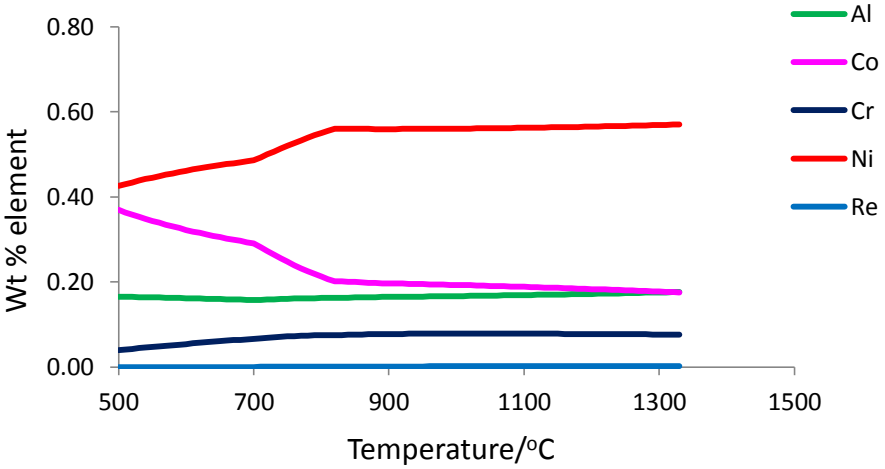

Figure 6.6 Thermodynamic prediction of the composition of the beta phase in the SC2464 coating with composition 48 Ni, 25 Co, 15.5 Cr, 10 Al, 1.5 Re Wt. %.

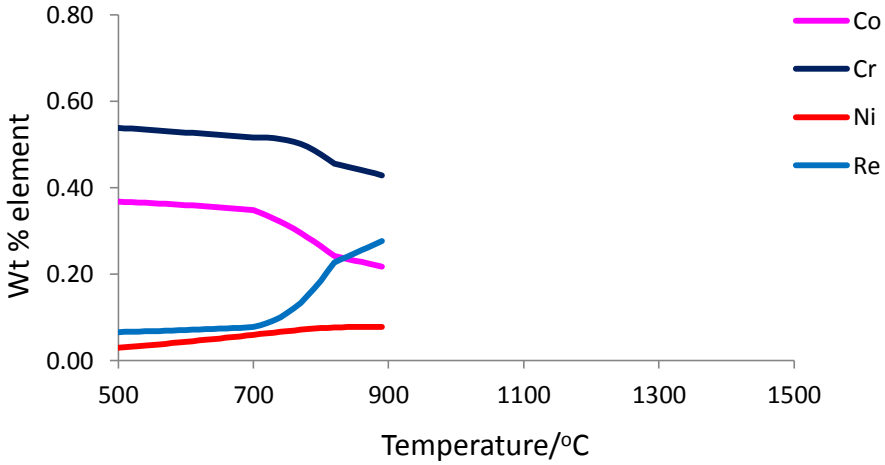

Figure 6.7 Thermodynamic prediction of the composition of the sigma phase in the SC2464 coating with composition 48 Ni, 25 Co, 15.5 Cr, 10 Al, 1.5 Re Wt. %

Thermodynamic calculations were also carried out for the substrate of the component, IN738LC. The measured composition from an unaged section of IN738LC is shown in Table 6.3 and the thermodynamic equilibrium calculation results are shown in Figure 6.8. It can be seen that the microstructure is predicted to be predominantly two-phase, consisting of the gamma and gamma prime phases.

Table 6.3 The measured coating composition of unaged IN738LC, the composition was used for thermodynamic equilibrium calculations. The composition of the substrate alloy was measured by Certified Alloys Inc., California, USA by EDS.

Element	Ni	Cr	Co	Al	Ti	W	Mo	Ta	C
Wt %	62.69	15.98	8.26	3.36	3.5	2.67	1.76	1.67	0.11

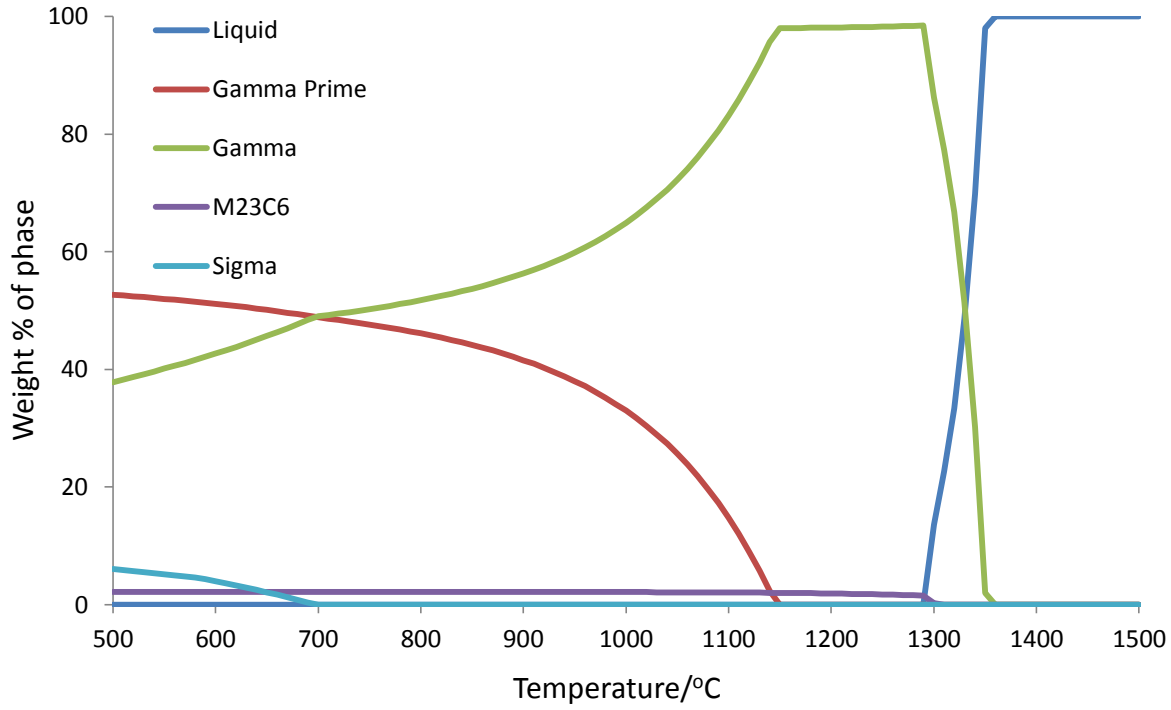

Figure 6.8 The thermodynamic prediction for the IN738LC substrate between 500 and 1500°C. The composition used for the calculations is shown in Table 6.3.

6.3 Characterisation of the Microstructure of an Ex-Service Blade

The characterisation of the microstructure of the MCrAlY and TBC coated IN738LC ex-service blade is discussed in this section. The blade had a 250 µm NiCoCrAlReY coating and an additional 250 µm TBC layer applied to an IN738LC substrate. The blade was received in the ex-service condition, having experienced 18,477 baseload hours operation. The MCrAlY and TBC layers can be observed in Figure 6.9; the micrograph was taken from the centre of the suction side of the blade, as detailed in Figure 6.2. Deposits can be observed on the outer layer of the TBC and it can be seen how the MCrAlY coating shows significant surface roughness. Due to problems associated with quantifying microstructures with a high surface roughness at the outer MCrAlY/TBC interface, as experienced within the work in previous chapters, the inner MCrAlY/substrate interface was the focus of this work.

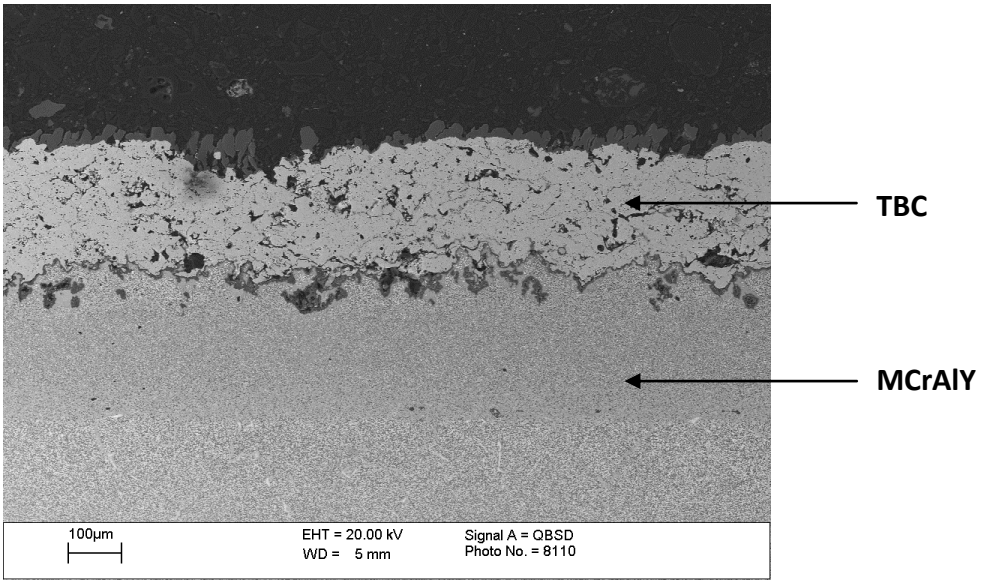

Figure 6.9 A back-scatter electron micrograph showing the MCrAlY and TBC coatings after 18477 hrs service; the micrograph was taken at the centre of the suction side of the blade.

To enable the characterisation and quantification of the microstructure around the profile of the blade, a number of imaging techniques were used. The use of a solid state back-scatter detector for electron back-scatter imaging in a dual beam FIB-FEGSEM was found to be the most suitable for quantification purposes; an image taken using the back-scatter detector is shown in Figure 6.10. This technique reveals the typical microstructure and differences in composition can be identified from contrast differences. Contrast increases as atomic number density increases therefore a phase rich in Al will appear darker than a phase rich in Cr.

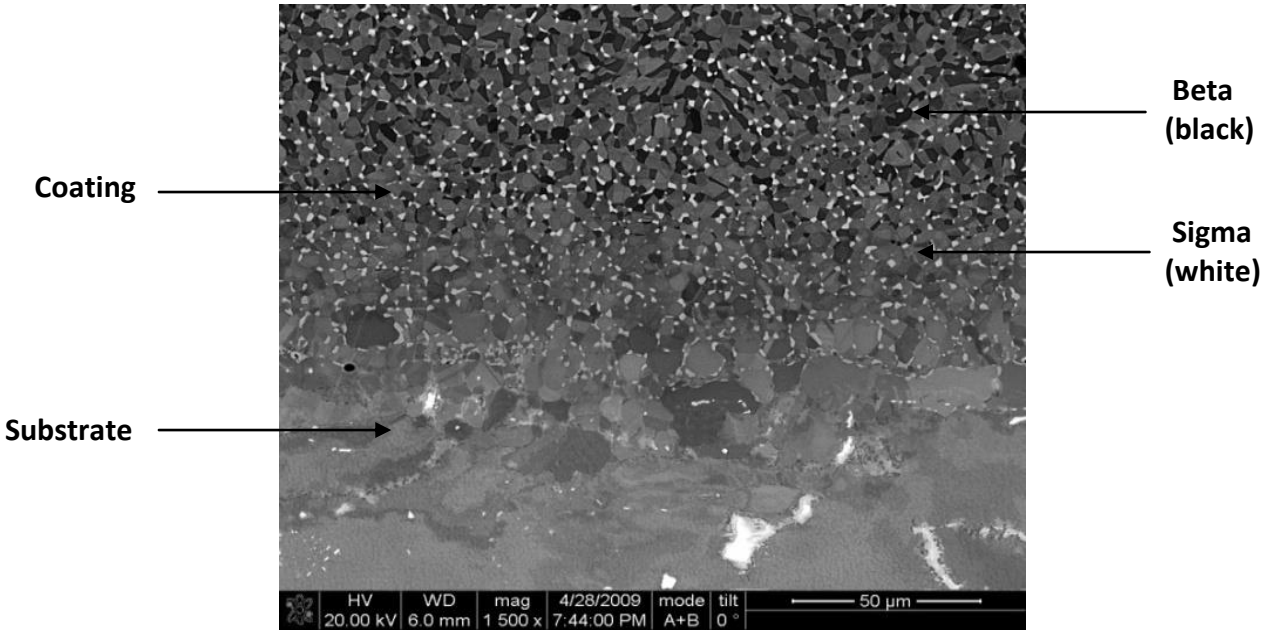

Figure 6.10 A micrograph collected using a solid state back-scatter detector showing the MCrAlY layer and substrate. The different levels of contrast within the image highlight variations in composition, which can be used to discriminate between phases.

Table 6.4 The table shows the measured composition of the each of the phases within the coating carried out by EDS in conjunction with back-scatter images.

Element wt %	Al	Cr	Co	Ni	Re
γ (grey)	3.9	23.4	34.4	37.5	0.9
β (black)	19.9	4.4	13.7	61.9	0.2
σ (white)	0.7	44.2	25.6	9.9	19.6

For the image shown in Figure 6.10, the different regions were characterised using spot EDS analysis. The bright regions were identified to be have a high concentration of Re and Cr compared to the other phases present and the phase appearing dark was identified to have the highest concentration of Al. Using the chemistry information from thermodynamic predictions in section 6.2 it was, therefore, possible to discriminate between the phases present. In Figure 6.4 it was shown how the gamma phase is predicted to be approximately 40 Ni, 30 Co, 20 Cr wt. %. In Figure 6.6 it can be seen how the beta phase above 800^{o}C is predicted to be approximately 55 Ni, 18 Co, 17 Al and 7 Cr wt. %. The sigma phase was shown in Figure 6.7 above 800^{o}C to be approximately 44 Cr, 18-27 Re, 20-26 Co and 8 Ni wt. %. It can be seen that the spot EDS analysis results in Table 6.4 show a good agreement between the predicted measured compositions and the phases can be distinguished from the chemical information.

The phase chemistry characterised by EDS shows that the contrast gradient within the back-scatter micrograph correlates with the individual phase chemistry. The phases identified by EDS analysis were also characterised by electron back-scatter diffraction (EBSD). An EBSD map was used to identify the phases using crystallographic information and the results can be compared with the phase chemistry information. Figure 6.11 shows an EBSD phase map; gamma/gamma prime cannot be distinguished using EBSD due to their crystallographic similarity; the gamma and gamma prime phases are shown in red and the beta phase in green. Due to the correlation between the contrast gradient within images collected using the back-scatter technique and the EDS and EBSD information it has been shown how it is possible to discriminate between phases based on the contrast levels within the MCrAlY coating from back-scatter images, as shown previously and the results correlated with phases that can be identified by EBSD. One of the aims of collecting images that could be quantified by phase content was so that a comparison could be made with the output from microstructure models. In Chapter 5 it was shown how isothermally aged material can be used to compare the microstructural evolution predictions of a coupled thermodynamic/kinetic model with experimentally thermally exposed microstructures. The model was also used in Chapter 5 to derive an estimation of service temperature for a series of heat shield tiles. The ex-service blade which is the focus of this chapter had been in service for 18,477 hours and one of the aims of this work was by using microstructural characterisation techniques and microstructure quantification, to estimate the temperature profile around a curved section of the blade.

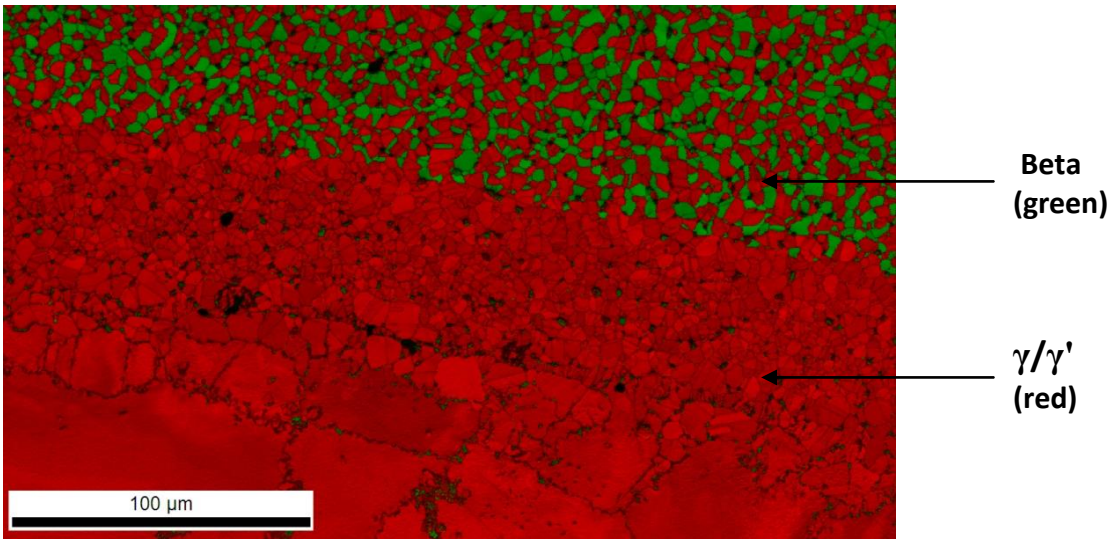

Figure 6.11 An EBSD crystallographic information map collected within the trailing edge region of the blade, covering both the MCrAlY and the substrate regions. The beta phase is shown in green and the gamma/gamma prime phases in red.

6.3.1 Characterisation of the Blade Profile

In this section the microstructure changes around the circumference of the blade are characterised. Figure 6.12 shows how the TBC layer that is applied to the blade can be degraded during service. The leading edge of the blade is expected to be exposed to the highest temperature during service; it can be seen that the leading edge shows degradation of the TBC layer. It can also be seen that deposits are present on the leading edge, which were found to be predominantly rich in Fe and Al with small amounts of Ca, Mg and Si. The source of these elements is particles present in the intake air and the Fe rich deposit could be due to wear debris from steel components within the compressor stage of the turbine (58). The deposits were present predominantly at the suction side of the leading edge, in a layer ~70 µm thick. At the pressure side of the leading edge, deposits were still present but the layer was only ~40-50 µm thick.

From Figure 6.12 it can be seen how the thickness of the TBC layer varies around the profile of the blade after exposure in-service. It must be noted that the target TBC thickness when sprayed was 250 µm, however, during coating application it can be difficult to apply a consistent coating thickness around a complex component shape. As unexposed material was not available, the actual thickness of the applied coatings before service exposure was unknown, however, it can be assumed that when the TBC is still present the MCrAlY layer cannot spall during service. It can be seen how the TBC thickness after service varies from 60 µm at the trailing edge (Figure 6.12a) to 200-220 µm at the pressure (Figure 6.12f) and suction (Figure 6.12b) sections in the centre. The leading edge area shows a change in the TBC around the profile, the suction side of the leading edge (Figure 6.12c) has a TBC layer of 120 µm and the pressure side (Figure 6.12e) 130 µm, however, in the middle of the leading edge (Figure 6.12d) next to the dominant cooling hole the TBC layer was 210 µm. Within the leading edge region the sample with the thinnest remaining TBC layer (Figure 6.12c) had the thickest layer of Ca, Mg, Si, Al and Fe rich deposits present.

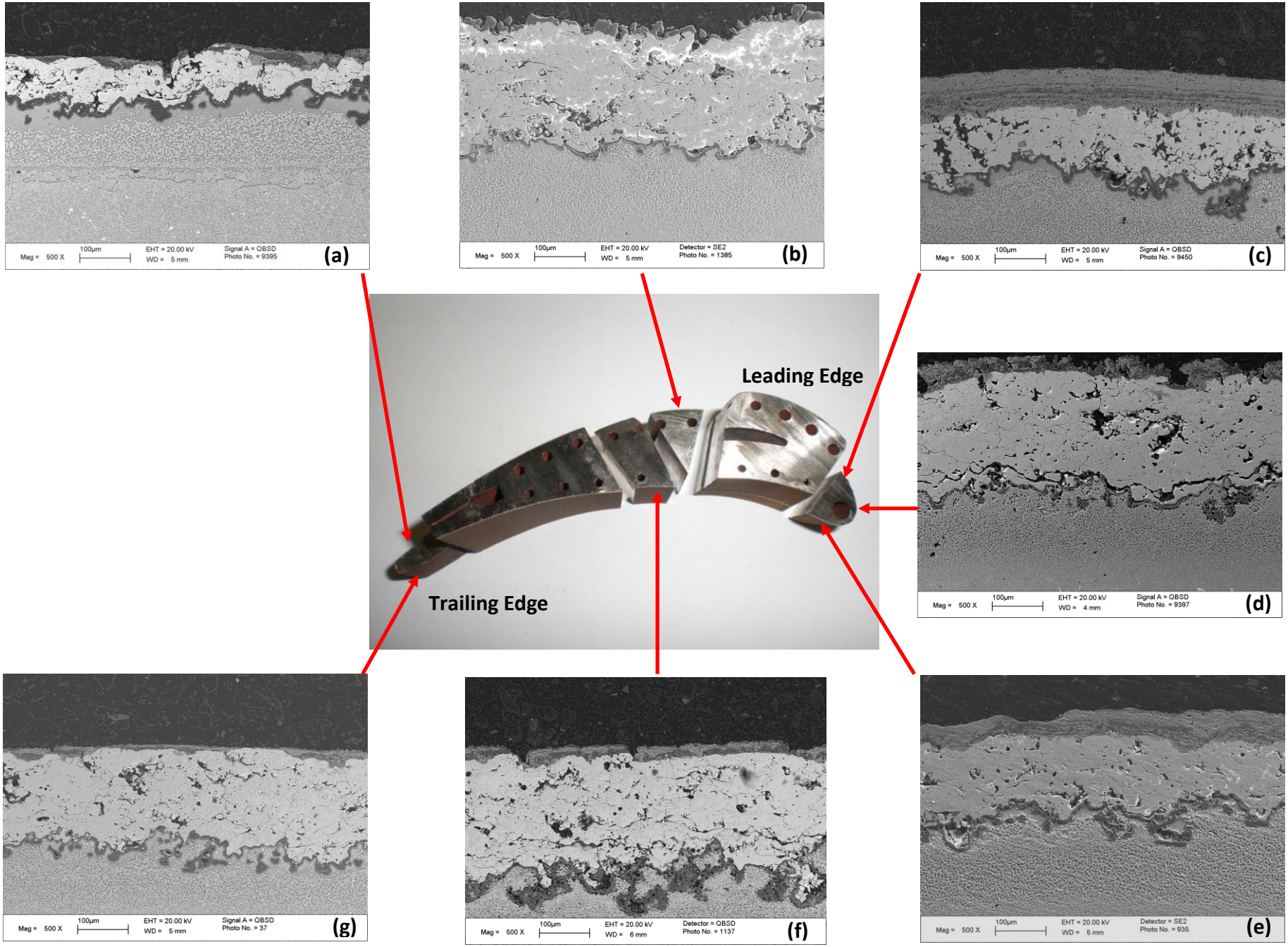

Figure 6.12 This figure shows the TBC coating thickness variation around the profile of the ex-service blade, the back-scatter micrographs (a-g) were all collected using the same microscope settings to allow for a comparison between the different regions of the blade.

6.3.2 Characterisation of the MCrAlY/Substrate Interface

The characterisation of the MCrAlY/substrate interface around the profile of the blade is discussed in this section. During exposure at elevated temperatures, elements diffuse along the chemical gradient between the MCrAlY layer and the substrate of the component. Figure 6.13 presents a series of back-scatter electron micrographs which show the variation around the profile of the blade, in which localised regions show significant microstructure variation. At the leading edge the three locations characterised have different phase content at the MCrAlY/substrate interface. At the suction side of the leading edge (Figure 6.13c) significant depletion of the beta phase is present. It can also be noted that the sigma phase, which appears as the bright white phase does not appear to be present in the MCrAlY coating. Ti and Ta rich carbides are present within the substrate in the interdiffusion zone along grain boundaries. The region in Figure 6.13c can be compared with the centre of the leading edge (Figure 6.13d) next to a large cooling hole where small amounts of the sigma phase are present. The beta phase appears to be less coarse than the suction side (Figure 6.13c) of the leading edge and small Ti and Ta rich carbides are present within the substrate. Both the suction side (Figure 6.13c) and the centre of the leading edge (Figure 6.13d) can be compared to the pressure side (Figure 6.13e) of the region. It appears that the pressure side of leading edge was exposed to the lowest temperature as large amounts of the sigma phase are present and there appears to be significantly less depletion of the beta phase.

Within the trailing edge and the centre of the blade, the sigma phase is present in all locations and the beta depletion is significantly less than that seen within the leading edge region of the blade. Ti and Ta rich carbides were found to be present along grain boundaries within the trailing edge, notably on the suction side (Figure 6.13a). Within the centre of the blade on both the pressure (Figure 6.13f) and suction sides (Figure 6.13b) the sigma phase can be observed and a similar amount of beta depletion. The characterisation of the beta and sigma within the coating at the MCrAlY/substrate interface suggests that the leading edge was exposed to the greatest temperature, as the beta depletion is greatest in this region and no sigma phase is present. Quantification of the beta phase is discussed in section 6.4.

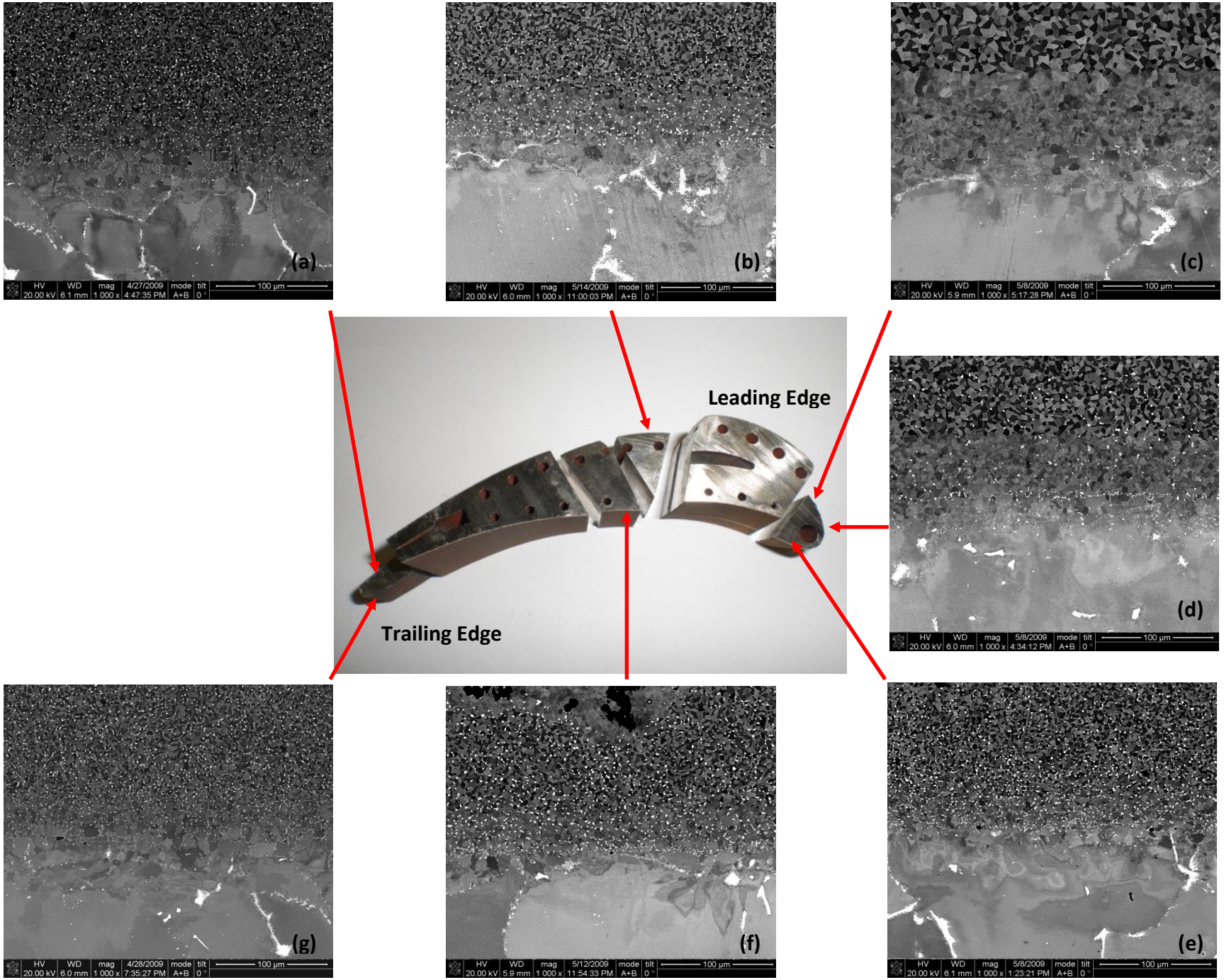

Figure 6.13 This figure shows the MCrAlY/substrate interface region around the profile of the ex-service blade. The back-scatter micrographs were all collected using the same microscope settings to allow for a comparison between the different regions of the blade.

6.3.3 Characterisation of the MCrAlY/TBC Interface

The outer region of the MCrAlY layer at the TBC interface was also characterised. It can be seen around the blade that the outer edge of the MCrAlY coating has a high level of surface roughness. Notably the centre and trailing edge regions of the suction side of the blade show significant roughness of the MCrAlY in Figure 6.14. The surface roughness affects characterisation measurements; this is the reason that the focus of this work was the inner MCrAlY/substrate interface.

It can be seen from Figure 6.14 how the beta phase is depleted at the outer edge of the MCrAlY, notably in the leading edge region on the suction side. The depletion of the beta phase at the suction side of the leading edge can be compared to the centre and pressure side of the same region. The suction side shows the greatest beta depletion, followed by the centre of the leading edge and the pressure side of the region the least depletion of the beta phase. The beta depletion at the outer edge of the MCrAlY is consistent with the depletion of the beta at the MCrAlY/substrate interface shown in Figure 6.13. The beta phase depletion is present within the centre of the blade on both the pressure (Figure 6.14f) and suction (Figure 6.14b) sides but the surface roughness of the MCrAlY makes quantification of the amount of depletion difficult. It can be seen that the pressure side of the trailing edge (Figure 6.14g) appears to have the lowest beta depletion at the outer edge, however surface roughness in this region is significant.

The presence of the sigma phase also shows changes at the outer region of the MCrAlY layer that are comparable to the substrate/MCrAlY region shown in Figure 6.13. The suction side of the leading edge (Figure 6.14c) has no sigma phase present after service exposure; this suggests that the microstructure in this region has been exposed to the highest temperature from thermodynamic predictions. The predictions suggest a temperature greater than 890^{o}C if no sigma is present. The centre of the leading edge (Figure 6.14d) shows small amounts of sigma present and at the pressure side (Figure 6.14e), the sigma phase can be seen throughout the MCrAlY region. In the trailing edge region, the sigma phase is present in both the suction (Figure 6.14a) and pressure (Figure 6.14g) sides. The characterisation of the presence of sigma phase also suggests that the leading edge has been exposed to the highest temperature.

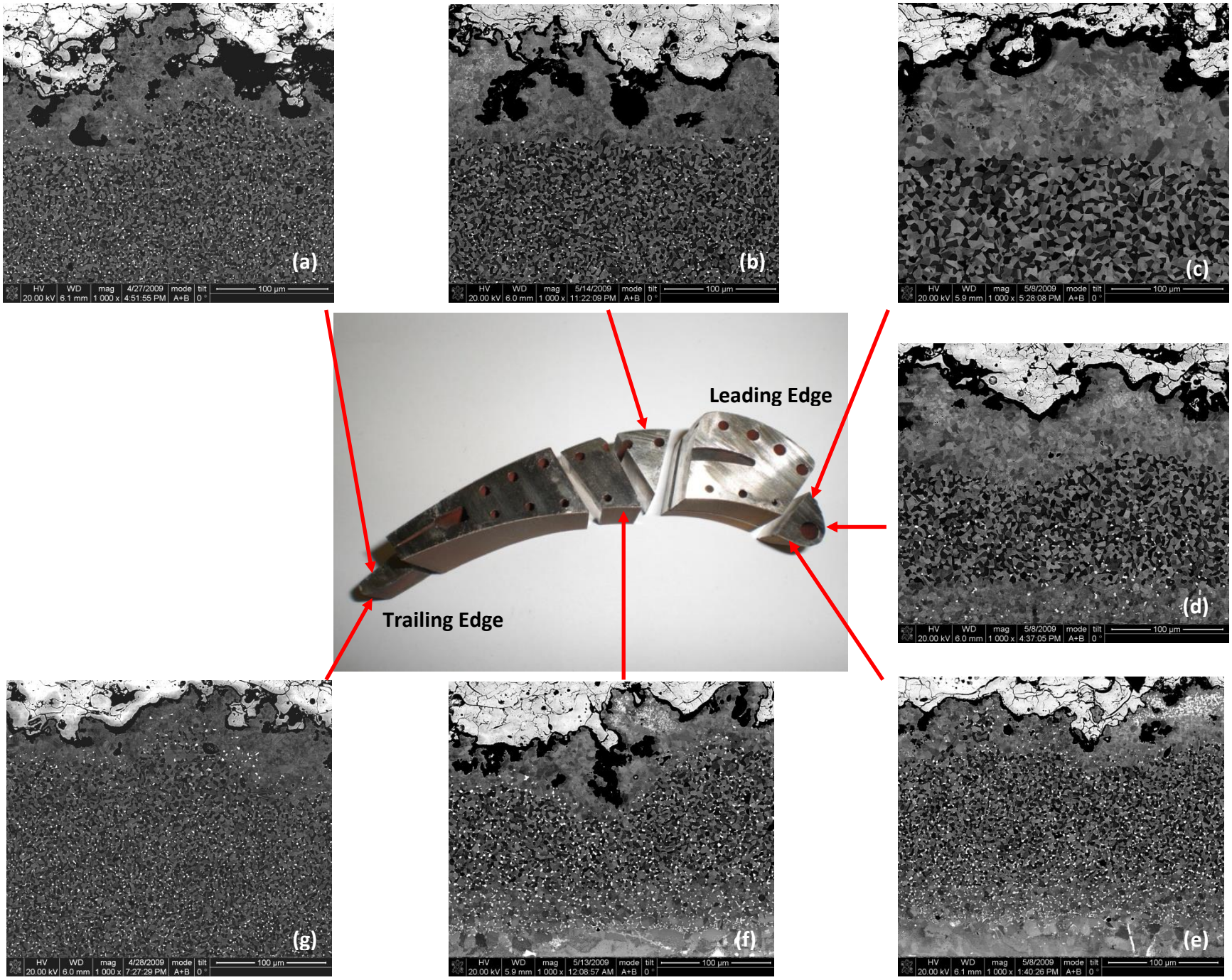

Figure 6.14 This figure shows the MCrAlY/TBC interface region of MCrAlY layer the around the profile of the ex-service blade. The back-scatter micrographs were all collected using the same microscope settings to allow for a comparison between the different regions of the blade.

6.4 Quantification of Beta Phase Depletion

After characterising the microstructure around the profile of the blade in general, selected microstructural features were quantified in detail. In the coating system in this work both thermally grown oxide (TGO) formation and substrate interdiffusion reduce the Al concentration within the MCrAlY coating. As the operating temperature increases, the rate of diffusion and TGO growth increases, resulting in a depletion of Al within the coating. Previous work has based a lifetime modelling approach on this basis and used the depletion of the aluminium rich beta phase as a coating lifetime indicator, assuming that the coating has reached its useable end life when the beta phase concentration is zero (40).

The linear depletion of the beta phase was quantified initially in each of the individual locations. It was shown in Chapter 5 how it was possible to measure the linear depletion of the beta phase and use the measurement to derive an estimation of exposure temperature experienced. It was also shown how isothermally aged material was used to validate the kinetic/thermodynamic model and how the beta depletion predictions do correlate with the experimentally observed values for linear beta depletion.

In order to quantify the depletion of the beta phase at the MCrAlY/substrate region, firstly the interface had to be defined. This was carried out using EDS linescans, and then using the EDS result in conjunction with the known chemistry of the coating and substrate and comparing the data with back-scatter images, this technique was detailed in section 5.3.2. In Figure 6.15 an EDS linescan result is shown that was taken in the centre of the blade on the suction side. The area of characterisation and the corresponding EDS analysis points are shown in Figure 6.16. It can be seen in the EDS graph that point 3 shows a change in composition compared to neighbouring areas and the composition of this region suggests it is the location of the gamma matrix. In Table 6.4 the chemistry of the individual phases was measured by EDS and compared with EBSD and back-scatter images, the gamma phase was measured to be 37.5 Ni, 34.4 Co, 23.4 Cr and 3.9 Al wt. %. EDS analysis points 1, 2, 4 and 5 have a composition which corresponds with the measured composition of the beta phase. The interface was identified to be within the region between EDS point 4 and 5 and by using the chemistry result in conjunction with back-scatter imaging the interface could then be identified in each location.

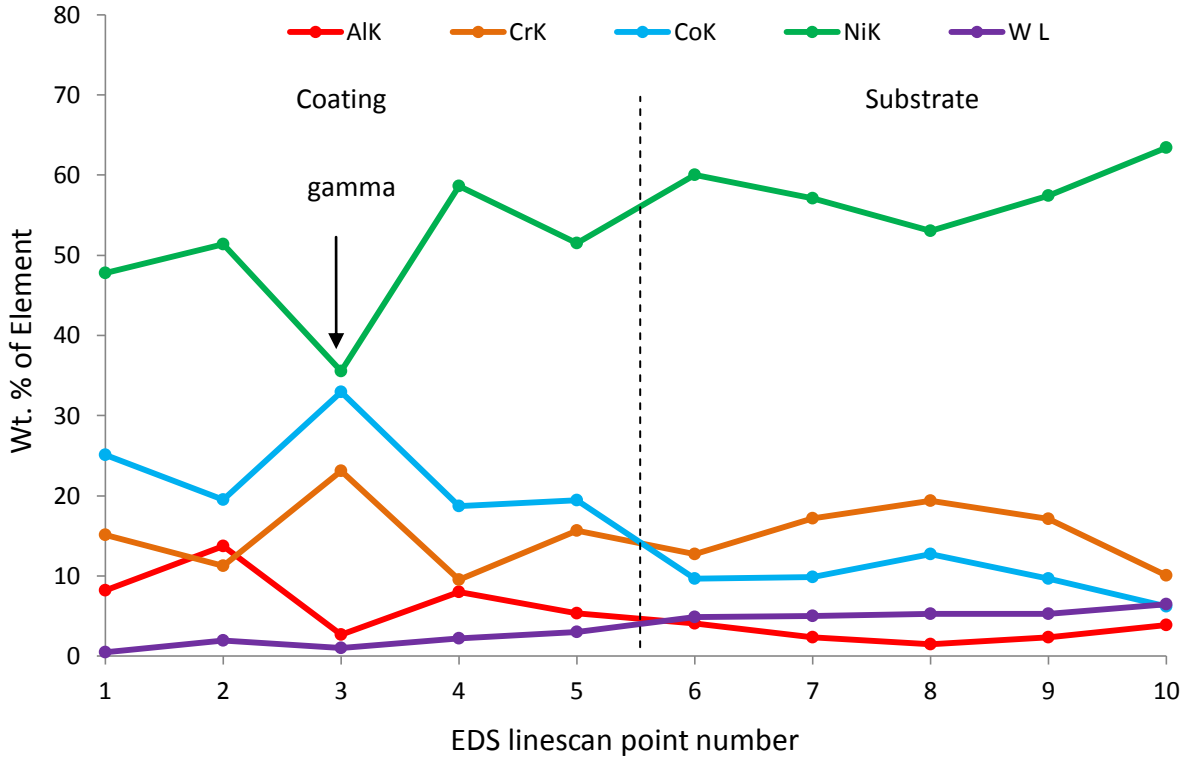

Figure 6.15 An EDS linescan for the suction side of the blade in the centre of the profile. The linescan results show the measured chemistry in 10 locations across the MCrAlY and substrate region.

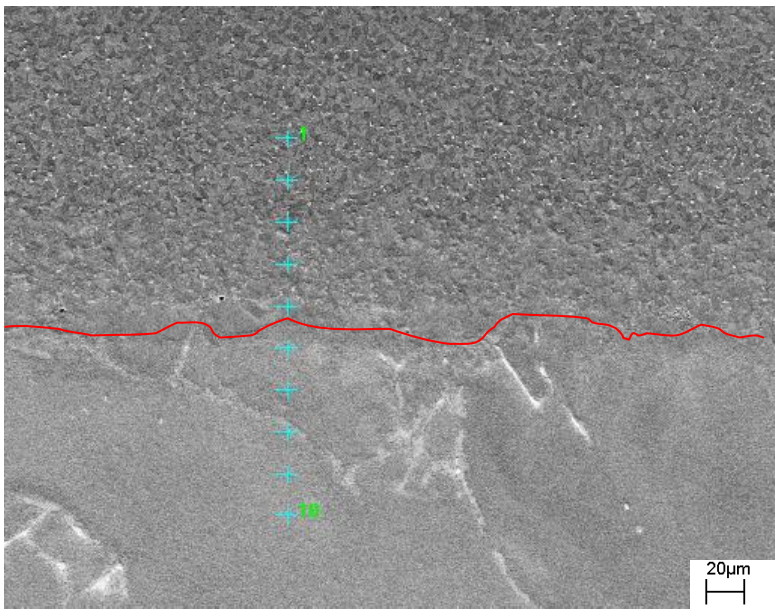

Figure 6.16 This secondary electron image shows the substrate and coating within the centre of the blade on the suction that was characterised using an EDS linescan method. The measured EDS chemistry result is shown in Figure 6.15.

A measurement of the linear beta depletion was then carried out using image analysis software to make multiple measurements. The measurements were made at each location around the blade using back-scatter micrographs taken at 1000x magnification. The same procedure as discussed in Chapter 5 was followed, resulting in a mean linear beta depletion measurement, an example of a micrograph used for beta depletion quantification is shown in Figure 6.17. The beta phase is easily defined using back-scatter imaging. Measurements for the linear beta depletion around the profile of the blade are displayed in Figure 6.18. It can be seen how the leading edge shows the region of greatest mean linear beta depletion.

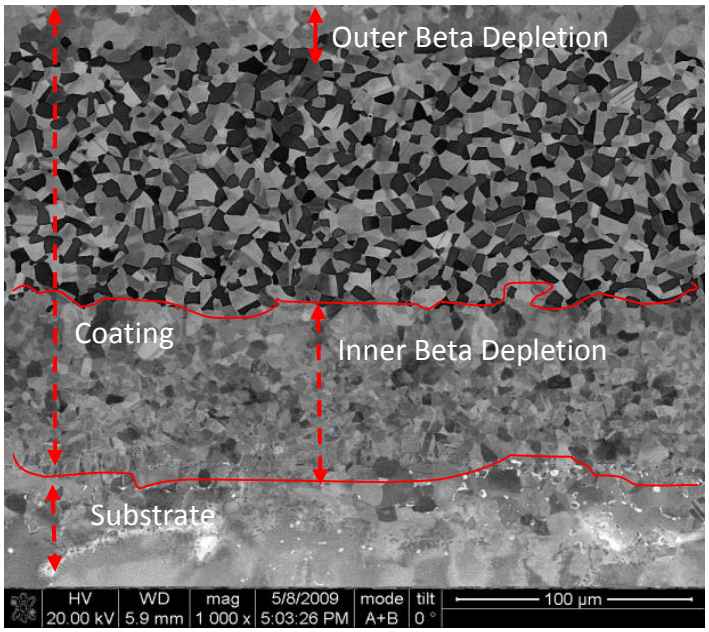

Figure 6.17 The back-scatter electron micrograph highlights the depletion of the beta phase and the MCrAlY substrate region, the micrograph was used to measure the linear beta depletion.

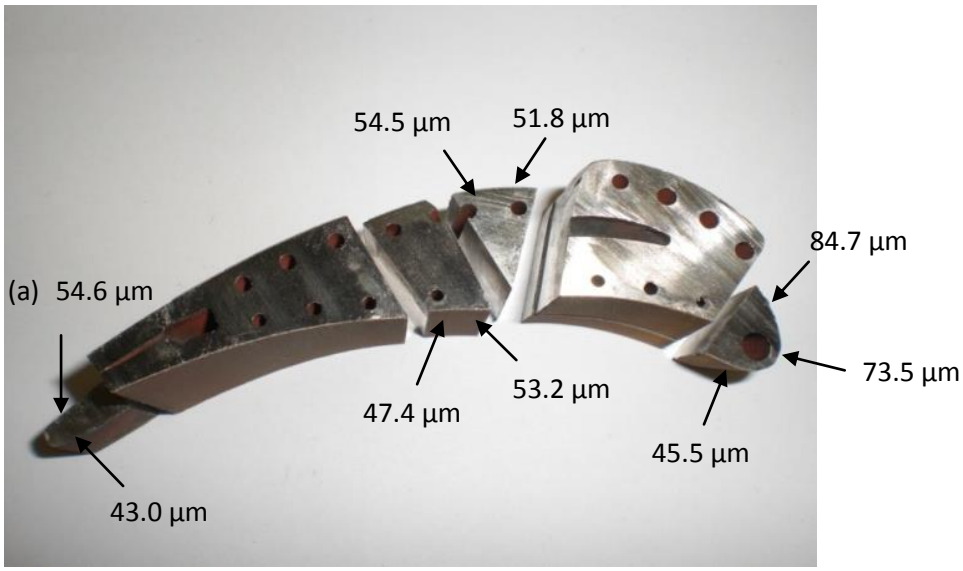

Figure 6.18 This figure shows the results for the measured linear inner depletion of the beta phase around the profile of the blade at the MCrAlY/substrate interface.

6.5 Quantification of Phase Area Fraction

After measuring the mean linear depletion of the beta phase around the profile of the blade, features within the microstructure were quantified. The quantification was carried out by selecting a region from the coating/substrate interface 100 µm out into the coating. The interface was identified by EDS linescans as discussed previously, and an example of the 100 µm region quantified is shown in Figure 6.19. Using image analysis software a single phase was selected from the image and then the area fraction quantified. In Figure 6.20 image (a) shows the area for quantification, (b) the beta phase, (c) sigma and (d) the matrix. The different regions were thresholded out by using a contrast segmentation tool.

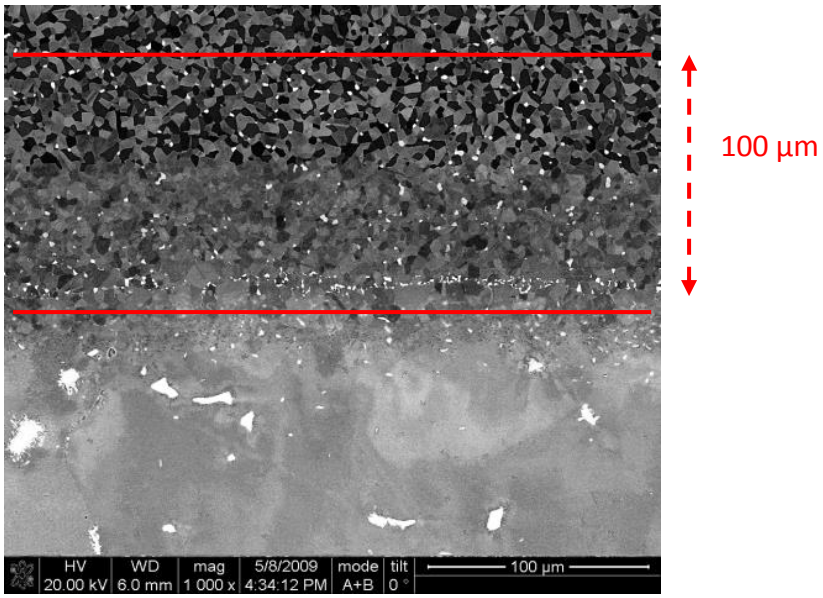

Figure 6.19 This figure shows a region of 100 µm from the interdiffusion zone interface that was selected for characterisation in a back-scatter micrograph.

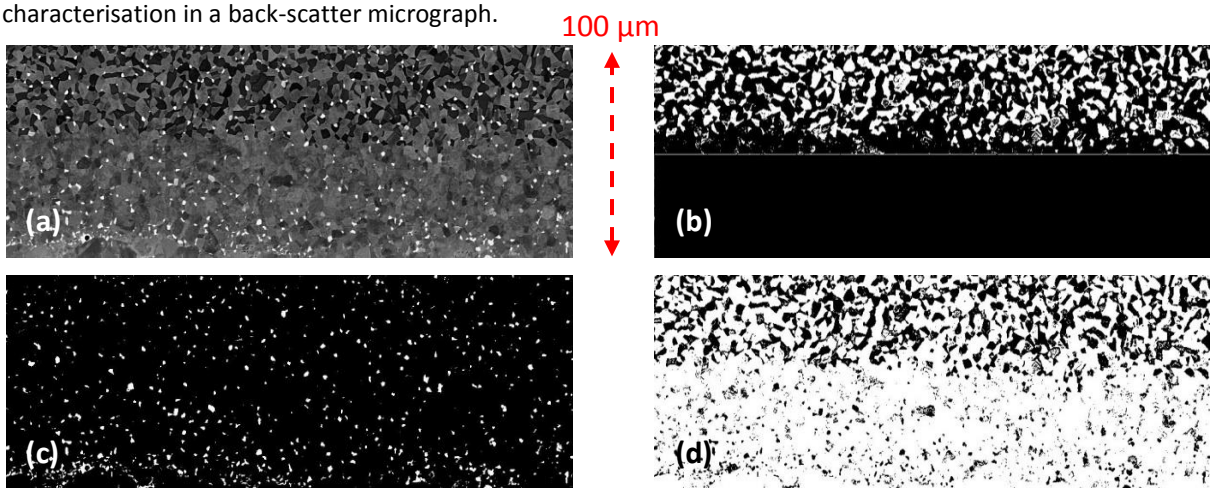

Figure 6.20 This figure shows a series of cropped thresholded images, (a) shows all phases within 100 µm of the MCrAlY coating (b) highlights the beta phase in white, (c) the sigma phase in white and (d) the gamma and gamma prime phases also in white.

The area fraction was then determined using image analysis software once the phase was selected, as shown in Figure 6.20. In this example 16.6% beta is present within a region 100 µm from the coating/substrate interface outwards into the coating. Around the profile of the component back-scatter electron images were collected and quantification repeated for the selected phases. The results for the beta and sigma area measurements are shown in Figure 6.21. It can be seen from the measurements how the leading edge region has the least amount of beta phase within 100 µm at the suction side. The trailing edge (Figure 6.21a and g) show measurements that are very similar suggesting that the microstructure has been exposed in these regions in similar service conditions.

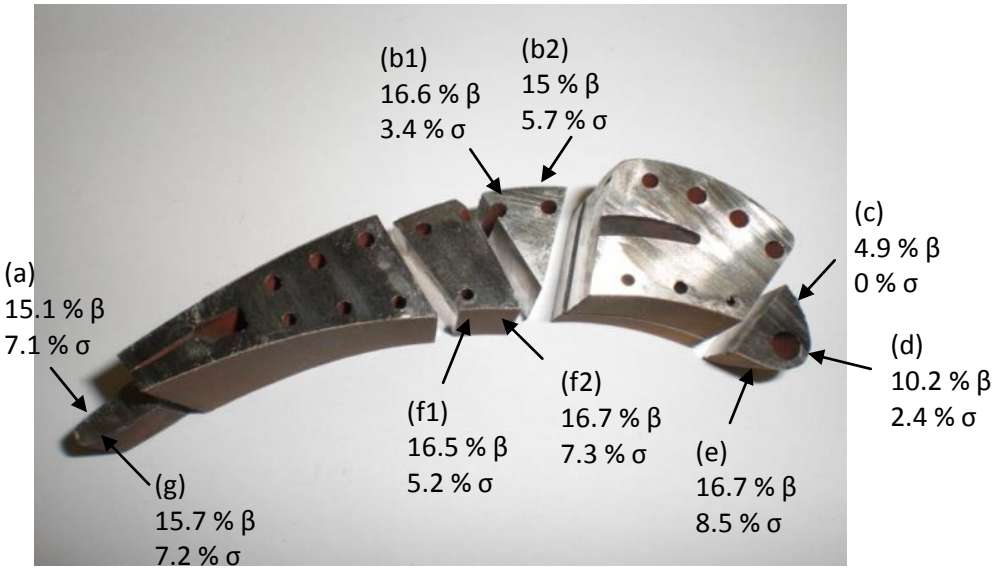

Figure 6.21 The selected region of the microstructure characterised using image analysis software, area percentage of the beta and sigma phases in each location is shown

After the characterisation of the phases present and the area fraction measurements were carried out, results could then be compared to simulation predictions. This was carried out by using the simulation model output for the wt % of phase present within a given distance from the TGO interface. The area under the curve within this region was then integrated to determine the wt % of each phase in the 100 µm region. It must be noted that in this chapter wt% of phase is compared with measurements of % area of phase present. Although the two values are not identical, if similar densities for each phase are assumed then a comparison can be made. The model used is the same as discussed in Chapter 5 and the same procedure carried out in order to derive a temperature estimation based on the observed microstructure after service exposure.

6.6 Microstructure Modelling

The quantification of the observed microstructure was compared with simulation predictions from a coupled thermodynamic/kinetic model described previously in section 5.5.2 and used as a tool to aid in the estimation of service temperature in Chapter 5. Within the previous chapter it was shown how the model was validated against isothermally aged material and how the simulations provided an accurate representation of the observed microstructure after service exposure. An example simulation is shown in Figure 6.22; the interface is highlighted at 250 µm which is the coating thickness in this example. The 100 µm region of interest is also highlighted. The simulations show the predicted phase content and the change with distance from the outer edge of the MCrAlY layer in towards the substrate region. This figure is for the same region of interest as shown in Figure 6.20. It can be seen how the prediction shows a beta depletion region within the MCrAlY layer at the MCrAlY/substrate interface. A linear predicted depletion was taken from the simulations at multiple temperatures to understand how the depletion of the beta phase is expected to change as the exposure temperature changes. The amount of each phase present within the region was also measured by using integration tools within graphical software.

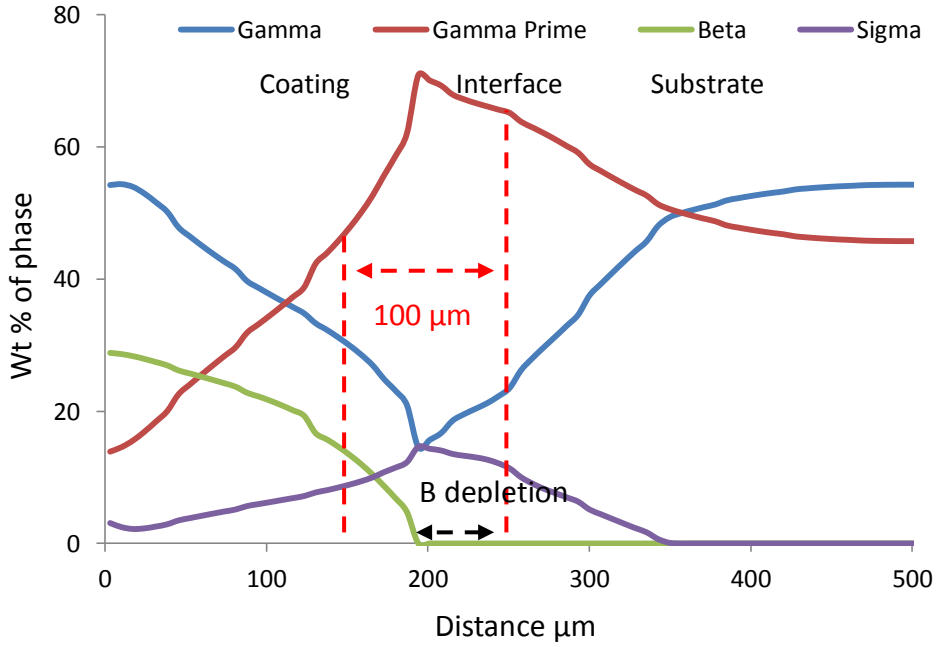

Figure 6.22 An example of a simulation output for the substrate and coating composition of the ex-service blade. The simulation shows the predicted phase content and change with distance from the edge of the MCrAlY layer after 18477 hours exposure.

6.7 Estimating the Service Temperature of the Microstructure

Linear beta depletion measurements were displayed around the profile of the component in Figures 6.18 and it was shown how the greatest linear depletion and the greatest area depletion occurs at the leading edge. A temperature estimate is then derived from thermodynamic and kinetic simulations as detailed in section 6.6. In order to estimate the temperature during service, multiple simulations were carried out to derive a graph, as shown in Figure 6.23, which shows how the predicted linear beta depletion is expected to change with temperature. In this work however, a variation of the MCrAlY thickness was observed around the profile of the blade, therefore, the effect of MCrAlY coating thickness on the simulation output was investigated by carrying out simulations for MCrAlY thicknesses of 250 and 300 µm. The beta depletion predictions for temperatures between 800-975^{o}C are shown in Figure 6.23 for both 250 and 300 µm MCrAlY layers. It should be noted that in the region 905 – 940^{o}C, the coating thickness is predicted to affect the temperature estimated. This was observed from the simulation results to be 30^{o}C for an additional 50 µm of MCrAlY coating.

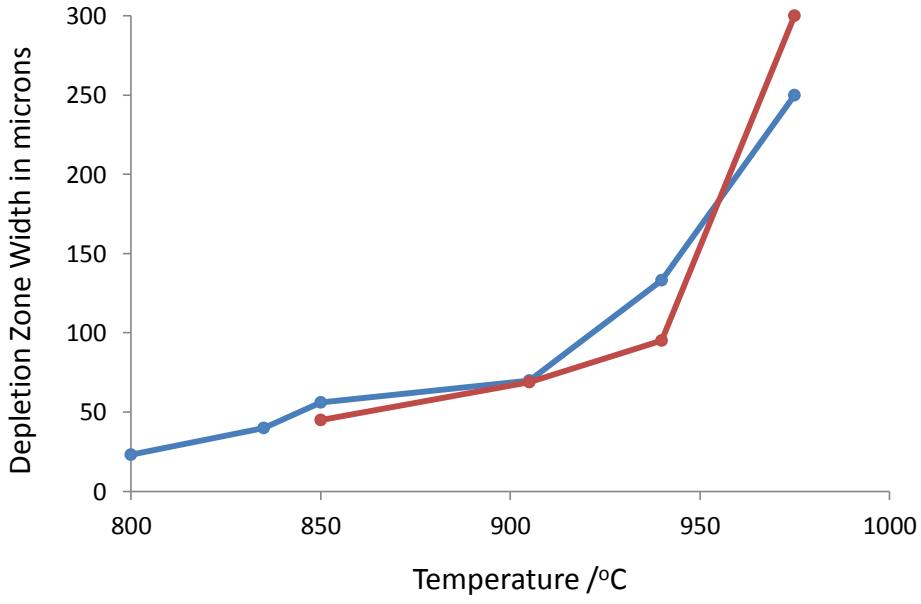

Figure 6.23 This graph shows the predicted linear beta depletion based on multiple kinetic/thermodynamic model simulations. The depletion change with temperature is shown for both 250 µm (blue) and 300 µm (red) MCrAlY coating thicknesses.

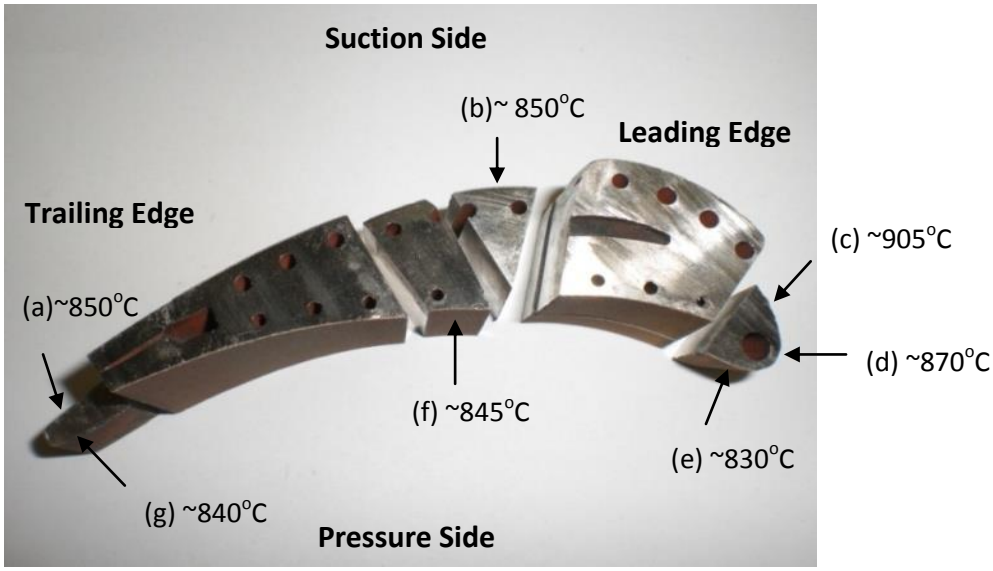

Figure 6.24 This figure shows the estimated temperatures experienced by the microstructure in the localised regions of the blade during service. The temperatures have been derived from the linear quantification of the depletion of the beta phase using a kinetic/thermodynamic model.

It was observed during characterisation that the MCrAlY thickness was not uniform around the blade, and this will have an impact on the depletion of the beta phase as the supply of the Al within the coating is reduced in localised regions with a thin MCrAlY. The thickness of the MCrAlY was, therefore, measured in each location; the results are shown in Table 6.5. It can be seen that the MCrAlY thickness ranges from ~183 µm at the centre of the blade on the pressure side, to ~284 µm at the leading edge on the suction side. The pressure side of the blade has a concave profile and during spraying this may have contributed to the thin MCrAlY layer applied. Similarly at the leading edge, the profile is convex, therefore, as powder is applied around the profile the protruding region is likely to be coated with a layer greater than desired due to multiple spray gun passes to coat the surrounding areas of the component.

Table 6.5 The table shows the measured mean MCrAlY thickness measurements in each individual location. The measurements were made from micrographs using image analysis software.

Region	Location	Coating Thickness
Centre	Suction	255 µm
Trailing Edge	Pressure	216 µm
Centre	Pressure	183 µm
Leading Edge	Pressure	197 µm
Leading Edge	Centre	238 µm
Leading Edge	Suction	284 µm

In Figure 6.25 the two micrographs show; (a) the centre of the blade on the pressure side, (f), where a thin MCrAlY layer was measured, and (b) the leading edge of the blade on the suction side, (c), where the MCrAlY coating is significantly thicker in a convex region than the MCrAlY applied in a concave region. Within this work the variation in MCrAlY thickness is significant, as linear quantification was carried out in order to derive an estimated exposure temperature. In Figure 6.26 an adjustment has been made for the localised temperature estimations based on the local MCrAlY thickness measurements. The adjustment was based on the effect of coating thickness on the prediction for the beta depletion.

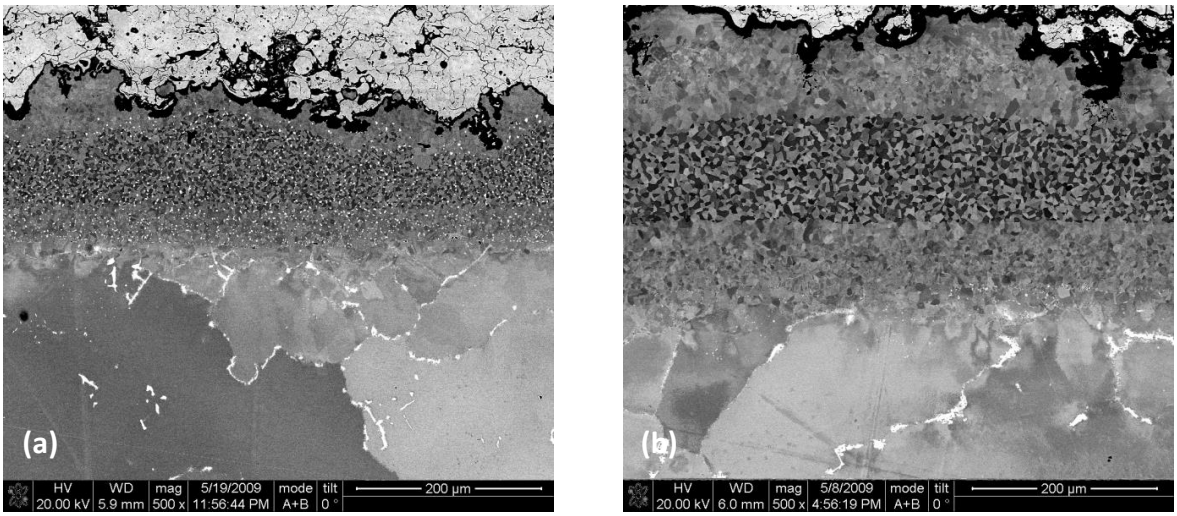

Figure 6.25 The two back-scatter electron micrographs show distinct regions of the blade that have a significant difference in MCrAlY coating thickness. (a) was taken from the centre of the blade on the pressure side (f) in Figure 6.26 and (b) from the leading edge region on the suction side, (c) in Figure 6.26.

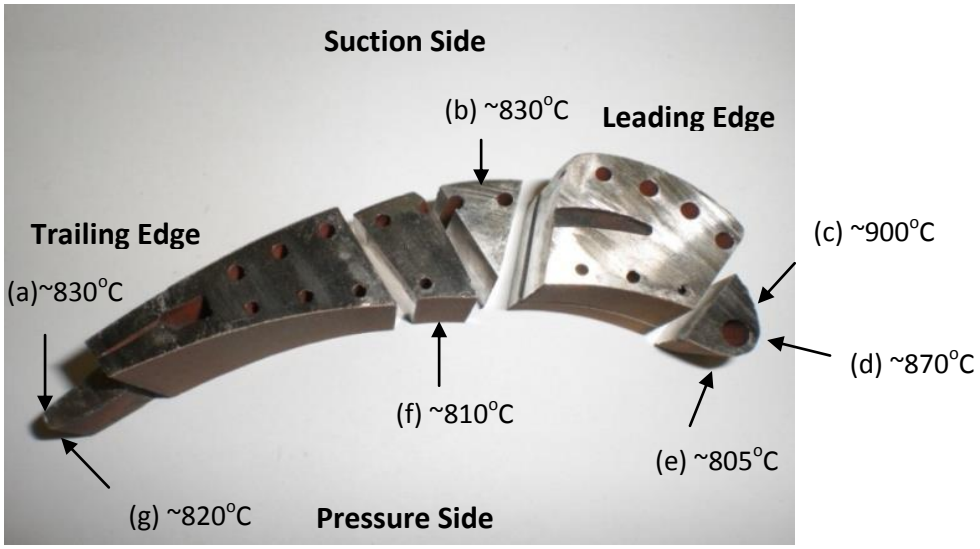

Figure 6.26 This figure shows the estimated temperatures experienced by the microstructure in the localised regions of the blade during service. The temperatures in this figure were adjusted from those in Figure 6.24 to take into account the variation in MCrAlY thickness around the blade.

In addition to the linear depletion of the beta phase, the area fraction of the beta phase was also determined, as shown in section 6.5, and the results compared with model predictions. The results from multiple simulations are plotted in Figure 6.27 for the beta phase, showing how the phase content is expected to change with temperature. Due to the variation in coating thickness, the simulations were carried out for a 250 µm and 300 µm coating to establish the sensitivity of the model predictions to MCrAlY thickness. The beta content was measured in localised regions of the blade in the first 100 µm of the coating from the substrate interface as presented in Figure 6.21. Measurements for the amount of beta phase within the microstructure were then used in conjunction with the simulation prediction in Figure 6.27 to derive estimated temperature around the profile of the blade. The estimated temperatures are presented in Figure 6.28, it can be seen that the leading edge region is predicted to be have been exposed to the highest temperature, at 900^{o}C.

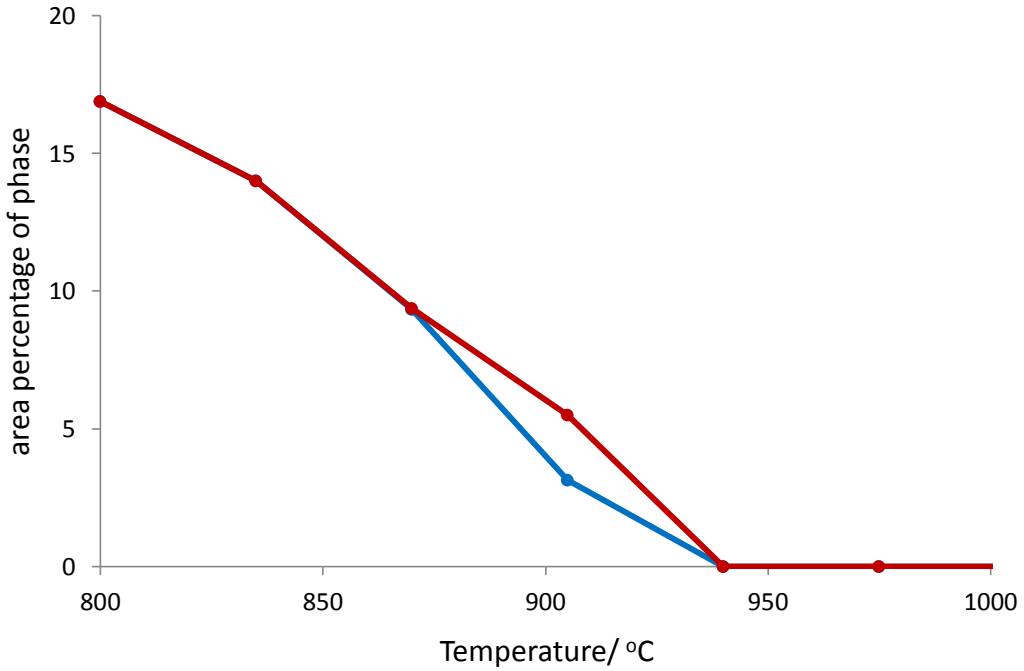

Figure 6.27 The graph shows the simulation predictions for the amount of beta phase present and the predicted change with temperature. Simulations were carried out for both a 250 µm (blue) and 300 µm (red) MCrAlY coating

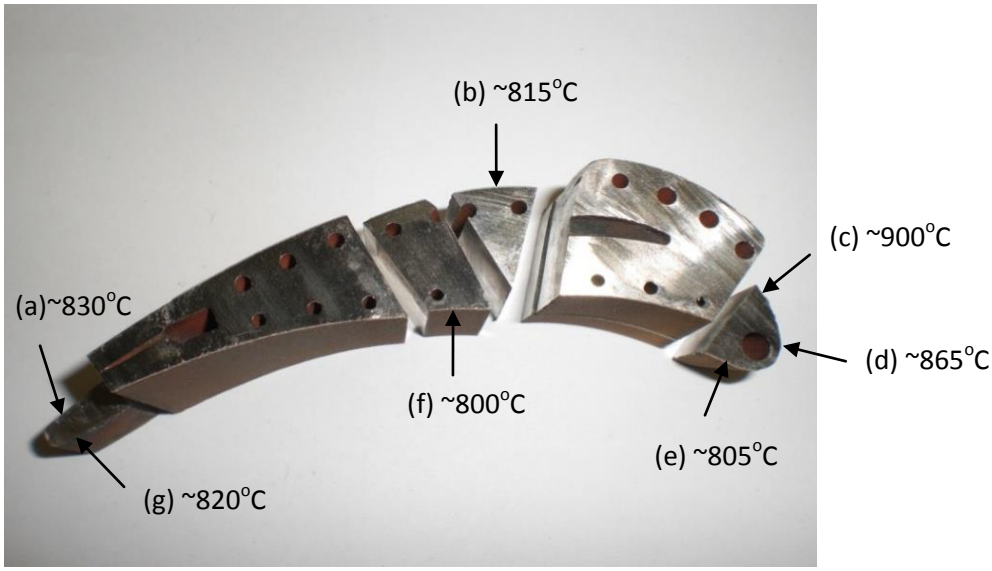

Figure 6.28 This figure shows the estimated temperature that is derived from simulation predictions for the area percentage of beta phase present.

6.8 Conclusions

In this work a kinetic/thermodynamic model has been used to aid in the temperature estimation of an ex-service stage 1 gas turbine blade. The blade was in service for 18,477 hours. Initially thermodynamic calculations were used to plot phase predictions and temperature effects on the microstructure for both the MCrAlY and substrate of the component.

A range of microstructure features were characterised around the profile of the blade including the TBC thickness, the gamma prime phase within the substrate and both the MCrAlY/substrate and MCrAlY/TBC interface. Chapter 5 had shown that the surface roughness of the MCrAlY makes comparisons with simulations difficult. In this work the inner MCrAlY/substrate region was used to make comparison between the ex-service microstructure and the simulation outputs. Quantification was carried out at the inner interface including linear depletion and area measurements of the beta phase within the first 100 µm of the MCrAlY layer. The quantification of both methods was then compared against simulations, in section 6.7 the simulations were used to make an estimation of the exposure temperature experienced during service. It was observed that the coating thickness variation would affect the accuracy of the simulation predictions, therefore, where possible adjustments were made to the predicted temperatures to account for this variation. In Figures 6.26 and 6.28 both methods were used to predict the temperature and a qualitative and quantitative correlation can be observed. In both cases the highest temperature regions are consistently showing that the leading edge of the blade at the suction side and in the centre has been exposed to the highest temperature. The microstructure of the gamma prime phase was also investigated but it was found that there were no significant changes in morphology around the profile of the blade. The temperature estimations suggest the majority of the blade was only exposed to a temperature difference of ~65^{o}C, which would not be enough at the temperatures used in this work to cause any significant change in gamma prime size and shape.

Within this chapter temperature estimation methods have been developed that can remove the effect of spray technique and dimensional effects. It is important that exposure history and coating application information is known to improve the accuracy of the simulation estimations. The combination of thermodynamic/kinetic modelling with the quantification of an ex-service microstructure has been successfully used in order to derive an estimated localised service temperature.

7 Three-Dimensional Characterisation of Microstructures

7.1 Introduction

Developments in characterisation techniques in recent years have allowed for three-dimensional (3D) characterisation. Previous work has shown how a slice and view technique has become an established process for collecting electron backscatter diffraction (EBSD) and energy dispersive X-ray spectroscopy (EDS) data. There have however been some limitations with processing and analysis due to large data volumes collected.

In this work an automated method for collecting combined EBSD and EDS data is presented and the offline processing to enable a 3D reconstruction of a microstructure discussed. This technique gives distinct advantages over conventional two dimensional (2D) characterisation as information regarding actual grain size and shape, phase morphology and interconnectivity can be obtained.

An FEI Nova 600 Nanolab dual-beam focussed ion beam (FIB) / field emission gun scanning electron microscope (FEG-SEM) was used to collect simultaneous data across a number of slices to enable a volume of material to be reconstructed. The data acquisition process is dependent on scripts developed specifically to enable the collection of EBSD data and subsequent ion beam milling of the collected region to reveal a new surface area of interest. Data is collected as a series of 2D maps that are then stitched together using dedicated offline 3D image reconstruction software. In this work the technique has been applied to a coated ex-service industrial gas turbine blade, which had MCrAlY and TBC coatings applied to an IN738LC substrate. The MCrAlY coating composition is shown in Table 7.1. The area analysed by 3D EBSD/EDS was primarily within the complex interdiffusion zone (IDZ) that evolves during service as elements diffuse across the substrate/coating interface.

Table 7.1 The table shows the coating composition of SC2464 applied to the ex-service blade studied in this chapter. The coating composition was provided by the component user and is consistent with EDS measurements.

Element	Co	Ni	Cr	Al	Re
Wt. %	26	45	18	9	2

7.2 Two Dimensional Electron Back Scatter Diffraction

The component studied within this work is the same blade that is the subject of discussion within Chapter 6. Initially the area of interest was characterised using 2D techniques including EBSD, in order to collect quantitative crystallographic information. Figure 7.1a shows an image quality map of the region of interest, darker regions show areas of poor pattern quality; this is influenced by the composition of a region, specific phases often result in lower quality EBSD patterns (34). Figure 7.1b shows an inverse pole figure (IPF), it can be seen that within the area of interest both the coating and substrate are present, it must be noted that the substrate and coating have different compositions. The substrate grain size is significantly greater than within the MCrAlY layer. In Figure 7.1c a phase map based on crystallographic information is shown, due to the similarity in the lattice parameter of the gamma and gamma prime phases the software used to process the data, which consisted of 400,000 data points, is not able to distinguish between the two phases. The area shown in green, therefore, consists of both gamma and gamma prime, the beta phase is shown in red. It can be observed how there is a depletion region of the beta phase at the coating interface and also at the outer edge of the coating towards the oxide interface.

.

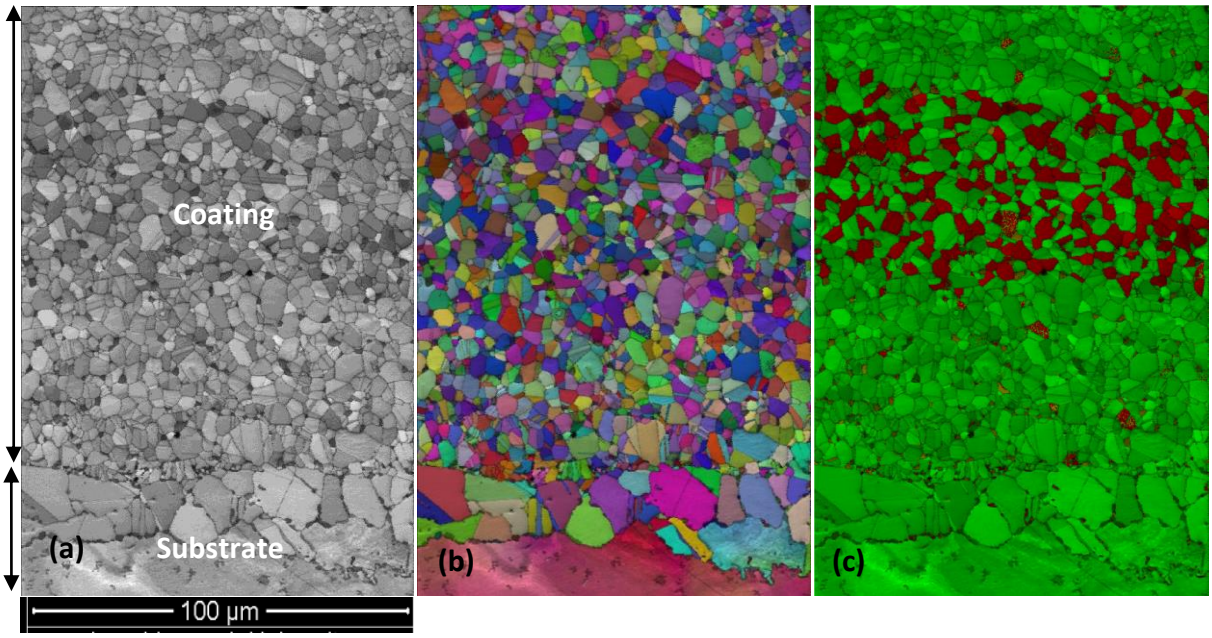

Figure 7.1 (a) 2D EBSD image quality map, (b) inverse pole figure map and (c) a phase map, collected within the IDZ of an ex-service blade. The phases shown within (c) are gamma/gamma prime in green and beta in red. EBSD is unable to distinguish between gamma and gamma prime due to their crystallographic similarities.

7.3 Thermodynamic Calculations

As it was not possible to distinguish between the gamma and gamma phases using crystallographic information, therefore, the chemistry of the phases was studied. Thermodynamic equilibrium calculations were initially carried out for the MCrAlY coating that was applied to the blade to calculate the predicted chemical compositions of the individual phases. It can be seen in Figure 7.1c how only two phases appear to be present in the micrograph. However, it can be observed from thermodynamic calculations in Figure 7.2 that within the temperature window of interest it is possible for more than two phases to be present. Figures 7.3 and 7.4 show the composition of the gamma and gamma prime phases. It can be seen how Ni, Al, Cr and Co have distinctive concentrations that make it possible to discriminate between gamma and gamma prime based on chemical composition within a region of the MCrAlY coating where both phases are present. Figures 7.5 and 7.6 show the composition of the beta and sigma phases, from which it can be observed that the Al, Co and Cr level within beta show differences from gamma and gamma prime and how the sigma phase is rich in Cr. It should be noted that the Ni concentration within gamma prime and beta is very similar, therefore Ni data should not be used to discriminate between these phases.

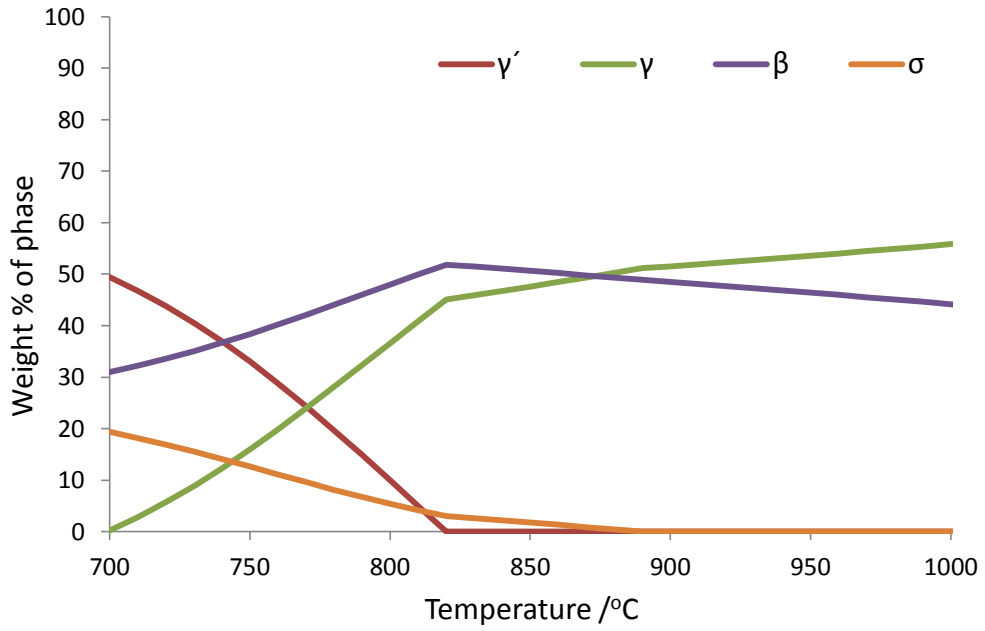

Figure 7.2 Thermodynamic equilibrium calculation results for the temperature range 700-1000°C for the coating applied to an ex-service blade of composition Co 26, Ni 45, Cr 18, Al 9, Re 2 Wt %. The graph shows the Wt % of phase predicted and how it is predicted to change with temperature.

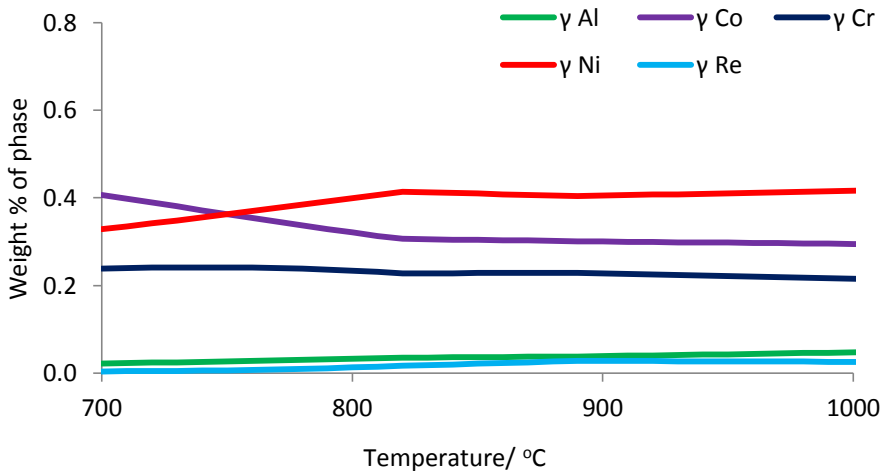

Figure 7.3 Thermodynamic prediction of the composition of the gamma phase within the blade coating of composition 9 Al, 26 Co, 18 Cr, 45 Ni, 2 Re Wt. %.

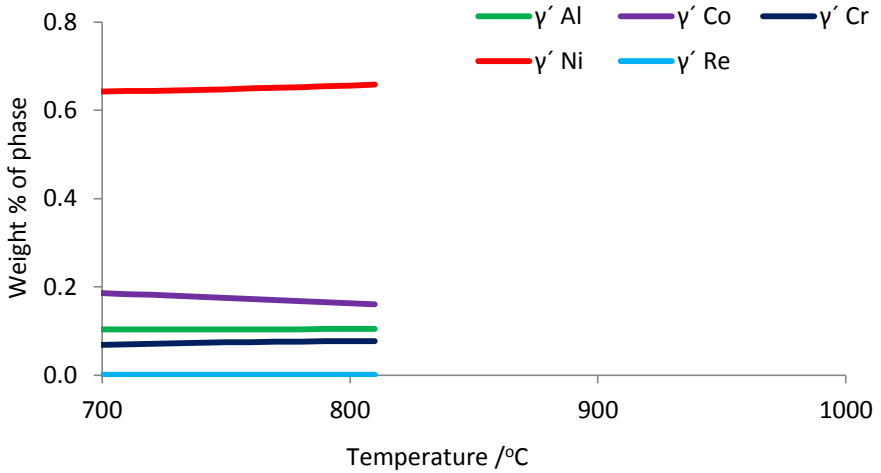

Figure 7.4 Thermodynamic prediction of the composition of the gamma prime phase within the blade coating of composition 9 Al, 26 Co, 18 Cr, 45 Ni, 2 Re Wt. %.

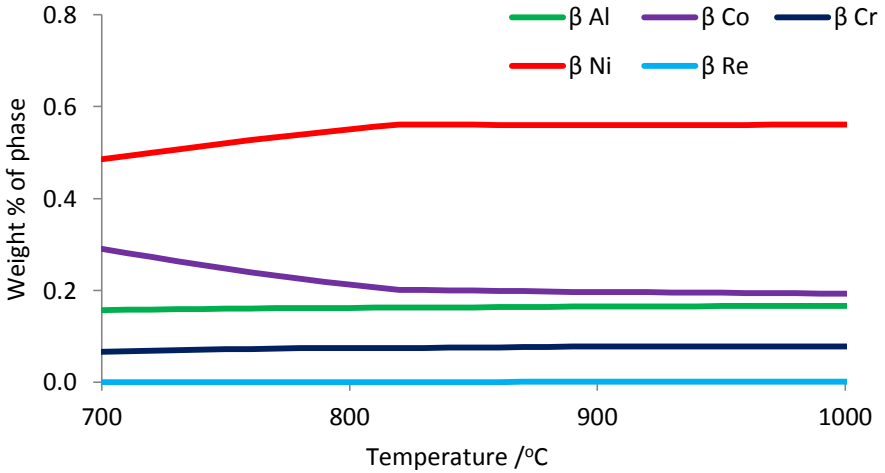

Figure 7.5 Thermodynamic prediction of the composition of the beta phase within the blade coating of composition 9 Al, 26 Co, 18 Cr, 45 Ni, 2 Re Wt. %.

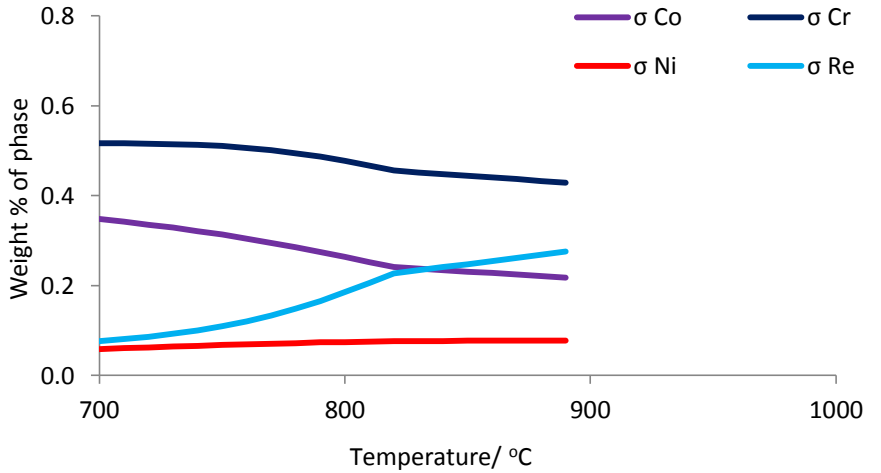

Figure 7.6 Thermodynamic prediction of the composition of the sigma phase within the blade coating of composition 9 Al, 26 Co, 18 Cr, 45 Ni, 2 Re Wt. %.

7.4 Two Dimensional Energy Dispersive X-Ray Spectroscopy

Thermodynamic equilibrium calculations show distinctive differences in the chemistry of the phases present. EDS was carried out and elemental maps showed the different phases present in line with the thermodynamic predictions. The EDS maps for Ni, Al, Co and Cr are shown in Figure 7.7a-d. The elements for EDS analysis were selected using the results of thermodynamic calculations, and were chosen so that they would assist in the identification of individual phases. The EDS maps presented show that it is possible to distinguish between phases using the chemistry information as multiple regions of varying composition are present. It can be seen that there are four individual regions of unique chemistry within the region of interest. Different elements highlight each phase better than others due to the differences in concentration within each phase. It can be seen how the Ni and Cr information show the small sigma precipitates clearly, and how the Al information highlights the Al rich beta phase. By combining the chemistry of multiple elements and using the known composition of the individual phases a phase map based on EDS data can be derived as shown in Figure 7.7e. Beta (yellow), gamma prime (green), gamma (purple) and sigma (red) can be identified. By constructing the phase map it can be seen how the area of interest is a complex multi phase region. EBSD in 2D does reveal information about the phases present and their distribution, but 2D characterisation does not provide information about topological properties including phase morphology and interconnectivity; both attributes have an effect on coating performance.

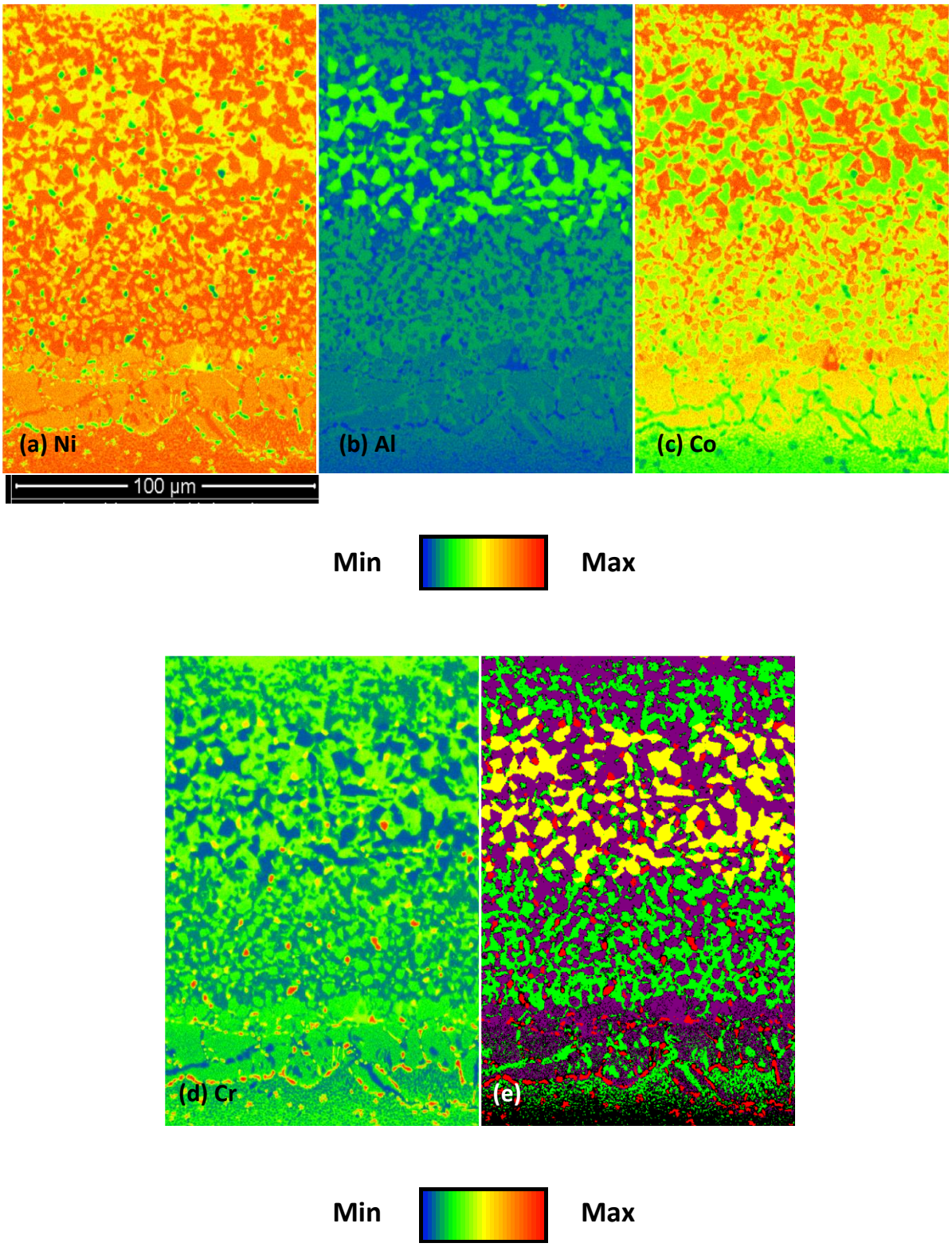

Figure 7.7 EDS maps for Ni (a), Al (b), Co (c) and Cr (d) of the region of interest within the MCrAlY coating, (e) shows a combined phase map where the different phases are derived using collected EDS data. The phases present are beta (yellow), gamma prime (green), gamma (purple) and sigma (red).

7.5 Three Dimensional Characterisation

In sections 7.2 and 7.4 it was shown that combined EBSD/EDS is a powerful technique for studying multiphase regions in coatings. The ability to extend this analysis into 3D to provide phase morphology and interconnectivity information is highly desirable and can be achieved with recent developments of 3D combined EBSD/EDS (35).

7.5.1 Sample Preparation

To characterise microstructures using 3D EBSD/EDS advanced preparation of the sample edge is required, and initially a process is carried out to isolate the volume of interest. In Figure 7.8 the area of interest within a coated Ni-based superalloy is shown, and it can be seen how the area is revealed using the FIB. This procedure is carried out so that during slice milling processes the material that is removed does not redeposit at the edge of the cutting surface that can block both the EBSD and/or EDS signals. A 500 nm thick platinum cap is applied to the top layer of the sample, in order to homogenise the surface that is to be milled.

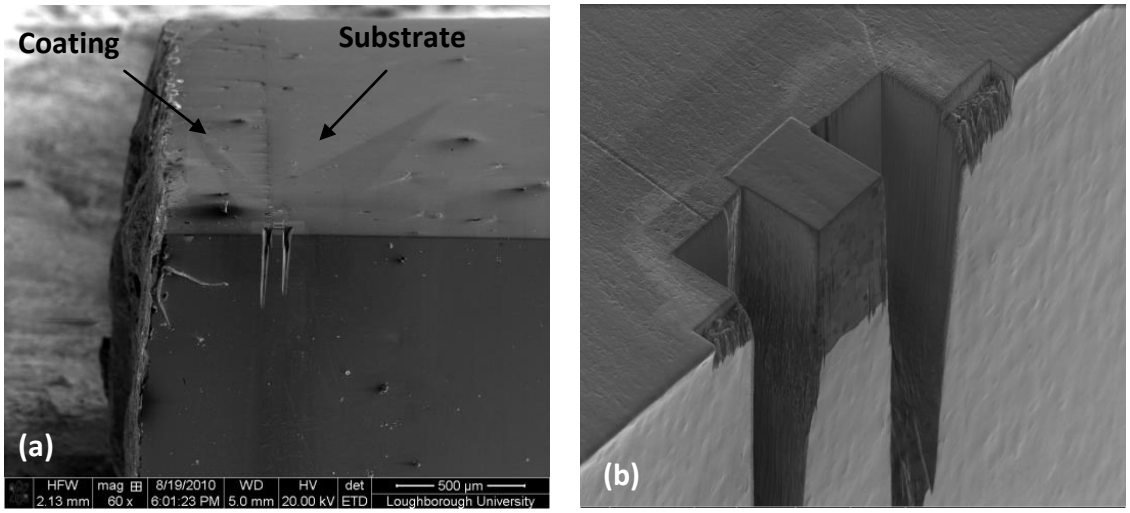

Figure 7.8 In this figure sample preparation for 3D characterisation revealing the region of interest using the ion beam is shown. A platinum layer can be observed in (b) that is used to help homogenise the cutting of the surface, both images were taken during the setup for 3D characterisation.

7.5.2 Sample and System Setup for Combined EBSD EDS

Figure 7.9 shows inside the microscope chamber and it can be seen that the EBSD camera and FIB column are on the same side of the chamber. This configuration results in the requirement for a 180° stage rotation between FIB milling and EBSD/EDS data acquisition positions; the FIB column is positioned at 52°. Figure 7.10 shows how a pre-tilt angle of 36° for ion milling and 54° for EBSD/EDS allows a stage tilt of 16° to be used for both the ion beam and EBSD/EDS positions. EBSD information is collected at 70° for optimum data collection.

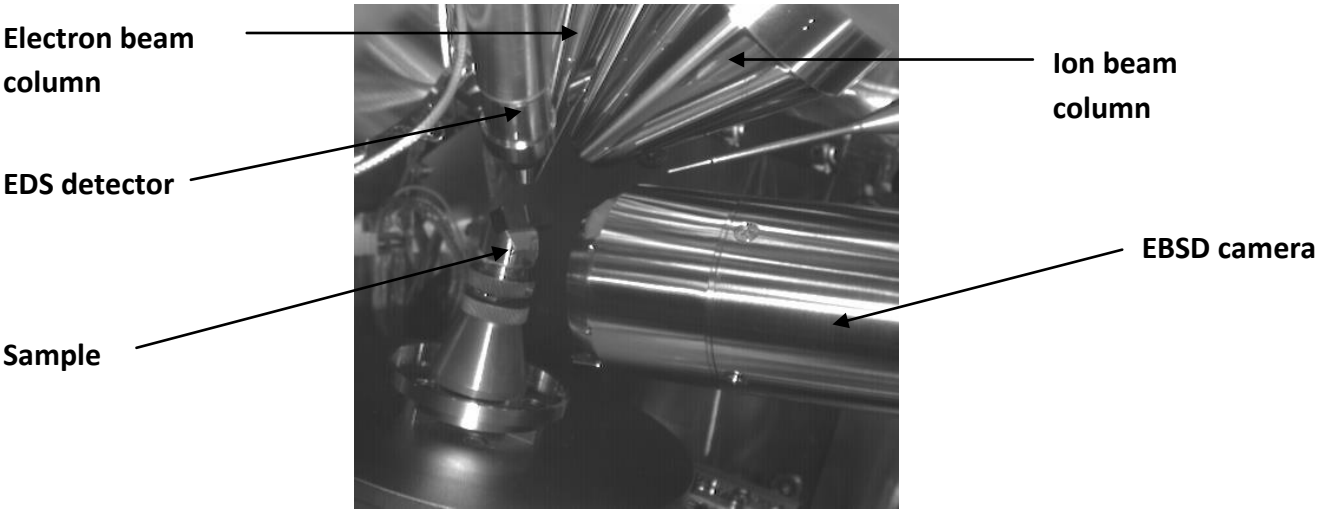

Figure 7.9 The view within the FEI Nova 600 Nanolab microscope chamber, the electron column, EDS detector and the ion beam column inclined to 52° can be observed. Also of note is the position of the EBSD detector and ion column on the same side of the chamber resulting in the need for a 180° rotation in between milling and EBSD positions.

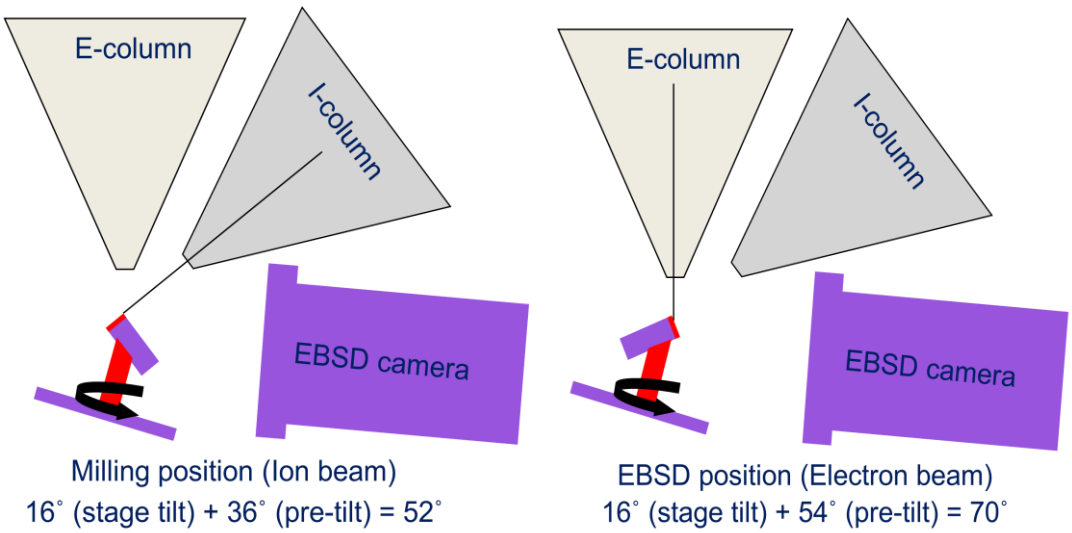

Figure 7.10 A schematic highlighting the sample and pre tilt angles and how a stage tilt of 16° results in only a 180° rotation of the sample required between milling and EBSD positions.

As a stage rotation is required, accurate repositioning of the sample is crucial to the ability of collecting data to represent a full volume. To aid in the repositioning of the sample two fiducial markers are used, they consist of two circles of different diameters milled adjacent to the surface that is to be characterised, as shown in Figure 7.11. Stage movements are used to make large movements, then beam shifts are used to reposition the sample relative to the fiducial markers accurately into to the positions pre-defined during the setup. The markers are used to reposition for milling of the surface and also EBSD/EDS. The repositioning accuracy is routinely found to be within 1 pixel, which is magnification dependent, but typically results in a repositioning accuracy of 100 nm. After sample preparation is complete the FIB is used to mill the surface of the sample to reveal the first region of interest. The number of slices to collect information from, to represent a chosen volume is selected; the typical slice thickness is 250 nm. After revealing the first surface for characterisation a rotation of 180^{o} is then used to allow for the data acquisition parameters for EBSD and EDS to be defined. This process is similar to 2D EBSD/EDS, however, the parameters are then repeated for each subsequent slice. Within the example presented in this work the EBSD/EDS maps were collected for dimensions 50 µm x 40 µm with a defined depth of 18.5 µm based on 74 slices of data with a individual slice thickness of 250 nm.

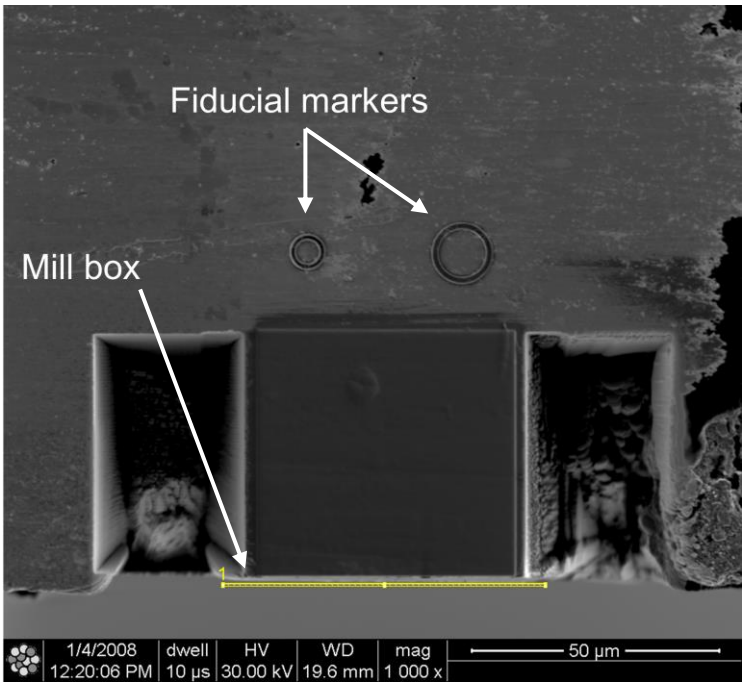

Figure 7.11 An image highlighting the fiducial markers used to aid in the repositioning of the sample in between milling and EBSD positions. The mill box highlights the area of material removed to reveal the first surface to be characterised by EBSD/EDS.

A key strength of the system used to collect the data presented within this work is the ability of the microscope to be able to communicate with non-integrated third party software. Upon the completion of the initial slice setup the data collection is fully automated, the cycle that is used to collect a volume of data is highlighted in Figure 7.12. After the initial setup is completed the surface is milled to reveal the first slice of interest, both EBSD and EDS information is collected using the EDAX EBSD software. Upon the completion of the first data set the microscope then takes control and the sample is repositioned as shown in Figure 7.11, the repositioning is used so that the region characterised can be milled and a new area of interest revealed. The sample then moves back to the EBSD position and the EBSD system is engaged, the second data slice is then collected. This process is then repeated until a full volume is analysed. Upon the completion of the data acquisition process the data is exported as a series of 2D datasets for the predefined number of slices. The data is then realigned using OIM Analysis 5 software and the EBSD and EDS data converted to be exported as input files into 3D visualisation software for post-processing and to display the series of 2D data in a 3D format. The data processing techniques are detailed in section 7.5.3.

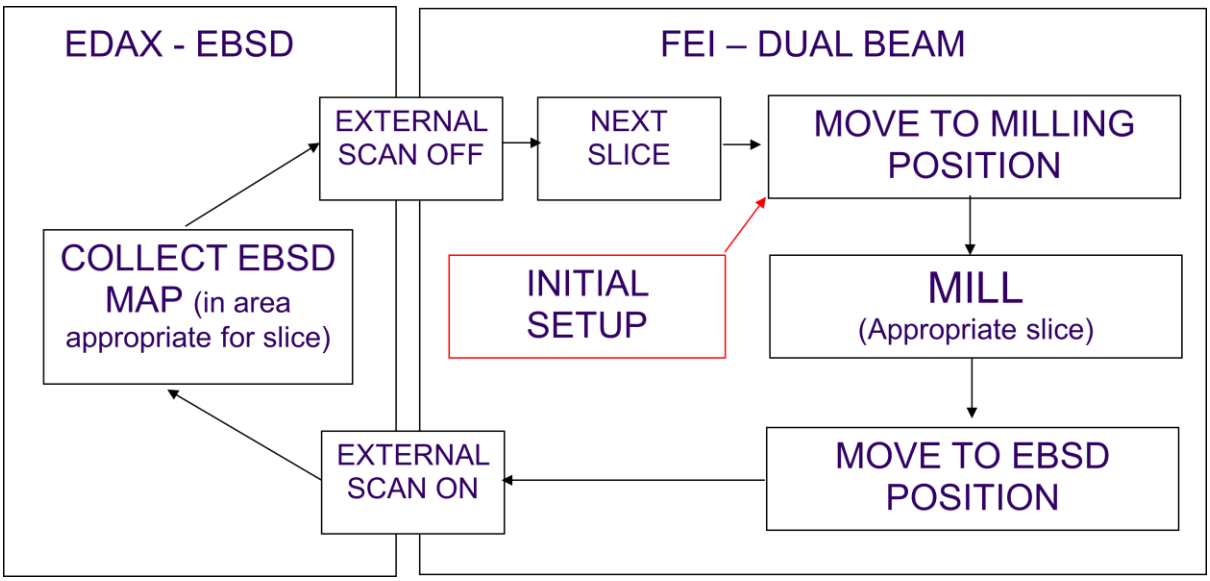

Figure 7.12 A schematic diagram outlining the individual processes carried out during the collection of 3D EBSD/EDS information. This layout highlights the two systems that are not integrated, and shows that during the automated data acquisition process separate systems are able to communicate.

7.5.3 Characterisation of a NiCoCrAlReY Coated IN738LC Ex-Service Blade

In this work a volume of interest was analysed in an ex-service industrial gas turbine blade. The specific region of interest was in the multi-phase interdiffusion zone that occurs at the substrate/MCrAlY interface, although the region chosen is in the original coating material, this region is highlighted in Figure 7.13. 2D analysis of the same component in section 7.2-4 showed that the coating consists of four phases; beta, gamma prime, gamma and sigma. Combined 3D EBSD/EDS information was collected across the region of interest using the technique discussed in sections 7.5.1 and 7.5.2. It can be seen within the micrograph how the beta phase, which appears as the dark region, shows an area of depletion at the substrate side of the coating, this depletion region falls within the region of interest for 3D characterisation.

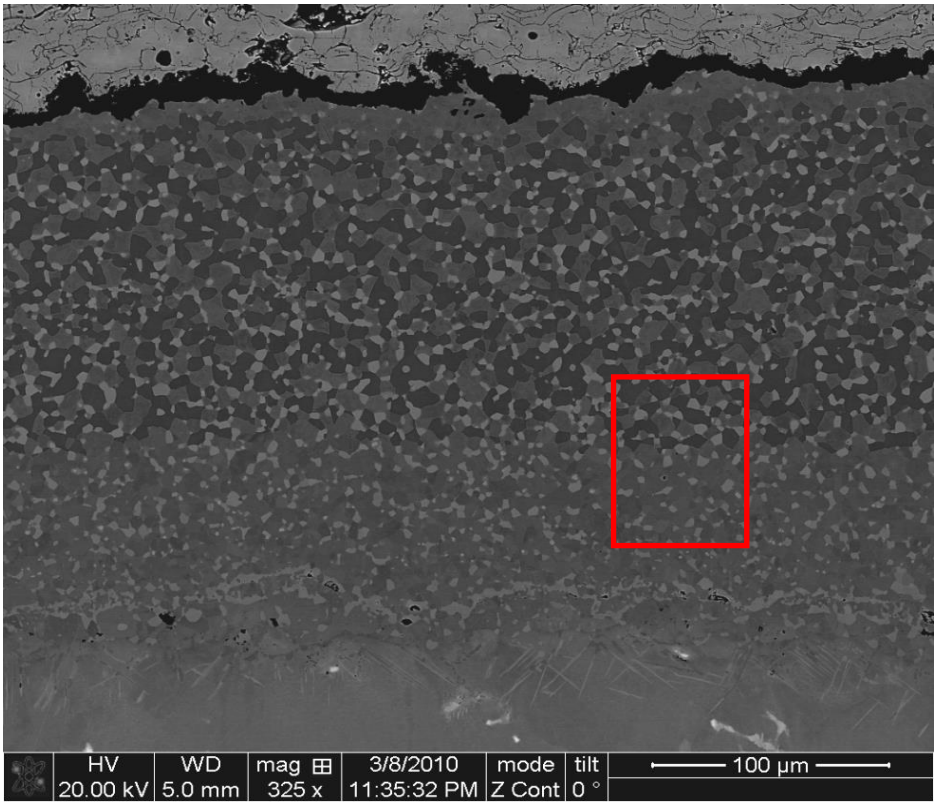

Figure 7.13 A backscatter image of the MCrAlY coating applied to an ex-service industrial gas turbine blade is shown. The area of interest characterised using the 3D technique is highlighted. The beta and sigma phases appear as the dark and bright regions respectively.

The region of interest consisted of 74 slices of data, each slice consisting of an area 50 µm x 40 µm. Data were collected for each slice, of a thickness predefined as 250 nm, enabling a volume of 50 x 40 x 18.5 µm to be characterised. The data were exported as a series 74 2D datasets. The data sets were processed initially using the OIM Analysis 5 software. The software was used to batch process the raw EBSD/EDS data into useable formats. The EBSD data was converted to IPF and IQ maps, the first slice IPF and IQ maps are shown in Figure 7.14. The beta phase can be observed as the dark grey region within Figure 7.14b and sigma as the black region resulting from poor pattern quality.

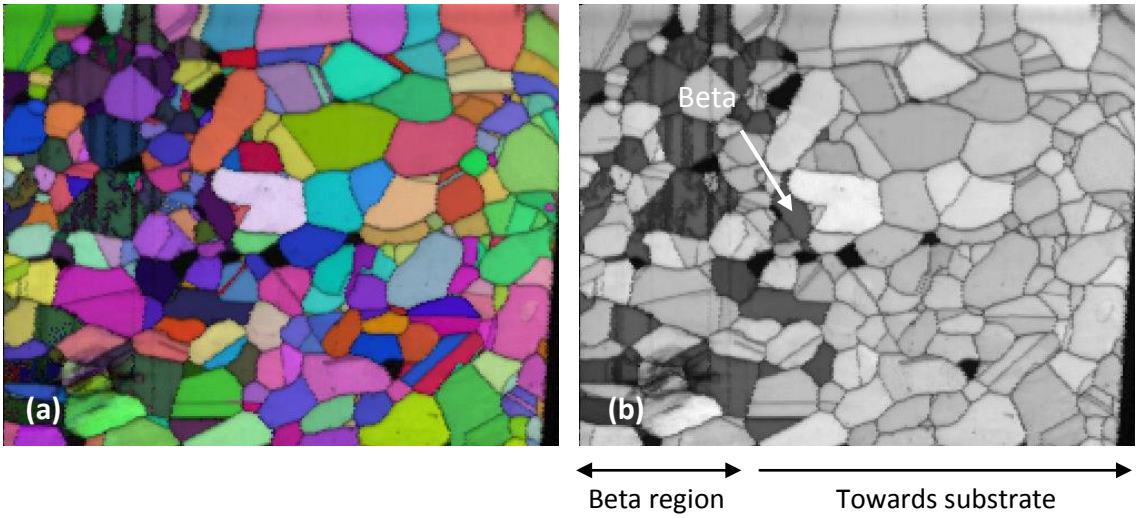

Figure 7.14 (a) IPF map of the first slice of the 3D data set showing the individual grains, the beta phase shows poor EBSD pattern quality within the (b) IQ map.

Due to the similarity in the lattice parameter of the gamma and gamma prime phases it was shown within section 7.2 how EBSD alone is not able to distinguish between the two phases. Therefore, chemistry information was collected during the 3D data collection procedure that can be used to discriminate between each phase. The elements chosen were Al, Co, Cr, Ni and W. Al was identified as a key element to segment the gamma, gamma prime and beta phases and W for distinguishing the sigma phase. Figure 7.15 shows the equivalent chemistry information for the slice of data presented in Figure 7.14. The Al distribution shows that it is possible to observe the individual gamma and gamma prime phases. The beta phase can be observed with a high concentration of Al and the gamma phase with the lowest Al concentration. The Al concentration within the gamma phase results in some overlap with the sigma phase; this highlights the need for multiple element data.

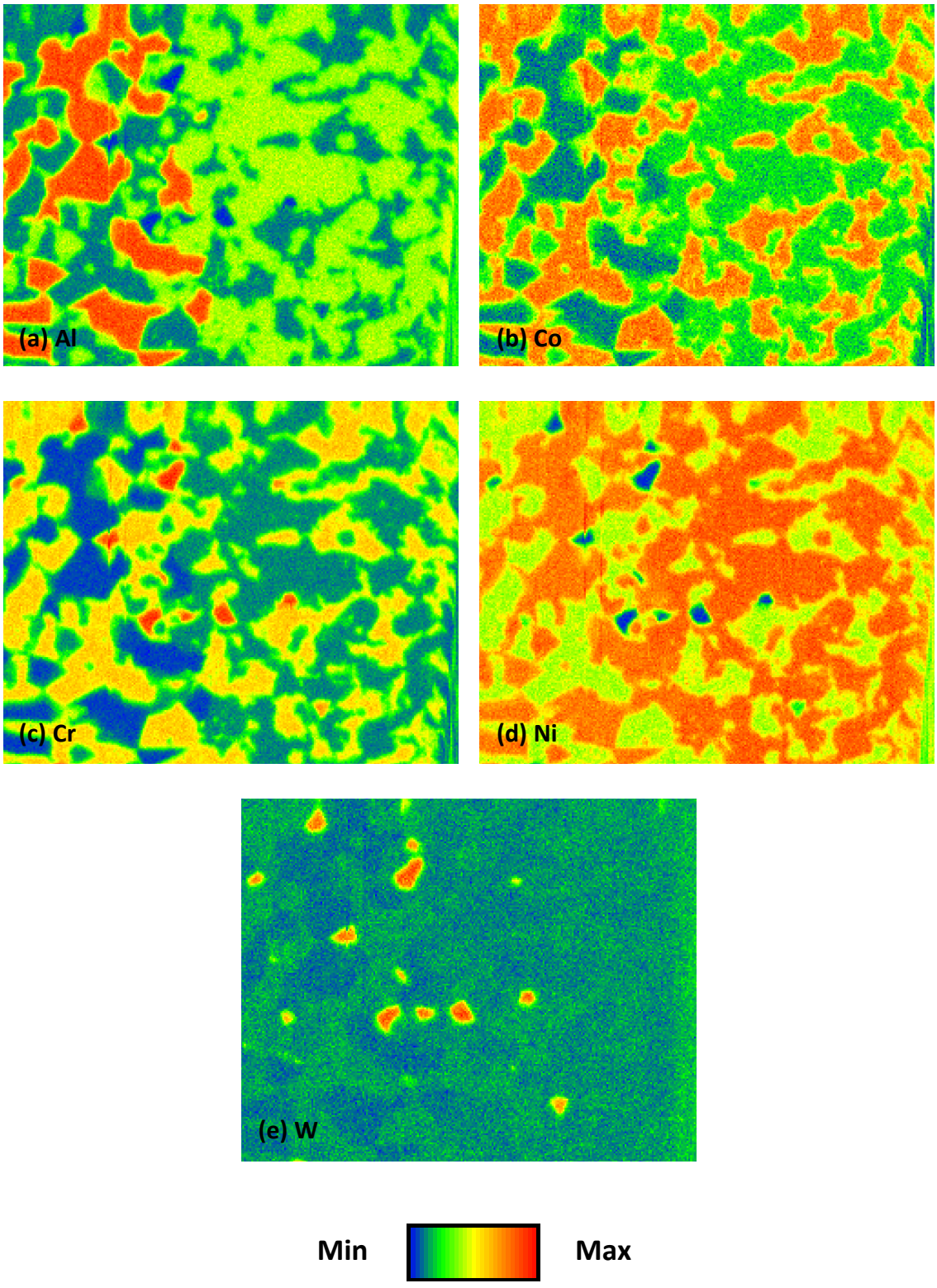

Figure 7.15 This figure shows colour EDS images for five elements collected during the 3D characterisation process. The images were generated from the first slice of the dataset. The data show the distribution of the elements Al (a), Co (b) , Cr (c), Ni (d) and W (e).

7.5.4 Processing of Data to Reconstruct in Three Dimensions

The EDS data were converted to greyscale to allow for input into Avizo 6.0 image processing and visualisation software. The EDS data were imported as individual slice data sets for each element. Each dataset consists of 74 slices of data, the slice thickness of 250 nm is important in the reconstruction process. The voxel size can be determined in XYZ directions based on the pixel size of the EDS maps and the sample slice thickness. In this set of data the area of interest was 50 µm x 40 µm, the slice thickness was 250 nm and 74 slices of data were collected, resulting in a 18.5 µm Z depth. The Z voxel can then be calculated from the ratio of pixels to actual measurement in µm in the X/Y directions. When the voxel size has been defined the greyscale images can then be segmented using a histogram contrast method.

It can be seen within Figure 7.16 how the individual beta, gamma prime and gamma phases can be identified within a single Al EDS data slice. To segment the beta phase areas of high Al concentration, which appear as the bright regions, are selected. This is carried out by using a contrast discrimination tool where individual parameters can be set and then applied to the full data series of 74 slices. Figure 7.17 shows how by identifying the beta phase using the Al data the phase can be segmented from the full series of data. Figure 7.18 highlights the beta phase segmented throughout the volume, this process can be repeated for each phase present, for the Al EDS data this includes the gamma prime and gamma phases. To identify all of the phases present multiple chemistry information can be used and combined within the reconstruction software. In the dataset presented the W data was used to identify the sigma phase throughout the volume of interest.

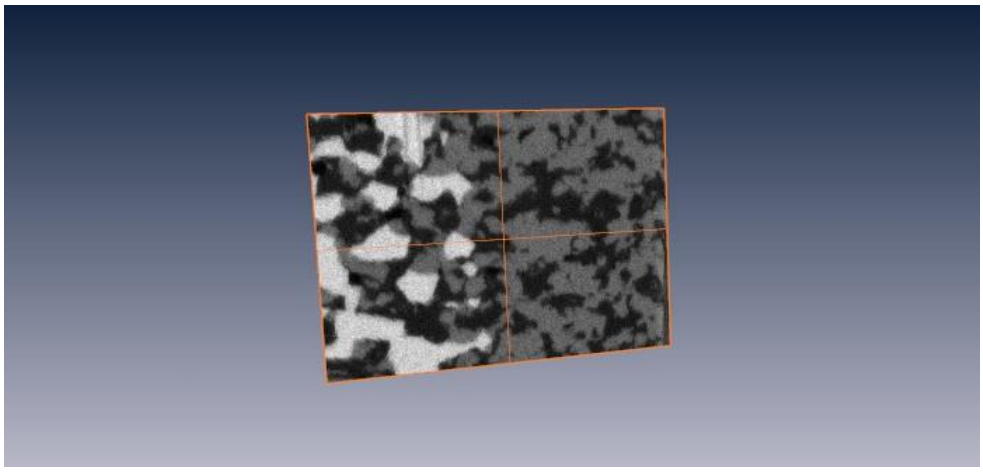

Figure 7.16 A single greyscale EDS Al data slice of 50 x 40 µm in Avizo, the contrast difference between each phase can be observed. A contrast histogram tool can be used to select the individual phases.

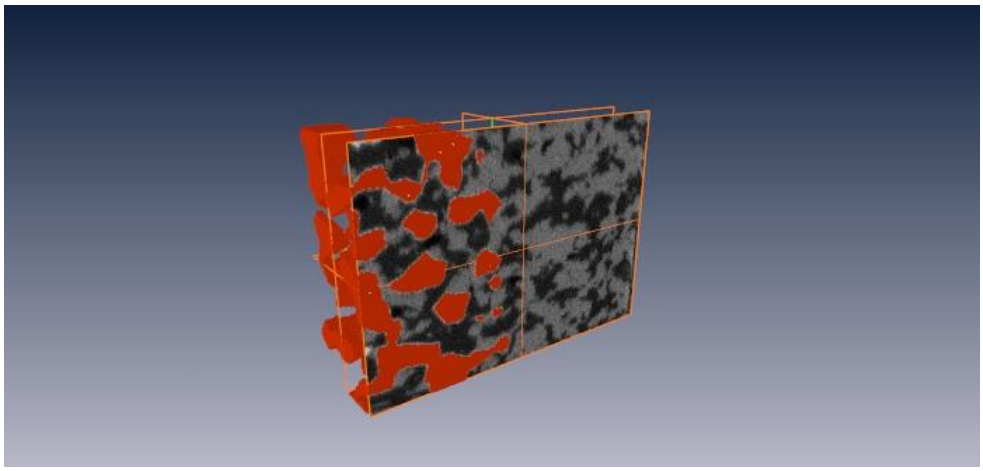

Figure 7.17 Using a contrast segmentation tool the beta phase which appeared as the bright phase high in Al content is selected throughout the full dataset. The Z depth can be observed for the first time.

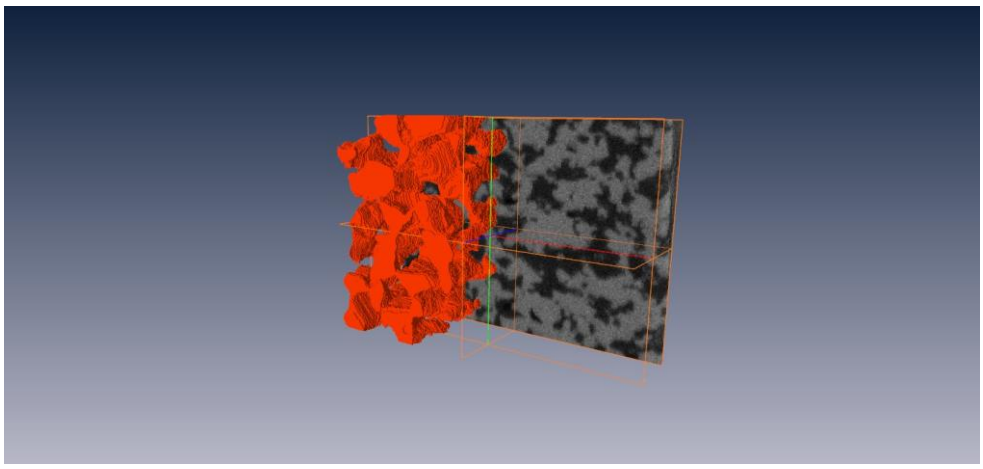

Figure 7.18 A full reconstruction of the beta phase, the depletion region can be observed on the right hand side of the reconstruction, this is towards the coating substrate interface as observed in Figure 7.13.

7.5.5 Three Dimensional Reconstruction of NiCoCrAlReY Coated IN738LC

Using the Al EDS information and segmenting the beta, gamma prime and beta phases, the data can then be used to reconstruct the phase microstructures in 3D. The individual phase reconstructions in Figure 7.19 show microstructure topological and morphological properties that are not able to be identified from conventional 2D analysis. The beta phase reconstruction shown in Figure 7.19a appears to show full phase interconnectivity. The phase interconnectivity can influence the mechanical properties and performance of the coating.

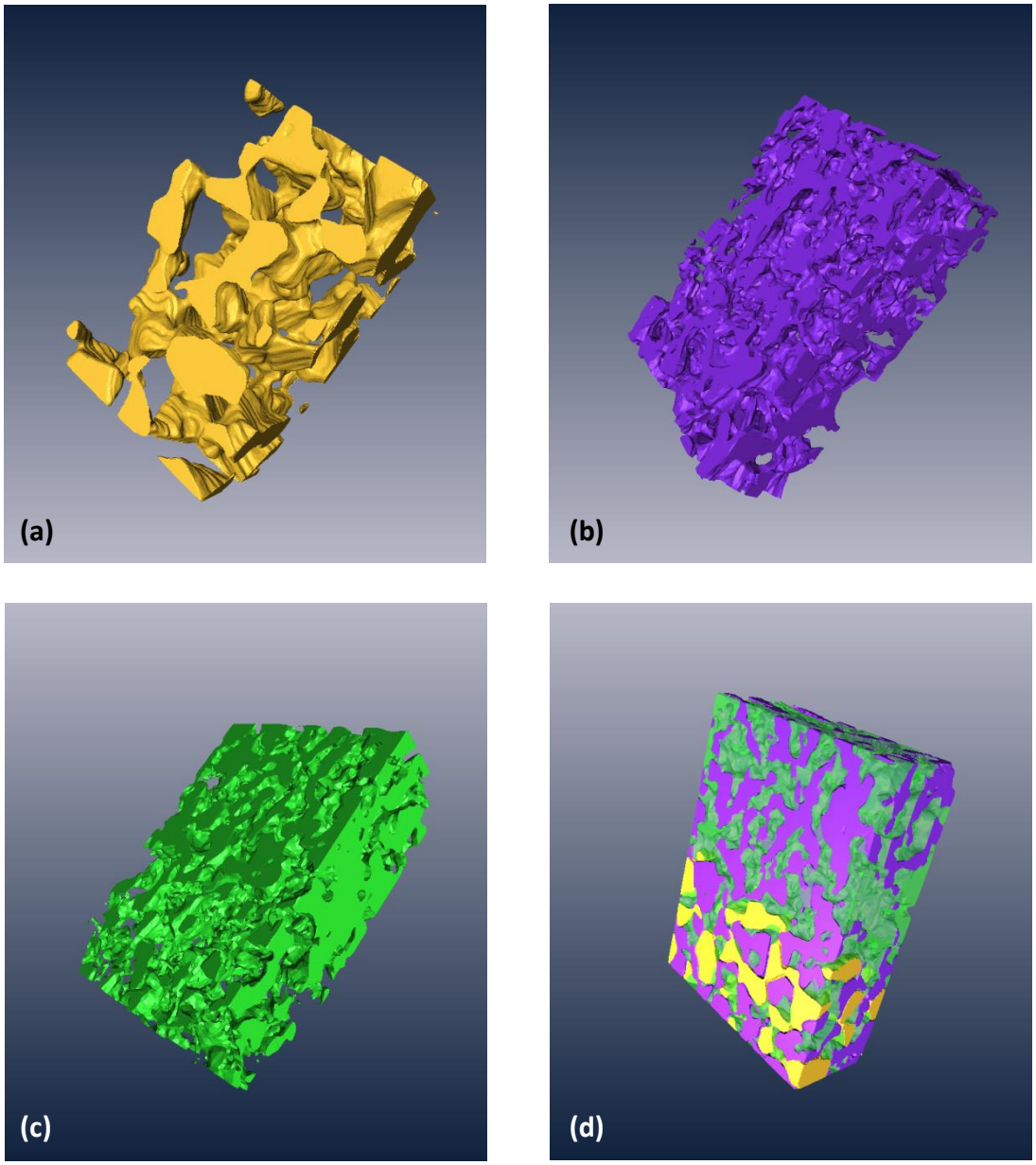

Figure 7.19 Reconstructions of the (a) beta, (b) gamma and (c) gamma prime phases in 3D using the Al EDS data. The phases can be combined to show the volume of microstructure in 3D as shown in (d). The dimensions are 50 x 40 x 18.5 µm.

The depletion of the beta phase can be observed in Figure 7.20a, the substrate/MCrAlY interface is towards the right of the reconstruction showing a beta depletion zone that occurs as elements diffuse across the interface. The full connectivity of the beta phase can also be observed within this figure. By combining multiple chemistry information a multi-phase region can be reconstrucuted. In this work the TCP sigma phase is present, using the W data the sigma phase was reconstrucuted, and in Figure 7.20b it can be seen how the sigma phase is dispersed throughout the volume in isolated regions. It can be seen how the volume fraction of sigma is greater in the region where there is no depletion of the beta phase.

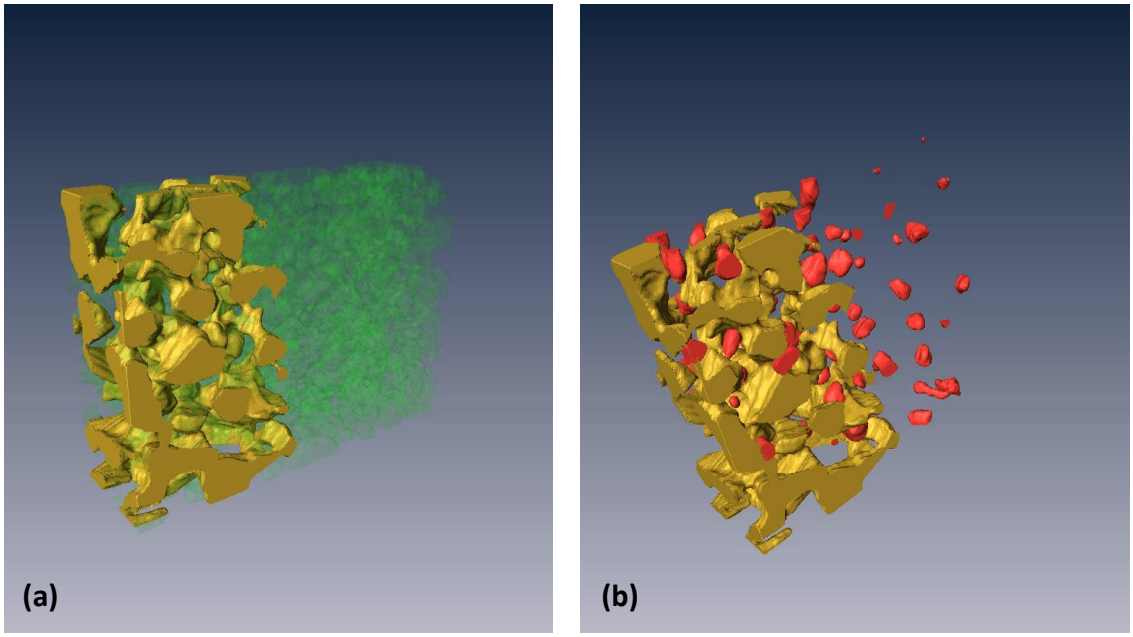

Figure 7.20 The reconstruction (a) shows the interconnectivity of the beta phase in gold, the gamma prime phase is shown in green. In the second reconstruction (b) the TCP phase sigma is present. The sigma reconstruction was carried out using the W data.

The reconstructions formed can be used qualitatively to observe topological properties, however, in order to be able to use the technique to compare coating performance and microstructural evolution quantitative analysis is required. The beta phase reconstructions presented appear to show a phase that is fully interconnected. It was calculated that the beta reconstruction consists of six independent bodies within the volume characterised. As a small volume of material was characterised from a much larger volume of coating it is possible that the isolated regions observed at the edge of the bounding box are in fact fully interconnected within the bulk of the material. By defining the interconnectivity of the phase and the volume fraction it will improve the level of characterisation in 3D and comparisons with microstructure models.

The Euler characteristic of the beta phase can be defined from the reconstructions. The Euler-Poincare number, X, defines the topological characteristic of a structure. It is defined by the number of Vertices, Edges and Faces as: $X = V – E + F$. Structures that have the same number of connected bodies irrespective of the shape are defined by the same Euler characteristic, therefore it can provide information as to the interconnectivity of phases in comparison with volume fraction information. The genus, which is the maximum number of cuts required to disconnect a body without dividing it into two separate bodies, can be derived from the Euler characteristic. The genus, g, is defined as: $X = 2 - 2g$ for a closed surface, which is the case in this work as the data was collected within a defined volume. In this work the Euler characteristic was derived from Avizo software to be $X = -35$, therefore the genus was calculated to be 18. Studying topological properties can enable a comparison between the changes in connectivity of the same phase under different service conditions; the topological properties can be combined with geometric measurements to quantify the 3D properties of phases. A comparison can be made between volume fraction calculations from 2D data with volume fraction information derived from 3D reconstructions. Chemistry data collected in 2D were used to derive volume fraction measurements, the mean values are presented in Table 7.2 for each phase based on 74 individual calculations. The Al 2D EDS data were used to measure the volume fraction of beta, gamma prime and gamma phases, and the W data used for sigma by taking area fraction measurements. In addition to the Al data, other element data sets were used to confirm the beta, gamma prime and gamma measurements, these included Co for beta, Co and Cr for gamma prime and Co and Ni for gamma. The sigma data were confirmed by using the Cr and Ni data in addition to W. The choice of element was based on the contrast difference within the datasets. The data used correlated with thermodynamic calculations in section 7.3 where it can be seen from the results which elements show the greatest range of concentrations within the individual phases, resulting in the greatest contrast difference within the greyscale EDS data sets. The 2D volume fraction can then be compared with a volume fraction derived from the 3D microstructure reconstructions in Table 7.2. It can be seen how the 3D volume fraction measurements do correlate with the 2D information which is to be expected as the same initial data is used, it does, however, show that the processing of individual 2D data slices to full microstructural reconstructions is able to represent accurately the microstructure characterised in 3D.

Phase	Volume % from 2D	Volume % from 3D
Beta	14.22%	13.56%
Gamma Prime	48.11%	44.88%
Gamma	35.67%	39.94%
Sigma	1.78%	1.63%

Table 7.2 The volume of phase based on 2D information, which was derived from the individual EDS slice datasets for multiple elements, and a mean value is shown for each phase. The 3D reconstruction value was calculated using information obtained from the reconstructions within the Avizo image processing software.

Within Figure 7.21 the multi phase region within the interdiffusion has been reconstructed. All four phases present have been reconstructed and it has been shown how topological and geometrical measurements have been made. Within the reconstruction present multiple chemistry data was used and combined within the image analysis software to allow for a multi phase coating to be characterised qualitatively and quantitatively in 3D.

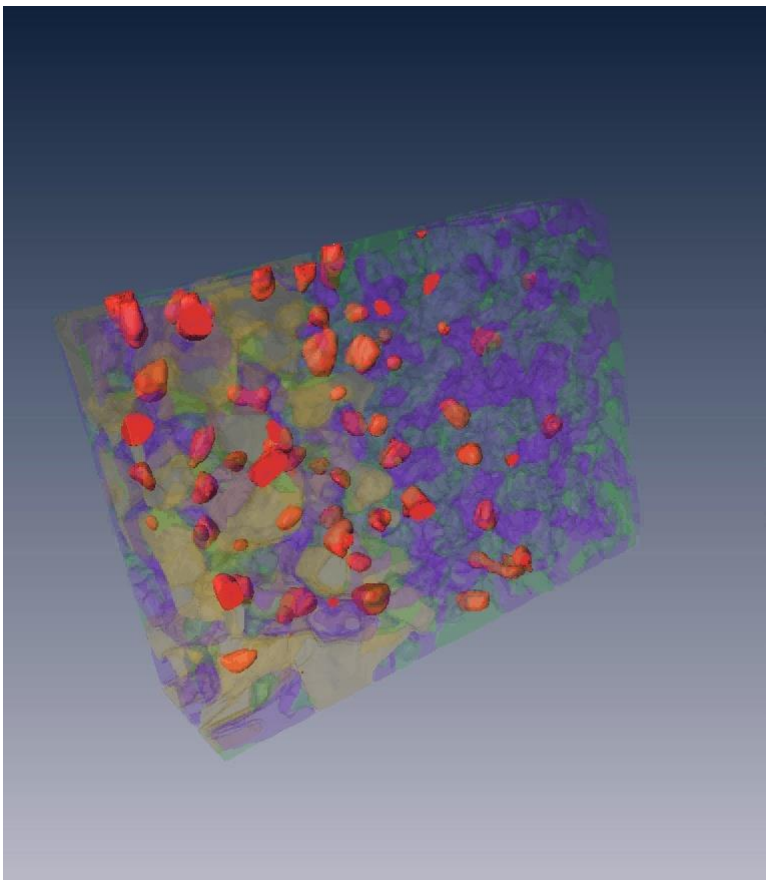

Figure 7.21 A full reconstruction of the volume including the beta (gold), gamma prime (green), gamma (purple) and sigma (red) phases. The reconstruction was carried out using Avizo 6.0 software.

7.5.6 Generating Mesh Reconstructions

A key driver for characterising microstructures in three dimensions was the requirement for accurate input data into microstructure models. Previously, idealised grain shapes have been used to represent a bulk microstructure. It has been observed within this study that the grains within the coating are not 'ideal' and it has revealed topological properties including phase interconnectivity. An example is shown within Figure 7.22 of a fine mesh generated from the reconstruction of the beta phase. The mesh format generated can be used as an input into various forms of commercially available finite element solvers. A potential limitation of the reconstructions generated is the number of points/nodes used to form the reconstruction. This can be adjusted during the meshing procedure, a smoothing tool can be used to reduce or limit the number of nodes used to generate a mesh for a specific volume. The complexity of the FEA mesh can have a significant impact on the simulation time of the models used. Figure 7.23 shows a sample area of the beta phase, a smoothing function was applied to the data shown to reduce the number of co-ordinates for the sample area, the tetrahedral polygons that define the mesh can be observed. This can be compared with the microstructural reconstructions where visualisation techniques were used that maximise the data available to reconstruct to the greatest resolution attainable from the data.

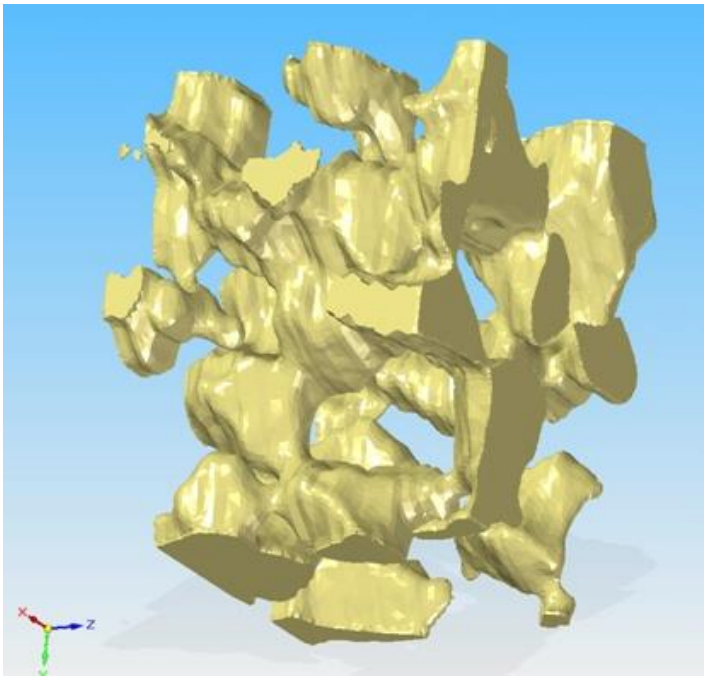

Figure 7.22 A mesh reconstruction of the beta phase. The mesh was generated within the Avizo software and is able to be used as an input file into Finite Element Analysis software.

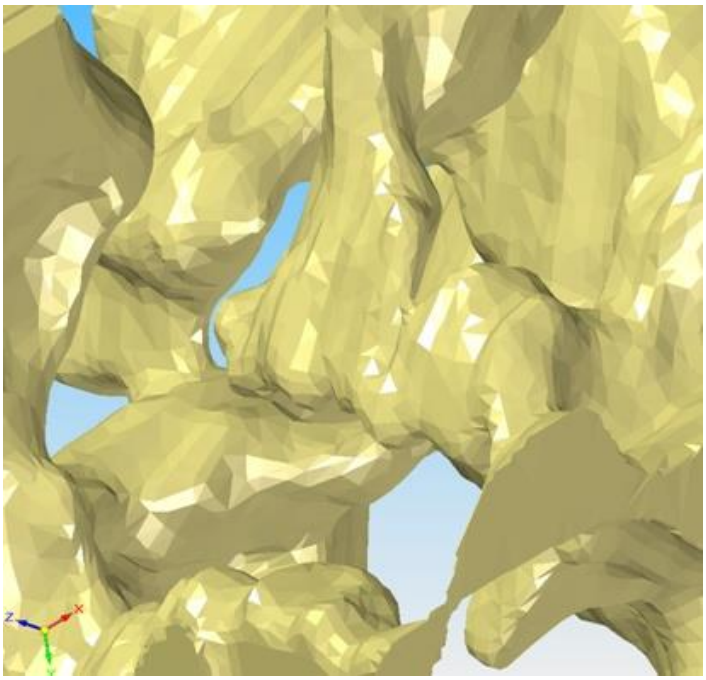

Figure 7.23 The tetrahedral mesh can be seen within this figure. The mesh shown was simplified within Avizo to reduce the number of nodes within the dataset.

7.6 Conclusions

It has been seen within this chapter how a technique has been developed that allows for a multiphase coating to be reconstructed in 3D. The technique uses a fully automated collection procedure to collect 2D data across a number of slices, and the data collected and then used to form a 3D reconstruction. Offline processing of the 2D data is shown to be an important step in the ability to be able to obtain microstructural information about a volume of material. It is shown how characterising in 2D does have several limitations and it is not possible to accurately provide information in the third dimension. In this piece of a work the interdiffusion zone in a coated ex-service blade was characterised using a combined 3D EBSD/EDS technique, the data acquisition steps are a key strength in the ability to collect information for a bulk region of a microstructure. It was also shown that alongside qualitative visual representations of the microstructure, quantitative characterisation can be carried out.

It was shown how the beta phase within the coating has a high level of phase interconnectivity, which was not previously apparent from 2D characterisation techniques. The volume fraction and topological measurements, including the Euler characteristic, were derived in 3D and the volume fraction information showed a strong agreement with volume fraction information calculated from 2D data.

In addition to analysing the volume of the microstructure collected, the data can be used as an input into microstructure models. Previously idealised grain shapes were used within mechanical properties models but it is seen within this work how the grains within the coating are not ideal and are interconnected. It is shown how the reconstruction can be used to generate a FEA mesh that can then be used to provide accurate grain shape information within FEA based models of mechanical behaviour.

8 Conclusions and Further Work

8.1 Introduction

In this work the microstructural evolution of a series of IN738LC coated samples and components was characterised. The microstructural evolution of the protective coating system consisting of both MCrAlY and TBC layers was investigated. One of the aims of the characterisation was to understand ageing time and temperature effects on the microstructural evolution, so that a methodology could be developed where the characterisation of a thermally exposed microstructure can be used to estimate unknown service exposure conditions. Isothermally aged material was used to benchmark a thermodynamic and kinetic model developed within the research group that is able to predict the microstructure after thermal exposure. A technique was developed that used oxide scale thickness and both inner and outer beta depletion measurements to derive an estimated exposure temperature using the model. The technique has shown that it is possible to measure the microstructural features within a complex coating system and to derive a predicted exposure temperature.

The characterisation of the isothermal samples was also compared with a series of combustion chamber heat shield tiles that had the same protective coating system applied before they were entered into service. The temperature estimation technique was carried out for both the ex-service combustion chamber tiles and also an ex-service stage 1 blade. In parallel with the characterisation of exposed material, a technique was developed that has enabled the reconstruction of a microstructure in 3D, and the quantification of 3D properties.

8.2 Conclusions

The microstructural characterisation of MCrAlY coated IN738LC isothermally aged samples with and without a TBC showed that the rate of oxidation of the MCrAlY layer was dependent on the presence of an outer protective TBC layer. It was found that when only an MCrAlY layer was applied, the thickness of the oxide scale forming was three to four times greater compared to when an additional outer TBC layer is applied. It was found for all samples, with an MCrAlY and both an MCrAlY and TBC coating applied, that as the temperature increased the thickness of the oxide formed increased. A correlation was also observed with the increase in ageing time, however, it was found that the TGO thickness was more dependent on the exposure temperature. The chemistry of the oxide forming was found to be dependent on both the presence of a TBC layer and ageing temperature. When an additional TBC layer was applied the oxide that formed was a dense alumina layer, whereas

when only an MCrAlY layer was applied a range of oxides were formed. When only an MCrAlY layer was applied clusters of Ni, Co and Cr rich oxide were found to be present which also correlated with a significant increase in oxide thickness. Short term ageing showed that the Al layer formed first and after the supply of Al was depleted within the MCrAlY layer regions of mixed oxides formed. However, it was also observed that the thickness of the Cr rich layer decreased as the time period for ageing increased. The surface of the oxide scale was characterised for samples that were aged isothermally for 15 months. It was observed that the oxides forming after exposure at 850 and 900^{o}C consisted of an Al rich layer with localised regions of a Cr rich oxide. After 15 months at 950^{o}C only small traces of a Cr rich layer were present, suggesting that the Cr rich oxide maybe subliming after long term exposure. An oxidation model was used to predict the alumina thickness, and the thickness predictions were compared with the measurements of the alumina scale that had formed after isothermal exposure. It was observed that the model correlation with experimental results was strongest when a TBC coating was applied. This was in agreement with the fact that the original oxidation model used was based on observations on samples which had been exposed with a TBC layer on top of an MCrAlY coating. The study into isothermal samples with and without a TBC present after ageing shows that the TBC layer, although of open porosity, does affect the rate of oxidation of the MCrAlY coating. The beta phase depletion within the MCrAlY layer was also investigated and it was found that when no TBC layer was present, the increase in exposure temperature resulted in rapid depletion of the beta phase at elevated temperatures. Above 900^{o}C no beta was present in any of the isothermal samples, and the oxide layer on the same samples was also found to be rich in Cr, Co and Ni suggesting that the depletion of the Al from within the MCrAlY layer resulted in depletion of the beta phase at the MCrAlY/TBC interface. At the substrate/coating interface diffusion of elements across the interface resulted in depletion of the beta phase. The depletion at both the inner and outer interface was found to be at a similar rate, as symmetrical beta depletion was observed. A combined thermodynamic and kinetic model that was benchmarked using the isothermally aged material was used to predict the microstructure present after thermal exposure. Notably the inner depletion of the beta phase can be predicted by the model. The inner interface was studied as it was found that the outer beta depletion was susceptible to measurement distortion by the severity of the surface roughness of the MCrAlY layer.

The characterisation of ex-service material was then compared with that from the isothermally aged samples. The ex-service and isothermal samples were coated at the same time using the same coating process so that the coating systems were of an identical composition prepared under the same conditions. The ex-service material was in the form of combustion chamber heat shield tiles. The distortion of the tiles was initially characterised and it was found that two neighbouring tiles showed effects of elevated temperature exposure by experiencing distortion at the edges of the tile of ~10 mm. The TBC layer had spalled on both tiles and within the MCrAlY coating the beta phase was fully depleted. Based on the isothermal characterisation this suggested an exposure temperature for both tiles to be above 950^{o}C. The thermodynamic and kinetic model was then used in conjunction with an oxidation model to predict the exposure temperature during service. A temperature estimation correlation was observed, based on independent measurements, between the spallation of the TBC layer, the thickness of oxide scale, if still present, and the depletion of the beta phase. The difference in post-service microstructure of the tiles and the estimated temperatures suggests that there is a variation in service conditions around the combustion chamber.

The temperature estimation technique was also used to determine the exposure conditions of an MCrAlY and TBC coated ex-service component where the thermal history was unknown. The MCrAlY layer was of a different composition compared to all of the other samples characterised in this work. The temperature estimation technique was applied to an ex-service stage 1 blade and it was found that there was ~70^{o}C variation in predicted exposure temperature around the profile of the blade. The highest predicted service temperature of ~900^{o}C was predicted to occur at the leading edge; this was also the only location characterised where the sigma phase was not present, suggesting that it was the only area that had experienced temperatures above 890^{o}C.

A new technique has been developed which enabled the 3D properties of microstructures to be characterised. The technique was possible due to advances in electron microscopy hardware and software. An FEI Nova 600 Nanolab dual-beam focussed ion beam (FIB) / field emission gun scanning electron microscope (FEG-SEM) was used to collect a series of 2D data. The same ex-service blade that was characterised to estimate the exposure temperature in service was used in this work. The multiphase MCrAlY coating was the region of interest characterised in 3D. A fully automated data collection procedure was used whereby after initial setup multiple slices of EBSD and EDS data were collected. The microscope was able to switch between milling and data collection modes automatically; the cycle was repeated in

this work to collect 74 slices of 2D data. The series of 2D data was then stitched together using dedicated off line processing software. Specialist visualisation software was then used to reconstruct the volume of material characterised using the multiple 2D data slices. The 3D reconstruction could then be quantified and 3D properties revealed, including phase interconnectivity. It was possible to observe in this work that the beta phase is fully interconnected within the MCrAlY layer, which could not be previously derived from 2D characterisation techniques. The volume fraction and topological measurements were derived in 3D and the volume fraction information showed a strong agreement with volume fraction information calculated from 2D data. In addition to analysing the volume of the microstructure collected, the data can be used as an input into microstructure and mechanical property models. Previously idealised grain shapes were used within mechanical properties models but it was seen within this work how the grains within the coating are not uniform and are interconnected. It was shown how the reconstruction can be used to generate a FEA mesh that can then be used to provide accurate grain shape information within FEA based models.

8.3 Further Work

In this work a series of microstructural features were quantified, which showed a correlation with ageing time and temperature, and were used to develop a temperature estimation technique for ex-service material. The technique is dependent on a previously benchmarked thermodynamic and kinetic model. There is scope to improve the technique possibly by expanding the range of microstructure features quantified, using known temperature effects including beta phase coarsening. The benchmarking of the model using the quantification of features within the microstructure of isothermally aged material did show that the model is accurately able to predict the microstructure after thermal exposure. As expected the model was able to predict the microstructures of isothermally aged material with greater accuracy than a component that is exposed in a dynamic and aggressive service environment.

Improvements to the technique can be made by understanding further the effect of complex cooling methods within service components. One of long term goals of the wider research project is to develop a tool for predicting the remaining useful lifetime of components. The first stage of developing this technique is to be able to predict the localised temperature experienced during service, which has been demonstrated within this work. By understanding the effect of exposure time on the microstructural evolution and how the microstructure can be used to predict the evolution after further exposure will be a step towards remaining useful lifetime models. The 3D reconstruction technique showed how it is a powerful

characterisation tool that can reveal information about the microstructure that is not attainable from conventional 2D techniques. The technique allows for accurate input information of phase geometrics into models predicting mechanical properties. In this work it was shown how a 3D dataset can be generated, the potential of the technique and the information that can be derived were introduced. By developing the data analysis will lead to new and novel characterisation techniques for comparing microstructural evolution in complex superalloy coating systems.

9 References

(1) Harman RTC. Gas Turbine Engineering: Applications, Cycles and Characteristics. London; Macmillan; 1981.

(2) Rolls Royce. The Jet Engine. 5th Edition. Derby: Rolls Royce; 1996.

(3) Frutschi HU. Closed-Cycle Gas Turbines: Operating Experience and Future Potential. New York; ASME Press; 2005.

(4) Sims CT, Stoloff NS, Hagel WC. Superalloys II - High Temperature Materials for Aerospace and Industrial Power; John Wiley & Sons; 1987.

(5) Durand-Chare M. The Microstructure of Superalloys; Gordon & Breach Science Publications; 1997.

(6) Bose S. High Temperature Coatings; Elsevier; 2007.

(7) Heubner U. Nickel Alloys; CRC Press; 1998.

(8) Rae CMF, Reed RC. The Precipitation of Topologically Close-Packed Phases in Rhenium-Containing Superalloys. Acta Materialia, 2001 vol 49 issue 19 pg 4113-4125.

(9) Mousavi Anijdan SH, Bahrami A. A New Method in Prediction of TCP Phases Formation in Superalloys. Materials Science and Engineering A. 2005 vol 396 issue 1-2 pg 138-142.

(10) Boyce MP. Gas Turbine Engineering Handbook; Gulf Professional Publishing; 2006.

(11) Donachie MJ, Donachie S. Superalloys: A Technical Guide. 2nd Edition. Ohio; ASM International; 2002.

(12) Hiramatsu N, Uematsu Y, Tanaka T, Kinugasa M. Effects of Alloying Elements on NaCl-Induced Hot Corrosion of Stainless Steels. Materials Science and Engineering A. 1989 vol 120-121 issue Part 1 pg 319-328.

(13) Trubelja MF, Nissley DM, Bornstein NS, Marcin TD. Pratt & Whitney Thermal Barrier Coating Development. 1997.

(14) Wang CJ, Chang YC, Su YH. The Hot Corrosion of Fe-Mn-Al-C Alloy with $NaCl/Na_2SO_4$ Coating Mixtures at 750^{o}C. Oxidation of Metals. 2003 vol 59 issue 1/2 pg 115-133.

(15) Wilkes C. Power Plant Layout Planning-Gas Turbine Inlet Air Quality Considerations. 2007.

(16) Song Y, Zhou C, Xu H. Corrosion Behaviour of Thermal Barrier Coatings Exposed to NaCl Plus Water Vapour at 1050 °C. Thin Solid Films. 2008 vol 516 issue 16 pg 5686-5689.

(17) Strafford KN, Datta PK, Googan CG, Institution of Corrosion Science and Technology. Coatings and Surface Treatment for Corrosion and Wear Resistance. Chichester; Published for the Institution of Corrosion Science and Technology by Ellis Horwood; 1984.

(18) Nesbit JA. COSIM A finite difference computer model to predict ternary concentration profiles assocaited with oxidation and interdiffusion of overlay-coated substrates. August 2000; Technical Report NASA/TM-2000-209271, National Aeronautics and Space Adminstration, Glenn Research Centre.

(19) Wu F, Jordan EH, Ma X, Gell M. Thermally Grown Oxide Growth Behaviour and Spallation Lives of Solution Precursor Plasma Spray Thermal Barrier Coatings. Surface and Coatings Technology. 2008 vol 202 issue 9 pg 1628-1635.

(20) Brindley WJ, Miller RA. Thermal Barrier Coating Life and Isothermal Oxidation of Low-Pressure Plasma-Sprayed Bond Coat Alloys. Surface and Coatings Technology. 1990 vol 43-44 issue Part 1 pg 446-457.

(21) Xu H, Guo H, Liu F, Gong S. Development of Gradient Thermal Barrier Coatings and Their Hot-Fatigue Behaviour. Surface and Coatings Technology. 2000 vol 130 issue 1 pg 133-139.

(22) Schulz U, Fritscher K, Peters M. EB-PVD Y_2O_3- and CeO_2/Y_2O_3-Stabilized Zirconia Thermal Barrier Coatings - Crystal Habit and Phase Composition. Surface and Coatings Technology. 1996 vol 82 issue 3 pg 259-269.

(23) Evans HE, Taylor MP. Oxidation of High Temperature Coatings. Proceedings of the Institution of Mechanical Engineers. 2006 vol 220 issue 1 pg 1-10.

(24) Seo D, Ogawa K, Suzuki Y, Ichimura K, Shoji T, Muruta S. Comparative Study on Oxidation Behaviour of Selected MCrAlY Coatings by Elemental Concentration Profile Analysis. Applied Surface Science. 2008 vol 255 issue 5 pg 2581-2590.

(25) Nesbitt JA, Heckel RW. Modeling Degradation and Failure of Ni-Cr-Al Overlay Coatings. Thin Solid Films. 1984 vol 119 issue 3 pg 281-290.

(26) Chen WR, Wu X, Marple BR, Nagy DR, Patnaik PC. TGO Growth Behaviour in TBCs with APS and HVOF Bond Coats. Surface and Coatings Technology. 2008 vol 202 issue 12 pg 2677-2683.

(27) Nicholls JR, Simms NJ, Chan WY, Evans HE. Smart Overlay Coatings - concept and practice. Surface and Coatings Technology. 2002 vo1 149 issue 2-3 pg 236-244.

(28) Nicoll AR, Wahl G. The Effect of Alloying Additions on MCrAlY Systems - an Experimental Study. Thin Solid Films. 1982 vol 95 issue 1 pg 21-34.

(29) Czech N, Schmitz F, Stamm W. Improvement of MCrAlY Coatings by Addition of Rhenium. Surface and Coatings Technology. 1994 vol 68-69 pg 17-21.

(30) Sohn YH, Lee EY, Nagaraj BA, Biederman RR, Sisson RD. Microstructural Characterization of Thermal Barrier Coatings on High Pressure Turbine Blades. Surface and Coatings Technology. 2001 vol 146-147 pg 132-139.

(31) Schulz U. Phase Transformation in EB-PVD Yttria Partially Stabilised Zirconia Thermal Barrier Coatings During Annealing. J Am Ceram Soc. 2000 vol 83 issue 4 pg 904-910.

(32) Sohn YH, Biederman RR, Sisson RD. Microstructural Development in Physical Vapour-Deposited Partially Stabilised Zirconia Thermal Barrier Coatings. Thin Solid Films. 1994 vol 250 issue 1-2 pg 1-7.

(33) Zhou C, Yu J, Gong S, Xu H. Influence of Water Vapour on the High Temperature Oxidation Behaviour of Thermal Barrier Coatings. Materials Science and Engineering A. 2003 vol 348 issue 1-2 pg 327-332.

(34) Zhou C, Song Y, Wang C, Xu H. Cyclic Oxidation Behaviour of Thermal Barrier Coatings Exposed to NaCl Vapour. Oxidation of Metals. 2008 vol 69 issue 1-2 pg 119-130.

(35) Xu W, Ferry M, Mateescu N, Cairney JM, Humphreys FJ. Techniques for Generating 3D EBSD Microstructures by FIB Tomography. Materials Characterisation. 2007 vol 58 issue 10 pg 961-967.

(36) West GD, Thomson RC. Combined EBSD/EDS Tomography in a Dual-Beam FIB/FEG-SEM. Journal of Microscopy. 2009 vol 233 issue 3 pg 442-450.

(37) Orloff J, Utlaut M, Swanson L. High Resolution Focused Ion Beams - FIB and its Applications. New York; Kluwer Academi/Plenum Publishers; 2003.

(38) Davies RH, Dinsdale AT, Gisby JA, Robinson JAJ, Martin SM. MTDATA – Thermodynamics and Phase Equilibrium Software from the National Physical Laboratory. CALPHAD. 2002. Vol 26 issue 2 pg 229-271.

(39) Karunaratne MSA, Ogden SL, Kenny SD, Thomson RC. A Multicomponent Diffusion Model for Prediction of Microstructural Evolution in Coated Ni Based Superalloy Systems. Materials Science and Technology. 2009 vol 25 issue 2 pg 287.

(40) Berthod P, Kinetics of High Temperature Oxidation and Chromia Volatilisation for a Binary Ni-Cr Alloy. Oxidation of Metals. 2005 vol 64 issue 3/4 pg 235-252

(41) Krukovsky P, Tadlya K, Rybnikov A, Kryukov I, Mojaiskaya N, Kolarik V. Lifetime Modelling for MCrAlY Coatings in Industrial Gas Turbine Blades. Materials Research Brazil. 2004 vol 7 issue 1 pg 43-47.

(42) Pace MT, Thomson RC. Oxidation of MCrAlY Coatings on Ni based Superalloys. Energy Materials: Materials Science and Engineering for Energy Systems. 2007 vol 2 issue 3 pg 181-190.

(43) Gil A, Shemet V, Vassen R, Subanovic M, Toscano J, Naumenko D. Effect of Surface Condition on the Oxidation Behaviour of MCrAlY Coatings. Surface and Coatings Technology. 2006 vol 201 issue 7 pg 3824-3828.

(44) Chen WR, Wu X, Marple BR, Lima RS, Patnaik PC. Pre-Oxidation and TGO Growth Behaviour of an Air-Plasma-Sprayed Thermal Barrier Coating. Surface and Coatings Technology. 2008 vol 202 issue 16 pg 3787-3796.

(45) Smialek JL, Zhu D, Cuy MD. Moisture-Induced Delamination Video of an Oxidised Thermal Barrier Coating. Scripta Materialia. 2008 vol 59 issue 1 pg 67-70.

(46) Combination of Active Instability Control and Passive Measures to Prevent Combustion Instabilities in a 260MW Heavy Duty Gas Turbine. ; 8-11 May; NATO Research and Technology Organisation; 2000.

(47) Mastrodonato B. Performance of Siemens V84.3A Combustion Turbine Peaking Service Experience at Kansas City Power and Light Hawthorn Station. EPRIGEN 1999

(48) McDonald J. RWE npower project meeting.

(49) Zhu D, Miller RA. Development of Advanced Low Conductivity Thermal Barrier Coatings. International Journal of Applied Ceramic Technology. 2004 vol 1 issue 1 pg 86-94.

(50) High Heat Flux Thermal Cycling of Multi-Layered Deposits Using a HVOF Gun. Conference Date: 25-29 May 1998.

(51) Betz W, Brunetaud D, Coutsouradis D, Fischmeister H, Gibbons TB, Kvernes I. High Temperature Alloys for Gas Turbine Applications and Other Applications. Dordrecht, Holland: D. Reidel; 1986.

(52) Bonifaz EA, Richards NL. Modeling cast IN-738 Superalloy Gas Tungsten Arc Welds. Acta Materialia. 2009 vol 57 issue 6 pg 1785-1794.

(53) Wells J. RWE npower project meeting.

(54) Han JC, Dutta S, Ekkad S. Gas Turbine Heat Transfer and Cooling Technology. London: Taylor & Francis; 2000.

(55) Evans AG, Mumm DR, Hutchinson JW, Meier GH, Pettit FS. Mechanisms Controlling the Durability of Thermal Barrier Coatings. Progress in Materials Science. 2001 vol 46 issue 5 pg 505-553.

(56) Bäker M, Rösler J, Affeldt E. The Influence of Axial Loading on the Interface Stresses of Thermal Barrier Coatings. Computational Materials Science. 2009 vol 47 issue 2 pg 466-470.

(57) Steffens H, Babiak Z, Gramlich M. Some Aspects of Thick Thermal Barrier Coating Lifetime Prolongation. Journal of Thermal Spray Technology. 1999 vol 8 pg 517-522.

(58) Feng S, Shollock B, Reed RC, Ryan MP. Analysis of Surface Chemical Contamination on Ex-Service Industrial Gas Turbine Components. TMS Superalloys 2008 pg 681-687.